Faculdade de Engenharia da Universidade do Porto

Near-Infrared Device-Assisted Nanomedicines-Based Cancer Therapy

Sara Inês Pinto Ribeiro do Amaral

Dissertação realizada no âmbito do
Mestrado em Engenharia Biomédica

Supervisor: Dr. Artur M. Pinto, FEUP
Co-supervisor: Dra. Raquel Costa e Almeida, i3S
Co-supervisor: Dra. Inês C. Gonçalves, i3S

Julho 2021

Abstract

Non-melanoma skin cancer has been reported as the most common cancer worldwide with over 3 million diagnoses per year in the USA. Basal cell carcinoma (BCC) comprises about 80% of non-melanoma skin cancers. Current therapies based on surgery or chemotherapy still present unsatisfactory clinical outcomes or associated side effects, demanding alternative treatments.

Phototherapy is a medical treatment based on light exposure and it has been studied as a promising approach for multiple diseases, including skin cancer. Photothermal therapy (PTT) is a minimally invasive phototherapy modality that uses agents capable of converting near-infrared (NIR) light into heat, ultimately inducing cancer cell death, with decreased harm to surrounding healthy tissues. Carbon nanomaterials (CNM) have been studied as phototherapeutic agents, as many of them present high NIR absorbance and high surface area. Among CNM, graphene-based materials (GBM) present exceptional optical and electronic properties, as well as good biocompatibility. The main goal of this dissertation is to apply GBM/anticancer drug-loaded hydrogels as photothermal therapy combined with chemotherapy for skin cancer treatment, namely BCC. To achieve that, specific objectives include: i) production and characterization of GBM, namely nanographene oxide (GOn) and partially reduced nanographene oxide (p-rGOn); ii) production and characterization of a hydrogel (Carbopol 974P NF) loaded with GBM and an anticancer drug, 5-Fluorouracil (5-FU); iii) assessment of their biocompatibility and phototherapeutic effect with and without NIR irradiation on a normal skin cell line and a skin cancer cell line.

GOn was produced using the modified Hummers method (MHM), followed by recirculation through a custom-built high-power ultrasonication probe, while p-rGOn was partially photo-reduced by UV irradiation. Physical characterization by TEM and Zetasizer revealed that graphene sheets with nanometric sizes were achieved, ideal for biomedical applications. Particle size measured by TEM image analysis was 107.0 ± 62.0 and 168.8 ± 149.0 nm for GOn and p-rGOn, respectively. Both materials presented very good water stability for at least 4 months, having zeta potential values below -30 mV. Typical oxygen-containing functional groups were identified in GOn and the intensity of their bands decreased after UV reduction. Similarly, TGA revealed weight losses of 95.5% in GOn correspondent to oxygen-functionalities, which were lower in p-rGOn (68.9%), further confirming that an effective partial reduction took place. UV-Vis spectroscopy demonstrated that p-rGOn presented a 4.4-fold NIR (810 nm) absorption increase, compared with GOn. NIR irradiation assays (810 nm, 150 $mWcm^{-2}$, 30 min) revealed that p-rGOn presented a higher light to heat conversion, within temperatures of interest for phototherapy (> 50 °C), while GOn only achieved a maximum temperature of ≈ 38 °C when irradiated. After identification of p-rGOn increased photoproperties, and previous confirmation

of its water stability, this material was selected for further assays envisioning the desired phototherapeutic application. The achievement of a material with such properties constitutes a complete novelty. The new GBM, p-rGOn, was further studied envisioning incorporation in a Carbopol 974P NF hydrogel together with 5-FU, to assess a potential combined PTT and chemotherapeutic effect.

Regarding the biological assays, first, 5-FU was incubated with human skin fibroblasts (HFF-1) to select a safe range that could be used in pharmaceutical formulations. Concentrations between 0.1 and 1 μg mL^{-1} were considered non-toxic after an exposure time of 72 h (> 70% cell viability, ISO 10993-5:2009(E)). Similarly, 5-FU concentrations that could induce cancer cell death were studied. It has been observed that a concentration of 0.1 μg mL^{-1} was enough to lead to 45% A-431 cancer cells death, after 72 h of incubation.

The biocompatibility of p-rGOn was also evaluated envisioning assuring treatment selectivity. Concentrations below 100 μg mL^{-1} were considered non-toxic to HFF-1 cells after 72 h of incubation. 5-FU was then incorporated in a Carbopol 974P NF hydrogel and incubated with the same cells in the same concentration range, to assess its efficacy when included in the hydrogel. The maximum non-toxic concentration was identified to be 0.5 μg mL^{-1}. Regarding anti-cancer efficacy, a concentration of 0.25 μg mL^{-1} was found to be sufficient to kill 30% of A-431 cells after 72 h.

After ideal p-rGOn (100 μg mL^{-1}) and 5-FU (0.25 μg mL^{-1}) concentrations for incorporation in the Carbopol 974P NF being selected, both HFF-1 and A-431 cells were exposed to NIR irradiation (810 nm, 150 $mWcm^{-2}$, 10 min) in presence of Carbopol 974P NF/p-rGOn/5-FU hydrogels. It has been observed that after 72 h, A-431 cell number reductions of about 78% were achieved. However, without irradiation, similar values were obtained. Moreover, no synergistic effect was observed between 5-FU and p-rGOn. However, all conditions tested were non-toxic for HFF-1 cells.

Hence, a higher irradiation time of 30 minutes was tested, which resulted in almost complete eradication of the cancer cells (90%) after incubation for 72 h with Carbopol 974P NF/p-rGOn/5-FU. However, the increased exposure to irradiation also caused a reduction of 80% on HFF-1 cell number. Therefore, this cancer phototherapy treatment could only be used with careful placement of the formulations at the tumour site and with NIR irradiation focused on it, to avoid damages in healthy cells. Future work will focus on optimizing the irradiation doses needed to achieve a selective treatment, and achieve synergy between p-rGOn and 5-FU effects if possible.

Resumo

O cancro da pele não melanoma tem sido reportado como o cancro mais comum a nível mundial, com mais de 3 milhões de diagnósticos por ano nos EUA. O carcinoma basocelular (BCC) compõe cerca de 80% dos cancros de pele não melanoma. As terapias atuais baseadas em cirurgia ou quimioterapia ainda apresentam resultados clínicos insatisfatórios ou efeitos secundários associados, sendo necessários tratamentos alternativos.

A fototerapia é um tratamento médico baseado na exposição à luz e tem sido estudada como uma abordagem promissora para múltiplas doenças, incluindo o cancro de pele. A fototerapia térmica (PTT) é uma modalidade de fototerapia minimamente invasiva que utiliza agentes capazes de converter luz de infravermelho próximo (NIR) em calor, que por sua vez pode induzir a morte de células cancerígenas, com reduzidos danos nos tecidos saudáveis circundantes. Os nanomateriais de carbono (CNM) têm sido estudados como agentes fototerapêuticos, uma vez que muitos deles apresentam uma elevada absorção NIR e elevada área de superfície. Entre os CNM, os materiais baseados em grafeno (GBM) salientam-se pelas suas propriedades óticas e eletrónicas excecionais, bem como pela sua biocompatibilidade. O principal objetivo da presente dissertação é aplicar hidrogéis contendo GBM/fármacos anticancerígenos em fototerapia combinada com quimioterapia para o tratamento do cancro da pele, nomeadamente o BCC. Para o conseguir, os objetivos específicos incluem: i) produção e caracterização dos GBM, nomeadamente o óxido de grafeno nanométrico (GOn) e o óxido de grafeno parcialmente reduzido nanométrico (p-rGOn); ii) produção e caracterização de um hidrogel (Carbopol 974P NF) com GBM e o fármaco anticancerígeno 5-Fluorouracil (5-FU); iii) avaliação da sua biocompatibilidade e efeito fototerapêutico com e sem irradiação NIR numa linha de células normais da pele e numa linha de células de cancro da pele.

O GOn foi produzido através do método de Hummers modificado (MHM), seguido de recirculação através de uma sonda de ultrassons de alta potência de construção personalizada, enquanto o p-rGOn foi parcialmente foto-reduzido por irradiação com ultravioleta (UV). A caracterização física por TEM e Zetasizer revelou que os GBM eram constituídos por folhas com tamanhos nanométricos, ideais para aplicações biomédicas. O tamanho das partículas medidas pela análise de imagens de TEM foi de 107.0 ± 62.0 e 168.8 ± 149.0 nm para o GOn e o p-rGOn, respetivamente. Ambos os materiais apresentaram boa estabilidade em água durante pelo menos 4 meses, tendo valores de potencial zeta inferiores a -30 mV. Os típicos grupos funcionais contendo oxigénio foram identificados no GOn e a intensidade das suas bandas diminuiu após a redução por UV. Da mesma forma, o TGA revelou perdas de peso de 95.5% para o GOn correspondentes às funcionalidades de oxigénio, que foram inferiores para o p-rGOn (68.9%), confirmando mais uma vez que se verificou uma redução parcial efetiva. A espectroscopia de

UV-Vis demonstrou que o p-rGOn apresentou um aumento de absorção NIR (810 nm) de 4.4 vezes, em comparação com o GOn. Os ensaios de irradiação NIR (810 nm, 150 $mWcm^{-2}$, 30 min) revelaram que o p-rGOn apresentou uma maior conversão da luz em calor, dentro das temperaturas com interesse para a fototerapia (> 50 °C), enquanto o GOn só atingiu uma temperatura máxima de ≈ 38 °C quando irradiado. Após a identificação de que o p-rGOn possuía fotopropriedades superiores e a confirmação prévia da sua estabilidade em água, este material foi selecionado para novos ensaios, tendo em vista a aplicação fototerapêutica desejada. A obtenção de um material com tais propriedades constitui uma completa novidade. O novo GBM, p-rGOn, continuou a ser estudado, tendo em vista a sua incorporação num hidrogel de Carbopol 974P NF juntamente com o 5-FU para avaliar um potencial efeito sinérgico entre PTT e quimioterapia.

Relativamente aos ensaios biológicos, primeiro o 5-FU foi incubado com fibroblastos de pele humana para selecionar uma gama segura que pudesse ser utilizada nas formulações farmacêuticas. Concentrações entre 0.1 e 1 µg mL^{-1} foram consideradas não tóxicas após um tempo de exposição de 72 h (> 70% de viabilidade celular, (ISO 10993-5:2009(E))). Do mesmo modo, foram estudadas concentrações de 5-FU que poderiam induzir morte das células cancerígenas. Observou-se que uma concentração de 0.1 µg mL^{-1} era suficiente para levar à morte de 45% das células cancerígenas A-431, após 72 h de incubação.

A biocompatibilidade do p-rGOn foi também avaliada de forma semelhante com o intuito de assegurar a seletividade do tratamento. Concentrações inferiores a 100 µg mL^{-1} foram consideradas não tóxicas para células HFF-1, após 72 h de incubação. O 5-FU foi então incorporado num hidrogel de Carbopol 974P NF e incubado com as mesmas células na mesma gama de concentrações para avaliar a sua eficácia quando incluído no hidrogel. A concentração máxima não tóxica foi identificada como sendo de 0.5 µg mL^{-1}. Em relação à eficácia anticancerígena, uma concentração de 0.25 µg mL^{-1} foi considerada suficiente para matar 30% das células A-431, após 72 h.

Após as concentrações ideais de p-rGOn (100 µg mL^{-1}) e de 5-FU (0.25 µg mL^{-1}) serem selecionadas para incorporar no Carbopol 974P NF, ambas as células HFF-1 e A-431 foram expostas a radiação NIR (810 nm, 150 $mWcm^{-2}$, 10 min) na presença de hidrogéis de Carbopol 974P NF/p-rGOn/5-FU. Observou-se que após 72 h, foram conseguidas reduções do número de células A-431 de cerca de 78%. No entanto, sem irradiação, foram obtidos valores semelhantes. Além disso, não foi observado qualquer efeito sinérgico entre o 5-FU e o p-rGOn. Contudo, todas as condições testadas foram não tóxicas para as células HFF-1.

Assim, foi testado um tempo de irradiação mais elevado de 30 minutos que resultou na erradicação quase completa das células cancerígenas (90%) após incubação durante 72 h com o Carbopol 974P NF/p-rGOn/5-FU. Contudo, a maior exposição à irradiação também causou uma redução de 80% no número de células HFF-1. Por conseguinte, este tratamento de fototerapia do cancro só poderia ser utilizado com uma colocação cuidadosa das formulações no local do tumor e com irradiação localizada no mesmo, para evitar danos nas células saudáveis. O trabalho futuro irá consistir na otimização das doses de irradiação necessárias para se conseguir um tratamento seletivo e conseguir sinergias entre os efeitos do p-rGOn e do 5-FU, se possível.

The work described in this thesis was conducted at:

LEPABE/FEUP – Laboratório de Engenharia de Processos, Ambiente, Biotecnologia e Energia; Universidade do Porto

i3S/INEB – Instituto de Investigação e Inovação em Saúde; Universidade do Porto

The work described in this thesis was financially supported by:

This work was financed by FEDER funds through the COMPETE 2020 - Operacional Programme for Competitiveness and Internationalisation (POCI), Portugal 2020, and by national funds (PIDDAC) through FCT/MCTES in the framework of the project POCI-01-0145-FEDER-031143, and Base Funding - UIDB/00511/2020 of the Laboratory for Process Engineering, Environment, Biotechnology and Energy – LEPABE. Project 2SMART - engineered Smart materials for Smart citizens, with reference NORTE-01-0145-FEDER-000054, supported by Norte Portugal Regional Operational Programme (NORTE 2020), under the PORTUGAL 2020 Partnership Agreement, through the European Regional Development Fund (ERDF). Artur Pinto thanks the Portuguese Foundation for Science and Technology (FCT) for the financial support of his work contract through the Scientific Employment Stimulus - Individual Call – [CEECIND/03908/2017].

Agradecimentos

A todas as pessoas que passaram pelo meu percurso nestes breves e ao mesmo tempo longos dois anos e àqueles que me acompanham há muitos mais, escrevo esta secção numa tentativa de vos agradecer do fundo do coração.

Ao meu orientador, Artur Pinto, muito obrigada pela oportunidade, por todos os conselhos e correções. À minha co-orientadora, Raquel Almeida, obrigada por tudo o que fizeste por mim. Obrigada por teres "suportado" todas as minhas dúvidas e perguntas de todo o tipo e a todo o momento, obrigada. À minha co-orientadora Inês Gonçalves, obrigada pelas perguntas certas que me "obrigaram" a pensar e a aprender, pelos conselhos e chamadas. Ao Professor Fernão, obrigada por todo o apoio e sugestões essenciais. Filipa, obrigada por toda ajuda no laboratório, quase que foste como uma terceira co-orientadora. Obrigada por aturares todos os meus lamentos, por me "empurrares" para a frente e pelos desabafos. Licínia, obrigada pela tua simpatia, disponibilidade e boa disposição. Por isso e muito mais, obrigada NovaDerma.

Ao meu grupo, "Bioengineering Surfaces", obrigada por me terem integrado mesmo nesta fase difícil. Obrigada por estarem sempre dispostos a ajudar e por me guiarem no "labirinto" que é o i3S. Um obrigada especial a ti Inês, por todos os desabafos, fico à espera do meu vídeo.

Aos meus pais, não há obrigadas que cheguem, mas obrigada por serem a minha força e ânimo, não tinha conseguido sem vocês. Sempre me impulsionaram a seguir o que quisesse e nem pestanejaram depois de ter dito que queria seguir para o mestrado, "faz o que te fizer feliz". Ao meu irmão, obrigada por me chateares a cabeça, por me fazeres rir e por me conheceres tão bem. Aos meus queridos avós, que semana após semana me perguntavam "como estava a bicharada". Obrigada por serem a luz que guia o meu caminho. Aos meus tios e primos, obrigada pelo apoio. Tenho a melhor família do mundo.

Aos meus amigos da faculdade, que cá estão para o bem e para o mal. Silvana, tu mereces todo o meu agradecimento e mais algum, obrigada por seres a minha companheira de todas as horas, obrigada por me teres aturado todos os dias, obrigada não é suficiente. Raquel, Nair e Marco, obrigada por serem os meus Lokos, pelas mensagens, por me aturarem e apoiarem. Inês, eterna parceira, obrigada pelo apoio e por estares sempre lá.

Aos amigos de sempre, Inês, Rita, Alberto, Gonçalo e Maria, obrigada por estarem lá para mim, pelos jantares, pelo convívio, pelas chamadas. Obrigada, família.

Aos amigos do secundário, que grupo tão bonito, o eterno A6. Com vocês sei que posso contar sempre, independentemente do tempo que passe. Bessa, Carol, Mafalda, Bia, Chow, Babi, Mariana e Ruivo, obrigada por bombardearem o meu WhatsApp e me fazerem rir mesmo quando parece impossível.

A todas as pessoas que não estão aqui mencionadas, mas de alguma forma contribuíram para o meu percurso, o meu honesto obrigada.

Sara Amaral

Contents

List of figures

List of tables

Abbreviations, Acronyms and Symbols

0D	Zero dimensional
1D	One dimensional
2D	Two dimensional
3D	Three dimensional
BCC	Basal cell carcinoma
CD	Carbon dots
CNH	Carbon nanohorns
CNM	Carbon nanomaterials
CNT	Carbon nanotubes
DLS	Dynamic light scattering
EPR	Enhanced permeability and retention effect
FTIR	Fourier transform infrared spectroscopy
GBM	Graphene-based materials
GO	Graphene oxide
GOn	Nanographene oxide
GQD	Graphene quantum dots
MWCNT	Multi-walled carbon nanotubes
NIR	Near-infrared radiation
NMSC	Non-melanoma skin cancer
PDT	Photodynamic therapy
p-rGOn	Partially reduced nanographene oxide
PS	Photosensitizer
PTT	Photothermal therapy
rGO	Reduced graphene oxide
ROS	Reactive oxygen species
SWCNH	Single-walled carbon nanohorns
SWCNT	Single-walled carbon nanotubes
TGA	Thermogravimetric analysis
TEM	Transmission electron spectroscopy

Chapter 1

Introduction

1.1 - Context

Non-melanoma skin cancer (NMSC) has been reported as the most frequent cancer worldwide with over 3 million diagnoses per year in the USA [1]. Basal cell carcinoma (BCC) compose about 80% of NMSC [2]. Despite the low mortality or metastasis, BCC may give rise to substantial morbidity because of its damaging local spread [3]. The main cause for this type of skin cancer is exposure to ultraviolet (UV) radiation, being the most common occurrences on body parts frequently unprotected from the sun [2]. The risk of recurrence is significant [3], especially in the first five years after the treatment [2]. Depending on the risk of recurrence or location of the lesion, different therapies are used such as electrodesiccation and curettage, surgery or topical creams for low-risk BCC and chemotherapy and radiotherapy for high-risk BCC. Multiple problems have been reported with these approaches, for instance, electrodesiccation and curettage are invasive, cause poor cosmetic outcomes and possible extended growth in the scar tissue may lead to significant destruction [3]. Besides, topical treatments are only applicable to superficial BCC and have been reported to cause cutaneous reactions [2]. Nowadays, these therapies are based on semi-solid formulations including anticancer drugs such as 5-Fluorouracil (5-FU), Diclofenac and Imiquimod [4]. These secondary effects increase the demand for alternative treatments.

Phototherapy has collected great interest in the scientific community due to its low invasiveness, negligible toxicity, reduced secondary effects, and avoidance of drug resistance. The first uses of light therapy date as far back as 3,500 years ago in the form of sunlight exposure to treat skin conditions (*e.g.*, vitiligo) by ancient Indians and Egyptians [5]. Nowadays, modern phototherapy uses artificial light sources. Photodynamic therapy (PDT) and photothermal therapy (PTT) are the most used phototherapy modalities [6]. PDT is a therapeutic approach relying on photosensitizer (PS) agents to generate reactive oxygen species (ROS), such as singlet oxygen, to destroy tumour cells, under light irradiation [7]. The cytotoxic ROS can harm cells by oxidation of their components, including cellular membrane, proteins or DNA [8]. PDT is more selective than standard treatments because PS can accumulate in the tumours and irradiation can be limited to the lesion site [9]. Besides, this therapy allows multiple cycles of treatment with low invasiveness and minimal systemic effects [10]. PTT is a therapeutic approach that relies on

visible or NIR absorbing agents, which enable light energy conversion into heat, ultimately causing thermal ablation of cancer. Similar to PDT, PTT has increased specificity as the PTT agents preferably accumulate in the lesion site and the irradiation is focused on the tumour site, with no invasiveness [11]. In cancer, tumour tissues vasculature is very dissimilar from normal tissue blood vessels. Their lack of vasculature supporting tissues allows the development of leaky vessels presenting pores with diameters in the range of 100 to 2000 nm in the endothelial gaps. Besides, the ineffective lymphatic system leads to the non-filtering of external molecules as it happens in normal tissues. The small sizes of nanoparticles allow them to permeate and accumulate into tumours, a phenomenon that is known as the enhanced permeability and retention (EPR) effect [12]. An ideal agent for phototherapy should present high radiation absorbance in the desired wavelength and possess the ability to convert light into heat and/or ROS. The capacity of NIR light to penetrate tissues is superior to that of visible light and the biological tissues do not absorb in this range (750-1700 nm) [6].

In the clinics, PDT of cancer has been applied to precancerous keratosis skin lesions and few non-melanoma skin cancers [5]. Some PS are approved by the Food and Drug Administration (FDA, USA) and the European Medicines Agency (EMA, Europe) for cancer treatment. Photofrin® was the first despite its low tissue selectivity, decreased light absorption and it is activated in a wavelength where light has low tissue penetration. To achieve effective treatment, high concentrations of this PS are required, which result in long blood circulation periods. Foscan® was afterwards approved for the treatment of advanced head and neck squamous cell carcinomas and is capable of absorbing light in higher wavelengths. Besides, formulations of aminolaevulinic acid have been approved for dermatological diseases such as actinic keratoses or superficial basal cell carcinomas. Nevertheless, its application is restricted to superficial lesions due to its low tissue penetration [13]. Regarding PTT for cancer treatment, clinical therapies have been mostly focused on device-only approaches since the use of a PTT agent complicates regulatory frameworks and increases costs. Despite being reported as promising, the clinical development of PTT agents is significantly behind PDT ones [5].

Several nanomaterials that absorb light and produce ROS and/or heat have recently been reported in the literature for phototherapy. Nanoparticle-based approaches have been designed including liposomes, gold nanostructures, magnetic nanoparticles or palladium nanosheets, as reviewed elsewhere [14, 15]. However, CNM have been distinguished by their high absorption properties in NIR and visible light regions, meaning that small energy and laser strength is required for a phototherapeutic effect. Also, their suitable dimensions allow them to accumulate in the lesion site, and the high surface area allows their use as drug delivery systems, making them ideal platforms to enable new developments toward improving phototherapy efficiency [6, 16].

As previously mentioned, 5-FU is a US FDA approved anticancer drug used for topical treatments of skin cancers which mechanism of action is based on the inhibition of the enzyme thymidylate synthetase, consequently interfering with the DNA replication. It can be used as a cream or a solution and it has been reported to cause acute local inflammation which lowers patient compliance. Furthermore, the treatment with this anticancer drug is relatively prolonged and its skin penetration is limited [4].

Drug delivery systems such as nanoparticles, liposomes or hydrogels have been extensively studied for a controlled delivery with high cell availability for prolonged periods and specific locations and even using lower doses [17]. Carbopol is a cross-linked polyacrylic acid derivative with a hydrophilic behaviour [18] that has been reported to improve drug delivery to a specific location [19]. The use of these polymers as drug carriers has been significant in dermal

applications with many advantages such as high viscosity, drug compatibility, thermal stability and biocompatibility [20]. Carbopol-based hydrogels are approved (US FDA) for pharmaceutical use with different administration routes due to their long residue time at the lesion site, skin permeation and controlled release properties [21]. Carbopol 974P is widely applied in viscous gels, emulsions and mucoadhesive formulations with elevated treatment specificity to the lesion site [19].

1.2 - Motivation

The secondary effects or low efficiency of current treatments for non-melanoma skin cancer have potentiated the search for alternative approaches such as PTT. Graphene-based materials (GBM) unique properties such as high NIR absorption, nanometric size, large surface area, and biocompatibility justify the increasing number of studies on those materials for biomedical applications, including PTT. The objective of this dissertation was to study PTT combined with chemotherapy using GBM/anticancer drug-loaded hydrogels for transcutaneous delivery of both agents and treatment of dermatological conditions. The use of GBM hydrogels together with drugs used in BCC treatment and their combination with LED-based phototherapy systems constitutes a completely novel approach. The study of a non-invasive selective therapy such as PTT, with low drug doses and minimal or non-secondary effects, might result in an innovative treatment to fight the most common type of cancer.

Multiple works have described GBM potential for cancer phototherapy applications [10]. Yang *et al.* developed PEGylated graphene sheets with nanometric sizes with high absorbance in the NIR region. An efficient *in vivo* PTT was achieved with tumour ablation after NIR laser irradiation [22]. Chang *et al.* used a hydrogel with spinach extract, rGO, gold nanocages and 5-FU for a synergistic treatment that decreased HeLa cells viability to 1.2% after NIR irradiation [23]. These results motivated the use of GBM as efficient phototherapy systems for skin cancer. However, the literature lacks studies that show the selectivity of the treatment by using both cancer cells and healthy ones. Furthermore, there is currently no rGO described as water stable without any functionalization or the use of stabilizing agents. Hence, it would be of great importance to develop a production method to obtain a rGO without further surface modifications, that might lead to the decay of its optical and biological properties, important in the context of PTT.

1.3 - Goals

The main goal of this thesis is to develop GBM hydrogels conjugated with anticancer drugs for combined chemotherapy and photothermal therapy of skin cancer. To achieve this, the following specific aims were addressed:

- Collection of information and organization of a literature review regarding state-of-the-art studies using carbon nanomaterials for application in cancer phototherapy.
- Development of GBM with suitable physico-chemical properties and photothermal effect.
- Production of Carbopol 974P NF hydrogels loaded with GBM and anticancer drugs, namely 5-FU.
- Understanding the effect of GBM/drug-loaded hydrogels on the behaviour of healthy human skin fibroblasts in the presence or absence of NIR irradiation.

- Understanding the phototherapeutic potential of GBM/drug-loaded hydrogels over skin cancer cells, in the presence or absence of NIR irradiation.

1.4 - Structure

This document is divided in six chapters. Besides this introduction, Chapter 2 reviews the state-of-the-art on CNM for phototherapy of cancer, presenting, also the main features of CNM, modifications of interest for desired applications, and biocompatibility and safety issues that should be considered. It is important to mention that this literature review is part of a review article with the title “Carbon nanomaterials for phototherapy of cancer and infections” that is currently being finalized for publication. Chapter 3 describes the materials and methods used in the experimental work performed and Chapter 4 presents the results obtained. Chapter 5 contains the discussion of the most important results, in the light of current literature. Chapter 6 presents the main conclusions withdrawn from the state-of-the-art and the work performed.

Chapter 2

Carbon nanomaterials-based cancer phototherapy

Carbon is a six electron atom with exceptional properties and high plasticity that allows the formation of covalent bonds with other carbon atoms or elements, growing their complexity. CNM unique physical and chemical properties have motivated multiple applications in the biomedical field from bioimaging, to tissue engineering, drug delivery and phototherapy [6, 24]. These materials have a wide range of dimensions, they can be zero-dimensional (0D) with all dimensions below 100 nm, for example, fullerenes, one-dimensional (1D) like CNT, two-dimensional (2D), such as graphene, and three-dimensional (3D), like graphite [25]. Furthermore, crystallinity ranges from complete crystalline allotropic materials, for example, graphite, to complete amorphous such as carbon dots (CD). The hybridization state of the carbon atoms can also vary from sp^2 hybridized carbon, like fullerenes, or sp^3 hybridized atoms such as CD. In this chapter, the principal features of CNM with interest for phototherapy are highlighted and multiple surface modification strategies to enhance their effectiveness are addressed. Then, their multiple applications in cancer are presented and finally, key safety and biocompatibility concerns regarding these nanomaterials are discussed.

2.1 - Structures and properties

Fullerenes consist of 0D nanoparticles with sp^2 hybridized atoms. These CNM are crystalline forms of carbon with most of them being closed hollow cages made of 12 pentagons and several hexagons depending on the total number of carbon atoms [25]. Diameters are in the range of 0.7 to 1.0 nm, with the most commonly studied one, C_{60}, also being considered the lowest size CNM (size $\approx$ 0.71 nm) [25]. Most fullerenes can produce ROS when irradiated by light, therefore having applications as PDT agents [6].

CD consist of 0D nanoparticles mostly composed by sp^3 hybridized atoms. These CNM are quasispherical and amorphous forms of carbon, with diameters in the range of 2 to 10 nm [25]. Increased photoluminescence emission and stability in aqueous solutions are some of their most important characteristics. The first depends on the dimensions of the CD, excitation wavelength or functionalization, while the second is dependent on the number of hydrophilic groups at their surface [6].

Graphene quantum dots (GQD) consist of 0D nanoparticles with sp^2 hybridized atoms. These CNM are crystalline forms of carbon with diameters ranging from 2 to 20 nm [25]. GQD present a structure comparable to a disk and, similar to CD, high photoluminescence emission and water dispersibility [6].

CNT consist of 1D nanoparticles mostly composed by sp^2 hybridized carbon atoms. These CNM are hollow cylinders and hexagonal lattice crystalline forms of carbon, with diameters ranging from 1 to 100 nm. Single-walled carbon nanotubes (SWCNT) have one graphene layer thick walls and usually present diameters between 0.2 and 2 nm, while multi-walled carbon nanotubes (MWCNT) have two or more layers of graphene walls and can be numerous micrometres long [25]. Due to their shape, amphiphilic surface (when functionalized) and size range, CNT can usually navigate through biological membranes or barriers [26].

Carbon nanohorns (CNH) consist of 1D nanoparticles mostly composed by sp^2 hybridized atoms. These carbon materials are closed cages with a similar shape to a horn usually with 2 – 5 nm in diameter and 40 – 50 nm in length. Their chemistry is very similar to that of CNT [27]. While CNT production methods include the deposition of metal as a catalyst causing some cytotoxicity issues, CNH preparation contains metal-free catalysts, reducing the biological toxicity [6].

Graphene consists of two-dimensional (2D) nanoparticles with sp^2 hybridized atoms. This one atom thick sheet composed by hexagons is a crystalline form of carbon that is the base of carbon materials, including fullerenes and CNT. Its structure has a honeycomb lattice with six rings composed of a carbon atom connected to three other [25]. Graphene is the elementary structure of graphite and presents unique properties, such as large surface area, mechanical strength, and electrical and thermal conductivity [28]. However, this nanomaterial is hydrophobic and subsequently difficult to disperse in an aqueous medium, which constitutes a disadvantage regarding its application in the biological field [10]. Its derivatives, on the other hand, commonly named graphene-based materials (GBM) have been extensively used in biomedical applications. Graphene oxide (GO) is analogous to graphene but possesses oxygen-containing functional groups, for example, carboxylate or hydroxyl groups [10]. The polarity and reactiveness of these groups diminish the thermal stability and optical absorption properties, but it might be relevant for promoting dispersibility in polar solvents [28]. Due to its hydrophilic character, GO presents stability in aqueous solutions and low cytotoxicity [10]. Reduced graphene oxide (rGO) is a GO derivative with decreased oxygen-containing groups content, as a consequence of a chemical, thermal or electrochemical reduction procedure. This process partially restores the optical absorbance and the electrical and thermal conductivity, which is relevant regarding uses in PTT. However, it becomes more hydrophobic, decreasing aqueous stability, when compared with GO [10], with further surface functionalization or use of stabilizing agents being a common procedure.

2.2 - Surface modification strategies

Water stability and biocompatibility are key features of nanomaterials when considering biomedical applications. The majority of pristine CNM usually aggregate and precipitate in aqueous solutions because of their strong hydrophobic and π–π interactions. To overcome this disadvantage, covalent and non-covalent surface functionalization and other modifications can be performed, such as element doping [6, 7]. To use these nanomaterials in a phototherapy approach, a balanced functionalization is essential where the stability and integrity of the key properties of the materials are preserved. Details of surface modification strategies used for specific

applications will be presented and discussed in the next sections of this work, therefore only a short introduction is presented in this part. Figure 2.1 depicts representative examples of relevant surface modification approaches for enhancing CNM properties for phototherapeutic applications.

Covalent functionalization is based on chemical reactions with compounds that allow introducing new chemical features of interest at CNM surface to tune desired properties [14]. It can be achieved through chemical oxidation to introduce reactive oxygen-containing functional groups at the CNM surface, such as hydroxyls (-OH) and carboxyls (-COOH). Those groups allow further chemical reactions to form covalent bonds with other molecules, including hydrophilic polymers, drugs/genes or targeting ligands. Both chemical oxidation and the introduction of the previously mentioned molecules can increase water stability and biocompatibility. Fullerenes modification with trimalonic acid increases the carboxylate groups on their cages and allows further conjugation with targeting molecules, such as aptamers, through amide linkage, toward increasing target specificity [29]. GO has been reported multiple times as an effective phototherapy agent when its biocompatibility is increased by PEGylation. An example of this reaction involves the carboxylation of GO and further reaction between the -COOH groups and the -NH_2 groups of aminated poly(ethylene glycol) (PEG) [30]. However, even if the nanomaterial becomes more dispersible and stable in water, covalent functionalization may change its structure, by disrupting the delocalized π-π systems. This can lead to a decrease in CNM key characteristics, such as the photothermal conversion capacities, hindering the phototherapy performance, therefore, covalent functionalization might not always be the ideal solution for enhancing CNM properties [6, 31].

Non-covalent functionalization is based in the coating of CNM with different molecules using several strategies such as electrostatic forces, π–π stacking, van der Waals forces, hydrogen bonding, or hydrophobic and hydrophilic interactions. In the case of amphiphilic molecules, the hydrophobic part is non-covalently anchored to the surface of the nanomaterials and the hydrophilic end extends into the solution providing some stability. Non-biological molecules as pyrene, porphyrin or phthalocyanine derivatives have a high capacity to form π–π stacking at CNM surface, but can be conjugated through the other noncovalent interactions, such as hydrophobic interactions. Nevertheless, biomacromolecules, for example, DNA, RNA or proteins can also stabilize these materials [6, 14, 31]. Although non-covalent functionalization does not disrupt the π-π systems as the covalent modification does, it originates conjugates with weaker stability [6, 31]. In the literature, several studies explore this type of functionalization. CD have been derived from manganese (II) phthalocyanine and conjugated with a PEG derivative through hydrophobic interactions to improve water stability and biocompatibility [32]. CNT can non-covalently bind PS at their surface, as it is the case of chlorine e6 (Ce6) that has been adsorbed at SWCNT surface by π–π interaction [33]. rGO non-covalent functionalization with amphiphilic molecules (grafted hyaluronic acid (HAc) to a poly(maleic anhydride-*alt*-1-octadecene)), has been shown to improve its stability, biocompatibility and targeting capability [34]. Surface adsorption of PEG onto GO surface has been also demonstrated to improve the extent of GO thermal reduction in a single-step protocol, rendering a nanomaterial (rGO-PEG) that is stable in an aqueous environment and possesses high NIR absorption [35, 36]. Additionally, conjugation with PS is usually accomplished through π–π stacking [37-40].

Besides functionalization, other modifications can be done to CNM to enhance their phototherapy characteristics. Element doping is one of them, for example, sulphur-doped CD have been prepared with increased singlet-oxygen quantum yield [41]. Also, GO nanosheets have

been doped with manganese dioxide that catalysed abundant tumour H_2O_2 into O_2, diminishing tumour hypoxia, among other advantages [42].

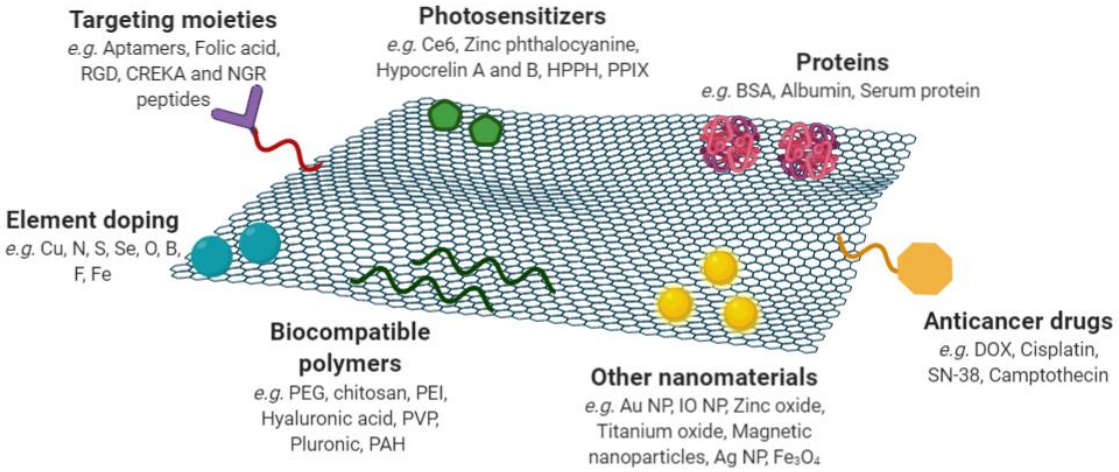

Figure 2.1 – Representative CNM surface modifications for enhancing their biological, drug delivery and phototherapeutic properties. Conjugation with photosensitizers is performed to induce ROS generation and lead to targeted cytotoxic effects. Surface functionalization using proteins, as well as polymers can increase biocompatibility and water stability of CNM in aqueous dispersions. Conjugation of CNM with anticancer drugs enables combined chemotherapy and phototherapy, increasing therapeutic efficiency. Targeting moieties, which may include peptides or other biomolecules are used to increase the specificity of the treatment. CNM can be conjugated with other nanomaterials with properties of interest for target applications, such as NIR absorption for increased photothermal effect. Doping can be used to directly introduce specific elements at CNM surface to alter its optical properties. Created with Biorender.com. Abbreviations: Ag NP, silver nanoparticles; Au NP, gold nanoparticles; BSA, bovine serum albumin; Ce6, chlorine e6; CNM, carbon nanomaterials; CREKA, Cysteinyl-arginyl-glutamyl-lysyl-alanyl peptide; DOX, doxorubicin; Fe_3O_4, iron oxide; HPPH, 2-(1-hexyloxyethyl)-2-devinyl pyropheophorbide-alpha; IO NP, iron oxide nanoparticles; NGR, Asparagine-glycine-arginine peptide; NIR, near-infrared radiation; PAH, poly(allylamine hydrochloride); PEG, poly(ethylene glycol); PEI, polyethylenimine; PPIX, protoporphyrin IX; PVP, polyvinylpyrrolidone; RGD, Arg-Gly-Asp peptide; ROS, reactive oxygen species; SN-38, 7-ethyl-10-hydroxycamptothecin.

2.3 - Cancer Phototherapy using CNM

Cancer phototherapy can be a highly selective treatment as tumour cells are targeted by nano-agents and the irradiation can be directed to the tumour site, minimizing consequences to surrounding normal tissues [43]. As discussed above, CNM are ideal for phototherapy applications due to their unique characteristics, such as suitable nanodimensions and large surface areas. Besides, their extensive ability to absorb light while being stable makes these materials promising phototherapy agents [25]. Different approaches can be used for cancer treatment using light therapy, including PDT, PTT or a combination of both. Such modalities can be used as a stand-alone treatment having minimal side effects in comparison to other cancer treatments (surgery, chemotherapy, radiotherapy), or they can be used as part of combination therapy, as for example, to augment chemotherapy effects and reduce necessary doses. This chapter explores the contribution of CNM or their drug conjugates toward advancing cancer phototherapy.

2.3.1 - Photodynamic therapy

PDT is based on the use of PS, which are capable of producing ROS when irradiated with the appropriate wavelength. Singlet oxygen ($^1O_2$), superoxide ($^{\bullet}O^-_2$) and hydroxyl radical ($^{\bullet}OH$), are examples of ROS, molecules with high cytotoxicity that might be generated to destroy cancer

cells as they uptake the PS [6]. In this approach, irradiation is usually performed in the visible range, from 350 to 700 nm, however, some studies also use NIR (750-1700 nm). Among other advantages, PDT shows insignificant harmful effects to surrounding healthy tissues and low-invasiveness [15]. There are numerous PS, most containing porphyrin molecules that selectively accumulate and persist in tumours, enabling a targeted therapy after light irradiation. Multiple nanomaterials have been conjugated with PS, including CNM, to increase their phototherapeutic efficiency. Also, some CNM such as fullerenes, CD and GQD can act as PS themselves without the need for additional PS molecules [7]. Table 2.1 summarizes the state-of-the-art literature regarding the use of CNM in PDT, including their main characteristics and biological effects. In the literature, promising results were reported using fullerenes, CD, GQD, CNT, GO and rGO, being fullerenes the most extensively studied.

Fullerenes have been widely studied as photodynamic agents due to their capacity of producing high amounts of ROS, under light irradiation [6]. The pristine form of fullerenes is hydrophobic so surface modification is necessary to increase water stability, which can be done with malonic acid [29, 44, 45], block copolymer micelles [46], liposomes [47-49], PEG [45, 50-52], amongst others. Fullerene-based PS might show reduced specificity to tumour cells, thus targeting molecules, such as aptamers [29], or asparagine-glycine-arginine (NGR) peptides [53], can be conjugated to overcome selectivity issues. For example, NGR peptides can recognize tumour vascular antigens. Hence, conjugating nanoparticles with this peptide allows a selective distribution and accumulation in tumour tissues, ultimately enhancing PDT effectiveness [53]. *In vitro*, concentrations commonly used for this nanomaterial vary from 0.45 to 100 µM, while incubation times range between 0.25 to 24 h. Irradiations are usually performed with lamps or lasers with wavelengths between 350-800 nm, and irradiances from 2.12 to 300 $mWcm^{-2}$, during 0.5 to 120 minutes. Fullerenes usually induce between 51 to 100% cancer cell death after PDT treatment. *In vivo*, materials are often injected intratumorously or intravenously, and concentrations used range between 0.424 and 10 mg kg^{-1}. Irradiations are performed with light probes or lasers with a wavelength between 400-700 nm, with irradiances between 89.2 to 100 $mWcm^{-2}$, during 5 to 20 minutes. This range of wavelengths corresponds to visible light as fullerenes are not capable of absorbing in higher wavelengths, such as the NIR region. Even though visible light has low tissue penetration, there are effective phototherapeutic treatments based on irradiation performed on those wavelengths. In the absence of light, fullerenes appear to induce no toxicity as there is no ROS generation. Fullerenes usually induce between 55 to 100% tumour reduction, 9 to 15 days after treatment [50, 51, 54]. Some authors have reported fullerenes to accumulate in the liver and kidney [45, 54], however, they usually end up clearing out of the body [45, 52]. Liu and Tabata used a fullerene (C_{60}) modified with pullulan for PDT using HepG2 hepatoma cell line. The goal was to increase the selectivity for hepatoma cells once pullulan is a water-soluble polysaccharide with high affinity for asialoglycoprotein receptors, expressed at hepatocytes surface. Cells were incubated with the modified fullerenes at a concentration of 1 µM and irradiated with a lamp (400-700 nm, 8 W) for 5 minutes after 6 h of culture, resulting in 60% cancer cell death. Besides, mice were subcutaneously inoculated with the same cell line to induce tumour formation. Modified fullerenes were intravenously injected at a concentration of 300 µM and after 6 h irradiated with a light probe (400-505 nm, 89.2 $mWcm^{-2}$) for 10 minutes. The treatment resulted in over 55% tumour reduction after 15 days, comparing with untreated control [55]. Fullerenes conjugated with drugs have been also explored, namely using 2-methoxyestradiol (2-ME) [53], hematoporphyrin monomethyl ether [54] and doxorubicin (DOX) [56]. For example, Shi *et al.* modified fullerenes with malonic acid and NGR peptide (DMA-C_{60}-NGR) to act as a

delivery system for 2-ME. The selective effect of this drug allows to cause apoptosis of certain tumour cell lines, while not having similar effect in normal cells; however, its cell internalization is limited. The combination of 2-ME with a tumour-targeting drug delivery system, such as DMA-C_{60}-NGR allows easier drug internalization, which was further combined with the ROS generation. A breast cancer cell line incubated with DMA-C_{60}-NGR-2ME at a concentration of 5 μg mL^{-1} and irradiated with a laser (400-700 nm, 60 $mWcm^{-2}$) for 60 minutes after 24 h of culture, has presented a cell death ratio of 100% [53]. Figure 3, illustrates a representative example of CNM applications in cancer PDT. Guan *et al.* conjugated fullerene (C_{70}) with trimalonic acid and Ce6, producing nanovesicles (FCNVs) for PDT in a human lung adenocarcinoma cell line. The nanovesicles were used to surpass Ce6 limitations, such as lack of water solubility and tumour specificity, enhancing fullerenes NIR absorption. Cells were incubated with FCNVs at a concentration of 200 μg mL^{-1} and irradiated with a laser (660 nm, 20 $mWcm^{-2}$) for 10 minutes after 3 h of culture, leading to 95% cancer cell death. Also, mice were subcutaneously inoculated with a modified murine breast cancer cell line to induce tumour formation. FCNVs were intravenously injected at a concentration of 10 mg kg^{-1} and after 4 h irradiated with a laser (660 nm, 100 $mWcm^{-2}$) for 10 minutes. The treatment resulted in 100% tumour reduction after 14 days, comparing with untreated control. Furthermore, histology revealed no significant damage in the main organs [45]. Besides being applied as the core nanomaterial, fullerenes have been used to decorate other nanomaterials and enhance their potential for PDT. Liu *et al.* used fullerenes (C_{60}) conjugated with malonic acid, a PEG derivative, and folic acid (FA) to decorate upconversion nanoparticles (UCNP). Human cervical cancer cells were then incubated with C_{60}-decorated UCNP at a concentration of 800 μg mL^{-1} and after 24 h irradiated with a laser (980 nm, 1.37 Wcm^{-2}) for 10 minutes, resulting in 75% cancer cell death [57].

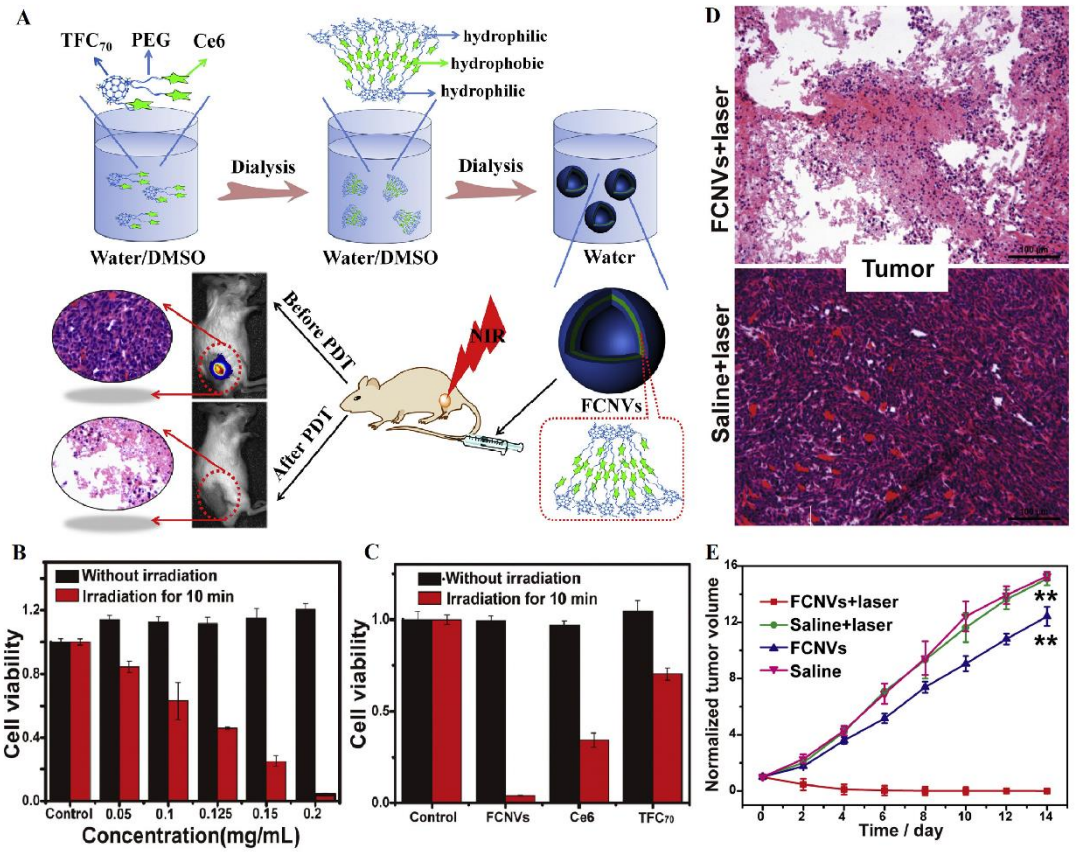

Figure 2.2 – Representative example of CNM use for cancer photodynamic therapy. (A) Production of fullerene/chlorine e6 nanovesicles (FCNVs) as phototherapeutic agent for PDT, by modifying the fullerene (C_{70}) with malonic acid and covalently linking with Ce6. (B) A549 cells viability after incubation with FCNVs at a range of concentrations, with or without laser irradiation (660 nm, 20 $mWcm^{-2}$). (C) A549 cells viability after incubation with FCNVs, free Ce6 and TFC_{70} alone (200 µg mL^{-1}), respectively, with or without laser irradiation (660 nm, 20 mV cm^{-2}). (D) Images of hematoxylin-eosin stained tumour tissue after PDT with FCNVs and respective control. (E) Normalized tumour volumes for the three groups under PDT treatment and control. Adapted from [45]. Abbreviations: A549 cells, human lung adenocarcinoma cell line; Ce6, chlorine e6; CNM, carbon nanomaterial; PDT, photodynamic therapy; TFC_{70}, tri-malonic acid modified fullerene.

CD are another type of CNM with potential to achieve effective PDT effects, as demonstrated in many successful studies [32, 41, 58]. These nanomaterials can either act as PS by directly producing ROS under irradiation or be conjugated with PS in case their ROS generation capacity is low or to further increase the PDT effect. PS usually applied together with CD are zinc phthalocyanine (ZnPc) [59] and boron dipyrromethene (BODIPY)-based PS [60]. *In vitro* studies use CD concentrations varying from 7.5 to 250 µg mL^{-1}, and incubation times ranging between 0.25 to 24 h. Irradiations are usually performed with lamps or lasers with wavelengths between 400-700 nm, and irradiances from 6.5 to 40 $mWcm^{-2}$, during 10 to 30 minutes. Studies often report between 50 to 99% cancer cell death after PDT treatment. *In vivo*, CD-based materials are often injected intratumorously or intravenously, and concentrations range between 0.5 and 10 mg kg^{-1}. Irradiations are performed with light probes or lasers with a wavelength between 540-660 nm, with irradiances between 10 to 300 $mWcm^{-2}$, during 10 to 30 minutes. Studies with these CNM usually result in 60 to 100% tumour reduction, 10 to 15 days after treatment [32, 59-62]. CD can be cleared through the renal route without causing necrosis or damage in the main organs [32, 58, 60, 61]. In a study by Liu *et al.*, manganese phthalocyanine derived CD (Mn-CD) were incubated at a concentration of 20 µg mL^{-1} with a human cervical cancer cell line. The objective

of the Mn-CD was to catalyse H_2O_2 and generate oxygen to overcome tumour hypoxia, enhancing the PDT effect. After 4 h of culture, laser (635 nm) irradiation was performed for 10 minutes, leading to 99% cancer cell death. Besides, mice were subcutaneously inoculated with a murine breast cancer cell line to induce tumour formation. Modified CD were injected at a concentration of 200 μg mL^{-1} and irradiated using the same setting from *in vitro* experiments. The treatment resulted in 100% tumour reduction after 14 days, comparing with untreated control [32]. Similar to fullerenes, efficient PDT treatment has been reported using CD decorating other nanomaterials. Zheng *et al.* used CD doped carbon nitride nanoparticles (PCCN) in a murine breast cancer cell line. Cells were incubated with PCCN at a concentration of 10 μg mL^{-1} and irradiated with a laser (630 nm, 40 $mWcm^{-2}$) for 5 minutes, resulting in approximately 40% cancer cell death [63].

GQD also have PS capabilities, being able to produce ROS after irradiation. These CNM can be further conjugated with PS, like Ce6 [64], when their effect is insufficient. *In vitro*, concentrations commonly used for this nanomaterial vary from 0.25 to 200 μg mL^{-1}, while incubation times range between 4 to 24 h. Irradiations are usually performed with lamps or lasers with wavelengths between 365-650 nm, and irradiances from 1.03 to 100 $mWcm^{-2}$, during 5 to 20 minutes. Studies with GQD usually result in 60 to 99.9% cancer cell death after PDT treatment. *In vivo*, they are often injected intratumorously or intravenously, and concentrations used range between 2.5 and 4 mg kg^{-1}. Irradiations are performed with light probes or lasers with a wavelength between 400-800 nm, with irradiances between 80 to 200 $mWcm^{-2}$, during 10 to 30 minutes. GQD PDT usually results in 80 to 100% tumour reduction, 14 to 25 days after treatment [58, 64-67]. Liver accumulation has been reported and justified once the reticuloendothelial system (RES) organs uptake graphene derivatives. However, after a few hours, the materials are cleared from the body [64]. Kuo *et al.* conjugated GQD with Ce6 through a disulfide linker (GQD-SS-Ce6) for PDT in a human cervical cancer cell line. The authors expected that the GQD-SS-Ce6 would selectively affect tumour cells, once the high glutathione concentration present in tumour tissues would cleave the disulfide linker and release the Ce6, that after irradiated by light would destroy the tumour. Cells were incubated with the GQD/Ce6 conjugate using a PS concentration of 2 μM and irradiated with a laser (650 nm, 20 $mWcm^{-2}$) for 5 minutes after 24 h of incubation, which induced 70% cancer cell death. *In vivo* studies were performed using mice with tumour xenografts through cancer cell inoculation. Modified GQD were intravenously administered at a PS concentration of 2.5 mg kg^{-1} and after 2 h irradiated with a laser (650 nm, 200 $mWcm^{-2}$) for 30 minutes. The treatment resulted in over 80% tumour reduction after 14 days, comparing with untreated control. Some liver accumulation was observed, however, after 4 hours, the materials were cleared from the body [64]. As a strategy to enhance treatment effectiveness, GQD have been conjugated with anticancer drugs. Ju *et al.* produced nanosized GQD modified with a charge-reversal agent (3-Aminopropyl)triethoxysilane (APTES). This nanoparticle acted as a drug carrier for DOX (N-GQD-DOX-APTES) leading to increased drug uptake in cancer cells, as seen by an intense fluorescence in the nuclei of breast cancer cells treated with N-GQD-DOX-APTES, as opposed to free DOX. Combining this drug carrier with PDT allowed enhanced treatment (80% cell death) when comparing with free DOX (70% cell death) [68]. Furthermore, effective PDT treatments have been described with GQD decorating other materials such as UCNP [65, 67, 69]. Zhang *et al.* doped UCNP with GQD and conjugated it with a rhodamine derivative, TRITC for PDT in a murine breast cancer cell line. Cells were incubated with conjugated nanoparticles at a concentration of 160 μg mL^{-1} and irradiated with a laser (980 nm, 1.5 Wcm^{-2}) for 8 minutes, resulting in approximately 75% cancer cell death [65].

CNT can load PS at their surface by covalent or non-covalent methods, such as 5-aminolevulinic acid (5-ALA) [70] and Ce6 [33, 71]. These CNM require further functionalization to improve their biocompatibility [70], dispersibility [33, 71, 72] or selectivity [72]. *In vitro*, concentrations commonly used for this nanomaterial vary from 10 to 100 μM, while incubation times range between 1 to 24 h. Irradiations are usually performed using lasers with wavelengths between 300-2600 nm, and irradiances from 98 to 150 $mWcm^{-2}$, during 10 to 120 minutes. As CNT usually present high NIR absorption, the use of such agents enables the treatment of deeper located tumours, given the penetration capacity of NIR radiation. Studies with CNT usually present a cancer cell death between 63 and 90% after PDT treatment. An *in vivo* study with CNT resulted in a 45% tumour reduction, 10 days after treatment with lamp irradiation (300-2600 nm, 500 W) [73]. In a study by Huang *et al.*, MWCNT were functionalized with a polyamidoamine dendrimer to act as a delivery vehicle to the PS 5-ALA for PDT of a human gastric cancer cell line. Cells were incubated with modified CNT at a concentration of 100 μM and irradiated with a laser (632.8 nm, 4.35 J cm^{-2}) for 10 minutes after 24 h of culture. The treatment resulted in 90% cancer cell death [70]. In the majority of the studies found in literature, CNT are combined with PS loaded at their surface to be used as PDT agents. However, a study was found where SWCNT covalently functionalized with polyethylenimine (SWCNT-PEI) were able to act as a PS by themselves. Wang *et al.* incubated a mice melanoma cell line with SWCNT-PEI at a concentration of 50 μg mL^{-1} and performed irradiation with a halogen lamp (300-2600 nm, 500 W, 120 min) after 6 h of culture. The treatment resulted in 65% cancer cell death. Furthermore, the PDT effect was also evaluated *in vivo* in female C57 mice subcutaneously injected with the same cell line. SWCNT-PEI were administered by intratumoral injection at a concentration of 50 μg mL^{-1} and irradiated as mentioned above. The treatment resulted in 45% tumour reduction after 9 days, comparing with untreated control [73].

GO can also load PS and be internalized into tumour cells, being able to be used to achieve effective PDT. Nonetheless, surface modifications can be used to increase targetability [39, 40, 74] and biocompatibility [39]. Some PS that were used with this nanomaterial include hypocrellin A (HA) [75], Ce6 [40, 76, 77], hypocrellin B [78] and ZnPc [79], among others. *In vitro*, concentrations commonly used for this nanomaterial vary from 0.49 to 100 μg mL^{-1}, while incubation times range between 1 to 24 h. Irradiations are usually performed using lasers with wavelengths between 400-1100 nm, and irradiances from 8 to 200 $mWcm^{-2}$, during 0.75 to 30 minutes. Studies with GO usually report between 40 to 92.4% cancer cell death after PDT treatment. *In vivo*, materials are often injected intratumorously or intravenously, and concentrations used between 0.5 and 1 mg kg^{-1}. Irradiations are performed using lasers with a wavelength between 660-671 nm and irradiances between 75 to 100 $mWcm^{-2}$, during 1 to 30 minutes. Studies with these CNM usually result in between 73 to 100% tumour reduction, 14 to 28 days after treatment [42, 80, 81]. Some studies reveal no damage or toxicity to be found in the main organs after treatment with GO [42, 80]. Huang *et al.* used GO conjugated with FA, as a targeted delivery system, for the PS Ce6 to perform PDT in a MGC803 cell line. Cells were incubated with modified GO at a concentration of 100 μM and irradiated with a laser (632.8 nm, 30 $mWcm^{-2}$) for 10 minutes after 24 h of culture, resulting in a cancer cell death of 90% [40]. Effective outcomes have been also obtained combining PDT with chemotherapeutics, for example, DOX [81], 7-ethyl-10-hydroxycamptothecin [38] or cisplatin (Pt) [42].

The reduced form of GO has also demonstrated potential as a PDT agent. The large surface area of this CNM allows the loading of PS, such as Ce6 [82] and protoporphyrin IX (PPIX) [83] or anticancer drugs, such as camptothecin (CPT) [84]. *In vitro*, concentrations commonly used

for this nanomaterial vary from 1 to 500 μg mL^{-1}, while incubation times are around 24 h. Irradiations are usually performed with lasers with wavelengths between 365-671 nm, and irradiances from 3.7 to 30 $mWcm^{-2}$, during 3 to 40 minutes. PDT treatment with rGO resulted in between 59.6 and 90% cancer cell death. *In vivo* studies were not found with this CNM, therefore, further research is required on this topic. A study by Huang *et al.* reported a rGO model that conjugates biocompatibility and receptor-targeted drug delivery. Authors coated rGO with polyvinylpyrrolidone (PVP) and functionalized it with arginine-glycine-aspartate (RGD) peptide and Ce6 for PDT assays using a human gastric cancer cell line. Cells were incubated with modified rGO at a PS concentration of 50 μM and irradiated with a laser (671 nm, 30 $mWcm^{-2}$) for 3 minutes after 24 h incubation. The treatment resulted in over 90% cell cancer death [82].

In the literature, PS and drug loading have been achieved through different methods. The most common strategies used include covalent functionalization through linkers [45, 64], non-covalent functionalization through π-π stacking [33, 75] or physical adsorption [53, 76]. Drug loading has been quantified in two main ways. As loading capacity (LC), also named loading amount which represents the weight of drug loaded per weight of the nanoparticle (often shown as mg of drug/mg of CNM); or as loading efficiency (LE), which represents the weight of the drug loaded in the nanomaterial divided by the total weight of drug initially available (often reported as a percentage). Several studies report loading values without describing the calculations presented, therefore Tables 2.1, 2.2, and 2.3 present LC or LE as described in the articles. Few studies report the combination of fullerenes with PS or anticancer drugs, obtaining extremely variable outcomes (LC of 140% [53] and LE between 57-125%). No loading quantification was found in studies reporting the use of CD and only one study quantified GQD LC with Ce6 which was of about 40% [64]. On the other hand, CNT, GO and rGO large surface area usually allows effective loading of PS. Studies have described the use of CNT in conjugation with PS, reporting a LE of 70% and a LC of 130%. In the case of GO, values reported are also quite variable (LC values are in the range of 3 to 115% and LE varies from 50-130%). Furthermore, rGO studies were found with LE values of 7% for the PS Ce6 [82] and LC values of 21 and 22% for the PS 4-hydroxy coumarin and the anticancer drug CPT [84]. Drug loading outcomes are strongly dependent on the method used, as well as on CNM properties, including size, surface chemistry and available surface area. Studies reporting PS or drug loading at CNM surface have been described above and further details can be found in Table 2.1.

For each nanomaterial, surface modification, concentration, and irradiation wavelength are only some of the many parameters that can influence the results. The lack of information in some studies, such as the concentration of the nanomaterial only or the duration of the incubation, for example, makes comparison and withdrawing of conclusions difficult. Taking this into consideration, the comparison between the presented studies was performed whenever possible and main conclusions are presented next.

In general, CNM can be divided into two groups. On one hand, fullerenes, CD and GQD are able of photo-induced ROS production by themselves, bypassing the need to incorporate any other photoactive agents. Among these three nanomaterials, fullerenes are the most well-studied in the literature, and their application in PDT usually resulted in cancer cell death ratios superior to 50%, even at low concentrations (below 10 μM), while *in vivo* studies have shown tumour reductions of over 55% after 9 to 15 days. Furthermore, fullerenes conjugated with trimalonic acid and Ce6 have been reported to be excreted without damaging other tissues [45] and fullerenes conjugated with PEG derivatives have been stated to be eliminated from blood circulation [51]. These modifications are examples of ways to minimize the potential toxicity of fullerenes, which is a

general concern regarding the biomedical use of nanomaterials, being therefore further discussed in detail in Section 5. CD usually resulted in over 50% cancer cell death ratios in concentrations up to 250 μg mL^{-1} *in vitro*, whereas *in vivo* studies often report tumour reductions of over 60% after 10 to 15 days of treatment. GQD have been showing promising results, inducing cancer cell death ratios over 60% after *in vitro* treatment using concentrations ranging between 0.25 and 200 μg mL^{-1}. *In vivo* studies with this CNM usually result in over 80% tumour reduction, 14 to 25 days after treatment. As seen above, the unique photoproperties of fullerenes, CD and GQD have contributed for the application of these CNM as active photosensitizing agents. Furthermore, decorating other core nanomaterials with these materials have also resulted in efficient therapies. On the other hand, researchers have taken advantage of CNT, GO and rGO large surface area to load different PS molecules, allowing the exploitation of these CNM for PDT. CNT have been studied using concentrations ranging between 10 and 100 μM that resulted in *in vitro* cancer cell deaths between 60 and 90%. An *in vivo* study has shown a tumour growth inhibition of 45% after 9 days with irradiation of 300-2600 nm and 500 W. As for GO and rGO, *in vitro* studies report the use of concentrations in the range of 0.5 to 500 μg mL^{-1} resulting in over 40% cancer cell death ratios. *In vivo* studies using GO usually report over 73% tumour reduction, 14 to 28 days after treatment. No *in vivo* studies were found using rGO for PDT.

Overall, cancer CNM-based PDT has been extensively studied in the literature. The first CNM group comprises fullerenes, CD and GQD, with excellent PS activity through ROS generation. The second group includes CNT and GBM, which exhibit poor PDT performance if unmodified, but can be improved with the loading of PS. By altering the nanomaterial surface or conjugating it with PS, CNM limitations can be surpassed, resulting in potential PDT approaches. The results already present in the literature potentiate the use of these materials in cancer PDT in the future, but more comprehensive studies regarding toxicity and CNM fate *in vivo* are needed.

Table 2.1 - Selected recent studies on carbon nanomaterials for cancer photodynamic therapy.

CNM	Particle size	Surface modification	Conjugated drug/PS	Biological studies *in vitro*		Biological studies *in vivo*		Ref.
				Parameters	Cell death	Parameters	Tumour reduction	
Fullerenes	s ≈ 150 nm	Trimalonic acid Aptamer R13	N/A	A549 cells [TF_{70}-R13] = 10 μM Incubation: 3 h I: 400–700 nm, 20 $mWcm^{-2}$, 30 min	≈ 99.9%	N/A	N/A	[29]
	N/S	Porphyrin	N/A	Hep-2 cells [P-C_{60}] = 1 μM Incubation: 24 h I: 350–800 nm, 60 $mWcm^{-2}$	≈ 80%	N/A	N/A	[85]
	N/S	One quarternary pyrrolidinium group (BF4)	N/A	[1]J774 cells, [2]LLC cells and [3]CT26 cells [BF4] = 2 μM Incubation: 24 h I: 400–700 nm, 150 $mWcm^{-2}$	≈ [1]95, [2]94 and [3]80%	N/A	N/A	[86]
	s ≈ 92 nm	Block copolymer micelle-incorporated	N/A	HeLa cells [C_{60}] = 2.5 μM Incubation: 24 h I: 350–500 nm, 19 $mWcm^{-2}$, 120 min	≈ 98.7%	N/A	N/A	[46]
	N/S	Diphenylaminofluorene modified with 1,1-dicyanoethylenyl (>CPAF-C_n)	N/A	HeLa cells [C_{60}(>CPAFC-$_{2M}$)] = 5.0 μM Incubation: 3 h I: 400–700 nm, 100 $mWcm^{-2}$, 33 min	≈ 60%	N/A	N/A	[87]
	N/S	Dimalonic acid (DMA)	N/A	HeLa cells [DMA C_{60}] = 40 μM I: Halogen lamp, 300 W, 30 min, 3x	≈ 63%	N/A	N/A	[44]
	N/S	Pyropheophorbide *a*	N/A	Jurkat cells [Pyro] = 2 μM	≈ 58%	N/A	N/A	[88]

		(Pyro) derivative: Hexa-adduct		Incubation: 24 h I: 668 nm, 2.12 $mWcm^{-2}$, 0.5 min				
Fullerenes	s ≈ 80 ± 27 nm	Lipid-membrane-incorporated (LMI)	N/A	HeLa cells [C_{70}] = 5 μM Incubation: 24 h I: 400–740 nm, 57 $mWcm^{-2}$, 60 min	≈ 89%	N/A	N/A	[47]
	s ≈ 170 ± 15 nm	Cerasome-incorporated (CI)	N/A	HeLa cells [CIC_{70}] = 5 μM Incubation: 24 h I: 400–740 nm, 57 $mWcm^{-2}$, 60 min	≈ 100%	N/A	N/A	[48]
	s ≈ 111 ± 27 nm	LMI	N/A	HeLa cells [LMI] = 50 μM Incubation: 24 h I: 350–500 nm, 19 $mWcm^{-2}$, 120 min	≈ 84.8%	N/A	N/A	[49]
	N/S	γ - cyclodextrin	N/A	HeLa cells [C_{70}] = 3.0 μM Incubation: 15 min I: 400–740 nm, 54 $mWcm^{-2}$, 30 min	≈ > 90%	N/A	N/A	[89]
	N/S	N-methylpyrrolidinium (BB4)	N/A	CT26Luc cells [BB4] = 2 μM Incubation: 24 h I: 400–700 nm, 150 $mWcm^{-2}$	≈ > 99%	BALB/c mice inoculated with CT26Luc cells [BB4] = 5 mg kg^{-1} I: 400–700 nm, 100 $mWcm^{-2}$	10 days survival advantage	[90]
	N/S	Pullulan	N/A	HepG2 cells [C_{60}] = 1 μM Incubation: 6 h I: 400–700 nm, 8 W, 5 min	≈ 60%	Nude mice inoculated with HepG2 cells [C_{60}-pullulan] = 300 μM I: 400–505 nm, 89.2 $mWcm^{-2}$, 10 min t: 15 days	≈ > 55%	[55]
	s ≈ 31 nm tn ≈ 9 nm	Trimalonic acid	Chlorin e6 (Ce6) Loading efficiency (LE): ≈ 57 wt %	A549 cells [FCNVs] = 200 μg mL^{-1} Incubation: 3 h I: 660 nm, 20 $mWcm^{-2}$, 10 min	≈ 95%	Female Balb/c mice injected with 4T1-*luc* cells [FCNVs] = 10 mg kg^{-1} I: 660 nm, 100 $mWcm^{-2}$, 10 min t: 14 days	≈ 100%	[45]
	N/S	Poly(ethylene glycol) (PEG) Gadolinium (Gd)	N/A	Meth AR1 cells [C_{60}-PEG-Gd] = 100 μM I: 400-700 nm, 8 W, 40 min	≈ 80%	CF1 mice inoculated with Meth AR1 cells [C_{60}-PEG-Gd] = 2780 μM I: 400–505 nm, 89.2 $mWcm^{-2}$, 10 min t: 10 days	≈ > 75%	[50]
	d ≈ 14–42 nm	PEG	N/A	Meth AR1 cells [C_{60}–PEG] = 10 μM I: 400–700 nm, 8 W, 40 min	≈ 80%	CF1 mice inoculated with Meth AR1 cells [C_{60}–PEG] = 0.3 mM I: 400–505 nm, 89.2 $mWcm^{-2}$, 10 min t: 10 days	≈ > 70%	[51]
	N/S	PEG	N/A	N/A	N/A	Female CDF_1 mice inoculated with Meth A cells [C_{60}–PEG] = 0.424 mg kg^{-1} I: 400–505 nm, 89.2 $mWcm^{-2}$, 20 min t: 11 days	≈ > 95%	[52]
	s ≈ 169.7 ± 2.9 nm	DMA Asparagine-glycine-arginine (NGR) peptide DSPE-PEG2000-maleimide	2-Methoxyestradiol (2ME) Loading capacity (LC): 140.1 wt%	MCF-7 cells [2ME] = 5 μg mL^{-1} Incubation: 24 h I: 400–700 nm, 60 $mWcm^{-2}$, 60 min	≈ 100%	N/A	N/A	[53]
	s ≈ 163.8 ± 3.7 nm d ≈ 5–10 nm	Iron oxide nanoparticles (IO NP) PEG	Hematoporphyrin monomethyl ether (HMME) LE: 125.3%	B16-F10 cells [HMME] = 10 μg mL^{-1}, [C_{60}-IO NP-PEG] = 7.98 μg mL^{-1} Incubation: 24 h I: 532 nm, 300 $mWcm^{-2}$, 5 min	≈ 95%	Female C57 mice injected with B16-F10 cells [HMME] = 5 mg kg^{-1}, [C_{60}-IO NP-PEG] = 4 mg kg^{-1} I: 532 nm, 100 $mWcm^{-2}$, 5 min t: 9 days	≈ > 70%	[54]

Fullerenes	s ≈ 100 nm	N/A	Doxorubicin (DOX) Release (R): ≈ 20%	CCRF-CEM cells [C_{60}-DOX] = 0.45 μM Incubation: 24 h I: 405 nm, 10 J cm^{-2}	≈ 51%	N/A	N/A	[56]
CD	d ≈ 110 nm HD ≈ 162 nm	Precursor: Manganese(II) phthalocyanine DSPE-mPEG	N/A	HeLa cells [Mn-CD] = 20 μg mL^{-1} Incubation: 4 h I: 635 nm, 10 min	≈ 99%	4T1-tumour-bearing mice [Mn-CD] = 200 μg mL^{-1} I: 635 nm, 10 min t: 14 days	≈ 100%	[32]
	d ≈ 4.5 ± 0.2 nm	Folic acid (FA) PEG	Zinc phthalocyanine (ZnPc)	HeLa cells [CD-PEG-FA/ZnPc] = 100 μg mL^{-1} Incubation: 12 h I: 660 nm, 30 $mWcm^{-2}$, 10 min	≈ 91.8%	Balb nude mice injected with HeLa cells [ZnPc] = 0.5 mg kg^{-1} I: 660 nm, 300 $mWcm^{-2}$, 20 min t: 10 days	≈ > 60%	[59]
	d ≈ 2.8 nm	Copper (Cu) doped	N/A	HeLa cells [Cu-CD] = 250 μg mL^{-1} Incubation: 24 h I: 400−700 nm, 40 $mWcm^{-2}$, 12 min	≈ 50%	N/A	N/A	[91]
	d ≈ 3.72 ± 0.67 nm	Precursors: Diketopyrrolopyrrole (DPP) Chitosan	N/A	HepG2 cells [DPP CD] = 200 μg mL^{-1} Incubation: 12 h I: 540 nm, 15 $mWcm^{-2}$, 10 min	≈ 70%	Female Kunming mice injected with H22 cells I: 540 nm, 15 $mWcm^{-2}$, 10 min t: 12 days	≈ > 80%	[61]
	d ≈ 3–6 nm	Precursor: Ruthenium (II) (Ru (II))	N/A	HeLa cells [Ru-CD] = 250 μg mL^{-1} Incubation: 4 h I: White light, 6.5 $mWcm^{-2}$, 30 min	≈ 82.5%	N/A	N/A	[92]
	d ≈ 3.6 ± 0.6 nm	Selenium and Nitrogen (Se/N) doped	N/A	MCF-7 cells [Se/N-CD] = 7.5 μg mL^{-1} Incubation: 15 min I: 550 nm, 10 $mWcm^{-2}$, 10 min	> ≈ 85%	Male BALB/c mice injected with 4T1 cells [Se/N-CD] = 2.5 mg kg^{-1} I: 550 nm, 10 $mWcm^{-2}$, 20 min t: 15 days	≈ > 60%	[62]
	d ≈ 22.26 nm h ≈ 4.28 nm	Sulphur (S) doped	N/A	UM1 cells [S-CD] = 100 nmol L^{-1} Incubation: 24 h I: 420 nm, 2.8125 W	≈ 95%	N/A	N/A	[41]
	s ≈ 218 nm	PEG	Boron dipyrromethene (BODIPY)	HeLa cells [CCOF-2@PEG] = 50 μg mL^{-1}	≈ 85%	U14 cells injected in mice [CCOF-2@PEG] = 10 mg kg^{-1} I: LED, 30 min t: 12 days	≈ > 85%	[60]
	s ≈ 5 nm HD ≈ 11.7 nm	Gd	N/A	SCC7 cells [Gd@GCNs] = 50 μg mL^{-1} Incubation: 2 h I: LED, 15 $mWcm^{-2}$, 20 min	≈ 85%	SCC7 tumour-bearing nude mice [Gd] = 0.1 mmol kg^{-1} I: LED, 100 $mWcm^{-2}$, 30 min t: 12 days	≈ 90%	[58]
GQD	d ≈ 56.6 ± 8.7 nm h ≈ 1.9 ± 0.8 nm	N/A	N/A	U251 cells [GQD] = 200 μg mL^{-1} I: 465−475 nm, 1 W, 10 min	≈ 60%	N/A	N/A	[93]
	d ≈ 2–6 nm	N/A	N/A	HeLa cells [GQD] = 1.8 μM Incubation: 4 h I: 6.5 $mWcm^{-2}$, 10 min	≈ 80%	Female BALB/nu mice injected with MDA MB-231 cells [GQD] = 4 mg kg^{-1} I: 400–800 nm, 80 $mWcm^{-2}$, 10 min t: 25 days	≈ 100%	[66]
	s ≈ 1.5–5.5 nm	N/A	N/A	[1]B16-F10 cells and [2]MCF-7 cells [GQD] = 0.23 μM Incubation: 4 h I: 365 nm, 1.03 $mWcm^{-2}$, 5 min	≈ [1]99.9 and [2]93%	N/A	N/A	[94]
	s ≈ 1.2–2.5 nm tn ≈ 1.7–2.5 nm	N/A	N/A	HeLa cells [GOQDs] = 0.25 μg mL^{-1} Incubation: 24 h I: white light, 100 $mWcm^{-2}$, 10 min	≈ 80%	N/A	N/A	[95]

GQD	d ≈< 10 nm	Disulfide bond (SS)	Ce6 LC: 42.54%	HeLa cells [Ce6] = 2 μM Irradiation: 24 h I: 650 nm, 20 mWcm^{-2}, 5 min	≈ 70%	Mice injected with HeLa cells [Ce6] = 2.5 mg kg^{-1} I: 650 nm, 200 mWcm^{-2}, 30 min t: 14 days	≈ > 80%	[64]
	d ≈ 4 nm	Nitrogen (N) doped 3-(aminopropyl) triethoxysilane (APTES)	DOX R: 36.0%	MDA-MB-231 cells [DOX] = 10 μg mL^{-1} Incubation: 12 h I: 622 nm, 6.8 mWcm^{-2}, 20 min	≈ 80%	N/A	N/A	[68]
CNT	N/S	Polyethylenimine (PEI)	N/A	B16-F10 cells [SWNT] = 50 μg mL^{-1} Incubation: 6 h I: 300−2600 nm, 500 W, 120 min	≈ 65%	Female C57 mice injected with B16-F10 cells [SWNT] = 50 μg mL^{-1} I: 300−2600 nm, 500 W t: 9 days	≈ 45%	[73]
	N/S	Polyamidoamine dendrimer	5-aminolevulinic acid (5-ALA)	MGC803 cells [5-ALA-dMNT] = 100 μM Incubation: 24 h I: 632.8 nm, 4.35 J cm^{-2}, 10 min	≈ 90%	N/A	N/A	[70]
	s ≈ 203 ± 6.6 nm	Hyaluronic acid (HAc)	Ce6 LE: 70%	Caco-2 cells I: 660 nm, 10 J cm^{-2}, 14 min	≈ 84.9%	N/A	N/A	[33]
	d ≈ 1–5 nm l ≈ 1–5 μm	FA	Zinc monoaminophthalocyanine (ZnMAPc)	A375 cells [ZnMAPc-FA-SWCNT] = 10 μM Incubation: 24 h I: 676 nm, 98 mWcm^{-2}	≈ 63%	N/A	N/A	[72]
	tn ≈ 1–2 nm	Chitosan	Ce6 LC: 128%	HeLa cells [Chitosan–Ce6–SWCNT] = 50 μg mL^{-1} Incubation: 1 h I: 630 nm, 150 mWcm^{-2}, 10 min	≈ 90%	N/A	N/A	[71]
GO	s ≈ 20 nm tn ≈ 0.77 nm	FA	Zinc oxide (ZnO)	HeLa cells [GO–FA–ZnO] = 100 μg mL^{-1} Incubation: 1 h I: 400–1100 nm, 48.6 J cm^{-2}, 20 min	≈ 90%	N/A	N/A	[74]
	Th ≈ 0.9 nm	N/A	Titanium dioxide (TiO_2)	HeLa cells [GOT] = 100 μg mL^{-1} Incubation: 1 h I: > 400 nm, 54 mWcm^{-2}, 20 min	≈ 90%	N/A	N/A	[96]
	s ≈ 200–400 nm	N/A	Hypocrellin A (HA) LC: 1 mg mg^{-1}	HeLa cells [HA] = 2.75 μg mL^{-1} I: 1 min	≈ 70%	N/A	N/A	[75]
	s ≈< 100 nm	HAc	Ce6 LC: 115% R: 30%	HeLa cells [Ce6] = 1 μg mL^{-1} Incubation: 6 h I: 670 nm, 1.8 J cm^{-2}	≈ 80%	N/A	N/A	[76]
	tn ≈ 1 nm	PEG FA	Cationic porphyrin derivative (MitoTPP) LC: 37.2 wt%	^{1}HeLa cells and ^{2}L929 cells [MitoTPP] = 5 μM Incubation: 8 h I: 650 nm, 10 mWcm^{-2}, 30 min	≈ ^{1}80 and ^{2}60%	N/A	N/A	[39]
	N/S	N/A	Hypocrellin B (HB) LC: 2 mg mg^{-1}	^{1}HeLa cells, ^{2}SMMC-7721 cells, ^{3}SGC-7901 cells, ^{4}A549 cells [HB] = 5 μM Incubation: 4 h I: 470 nm, 0.75 min	≈ > ^{1}80, > ^{2}90, ^{3}75 and ^{4}80%	N/A	N/A	[78]
	tn ≈ 1.2 nm	FA	Ce6 LE: 80%	MGC803 cells [FA-GO-Ce6] = 100 μM Incubation: 24 h I: 632.8 nm, 30 mWcm^{-2}, 10 min	≈ 90%	N/A	N/A	[40]
	s ≈< 200 nm tn ≈ 2-3 nm	Methoxy-poly(ethylene glycol) (mPEG)	ZnPc LE: 94%	MCF-7 cells [NGO-mPEG/ ZnPc] = 30 μg mL^{-1} Incubation: 24 h I: 400 nm, 200 mWcm^{-2}, 10 min	≈ 40%	N/A	N/A	[79]

GO	tn ≈ 1–2 nm HD ≈ 102.4 ± 15.2 nm	SS	Ce6	A549 cells [Ce6] = 1.5 μM Incubation: 24 h I: 670 nm, 20 J cm^{-2}	≈ 80%	N/A	N/A	[77]
	HD ≈ 112 ± 40 nm h ≈ 10–30 nm	Bovine serum albumin (BSA)	Ce6 LC: 5.5% (w/w)	HeLa cells [Ce6] = 10 μg mL^{-1} Incubation: 24 h I: 635 nm, 200 $mWcm^{-2}$, 1 min	≈ 91.05%	N/A	N/A	[97]
	s ≈< 50 nm tn ≈ 2 nm	PEG	2-(1-hexyloxyethyl)-2-devinyl pyropheophorbide-alpha (HPPH) LE: 131%	4T1 cells [HPPH] = 1 μM, [GO-PEG] = 0.49 μg mL^{-1} Incubation: 24 h I: 671 nm, 8 $mWcm^{-2}$, 3 min	≈ 85.78%	Mice bearing 4T1 tumours [HPPH] = 1 mg kg^{-1} I: 671 nm, 75 $mWcm^{-2}$, 20 min t: 14 days	≈ 100%	[80]
	h ≈ 17 nm l ≈ 200 nm w ≈ 79 nm	N/A	5,10,15,20-tetrakis(1-methyl4-pyridinio) porphyrin tetra(p-toluensulfonate) (TMPyP)	HeLa cells [GO/TMPyP] = 5.2275 μM Incubation: 24 h I: 740 nm, 33 $mWcm^{-2}$, 15 min and 414 nm, 10 $mWcm^{-2}$, 1.7 min	≈ 50%	N/A	N/A	[98]
	s ≈ 100–400 nm	Integrin αvβ3 monoclonal antibody (mAb)	Pyro	U87-MG cells [Pyro-NGO-mAb] = 1.5 μg mL^{-1} Incubation: 5 h I: 633 nm, 30 J cm^{-2}, 5 min	≈ 70%	N/A	N/A	[99]
	s ≈ 148.0 ± 18.0 nm tn ≈ 1 nm	PEG	Ce6 LE: 51.9 ± 5.1% DOX LE: 61.7 ± 4.4%	SCC7 cells [DOX] = 2.5 μM, [Ce6] = 5.0 μM Incubation: 24 h I: 660 nm, 30 min	≈ 80%	SCC7-bearing C3H/HeN mice [Ce6] = 10 mg kg^{-1}, [DOX] = 5 mg kg^{-1} I: 660 nm, 30 min t: 28 days	≈ 73%	[81]
	N/S	N/A	HA LC: 26.7% 7-ethyl-10-hydroxycamptothecin LC: 16.7%	A549 cells [HA-GO] = 6.00 μM Incubation: 4 h I: 470 nm, 25 mW, 5 min	≈ 92.4%	N/A	N/A	[38]
	s ≈ 380 nm tn ≈ 50 nm	Manganese dioxide (MnO_2) HAc	Cisplatin (Pt) LC: 7.7% R: 60% Ce6 LC: 3.1% R: 40%	MDA-MB-231 cells [Ce6] = 8 μg mL^{-1} Incubation: 24 h I: 0.1 Wcm^{-2}, 1 min	≈ 70%	BALB/c nude mice injected with MDA-MB-231 cells [GO/Pt/Ce6@MH] = 0.5 mg kg^{-1} I: 0.1 Wcm^{-2}, 1 min t: 14 days	≈ 80%	[42]
rGO	tn ≈ 2.81 ± 0.18 nm	Polyvinylpyrrolidone (PVP) Tripeptide L-arginyl-glycyl-Laspartic (RGD)	Ce6 LE: 7.41 wt%	MGC803 cells [Ce6] = 50 μM Incubation: 24 h I: 671 nm, 30 $mWcm^{-2}$, 3 min	≈ > 90%	N/A	N/A	[82]
	s ≈ 430 nm	N/A	Protoporphyrin IX (PPIX)	HeLa cells [rGO+PPIX] = 1 μg mL^{-1} Incubation: 24 h I: 635 nm, 5 min	≈ 59.6%	N/A	N/A	[83]
	s ≈ 14.88 nm	N/A	TiO_2	HepG2 cells [RGO-TiO_2] = 500 μg mL^{-1} I: 365 nm, 3.7 $mWcm^{-2}$, 40 min	≈ 65%	N/A	N/A	[100]
	s ≈ 54.8 nm HD ≈ 280 nm	Magnetic nanoparticles Allylamine	Camptothecin (CPT) LC: 22.5% R: 91.2% 4-hydroxy coumarin (4-HC) LC: 21.3% R: 72.32%	MCF-7 cells [CPTMrGO-AA-g-4-HC] = 100 μg mL^{-1} Incubation: 24 h I: 365 nm, 20 $mWcm^{-2}$, 3 min	≈ 62%	N/A	N/A	[84]

>CPAF-Cn, Diphenylaminofluorene modified with 1,1-dicyanoethylenyl; 2-ME, 2-Methoxyestradiol; 4-HC, 4-hydroxy coumarin; 4T1 cells, 4T1 murine breast cancer cell line; 4T1-luc-cells, Luciferase expressing breast cancer cell line; 5-ALA, 5-aminolevulinic acid; A375 cells, Human skin melanoma (A375) cell line; A549 cells, Human lung adenocarcinoma cell line; APTES, 3-(aminopropyl) triethoxysilane; B16-F10 cells, B16-F10 mice melanoma cell line; BB4, N-methylpyrrolidinium; BF6, Quarternary pyrrolidinium groups; BODIPY, Boron dipyrromethene; BSA, Bovine serum albumin; Caco-2 cells, Human epithelial colorectal adenocarcinoma cell line; CCRF-CEM cells, Human leukemic CCRF-CEM cell line; CD, Carbon dots; Ce6, Chlorine

e6; CI, Cerasome-incorporated; CNM, Carbon nanomaterial; CNT, Carbon nanotubes; CPT, Camptothecin; CT26 cells, Colon adenocarcinoma cell line; CT26Luc cells, CT26 cells genetically modified to express luciferase; Cu, Copper; d, diameter; DMA, Dimalonic acid; DOX, Doxorubicin; DPM, 1,2-distearoyl-sn-glycero-3-phosphoethanolamine-N-[methoxyPEG-2000]-maleimide; DPP Diketopyrrolopyrrole; DSPE-mPEG, 1,2-distearoyl-phosphatidylethanolamine-methyl-poly(ethylene glycol); DSPE-PEG2000-maleimide, 1,2-distearoyl-*sn*-glycero-3-phosphoethanolamine-N-[methoxy(polyethylene glycol)-2000]-maleimide; FA, Folic acid; Gd, Gadolinium; GO, Graphene oxide; GQD, Graphene quantum dots; h, height; H22 cells, H22 hepatocellular carcinoma cell line; HA, Hypocrellin A; HAc, Hyaluronic acid; HB, Hypocrellin B; HD, hydrodynamic size; HeLa cells, Human cervical cancer cell line; Hep-2 cells, Hep-2 human larynx-carcinoma cell line; HepG2 cells, Human hepatocellular carcinoma cell line; HMME, Hematoporphyrin monomethyl ether; HPPH, 2-(1-hexyloxyethyl)-2-devinyl pyropheophorbide-alpha; I, Irradiation; IO NP, Iron oxide nanoparticles; J774 cells, J774 reticulum sarcoma cell line; Jurkat cells, Human leukemia T-lymphocytes; l, length; L929 cells, Murine aneuploid fibrosarcoma cell line; LC, loading capacity; LE, loading efficiency; LLC cells, Lewis lung carcinoma cell line; LMI, Lipid-membrane-incorporated; mAB, Integrin αvβ3 monoclonal antibody; MCF-7 cells, Human breast cancer cell line; MDA-MB-231 cells, Human breast cancer cell line; Meth A cells, Meth A fibrosarcoma cell line; Meth AR1 cells, Meth AR1 fibrosarcoma cell line; MGC803 cells, Human gastric cancer cell line; MitoTPP, Cationic porphyrin derivative; MnO_2, Manganese dioxide; mPEG, Methoxy-poly(ethylene glycol); N/A, not applicable; N/S, not studied; NGR, Asparagine-glycine-arginine; N, Nitrogen; PEG, Poly(ethylene glycol); PEI, Polyethylenimine; PPIX, Protoporphyrin IX; PS, Photosensitizer; Pt, Cisplatin; PVP, Polyvinylpyrrolidone; Pyro, Pyropheophorbide *a*; R, release; RGD, Tripeptide L-arginyl-glycyl-Laspartic; rGO, Reduced graphene oxide; Ru (II), Ruthenium (II); s, size; S, Sulphur; SCC7 cells, Murine SCC7 squamous carcinoma cell line; Se/N, Selenium and Nitrogen; SGC-7901 cells, Human gastric cancer cell line; SMMC-7721 cells, Human hepatocellular carcinoma cell line; SS, Disulfide bond; tn, thickness; t, treatment time; Th, topographic height; TiO_2, Titanium dioxide; TMPyP, 5,10,15,20-tetrakis(1-methyl4-pyridinio) porphyrin tetra(p-toluensulfonate); U14 cells, Murine hepatocarcinoma U14 cell line; U251 cells, Human glioblastoma cell line U251; U87-MG cells, Adherent human glioblastoma (U87-MG) cell line; UM1 cells, Human tongue squamous carcinoma cell line; w, width; ZnMAPc, Zinc monoamino phthalocyanine; ZnO, Zinc oxide; ZnPc, Zinc phthalocyanine.

2.3.2 - Photothermal therapy

Temperature control is essential for the coordination of the growth and correct functioning of cells, tissues and organs. Often, an increase in the normal temperature of the human body (≈ 37 °C) is an indicator of disease. Nonetheless, if this increase is locally controlled it can have therapeutic advantages, especially in cancer treatment [6]. PTT has generated interest due to its ability to destroy cancer cells using photothermal agents, which create heat with minimal harm to the surrounding healthy tissues. An ideal photothermal agent, when irradiated by visible or NIR light, should be capable of absorbing and converting it to heat, thereby generating hyperthermia at the tumour site [15]. The NIR window (750-1700 nm) coincides with the optical tissue penetration where biological tissues do not absorb light, making it ideal for phototherapy [6]. PTT can be divided into two approaches. One of them is mild phototherapy, where the temperature can be usually increased in the range between 40 to 50 °C, interfering with the standard functioning of cells. Hyperthermia increases the permeability of the cellular membrane and cellular uptake and disrupts metabolic signalling. This allows a selective treatment as cancer cells are more sensitive to heat, also their membrane permeability is increased with temperature, enhancing nanomaterials/drug internalization. The second approach is photothermal ablation, where temperatures above 50 °C are most commonly used, leading to cellular membrane destruction and necrosis [10]. CNM are good candidates for being used as photothermal agents for this application, due to usually presenting suitable light absorption and thermal stability [25]. Table 2.2 summarizes the state-of-the-art literature regarding the use of CNM in PTT, including their main characteristics and biological effects. In the literature, promising results were reported using fullerenes, CD, GQD, CNT, CNH, graphene, GO and rGO being CNT, GO and rGO the most extensively studied.

Despite the lack of NIR absorption of pristine forms of fullerenes, Krishna *et al.* used polyhydroxy fullerenes for PTT in mice subcutaneously inoculated with a human breast cancer cell line. Polyhydroxy fullerenes were intratumorously injected at a concentration of 0.45 mg mL^{-1} and irradiated with a NIR laser (785 nm, 500 mW) for 10 min. The treatment resulted in a tumour volume reduction of 72%, comparing with untreated control [101]. Authors attributed the optical heating of these modified fullerenes to the effect caused by the NIR laser that breaks their balanced cage structure and releases heat [102].

CD have been reported as effective PTT agents with low toxicity and good water dispersibility, yet presenting low NIR absorption. This disadvantage can be surpassed by element doping [103, 104] or specific production methods, for example, regulating the pH or using formamide as the solvent [105, 106]. *In vitro*, concentrations commonly used for these

nanomaterials vary from 200 to 500 μg mL^{-1}, while incubation times range between 4 to 24 h. Irradiations are usually performed using lasers with wavelengths between 671-808 nm, and irradiances from 0.8 to 4 Wcm^{-2}, during 5 to 10 minutes. Studies using CD-based cancer PTT, usually result in between 57 to 100% cancer cell death. *In vivo*, materials are often injected intratumorously or intravenously, and concentrations used range between 200-1000 μg mL^{-1}. Irradiations are performed with lasers with a wavelength range of 655-808 nm, with irradiances between 0.8 to 1 Wcm^{-2}, during 5 to 10 minutes. Studies with CD usually report tumour volume reductions between 85 and 100%, 6 to 18 days after treatment [103, 104, 107]. CD usually present renal clearance and cause no significant organ damage or inflammation [104, 107]. After irradiation, these materials can achieve temperatures in the range between 30 to 80 °C. Bao *et al.* demonstrated that CD doped with both sulphur and nitrogen were non-cytotoxic *in vitro* when used in high concentrations, up to 1000 μg mL^{-1}. It has been also observed that such CD could be excreted through the renal route *in vivo.* Mice with hepatocellular carcinoma xenografts were treated by intravenous administration of doped CD at a concentration of 1000 μg mL^{-1} and irradiated with a laser (655 nm, 1 Wcm^{-2}) for 5 minutes. The treatment resulted in 100% tumour reduction after 14 days, comparing with the untreated control [104]. A study by Phan *et al.* reported the use of polydopamine-folate CD (PFCD) for PTT in a prostate cancer cell line. The authors expected FA to act as a recognition strategy for the prostate-specific membrane antigen receptor in the cancer cell line, increasing selectivity. Cells were incubated with PFCD at a concentration of 250 μg mL^{-1} and irradiated with a NIR laser (808 nm, 1.5 Wcm^{-2}) for 10 minutes after 4 h of culture. The treatment resulted in a cancer cell death of 90.1% [108]. Besides PTT application as the core nanomaterial, CD have been reported as effective phototherapy agents when decorating gold nanorods (GNR). Pandey *et al.* conjugated CD in GNR (C-dots@GNRs) for the controlled release of DOX. Human breast cancer cell lines were incubated with the C-dots@GNR-DOX and irradiated with a laser (800 nm, 120 mW) for 5 minutes after 48 h of culture. The treatment resulted in a IC_{50} of 0.01 mM, demonstrating enhanced efficacy in comparison to pure GNR (IC_{50} 0.02 mM) [109].

GQD have been proved effective in PTT. Some of their advantages include low toxicity and good dispersibility in aqueous solutions. The main disadvantage of this CNM is the weak absorption in the NIR region, therefore conjugation with NIR absorbing nanoparticles has been studied, for example, with iron oxide nanoparticles (IO NP) [110]. Other modifications have been reported such as the introduction of targeting moieties that increase the specificity of the treatment, for instance, aptamer [111], FA [112, 113] and mitochondria-targeting peptides [105]. *In vitro*, concentrations commonly used for these nanomaterials vary from 30 to 200 μg mL^{-1}, and incubation times range between 4 to 24 h. Irradiations are usually performed using lasers at 808 nm wavelength, and irradiances from 0.6 to 2.5 Wcm^{-2}, during 3 to 30 minutes. GQD-based PTT studies, usually report cancer cell death values between 59 and 97.9%. *In vivo*, materials are often injected intratumorously or intravenously, and concentrations used range between 2 and 4 mg kg^{-1}. Irradiations are performed with lasers with 808 nm wavelength, with irradiances between 1 to 1.5 Wcm^{-2}, during 5 to 10 minutes. GQD-based PTT usually results in between 85 to 95% tumour reduction, evaluated 14 to 25 days after the treatment [113-115]. Some studies have reported no tissue damage in normal tissues after treatment. Also, liver, kidney and spleen accumulation has been stated, but with excretion happening after 96 h [113, 114]. After irradiation, these materials can achieve temperatures in the range between 40 to 70 °C. Wang *et al.* reported the use of GQD dual-doped with nitrogen and boron (N-B-GQD), with potential for NIR imaging and NIR to heat conversion. N-B-GQD were incubated at a concentration of 100 μg mL^{-1} using a human

glioblastoma cell line and irradiated with a NIR laser (808 nm, 1.5 Wcm^{-2}) for 5 minutes after 24 h of culture. The treatment resulted in a cancer cell death of 96%. *In vivo* studies were performed using mice glioblastoma xenografts. N-B-GQD were intravenously injected at a concentration of 1 mg mL^{-1} and after 1 week irradiated using the same settings from the *in vitro* experiments. The treatment resulted in a tumour volume reduction of over 85% after 14 days, comparing with untreated control [114].

CNT were the first nanomaterials to be used in PTT [116] due to their high NIR absorption properties. However, CNT require functionalization toward improving water dispersibility and biocompatibility. Several molecules have been conjugated with CNT, such as polymers like PEG [116-124] or Pluronic F-127 [125, 126]. Other modifications have been done to improve treatment efficiency, for instance, adding targeting moieties such as FA [116, 117, 127], cysteinyl-arginyl-glutamyl-lysyl-alanyl (CREKA) [119] and NGR peptides [128]. *In vitro*, concentrations commonly used for this nanomaterial vary from 3.5 to 100 μg mL^{-1}, and incubation times range between 0.5 to 72 h. Irradiations are usually performed using lasers at wavelengths between 780-1400 nm (NIR region), and irradiances from 0.7 to 153 Wcm^{-2}, during 0.75 to 20 minutes. Studies using CNT for PTT usually report between 64.8 to 100% cancer cell death values. *In vivo*, CNT are often injected intratumorously or intravenously, and concentrations used range between 0.2 and 4.3 mg kg^{-1}. Irradiations are performed using lasers with a wavelength between 785-1064 nm, with irradiances between 0.2 to 76 Wcm^{-2}, during 0.5 to 20 minutes. Studies usually report between 75 to 100% tumour reduction, 10 to 38 days after treatment [118, 119, 129]. Some studies have reported CNT muscle, spleen, blood, liver and spleen, and skin accumulation [118, 119, 130]. However, some authors describe CNT to be excreted without causing significant abnormality or organ damage [120, 122, 126, 129, 131]. After irradiation, these materials can achieve temperatures in the range between 40 to 73 °C. In a study by Moon, Lee and Choi, SWCNT conjugated with PEG were used for PTT in mice subcutaneously inoculated with a human carcinoma cell line to induce tumour formation. SWCNT-PEG were intratumorously injected at a concentration of 120 μg mL^{-1} and immediately irradiated with a NIR laser (808 nm, 76 Wcm^{-2}) for 3 minutes. The treatment resulted in 100% tumour reduction after 25 days, comparing with untreated control [118]. Combined chemo-photothermal studies have been also performed. For example, Dong *et al.* functionalized MWCNT with a transactivator of transcription peptide and chitosan as a drug delivery system for the anticancer drug DOX. A DOX LC of 50% was reported and the PTT was applied in a Bel-7402 hepatoma cell line. Cells were incubated with MWCNT/DOX/TC at a concentration of 10 μg mL^{-1} and irradiated with a NIR laser (808 nm, 1 Wcm^{-2}) for 5 minutes after 72 h of culture, which led to 80% cancer cell death. Besides, mice were inoculated with the same cancer cell line to induce tumour formation. Functionalized CNT were intratumorously injected at a concentration of 4 mg mL^{-1} and irradiated with the same NIR laser. The treatment resulted in a tumour reduction of over 90% after 25 days, comparing with untreated control [132].

CNH have been less studied compared to other CNM, but some promising results have been reported using those. Some studies report effective PTT using this material, without significant toxicity being observed [133, 134]. After irradiation, CNH-based materials can achieve temperatures in the range between 43 to 85 °C. A study by Whitney *et al.* used single-walled carbon nanohorns (SWCNH) conjugated with pluronic for PTT applied to a murine kidney cancer cell line. Cells were incubated with the modified SWCNH at a concentration of 85 μg mL^{-1} and irradiated with a NIR laser (1064 nm, 40 Wcm^{-2}) for 6 minutes after 24 h of culture. The treatment resulted in 100% cancer cell death [135].

Graphene, in turn, is an example of a photothermal agent presenting high NIR absorption. As mentioned before, graphene is hydrophobic, requiring further surface modification. Markovic *et al.* used PVP functionalized graphene (G_{PVP}) produced by graphite exfoliation for PTT in a human glioblastoma cell line. Cells were incubated with G_{PVP} at a concentration of 5 μg mL^{-1} and irradiated with a NIR laser (808 nm, 2 Wcm^{-2}) for 5 minutes. The treatment resulted in over 90% cancer cell death. These results were compared to a CNT functionalized with DNA that after the same treatment needed 10 μg mL^{-1} to achieve the same cell death value. Authors attributed graphene nanoparticles superior effectiveness to their higher dispersibility and smaller size [136].

Alternatively to pristine graphene, other GBM present suitable properties for PTT, such as GO, due to its good dispersibility in aqueous solutions and versatility for surface functionalization. Different covalent and non-covalent approaches have been tested with this nanomaterial, for example, the addition of targeting moieties to increase treatment selectivity, like FA [137-141], RGD peptide [142] and aptamers [143, 144]. To improve biocompatibility several polymers such as PEG [22, 30, 145-153], PVP [137], Poloxamer 188 [154] and HAc [155, 156] have also been used. Furthermore, other nanomaterials have been conjugated to enhance the photothermal effect, for instance, IO NP [146, 147], gold nanoparticles (Au NP) [143, 144, 146], silver nanoparticles (Ag NP) [138] and manganese dioxide nanoparticles [139]. *In vitro*, concentrations vary from 1 to 1000 μg mL^{-1}, and incubation times ranging between 1 to 48 h have been used. Irradiations are usually performed using lasers with wavelengths between 785-980 nm, and irradiances from 0.5 to 6 Wcm^{-2}, during 2 to 15 minutes. PTT with GO usually results in between 60 to 100% cancer cell death. *In vivo*, materials are often injected intratumorously or intravenously, and concentrations used range between 10 to 20 mg kg^{-1}. Irradiations are performed using lasers with a wavelength between 785-980 nm, with irradiances between 0.75 to 2.5 Wcm^{-2}, during 1 to 15 minutes. Studies with GO usually result in between 55 to 100% tumour reduction, 6 to 30 days after treatment [22, 30, 138, 145, 146, 155]. Multiple studies report GO as presenting low toxicity, with no significant organ damage being observed after treatment [22, 138, 142, 147, 150, 156]. However, kidney accumulation and heart denaturation have been stated [30, 145]. After irradiation, these materials can achieve temperatures in the range between 45 to 85 °C. Guo *et al.* conjugated GO with PEG and cypate (GO-PEG-cypate) for PTT in a 4T1 murine breast cancer cell line. Cells were incubated with GO-PEG-cypate at a cypate concentration of 100 μg mL^{-1} and irradiated with a NIR laser (785 nm, 1.5 Wcm^{-2}) for 3 minutes after 24 h of culture. The treatment led to 90% cancer cell death. Besides, mice were subcutaneously implanted with the same cancer cell line to induce tumour formation. GO-PEG-cypate were intravenously injected at a cypate concentration of 7.5 mg kg^{-1} and after 24 h, irradiated at the tumour site with a NIR laser (785 nm, 1.0 Wcm^{-2}) for 3 minutes. The treatment resulted in 100% tumour reduction after 22 days, comparing with untreated control [145]. Yang *et al.* used PEGylated GO nanosheets (NGS-PEG) labelled with Cyanine7 for PTT in mice subcutaneously inoculated with a murine breast cancer cell line. NGS-PEG were intravenously injected at a concentration of 20 mg kg^{-1} and irradiated at the tumour site with a NIR laser (808 nm, 2 Wcm^{-2}) for 5 minutes. The treatment led to 100% tumour reduction after 1 day with no regrowth for 22 days [22]. Several anticancer drugs have been combined with GO to improve treatment efficiency. Wang *et al.* used GO conjugated with an aptamer, Au NP and DOX (GO-Au-Apt-DOX) for PTT using human lung adenocarcinoma and human breast cancer cell lines. Cells were incubated with GO-Au-Apt-DOX at a concentration of 8 μg mL^{-1} and irradiated with NIR light for 15 minutes after 12 h of culture. The treatment resulted in 90 and 80% cancer cell death, respectively [143]. In a study by Hou *et al.* HAc was conjugated with GO for PTT and drug delivery of mitoxantrone. Human breast cancer

cells were incubated with the modified GO conjugated with 51.2 μg mL^{-1} of drug and irradiated with NIR laser (808 nm, 2 Wcm^{-2}) for 3 minutes. The treatment led to a cancer cell death of 95%. Besides, mice were subcutaneously inoculated with the same cancer cell line to induce tumour formation. Drug loaded modified GO was intravenously injected at a drug concentration of 4 mg kg^{-1} and irradiated with NIR laser (808 nm) for 1 minute. The treatment led to 93.52% tumour reduction after 6 days, comparing with untreated control [156]. Besides, GO has been effectively deposited around other molecules, such as poly(lactic acid) microcapsules or gold nanorods [157], with efficient PTT outcomes being reported [158]. Figure 2.3 illustrates a representative example of CNM application in cancer PTT. Bai, Liu and Jiang conjugated GO with PEG, copper sulfide and DOX (PEG-GO/CuS/DOX) for PTT in a human cervical cancer cell line. Cells were incubated with PEG-GO/CuS/DOX at a concentration of 500 μg mL^{-1} and irradiated with a NIR laser (980 nm, 1 Wcm^{-2}) for 10 minutes after 24 h of culture, which resulted in 75% cancer cell death. Also, mice were subcutaneously inoculated with the same cancer cell line to induce tumour formation. PEG-GO/CuS/DOX were intratumorously injected at a concentration of 500 μg mL^{-1} and after 2 h irradiated using the same conditions. The treatment led to over 95% tumour reduction after 21 days, comparing with the untreated control [149].

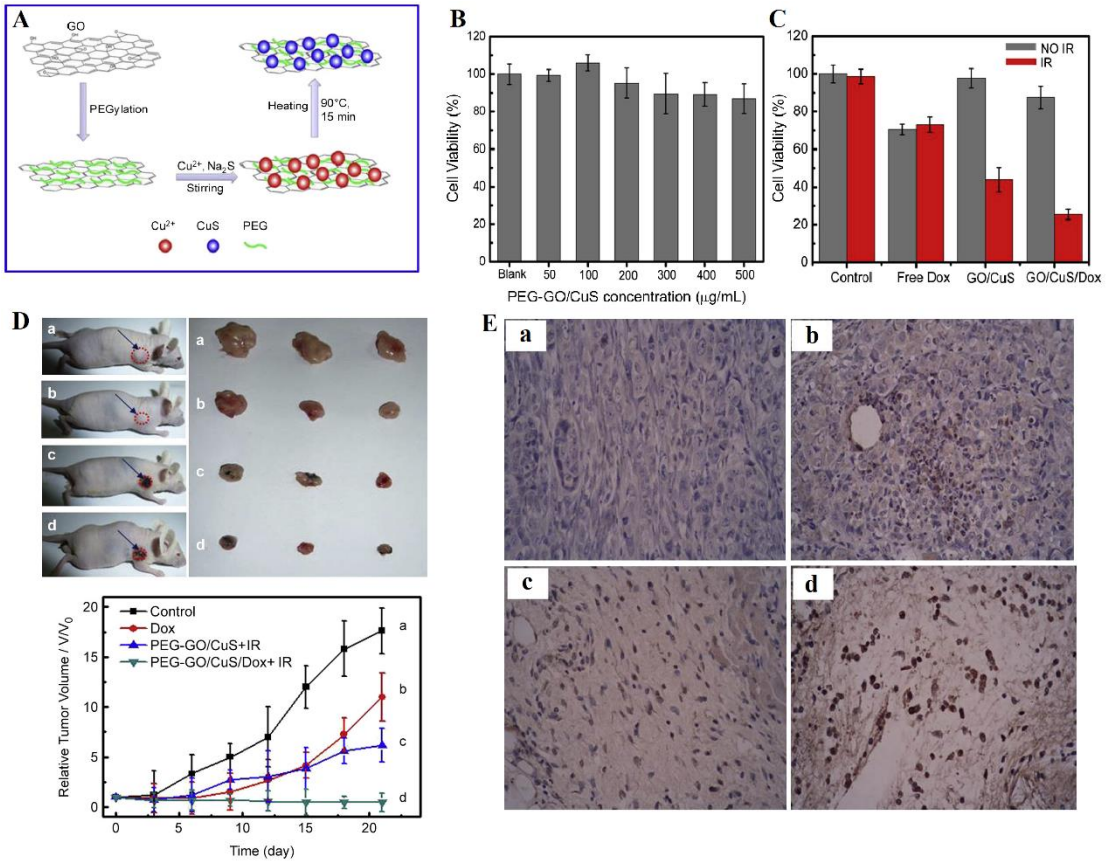

Figure 2.3 – Representative example of CNM use for cancer photothermal therapy. (A) Production of PEG-GO/CuS nanocomposites. GO was PEGylated through amide formation. Then, copper(II) iron was added and treated with sodium sulfide leading to the formation of PEG-GO/CuS. (B) *In vitro* HeLa cells viability after incubation for 24 h with increasing concentrations of PEG-GO/CuS nanocomposites; (C) *In vitro* HeLa cells viability after incubation with free Dox (10 μg mL^{-1}), PEG-GO/CuS nanocomposites (500 μg mL^{-1}) and PEG-GO/CuS/Dox nanocomposites (500 μg mL^{-1}), with and without NIR irradiation (980 nm, 1 Wcm^{-2}, 10 min). (D) Photographs of the tumour bearing mice and excised tumours from mice euthanized after the 21st day of treatment: (a) saline solution as control (0.9%), (b) free Dox (10.0 μg mL^{-1}), (c) PEG-GO/CuS nanocomposites (500 μg mL^{-1}) and (d) PEG-GO/CuS/Dox nanocomposites (500 μg mL^{-1}) at an injection volume of 0.1 mL/animal without (a, b) and with (c, d) NIR irradiation (980 nm, 1 Wcm^{-2}, 5 min); (E) Relative tumour volume for animal models exposed to the different conditions (F) TUNEL assay photographs of

tumour tissue, 21 days after treatment, from the different groups: (a) control group, (b) free Dox without irradiation, (c) PEG-GO/CuS nanocomposites with irradiation (980 nm, 1 Wcm^{-2}, 10 min) and (d) Dox-loaded PEG-GO/CuS nanocomposites with irradiation (980 nm, 1 Wcm^{-2}, 10 min). Adapted from [149]. Abbreviations: CuS, copper sulfide; DOX, doxorubicin; GO, graphene oxide; HeLa cells, human cervical cancer cell line; NIR, near-infrared irradiation; PEG, poly(ethylene glycol); TUNEL, terminal deoxynucleotidyl transferase-mediated nick-end-labelling.

Despite the advantages of GO, such as good water stability and biocompatibility, the introduction of oxygen-containing functional groups originates structural defects, consequently diminishing its NIR absorption capability. Hence, the reduction of this nanomaterial toward rGO translates into higher photothermal efficacy, however, at the same time it decreases water dispersibility. In terms of surface modifications, multiple approaches have been reported to improve rGO water stability, for example, using polymers such as PEG [35, 36, 159-162], PEI [162], and polydopamine (pDA) [163, 164]. Also, other molecules have been used to modify rGO surface, for instance, proteins like bovine serum albumin [165, 166], peptides such as RGD [159] or antiarrhythmic peptide 10 [164], polysaccharides such as HAc [34, 163, 167], polyphenols [168, 169], and other nanomaterials, for example, iron oxide (Fe_3O_4) [160, 170]. *In vitro*, concentrations commonly used for this nanomaterial vary from 3 to 1000 µg mL^{-1}, and incubation times range between 0.5 to 72 h. Irradiations are usually performed using lasers with wavelengths between 780-880 nm, and irradiances from 0.15-15 Wcm^{-2}, during 1 to 30 minutes. Studies using rGO report between 38 to 100% cancer cell death after PTT. *In vivo*, nanomaterials are often injected intratumorously or intravenously, and concentrations used range between 2 to 20 mg kg^{-1}. Irradiations are performed with lasers with a wavelength between 805-980 nm, with irradiances between 0.15 to 1.5 Wcm^{-2}, during 3 to 10 minutes. Studies usually report between 70 to 100% tumour reduction, 10 to 26 days after treatment [171-173]. Low accumulation was found in the liver, spleen and kidney, without significant damage being observed [36, 163, 165, 167, 171, 172]. After irradiation, these materials can achieve temperatures in the range between 40 to 80 °C. Robinson *et al.* used nano-rGO sheets with non-covalent PEGylation and peptide conjugation for PTT. Human glioblastoma cells were incubated with nano-rGO-PEG-RGD at a concentration of 6.6 µg mL^{-1} and irradiated with a NIR laser (808 nm, 15 Wcm^{-2}) for 8 minutes after 1 h of culture. The treatment resulted in 90% cancer cell death [159]. Yang *et al.* produced a rGO-IO NP-PEG nanocomposite for PTT in mice subcutaneously inoculated with a murine breast cancer cell line. rGO-IO NP-PEG was intravenously injected at a concentration of 20 mg kg^{-1} and irradiated with a NIR laser (808 nm, 0.5 Wcm^{-2}) for 5 minutes. The treatment resulted in 100% tumour reduction after 15 days, comparing with untreated control [172].

Similar to the above-mentioned for CNM PDT studies, PTT ones also often present variability of the experimental conditions, with not all experimental details being mentioned in some works, therefore conclusions presented next were withdrawn taking that into consideration. Standardization of nomenclature, units, procedures description and suitable controls are very important to allow comparison between the studies. In PTT, the anticancer drug loading is usually performed by hydrophobic interactions or π- π stacking [110, 113, 123, 174]. The most commonly used drug is DOX, however, Pt and other drugs are also conjugated with CNM. No loading quantification has been found in studies reporting the use of CD. Few studies have reported GQD conjugation with drugs, presenting LC around 30% and LE of 24-90%. CNT have been reported to have LC around 50%, while for CNH LE range from 40 to 60%. Reports on the use of GBM describe extremely variable drug loading outcomes. GO LC has been reported from 7 to 260% and LE from 11 to 90%. rGO have presented LC in a range from 100 to 310% and LE of 75 to 90%. PS or anticancer drug loading results have been described above and are presented also in Table 2.2.

In general, CNM used in cancer PTT can be divided into two main groups. On one hand, nanomaterials that were previously described as acting as PS in PDT approaches have poor capability of absorbing NIR. Indeed, fullerenes, CD and GQD require chemical modifications or conjugation with PTT agents to become effective NIR absorbents. Fullerenes have been relatively unexplored in this application but CD and GQD superior photostability and low cytotoxicity allow their use after conjugation with NIR absorbing molecules or surface modifications. In the literature, CD application in PTT usually resulted in over 57% cancer cell death using concentrations from 200 to 500 μg mL^{-1} *in vitro*, whereas *in vivo* studies report over 85% tumour reduction, 6 to 18 days after treatment. Besides, these CNM have been reported as excretable *in vivo*. GQD PTT application usually results in over 59% cancer cell death *in vitro* using concentrations from 30 to 200 μg mL^{-1}. *In vivo* studies with GQD usually report over 85% tumour reduction, 14 to 25 days after treatment. On the other hand, using nanomaterials with intrinsic NIR absorbances like CNT, CNH and GBM is advantageous due to their light-to-heat conversion ability, avoiding the need to add other PTT agents. In the case of CNT and CNH, low water dispersibility is the main disadvantage, however, proper conjugation with specific biomolecules has been shown to improve stability in physiological media. In the literature, CNT application in PTT usually results in over 65% cancer cell death *in vitro* using concentrations from 3.5 to 100 μg mL^{-1}, while *in vivo* studies present consistent outcomes with over 75% tumour reduction, 10 to 38 days after treatment. However, some biocompatibility issues have been reported such as accumulation in the liver and kidney of mice. Few articles report CNH application in PTT but some studies have reported cancer cell deaths over 85% and tumour reductions over 65%. However, further studies are required as literature is scarce regarding CNH PTT. GBM are the most extensively studied CNM for PTT. Studies using GO usually describe over 60% cancer cell death, using concentrations from 1.74 to 1000 μg mL^{-1}. *In vivo* studies with GO usually result in over 55% tumour reduction, 6 to 30 days after treatment. Similarly, rGO studies usually result in over 38% cancer cell death, using concentrations ranging from 3 to 1000 μg mL^{-1}. *In vivo*, it usually leads to over 70% tumour reduction, 10 to 26 days after treatment.

Overall, PDT and PTT studies suggest a complementary action between two major CNM groups. The first group comprises fullerenes, CD and GQD, which are all 0D nanomaterials with excellent PS activity through ROS generation. The second group includes CNT, CNH and GBM, which exhibit poor PDT performance if unmodified, but hold strong potential for PTT through their intrinsic NIR absorption capability and consequent local heat generation for cancer thermal ablation. Altogether, these results have been raising the attention toward combined therapies, as discussed in the next section.

Table 2.2 - Selected recent studies on carbon nanomaterials for cancer photothermal therapy.

CNM	Particle size	Surface modification	Conjugated drug	Biological studies *in vitro*		Biological studies *in vivo*		Ref.
				Parameters	Cell death	Parameters	Tumour reduction	
Fullerenes	s ≈ 57 ± 4 nm	Hydroxyl groups (OH) Chitosan	N/A	N/A	N/A	Nude mice inoculated with BT474 cells [CP-0.25] = 0.45 mg mL^{-1} I: 785 nm, 500 mW, 10 min t: 20 h	≈ 72%	[101]
CD	s ≈ 2.5–5.5 nm	N/A	N/A	MCF-7 cells [R-CD] = 200 μg mL^{-1} Incubation: 4 h I: 671 nm, 2.5 Wcm^{-2}, 10 min	≈ 100%	N/A	N/A	[106]
	s ≈ 100 nm	Poly(L-lactide-co-	N/A	HeLa cells [CD] = 400 μg mL^{-1}	≈ 97%	N/A	N/A	[175]

		glycolide)-block-poly(ethylene glycol)-Amine (PLGA-b-PEG-NH_2)		I: 671 nm, 2 Wcm^{-2}, 10 min				
CD	s ≈ 1.2–3.3 nm t ≈ 1.06 nm	Nitrogen and oxygen (N-O) co-doped	N/A	HeLa cells [N-O-CD] = 200 µg mL^{-1} Incubation: 4 h I: 808 nm, 0.8 Wcm^{-2}, 5 min	≈ 87%	Female Balb/c nude mice injected with HeLa cells [N-O-CD] = 200 µg mL^{-1} I: 808 nm, 0.8 Wcm^{-2}, 5 min t: 18 days	≈ 100%	[103]
	s ≈ 10–30 nm	Mitochondria-targeting peptide (MT)	N/A	HepG2 cells [CD-MT] = 500 µg mL^{-1} Incubation: 24 h I: 808 nm, 4.0 Wcm^{-2}, 10 min	≈ 57%	N/A	N/A	[105]
	s ≈ 2–5 nm h ≈ 0.5–2 nm	Sulphur and nitrogen (S-N) co-doped	N/A	N/A	N/A	H22 tumour models of the ICR mice [CD] = 1000 µg mL^{-1} I: 655 nm, 1 Wcm^{-2}, 5 min t: 14 days	≈ 100%	[104]
	s ≈ 4–12 nm	N/A	N/A	HeLa cells [CD] = 20 mg mL^{-1} Incubation: 24 h I: 808 nm, 10 min	≈ > 90%	BALB/C mice injected with HeLa cells [CD] = 20 mg mL^{-1} I: 808 nm, 10 min t: 6 days	≈ > 85%	[107]
	s ≈ 8.7 ± 2.9 nm HD ≈ 82.3 ± 5.1 nm	Polydopamine (pDA) FA	N/A	LNCaP cells [PFCD] = 250 µg mL^{-1} Incubation: 4 h I: 808 nm ,1.5 Wcm^{-2}, 10 min	≈ 90.1%	N/A	N/A	[108]
	HD ≈ 51.5 ± 19.5 nm d ≈ 25 nm	pDA	N/A	HeLa cells [CD-PDA] = 200 µg mL^{-1} Incubation: 24 h I: 808 nm, 2 Wcm^{-2}, 5 min	≈ 70%	N/A	N/A	[176]
GQD	t ≈ 1 nm	Aptamer AS1411	N/A	A549 cells [AS1411-GQD] = 5 µM Incubation: 24 h I: 808 nm, 2 Wcm^{-2}, 10 min	≈ 72.9%	N/A	N/A	[111]
	s ≈ 38 nm	rGO poly (L-lysine) (PLL) FA	N/A	MCF-7 cells [QD] = 20 mg cm^{-1} Incubation: 8 h I: 808 nm, 2 Wcm^{-2}, 9 min	≈ > 95%	N/A	N/A	[112]
	s ≈ 7.5–9.5 nm d ≈ 8.5 nm Th ≈ 1.356 nm	IR780 iodide LC: 33.19% FA	N/A	HeLa cells [IR780/GQD-FA] = 30 µg mL^{-1} Incubation: 12 h I: 808 nm, 1 Wcm^{-2}, 5 min	≈ 97.9%	Female Balb/c nude mice injected with HeLa cells [IR780/GQDs-FA] = 2 mg kg^{-1} I: 808 nm, 1 Wcm^{-2}, 5 min t: 15 days	≈ > 95%	[113]
	s ≈ 4.7 nm h ≈ 2.0 nm	Nitrogen and boron (N-B) co-doped	N/A	SF-763 cells [N-B-GQD] = 100 µg mL^{-1} Incubation: 24 h I: 808 nm, 1.5 Wcm^{-2}, 5 min	≈ 96%	Mice bearing C6 glioblastoma [N-B-GQD] = 1 mg mL^{-1} I: 808 nm, 1.5 Wcm^{-2}, 5 min t: 14 days	≈ > 85%	[114]
	d ≈ 7–10 nm	Triphenylphosphonium (TPP) N doped Ruthenium nitrosyl (Ru-NO) LC: 1.60 µmol mg^{-1}	N/A	HeLa cells [N-GQDs@Ru-NO@TPP] = 200 µg mL^{-1} I: 808 nm, 0.6 Wcm^{-2}, 10 min	≈ 90%	HeLa tumour-bearing mice [N-GQDs@Ru-NO@TPP] = 4 mg kg^{-1} I: 808 nm, 1.0 Wcm^{-2}, 10 min t: 25 days	≈ > 85%	[115]
	s ≈ 50−100 nm	Zeolitic imidazolate framework-8 (ZIF-8)	DOX Loading efficiency (LE): 90%	4T1 cells [DOX] = 5 µg mL^{-1}, [ZIF-8/GQD] = 100 µg mL^{-1} Incubation: 8 h	≈ 82%	N/A	N/A	[177]

			Release (R): 80%	I: 808 nm, 2.5 Wcm^{-2}, 3 min				
GQD	d ≈ 41.8 ± 8.1 nm h ≈ 2.3 ± 0.07 nm HD ≈ 61.4 nm	IO NP	Lidocaine hydrochloride Loading capacity (LC): 24 wt% R: 100%	HeLa cells [MGQD] = 50 μg mL^{-1} Incubation: 4 h I: 808 nm, 2.5 Wcm^{-2}, 30 min	≈ 59%	N/A	N/A	[110]
CNT	l ≈ 150 nm d ≈ 1.2 nm	PEG FA	N/A	HeLa cells Incubation: 12-18 h I: 808 nm, 1.4 Wcm^{-2}, 2 min	Extensive cell death	N/A	N/A	[116]
	N/S	Gold nanoparticles (Au NP) PEG FA	N/A	KB cells [SWNT-Au-PEG-FA] = 5 nM Incubation: 0.5 h I: 808 nm, 1 Wcm^{-2}, 5 min	≈ 80%	N/A	N/A	[117]
	d ≈ 8–12 nm	N/A	N/A	EAC cells [MWCNT] = 100 μg mL^{-1} Incubation: 12 h I: 780−1400 nm, 3.5 Wcm^{-2}, 1.5 min	≈ 95.2%	N/A	N/A	[178]
	l ≈ 1100 nm	Nitrogen dopants (CN_x)	N/A	CRL 1932 cells [CN_x-MWNT] = 83 μg mL^{-1} Incubation: 24 h I: 1064 nm, 3 Wcm^{-2}, 4 min	≈ 96.25%	N/A	N/A	[179]
	l ≈ 900 nm	Pluronic F-127 (PL-127)	N/A	PC3 cells [MWCNT] = 100 μg mL^{-1} I: 1064 nm, 15.3 Wcm^{-2}, 5 min	≈ 100%	N/A	N/A	[125]
	l ≈ 50–300 nm d ≈ 2–5 nm	PEG	N/A	N/A	N/A	KB cells injected in male nude mice [PEG-SWNT] = 120 μg mL^{-1} I: 808 nm, 76 Wcm^{-2}, 3 min t: 25 days	≈ 100%	[118]
	s ≈ 0.7–1.1 nm	Poly(maleic anhydride-*alt*-1-octadecene)-methoxy poly(ethylene glycol) (C_{18}-PMH-mPEG)	N/A	N/A	N/A	Mice bearing 4T1 tumours [(6,5) SWCNT] = 0.254 mg kg^{-1} I: 980 nm, 0.6 Wcm^{-2}, 5 min t: 1.5 months	≈ 100%	[131]
	l ≈ 140 nm	DSPE-mPEG C_{18}-PMH-mPEG	N/A	N/A	N/A	BALB/c mice bearing 4T1 tumours [SWNT] = 3.6 mg kg^{-1} I: 808 nm, 0.6 Wcm^{-2}, 5 min t: 25 days	≈ 100%	[129]
	d ≈ 10 nm l ≈ 50–150 nm	PEG Cysteinyl-arginyl-glutamyl-lysyl-alanyl (CREKA) peptide	N/A	N/A	N/A	A549 cells injected into male Balb/c nude mice [CMWNT-PEG] = 4 mg kg^{-1} I: 808 nm, 3.5 Wcm^{-2}, 1.5 min t: 12 days	≈ > 95%	[119]
	N/S	Poly(maleic anhydride-*alt*-1-octadecene)-poly(ethylene glycol) (C_{18}-PMH-PEG)	N/A	N/A	N/A	4T1-tumour-bearing mice [SWCNT-PEG] = 0.2 mg kg^{-1} I: 808 nm, 0.5-0.8 Wcm^{-2}, 10 min t: 60 days	≈ 100%	[180]
	d ≈ 4.3 nm l ≈ 580 nm	PEG	N/A	N/A	N/A	SCC7 tumour in C3H/HeN mice [SWNT-PEG] = 1 mg mL^{-1} I: 785 nm, 0.2 Wcm^{-2}, 10 min t: 11 days	≈ 100%	[120]
	l ≈ 1126 ± 389 nm	PEG	N/A	^{1}MCF-7 cells, ^{2}MDA-MB-231 cells	≈ ^{1}64.8 and ^{2}65%	Female Balb/c mice injected with EMT6 cells	≈ > 90%	[121]

				[MWNT] = 100 μg mL^{-1} Incubation: 24 h I: 808 nm, 5 Wcm^{-2}, 2 min		[MWNT] = 100 μg mL^{-1} I: 808 nm, 5 Wcm^{-2}, 1 min t: 10 days		
CNT	N/S	Manganese oxide (MnO) PEG	N/A	A549 cells [MWNT–MnO–PEG] = 40 μg mL^{-1} Incubation: 2 h I: 808 nm, 3 Wcm^{-2}, 5 min	≈ 88.41%	Nude male mice with A549 metastases [MWNT–MnO–PEG] = 3 mg mL^{-1} I: 808 nm, 2 Wcm^{-2}, 5 min	≈ > 75%	[122]
	s ≈ 0.81 nm	Phospholipid - poly(ethylene glycol) (PL-PEG) FA	N/A	EMT6 cells [FA-SWNT] = 3.5 μg mL^{-1} Incubation: 2 h I: 980 nm, 1 Wcm^{-2}, 2 min	≈ 90%	Female Balb/c mice injected with EMT6 cells [FA-SWNT] = 1 mg kg^{-1} I: 980 nm, 1 Wcm^{-2}, 5 min	Cell death rate *in vivo*: ≈ 88%	[127]
	N/S	PL-127	N/A	RENCA cells [MWCNT] = 100 μg mL^{-1} I: 1064 nm, 3 Wcm^{-2}, 0.75 min	≈ 100%	Female athymic mice bearing RENCA tumours I: 1064 nm, 3 Wcm^{-2}, 0.5 min t: 30 days	≈ 100%	[126]
	N/S	Oxygen PEG	N/A	N/A	N/A	Female C57BL/6J mice injected with B16-F10 cells [O-CNT-PEG] = 1 mg mL^{-1} I: 808 nm, 8 Wcm^{-2}, 10 min t: 3 days	≈ > 90%	[124]
	N/S	Gold nanostars	N/A	B16-F10 cells [MWCNSs/gold nanostars] = 0.32 nM Incubation: 24 h I: 808 nm, 1 Wcm^{-2}, 3 min	≈ > 80%	N/A	N/A	[181]
	h ≈ 2.5–5.0 nm	Annexin V	N/A	N/A	N/A	Balb/c female mice with implanted 4T1 cells [SWNT] = 0.8 mg kg^{-1} I: 980 nm, 1 Wcm^{-2}, 3 min t: 38 days	≈ > 90%	[182]
	N/S	Au NP Sodium alginate Chitosan	N/A	HeLa cells [AuSWNT] = 50 μg mL^{-1} Incubation: 24 h I: 808 nm, 1.6 W, 15 min	Cell necrosis	N/A	N/A	[183]
	l ≈ 50–500 nm	C_{18}-PMH-PEG	N/A	N/A	N/A	BALB/c mice bearing 4T1 tumours [SWNT] = 0.5 mg mL^{-1} I: 808 nm, 1 Wcm^{-2}, 5 min t: 14 days	≈ > 90%	[130]
	l ≈ 100–300 nm.	PEG Mesoporous silica (MS)	DOX LC: ≈ 2.3:1	4T1 cells [DOX] = 25 μM Incubation: 1 h I: 808 nm, 0.7 Wcm^{-2}, 20 min	≈ 100%	Mice bearing 4T1 tumours [SWNT] = 4.3 mg kg^{-1}, [DOX] = 10 mg kg^{-1} I: 808 nm, 0.5 Wcm^{-2}, 20 min t: 14 days	≈ > 90%	[123]
	s ≈ 251.85 ± 11.98 nm	Transactivator of transcription peptide Chitosan	DOX LC: 50% R: 70–90%	Bel-7402 cells [CNT] = 10 μg mL^{-1} Incubation: 72 h I: 808 nm ,1 Wcm^{-2}, 5 min	≈ 80%	Balb/c nude mice injected with Bel-7402 cells [CNT] = 4 mg mL^{-1} I: 808 nm ,1 Wcm^{-2}, 5 min t: 25 days	≈ > 90%	[132]
	s ≈ 182.8 ± 2.8 nm	NGR peptide DPM	Docetaxel	PC3 cells [SWNT] = 14.4 μg mL^{-1} Incubation: 6 h I: 808 nm, 1.4 Wcm^{-2}, 1 min	≈ 95.33%	S180 cells injected in female Balb/c mice [Docetaxel] = 25.125 mg kg^{-1} I: 808 nm, 1 min t: 13 days	≈ > 90%	[128]
CNH	d ≈ 50–100 nm	Pluronic	N/A	RENCA cells [SWNH] = 85 μg mL^{-1} Incubation: 24 h	≈ 100%	N/A	N/A	[135]

				I: 1064 nm, 40 Wcm^{-2}, 6 min				
CNH	HD ≈ 164 nm	Deoxycholic acid modified-hydropropyl chitosan (DCA-HPCHS)	DOX	4T1 cells [DOX-SWNH/DCA-HPCHS] = 10 μg mL^{-1} I: 808 nm, 0.6 Wcm^{-2}, 10 min	≈ 100%	Female Balb/c mice injected with 4T1 cells [DOX-SWNH/DCA-HPCHS] = 1 mg mL^{-1} I: 808 nm, 0.4 Wcm^{-2}, 10 min t: 12 days	≈ 65%	[184]
	HD ≈ 182 ± 3.2 nm	Poly (maleic anhydride-alt-1-octadecene) (C_{18}PMH) Methoxypolyethyleneglycol-b-poly-D, L-lactide (mPEG-PLA)	DOX LE: 44% R: 67.12% Pt LE: 66 wt% R: 12.13%	4T1 cells [SWNH] = 20 μg mL^{-1} Incubation: 24 h I: 808 nm, 0.4 Wcm^{-2}, 3 min	≈ > 90%	4T1 tumour bearing mice [SWNH] = 10 mg kg^{-1} I: 808 nm, 1 Wcm^{-2}, 5 min t: 16 days	≈ 100%	[133]
	s ≈ 178.8 ± 0.5 nm	Oxygen P-glyprotein antibody PEG	Etoposide (ETO) LC: 39.6% R: 81%	^{1}A549 cells, ^{2}A549R cells [ETO] = 100 μg mL^{-1} Incubation: 48 h I: 671 nm, 100 mW	≈ ^{1}85 and ^{2}90%	Male Balb/c nude mice injected with A549R cells [ETO] = 2.5 mg kg^{-1} I: 671 nm, 10 min t: 16 days	≈ > 75%	[134]
Graphene	d ≈ 50 nm	PVP	N/A	U251 cells [G_{PVP}] = 5 μg mL^{-1} I: 808 nm, 2 Wcm^{-2}, 5 min	≈ > 90%	N/A	N/A	[136]
GO	t ≈ 3.2 ± 0.9 nm s ≈ 24.5 ± 6.5 nm	PEG Cypate	N/A	4T1 cells [Cypate] = 100 μg mL^{-1} Incubation: 24 h I: 785 nm, 1.5 Wcm^{-2}, 3 min	≈ 90%	Mice bearing 4T1 tumours [Cypate] = 7.5 mg kg^{-1} I: 785 nm, 1 Wcm^{-2}, 5 min t: 22 days	≈ 100%	[145]
	d ≈ 200–600 nm	IO NP Au NP PEG	N/A	4T1 cells [GO] = 10 μg mL^{-1} Incubation: 2 h I: 808 nm, 2 Wcm^{-2}, 5 min	≈ > 90%	Female BALB/c mice bearing 4T1 tumours [GO] = 50 μg mL^{-1} I: 808 nm, 0.75 Wcm^{-2}, 5 min t: 18 days	≈ 100%	[146]
	N/S	Porphyrin RGD	N/A	U87-MG cells [PNG-RGD] = 100 μg mL^{-1} Incubation: 2 h I: 808 nm, 2.5 Wcm^{-2}, 10 min	≈ 78.07%	Female athymic nude mice injected with U87-MG cells [PNG-RGD] = 10 mg kg^{-1} I: 808 nm, 2.5 Wcm^{-2}, 5 min t: 30 days	≈ 100%	[142]
	s ≈ 10–50 nm	PEG Cyanine7	N/A	N/A	N/A	Balb/c mice bearing 4T1 tumours [NGS-PEG] = 20 mg kg^{-1} I: 808 nm, 2 Wcm^{-2}, 5 min t: 1 day	≈ 100%	[22]
	s ≈< 200 nm t ≈ 3.7–10.2 nm	IO NP PEG	N/A	BxPC-3 cells [GO] = 40 μg mL^{-1} Incubation: 2 h I: 808 nm, 3 Wcm^{-2}, 5 min	≈ 81.26%	Nude male mice injected with BxPC-3 cells [GO-IO NP-PEG] = 8 mg mL^{-1} I: 808 nm, 2 Wcm^{-2}, 5 min t: 15 days	≈ 61.76%	[147]
	s ≈ 250 nm t ≈ 4–5 nm	HAc	N/A	B16F1 cells [NGO-HA] = 250 μg mL^{-1} Incubation: 1 h I: 808 nm, 2 Wcm^{-2}, 10 min	≈ > 70%	B16F1 cells inoculated in SKH-1 hairless mice [NGO-HA] = 1 mg mL^{-1} t: 7 days	≈ 100%	[155]
	s ≈ 300 nm	Aptamer Au NP HSP70 inhibitor	N/A	MCF-7 cells [Apt-AuNP−GO] = 1.74 μg mL^{-1} Incubation: 24 h I: 808 nm, 3 W, 5 min	≈ 61%	N/A	N/A	[144]
	s ≈ 155 ± 3.9 nm	FA MnO_2	N/A	HeLa cells [MnO_2-FA-GO] = 30 μg mL^{-1} Incubation: 5 h I: 808 nm, 5 Wcm^{-2}, 3 min	≈ 75%	N/A	N/A	[139]

GO	s ≈ 200 nm t ≈ 1 nm	Indocyanine green (ICG) FA	N/A	HeLa cells [GO] = 20 μg mL^{-1} Incubation: 1 h I: 808 nm, 2 Wcm^{-2}, 10 min	≈ 92%	N/A	N/A	[140]
	w ≈ 100 nm	PEG	DOX LC: 142.5 wt% R: 68%	EMT6 cells [DOX] = 10 μg mL^{-1} Incubation: 24 h I: 808 nm, 2 Wcm^{-2} 3 min	≈ 82.1%	Balb/c female mice injected with EMT6 cells [DOX] = 10 mg kg^{-1} I: 808 nm, 2 Wcm^{-2}, 5 min t: 30 days	≈ 100%	[30]
	s ≈< 100 nm	PVP FA	DOX LC: 107.5 wt% R: > 70%	HeLa cells [DOX] = 20 μg mL^{-1} Incubation: 24 h I: 808 nm, 2 Wcm^{-2}, 5 min	≈ 90%	N/A	N/A	[137]
	s ≈< 200 nm h ≈ 2.5 nm t ≈ 1–2 nm	SS PEG	DOX LC: 110 wt% R: 65%	A549 cells [DOX] = 10 μg mL^{-1} Incubation: 24 h I: 808 nm, 2 Wcm^{-2}, 3 min	≈ 90%	N/A	N/A	[148]
	N/S	Aptamer Au NP	DOX LE: 11.3% R: ≈ 80%	[1]A549 cells, [2]MCF-7 cells [GO–Au–Apt–DOX] = 8 μg mL^{-1} Incubation: 12 h I: NIR, 15 min	≈ [1]90 and [2]80%	N/A	N/A	[143]
	N/S	Copper sulfide (CuS) PEG	DOX LE: 90.0% R: 45	HeLa cells [PEG-GO/CuS/Dox] = 500 μg mL^{-1} Incubation: 24 h I: 980 nm, 1 Wcm^{-2}, 10 min	≈ 75%	Male nude mice injected with HeLa cells [PEG-GO/CuS/Dox] = 500 μg mL^{-1} I: 980 nm, 1 Wcm^{-2}, 10 min t: 21 days	≈ > 95%	[149]
	N/S	Fluorine FA Silver nanoparticles (Ag NP)	DOX LC: 263% R: 30%	HeLa cells [DOX] = 1.6 μg mL^{-1} Incubation: 4 h I: 808 nm, 2.0 Wcm^{2}, 5 min	≈ 81%	Nude mice bearing tumours [FGO-FA+Ag_2+DOX] = 50 μg mL^{-1} I: 808 nm, 2.0 Wcm^{2}, 5 min t: 14 days	≈ > 55%	[138]
	s ≈ 50–250 nm	Silica PEG IL-13 peptide	DOX LE: 1.27 ± 0.11 μg $μg^{-1}$ R: 17%	U251 cells [GS] = 100 μg mL^{-1} Incubation: 2 h I: 808 nm, 6 Wcm^{-2}, 5 min	≈ 90%	N/A	N/A	[153]
	d ≈ 187.5 ± 0.2 nm	Silica Serum protein FA	DOX LE: 90% R: 90%	HeLa cells [SiO_2@GN-Serum-FA NPs] = 1000 μg mL^{-1} Incubation: 24 h I: 980 nm, 1.0 Wcm^{-2}, 10 min	≈ > 70%	U14 cells injected in female Balb/c mice [SiO_2@GN-Serum-FA-Dox+IR] = 500 μg mL^{-1}, [Dox] = 10.0 μg mL^{-1} I: 980 nm, 1.0 Wcm^{-2}, 5 min t: 19 days	≈ > 90%	[141]
	s ≈ 70 nm	PEG Poly(allylamine hydrochloride) (PAH)	DOX LE: ≈ 50% R: 23%	MCF-7/ADR cells [DOX] = 20 μg mL^{-1} Incubation: 48 h I: 808 nm, 0.5 Wcm^{-2}, 5 min	≈ 79%	N/A	N/A	[174]
	s ≈ 200 nm	Poloxamer 188	DOX Irinotecan (IRI) LC: 7% R: 60%	[1]SCC7 cells, [2]MCF-7 cells, [3]MDA-MB-231 cells [DOX/IRI] = 1 μg mL^{-1}, [GO] = 6 μg mL^{-1} Incubation: 6 h I: 808 nm, 3 Wcm^{-2}, 5 min	≈ [1]60, [2]40 and [3]60%	N/A	N/A	[154]
	s ≈ 10–70 nm	PEG	Pt R: ≈ 90%	4T1 cells [Pt] = 100 μM, [PEG-NGO] = 890 μg mL^{-1} Incubation: 24 h I: 785 nm, 1.5 Wcm^{-2}, 3 min	≈ > 90%	Female mice bearing 4T1 tumours [Pt] = 10 mg kg^{-1} I: 785 nm, 1.5 Wcm^{-2}, 3 min t: 14 days	≈ 100%	[150]
	N/S	HAc	Mitoxantrone (MIT) LC: 45 wt% R: 14.85%	MCF-7 cells [MIT] = 51.2 μg mL^{-1} I: 808 nm, 2 Wcm^{-2}, 3 min	≈ 95%	MCF-7-bearing mice [MIT] = 4 mg kg^{-1} I: 808 nm, 1 min t: 6 days	≈ 93.52%	[156]
	w ≈ 100 nm t ≈ 4 nm	PEG	Epirubicin (EPI) LC: 87% R: 46%	U87-MG cells [EPI] = 25 μg mL^{-1} Incubation: 24 h	≈ 100%	NU/NU mice injected with U87-MG cells [EPI] = 3 mg kg^{-1}	≈ 100%	[151]

			Anti-EGFR antibodies Conjugation: 71% R: 46%	I: 808 nm, 2 Wcm^{-2}, 2 min		I: 808 nm, 2 Wcm^{-2}, 2 min t: 27 days		
GO	s ≈ 182 nm	PEG	Artesunate	HepG2 cells [nGO] = 80 μg mL^{-1} Incubation: 4 h I: 808 nm, 2 Wcm^{-2}, 5 min	≈ 80%	Balb/c mice bearing 4T1 tumours [nGO] = 10 mg kg^{-1} I: 808 nm, 15 min t: 30 days	≈ 100%	[152]
rGO	s ≈ 521 nm	PEG	N/A	A-431 cells [rGOn-PEG] = 250 μg mL^{-1} Incubation: 24 h I: 810 nm, 0.15 Wcm^{-2}, 30 min	≈ 38%	N/A	N/A	[35]
	d ≈ 27 nm	PEG	N/A	N/A	N/A	4T1 cells injected in female BALB/c mice [nRGO-PEG] = 2 mg mL^{-1} I: 808 nm, 0.15 Wcm^{-2}, 5 min t: 15 days	≈ 100%	[171]
	s ≈ 20 nm	PEG RGD	N/A	U87-MG cells [nano-rGO-RAD] = 6.6 μg mL^{-1} Incubation: 1 h I: 808 nm, 15 Wcm^{-2}, 8 min	≈ 90%	N/A	N/A	[159]
	s ≈ 108 ± 51 nm	HAc Poly(maleic anhydride-alt-1-octadecene)	N/A	MCF-7 cells [rGO] = 75 μg mL^{-1} Incubation: 4 h I: 808 nm, 1.7 Wcm^{-2}, 5 min	≈ 94%	N/A	N/A	[34]
	N/S	Polyphenols	N/A	[1]HT29 cells and [2]SW48 cells [rGO] = 3 μg mL^{-1} Incubation: 6 h I: 780 nm, 0.25 Wcm^{-2}, 20 min	≈ [1]66 and [2]82%	N/A	N/A	[168]
	t ≈ 1.4 nm	Glucose Iron	N/A	LNCaP cells [GRGO-Fe] = 100 μg mL^{-1} Incubation: 24 h I: 808 nm, 7.5 Wcm^{-2}, 1 min	≈ 93%	N/A	N/A	[185]
	HD ≈ 50 nm	IO NP PEG	N/A	N/A	N/A	Mice bearing 4T1 tumours [RGO–IO NP–PEG] = 20 mg kg^{-1} I: 808 nm, 0.5 Wcm^{-2}, 5 min t: 15 days	≈ 100%	[172]
	t ≈ 1.1 nm	Polyphenols	N/A	A549 cells [rGO] = 1000 μg mL^{-1} Incubation: 0.5 h I: 808 nm, 2 Wcm^{-2}, 5 min	≈ 65%	N/A	N/A	[169]
	d ≈ 100 min	C_{18}-PMH-mPEG PL-PEG	N/A	N/A	N/A	Female C57BL/6 mice injected with Panc02-H7 cells [rGO] = 2 mg kg^{-1} I: 980 nm, 0.75 Wcm^{-2}, 10 min t: 10 days	≈ > 70%	[173]
	s ≈ 29 ± 4 nm	PEG Iron Oxide (Fe_3O_4)	N/A	4T1 cells [FNPs/rGO-PEG] = 250 μg mL^{-1} Incubation: 4 h I: 805 nm, 1 Wcm^{-2}, 5 min	≈ 80%	Balb/c mice injected with 4T1 cells m = 0.1 mg I: 805 nm, 1 Wcm^{-2}, 10 min t: 25 days	≈ 100%	[160]
	d ≈ 100 nm	PEG	N/A	HeLa cells and MDA-MB-231 cells [rGO-PEG] = 200 μg mL^{-1} Incubation: 72 h I: 808 nm, 6 Wcm^{-2}, 10 min	≈ 100%	N/A	N/A	[161]
	s ≈ 110 nm	HAc ICG LE: 92.3 ± 5.0%	N/A	KB cells [ICG/HArGO] = 20 μg mL^{-1} Incubation: 24 h I: 808 nm, 1.2 Wcm^{-2}, 3 min	≈ > 90%	KB tumour-bearing nude mice [ICG/HArGO] = 5 mg kg^{-1} I: 808 nm, 1.2 Wcm^{-2}, 3 min	≈ 100%	[167]

						t: 26 days		
rGO	s ≈ 70 ± 0.4 nm	BSA	N/A	MCF-7 cells [nano-rGO] = 100 μg mL^{-1} I: 808 nm, 1 Wcm^{-2}, 5 min	≈ 100%	Female BALB/c nude mice bearing MCF-7 tumours [nano-rGO] = 20 mg kg^{-1} I: 808 nm, 0.6 Wcm^{-2}	≈ 100%	[165]
	t ≈ 140 nm	N/A	N/A	OE-19 cells [RNGO] = 100 μg mL^{-1} I: 808 nm, 3 Wcm^{-2}, 8 min	≈ 100%	N/A	N/A	[186]
	s ≈ 0.8–2.5 μm	Fe_3O_4	N/A	HeLa cells [rGO-Fe_3O_4] = 100 μg mL^{-1} Incubation: 2 h I: 804 nm, 1 Wcm^{-2}, 5 min	≈ 76.3%	N/A	N/A	[170]
	N/S	Alanine	N/A	U87-MG cells [ARGO] = 100 μg mL^{-1} I: 808 nm, 0.6 Wcm^{-2}, 10 min	≈ 76%	N/A	N/A	[187]
	t ≈ 3.5 nm	Antiarrhythmic peptide 10 (AAP10) pDA	N/A	MCF-7 cells [AAP10-pDA/rGO] = 120 μg mL^{-1} I: 880 nm, 2.2 Wcm^{-2}, 5 min	≈ 99%	N/A	N/A	[164]
	d ≈ 100–200 nm t ≈ 15 nm	PEI PEG	DOX LC: ≈ 100% R: ≈ 45%	[1]PC3 cells, [2]HeLa cells [DOX] = 50 μg mL^{-1} I: 808 nm, 6 Wcm^{-2}, 30 min	≈ [1]60 and [2]80%	N/A	N/A	[162]
	s ≈ 200–300 nm	Mesoporous silica shell ($mSiO_2$) Thermoresponsive polymer valve (pNIPAM-co-pAAm)	DOX LC: 0.8221 ± 0.12 g g^{-1} R: ≈ 30%	HeLa cells [rNGO@$mSiO_2$@pNIPAM-co-pAAm] = 60 μg mL^{-1}, [DOX] = 12 μg mL^{-1} Incubation: 4 h I: 808 nm, 6 Wcm^{-2}, 10 min	≈ 100%	N/A	N/A	[188]
	N/S	BSA	DOX LE: 77% R: 23%	U87-MG cells [DOX-BSA-rGO] = 30 μg mL^{-1} Incubation: 4 h I: 808 nm, 5.5 Wcm^{-2}, 3 min	≈ 98.24%	N/A	N/A	[166]
	N/S	MS pDA HAc	DOX LC: 145 ± 25%	HeLa cells [DOX] = 5 μM Incubation: 12 h I: 808 nm, 1.5 Wcm^{-2}, 5 min	≈ 90%	Female Balb/c nude mice implanted with HeLa cells [DOX] = 5 mg kg^{-1} I: 808 nm, 1.5 Wcm^{-2}, 5 min t: 20 days	≈ 100%	[163]
	s ≈ 40 nm t ≈ 2 nm	N/A	DOX LC: 317% (w/w) R: 85%	[1]HepG2 cells, [2]Huh-7 cells, [3]A549 cells [nrGO/DOX] = 80 μg mL^{-1} Incubation: 3 h I: 808 nm, 5 min	≈ [1]68.3, [2]54.8 and [3]76.2%	N/A	N/A	[189]
	d ≈ 80 nm	PEG	Resveratrol (RV) LC: 175.6 w/w % R: 30%	4T1 cells [RV] = 50 μg mL^{-1} Incubation: 2 h I: 808 nm, 0.6 Wcm^{-2}, 3 min	≈ 60%	Female Balb/c mice injected with 4T1 tumours [NrGO] = 10 mg kg^{-1} I: 808 nm, 0.6 Wcm^{-2}, 5 min t: 18 days	≈ 100%	[190]

4T1 cells, 4T1 murine breast cancer cell line; A-431 cells, human skin carcinoma cell line; A549 cells, Human lung adenocarcinoma cell line; A549R cells, A549 cells resistant to paclitaxel; AAP10, Antiarrhythmic peptide 10; Ag NP, Silver nanoparticles; Au NP, Gold nanoparticles; B16F1 cells, murine melanoma cell line; B16-F10 cells, B16-F10 mice melanoma cell line; Bel-7402 cells, Bel-7402 hepatoma cell line; BSA, Bovine serum albumin; BT474 cells; Human breast cancer cell line; BxPC-3 cells, BxPC-3 cells human pancreatic cancer cell line; C_{18}PMH, Poly (maleic anhydride-alt-1-octadecene); C_{18}-PMH-mPEG, Poly(maleic anhydride-*alt*-1-octadecene)-methoxy poly(ethylene glycol); C_{18}-PMH-PEG, Poly(maleic anhydride-*alt*-1-octadecene)-poly(ethylene glycol); CD, Carbon dots; CNH, Carbon nanohorns; CNM, Carbon nanomaterial; CNT, Carbon nanotubes; CN_x, Nitrogen dopants; CREKA, Cys-Arg-Glu-Lys-Ala; CRL 1932, Renal carcinoma cell line; CuS, Copper sulfide; d, diameter; DCA-HPCHS, Deoxycholic acid modified-hydropropyl chitosan; DOX, doxorubicin; DPM, 1,2-distearoyl-sn-glycero-3-phosphoethanolamine-N-[methoxyPEG-2000]-maleimide; DSPE-mPEG, 1,2-distearoyl-phosphatidylethanolamine-methyl-poly(ethylene glycol); EAC cells, Erlich ascitic carcinoma cell line; EMT6 cells, murine mammary tumour line; Epirubicin (EPI); ETO, Etoposide; FA, Folic acid; Fe_3O_4, Iron Oxide; GO, Graphene oxide; GQD, Graphene quantum dots; h, height; H22 cells, H22 hepatocellular carcinoma cell line; HAc, Hyaluronic acid; HD, hydrodynamic size; HeLa cells, Human cervical cancer cell line; HepG2 cells, Human hepatocellular carcinoma cell line; HT29 cells, HT29 human colon adenocarcinoma cell line; Huh-7 cells, Hepatoma Huh-7 cell line; I, Irradiation; ICG, Indocyanine green; IO NP, Iron oxide nanoparticles; IRI, Irinotecan; KB cells, Human carcinoma KB cell line; l, length; LC, loading capacity; LE, loading efficiency; LNCaP cells, Human prostate cancer cell line; MCF-7 cells, Human breast cancer cell line; MCF-7/ADR cells, Drug-resistant MCF-7/ADR cell line; MDA-MB-231 cells, Human breast cancer cell line; MIT, Miroxantrone; MnO, Manganese oxide; MnO_2, Manganese dioxide; mPEG-PLA, Methoxypolyethyleneglycol-b-poly-D, L-lactide; MS, Mesoporous silica; $mSiO_2$, Mesoporous silica shell; MT, Mitochondria-targeting peptide; N, Nitrogen; N/A, not applicable; N/S, not studied; N-B, Nitrogen and boron; NGR, Asparagine-glycine-arginine; N-O, Nitrogen and

oxygen; OE-19 cells, Esophageal adenocarcinoma cell line; OH, Hydroxyl groups; PAH, Poly(allylamine hydrochloride); Panc02-H7 cells, Mouse pancreatic cancer cell line; PC3 cells, Prostate cancer 3 (PC3) cell line; pDA, Polydopamine; PEG, Poly(ethylene glycol); PEI, Polyethylenimine; PL-127, Pluronic F-127; PLGA-b-PEG-NH_2, Poly(L-lactide-co-glycolide)-block-poly(ethylene glycol)-Amine; PLL, Poly (L-lysine); PL-PEG, Phospholipid-poly(ethylene glycol); pNIPAM-co-pAAm, Thermoresponsive polymer valve; Pt, Cisplatin; U14 cells, Murine hepatocarcinoma U14 cell line; PVP, Polyvinylpyrrolidone; R, release; RENCA cells, RENCA murine kidney cancer cell line; RGD, Tripeptide L-arginyl-glycyl-Laspartic; rGO, Reduced graphene oxide; Ru-NO, Ruthenium nitrosyl; RV, Resveratrol; s, size; SCC7 cells, Murine SCC7 squamous carcinoma cell line; SF-763 cells, Human glioblastoma cell line; S-N, Sulphur and nitrogen; SS, Disulfide bond; S180 cells, Murine sarcoma cell line; SW48 cells, SW48 colon cancer cell line; t, thickness; t, treatment time; Th, topographic height; TPP, Triphenylphosphonium; U251 cells, Human glioblastoma cell line; U87-MG cells, Adherent human glioblastoma (U87-MG) cell line; w, width; ZIF-8, Zeolitic imidazolate framework-8.

2.3.3 - Combined phototherapy

Photodynamic and photothermal therapies have been studied as low invasive and selective therapeutic approaches, as mentioned in the previous sections. Nevertheless, the combined effect of these two modalities can further enhance their effectiveness for anticancer therapy [6, 10]. Several studies report multimodal treatment with these two types of light therapy. PTT can improve PDT efficiency once the heat generated after irradiation leads to increased cell permeability [191], which improves PS uptake. Higher temperatures, also increase blood flow and cause tumour tissues to become more oxygenated, both contributing to improved PDT, by generating increasing amounts of ROS. Furthermore, ROS production during PDT interferes with heat-shock proteins and stop them from protecting tumour cells from the PTT effects [5] CNM can be conjugated with various macromolecules, load PS and/or anticancer drugs and efficiently target and kill tumour cells [6]. Drug internalisation is more efficient and smaller doses are required, ultimately reducing toxicity and side effects. Besides, treatment effects are directed to tumour tissues as cancer cells more sensitive membrane becomes more permeable, allowing higher CNM/drug uptake and consequently increased selective anticancer effect.

While in PTT CNM therapeutic activity is usually triggered by performing irradiation in NIR wavelengths, in PDT, UV and visible light irradiations are mostly employed. Generally, NIR irradiation is more advantageous, because its penetration is deeper into biological tissues, which have minimal absorption in that range. Therefore, deeper located tumours can be reached, with minimal harm to surrounding healthy tissues. Some studies apply NIR together with UV or visible light using subsequent cycles of irradiation or combined treatment. The first involves the application of determined irradiation followed by another, while the second applies the two types of irradiation simultaneously. Table 2.3 summarizes the state-of-the-art literature regarding the use of CNM in combined phototherapy, including their main characteristics and biological effects. In the literature, promising results were reported using fullerenes, CD, GQD, CNT, CNH, graphene, GO and rGO, being GO the most extensively studied.

Non-functionalized fullerenes usually do not present suitable properties to be used for PTT, as mentioned before. Since they need to be modified to have a relevant phototherapeutic effect, agents that can have a synergistic effect for different therapeutic modalities can be employed, seeking enhanced effectiveness and selectivity. Lee *et al.* conjugated fullerene (C_{60}) with Ce6, PEG and folate to obtain increased light absorption, enhanced biocompatibility and targeted treatment, once folate receptors are overexpressed in tumours, promoting selective internalization. Combined therapy was used in a human carcinoma cell line. Cells were incubated with the modified fullerene at a concentration of 10 μg mL^{-1} and irradiated with a laser (670 nm, 300 $mWcm^{-2}$) for 10 minutes after 4 h of culture. The treatment led to 95% cancer cell death. Also, mice were subcutaneously inoculated with the same cancer cell line to induce tumour formation. Modified fullerenes were intravenously injected at a concentration of 10 mg kg^{-1} and after 2 h irradiated using the same settings as for *in vitro* tests. The treatment led to over 85% tumour reduction after 7 days, comparing with untreated control. The authors reported efficient

clearance from the body with no significant differences being observed in the organs [192]. Fullerene-based systems have been also conjugated with drugs to further increase their anti-cancer effectiveness. Wang *et al.* combined fullerenes with silica and hyaluronan to encapsulate DOX and ICG. A DOX LC of approximately 48% was reported. Combined therapy was used in two human breast cancer cell lines, MDA-MB-231 and MCF-7. Cells were incubated with modified fullerenes at a DOX concentration of 10 μg mL^{-1} and irradiated with laser (800 nm, 1.5 Wcm^{-2}) for 3 minutes after 12 h of culture. The treatment resulted in 100 and 95% cancer cell death, respectively for MDA-MB-231 and MCF-7. No significant damage in the main organs was observed in histological analysis [193].

Some CNM can be used for both PTT or/and PDT without any modifications because they can produce heat and ROS, leading to tumour cell death through different mechanisms. CD have gained increased interest due to their simultaneous PDT and PTT functions. *In vitro*, concentrations commonly used for this nanomaterial vary from 200 to 1000 μg mL^{-1}, and incubation times range between 10 to 24 h. Irradiations are usually performed using lasers at wavelengths between 650-808 nm, and with irradiances from 0.5 to 1 Wcm^{-2}, during 10 to 20 minutes. Studies with CD usually report between 79.1 and 95% cancer cell death after combined therapy. *In vivo*, CD are often injected intratumorously or intravenously, and concentrations used range between 1 and 3 mg mL^{-1}. Irradiations are performed using lasers with a wavelength between 650-808 nm, with irradiances between 0.5 to 1 Wcm^{-2}, during 10 to 20 minutes. Combined therapy usually results in between 70 to 100% tumour reduction, 13 to 22 days after treatment [194-196], with effective blood clearance and no damage or inflammation occurring [194, 196, 197]. Guo *et al.* doped CD with a Cu-N complex that was capable of absorbing in the NIR region, producing heat and ROS. Combined therapy was tested using a murine melanoma cell line. Cells were incubated with the modified CD at a concentration of 500 μg mL^{-1} and irradiated with a laser (808 nm, 1 Wcm^{-2}) for 10 minutes after 24 h of culture. The treatment led to 80% cancer cell death. Separate individual treatment allowed higher cell viabilities (PDT ≈ 50% and PTT ≈ 55%) demonstrating the increased effect when multimodal therapy is applied. Also, mice were subcutaneously inoculated with the same cancer cell line to induce tumour formation. Modified CD were intravenously injected at a concentration of 3 mg mL^{-1} and after 4 h irradiated using the same conditions. The treatment led to 100% tumour reduction after 14 days, comparing with the untreated control [194].

GQD is another example of CNM with PDT and PTT functions. *In vitro*, concentrations commonly used for this nanomaterial vary from 100 to 500 μg mL^{-1}, while incubation times range between 1 to 12 h. Irradiations are usually performed with lasers with wavelengths between 670-808 nm or 980 nm followed by a treatment at 635 nm, to obtain a synergistic effects. Irradiances vary between 0.3 to 0.5 Wcm^{-2}, during 5 to 30 minutes. Studies with GQD usually report between 65 to 70% cancer cell death after combined therapy. Only one *in vivo* study has been found using these materials. Nurunnabi *et al*. tested graphene nanodots in mice subcutaneously inoculated with a human breast cancer cell line. GQD were intratumorously injected at a concentration of 2.5 mg kg^{-1} and irradiated with a laser (670 nm, 0.3 Wcm^{-2}) for 30 minutes. The treatment resulted in over 55% tumour reduction after 21 days, comparing with untreated control. Some accumulation was observed in the liver, lung and kidneys [198]. GQD have been also reported as efficient when decorating other materials such as hollow magnetic nanospheres (HMNS). Wo *et al.* used HMNS coated with silica and conjugated with GQD for the loading of DOX (0.66 g of DOX/g HMNS), and synergistic effect in a human esophageal squamous carcinoma cell line. Cells were incubated with HMNS/SiO_2/GQD at a GQD concentration of 0.2 mg mL^{-1} and

irradiated with a laser (671 nm) for 20 minutes. The treatment resulted in approximately 90% cancer cells death [199].

CNT have been also studied for simultaneous PTT/PDT. *In vitro,* concentrations commonly used for this nanomaterial vary from 2.4 to 500 μg mL^{-1}, while incubation times range between 12 to 24 h. Irradiations are usually performed using lasers with single 808 nm wavelengths or dual irradiations where a 532-630 nm irradiation is followed by a treatment at 808 nm, to achieve a synergistic effect. Irradiances vary from 0.1 to 1.4 Wcm^{-2}, during 1 to 10 minutes. Studies with CNT usually report between 45 to 100% cancer cell death after combined therapy. *In vivo,* CNT are often injected intratumorously or intravenously, and concentrations used range between 0.3 and 5 mg kg^{-1}. Irradiations are performed with lasers with a wavelength between 650-808 nm or dual irradiations where a 532-630 nm irradiation is followed by a treatment at 808 nm. Irradiances are performed between 0.5 to 1 Wcm^{-2}, during 10 to 20 minutes. The treatment usually results in between 90 to 100% tumour reduction, 9 to 15 days after being applied [200-202], with no histological damage being reported [37, 200-202]. In a study by Zhang *et al.,* a ruthenium (II) (Ru (II)) complex was used to functionalize SWCNT (Ru@SWCNT) for bimodal cancer treatment. Upon NIR irradiation, Ru (II) was released and produced ROS, while SWCNT produced heat leading to efficient cancer treatment in a human cervical cancer cell line. Cells were incubated with the Ru@SWCNT at a concentration of 200 μg mL^{-1} and irradiated with a NIR laser (808 nm, 0.25 Wcm^{-2}, 5 min) after 12 h of culture. The treatment resulted in 100% cancer cell death. Besides, mice were subcutaneously inoculated with the same cancer cell line to induce tumour formation. Ru@SWCNT were intratumorously injected at a concentration of 5 mg kg^{-1} and irradiated using the same conditions. The treatment resulted in 100% tumour reduction after 15 days, comparing with the untreated control [202]. As mentioned before, for PDT applications, CNT usually are loaded with PS. Nevertheless, some studies describe its potential as ROS producers. Murakami *et al.* produced semiconducting SWCNT and further conjugated it with a high-density lipoprotein for combined PDT and PTT of a human lung cancer cell line. Cells were incubated with the modified CNT and irradiated with a NIR laser (808 nm, 800 mW) for 10 minutes. The treatment resulted in 45% cancer cell death [203]. Figure 2.4 illustrates a representative example of CNM application in combined phototherapy. Xie *et al.* conjugated SWCNT with albumin, Evans blue (EB) and Ce6 (ACEC). The PTT properties of CNT were combined with the PDT effect of the PS Ce6 leading to a synergistic effect in a murine squamous carcinoma cell line. Cells were incubated with ACEC at a SWCNT/EB concentration of 2.4 μg mL^{-1} and subsequently irradiated at 630 nm and 808 nm (0.15 Wcm^{-2}, 1 min and 1 Wcm^{-2}, 2 min). The treatment resulted in 90% cancer cell death comparing with 85% obtained with only PDT and 80% with only PTT. Besides, mice were inoculated with the same cell line. ACEC were administrated intravenously at a CNT concentration of 0.3 mg kg^{-1} and irradiated using the same conditions. The treatment led to a 100% tumour reduction after 15 days, comparing with the untreated control [200].

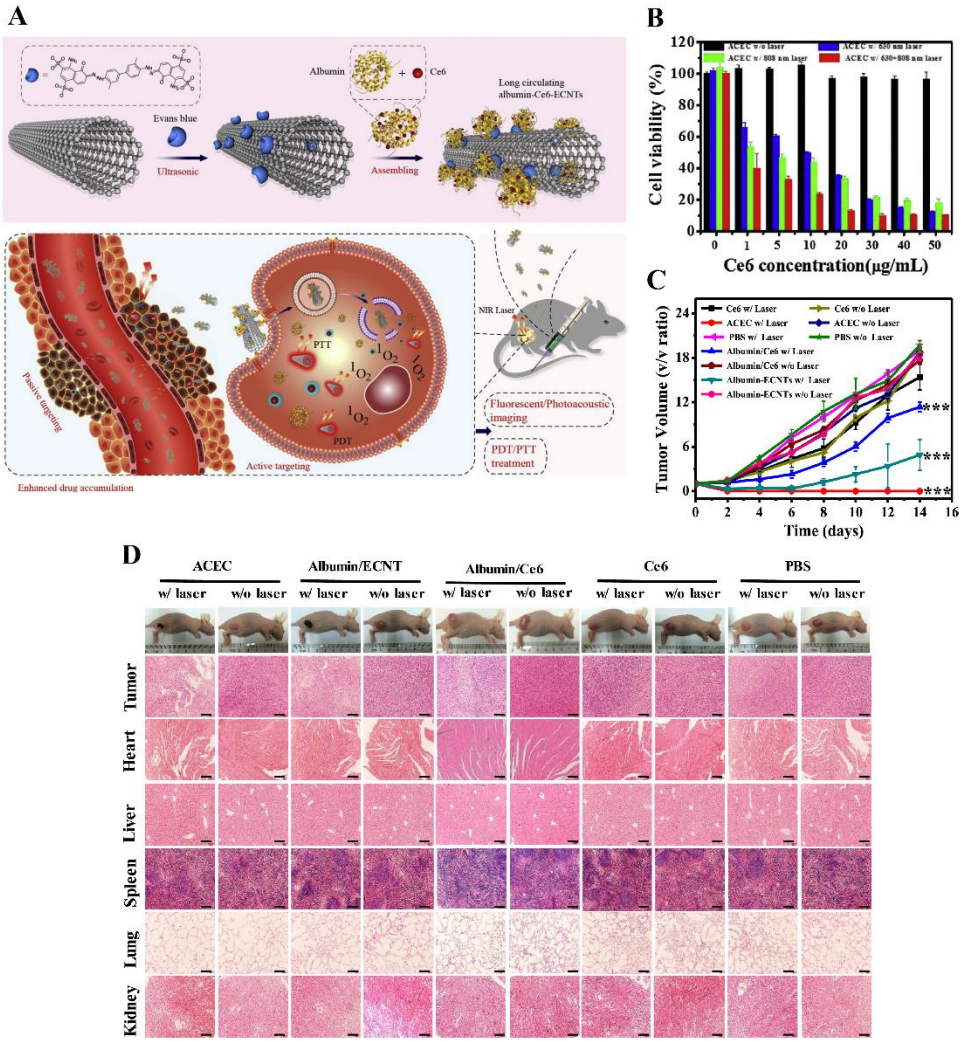

Figure 2.4 – Representative example of CNM use for cancer combined phototherapy. (A) Preparation and application of albumin/Ce6 fabricated EB/carbon nanotube-based delivery system (ACEC). SWCNT were conjugated with EB through high-frequency sonication and encapsulated the Ce6/albumin complex (B) SCC7 cell viabilities after incubation with different conditions. (C) Murine squamous carcinoma tumour bearing mice growth curves after receiving different treatments ($p < 0.001$). (D) Histology (Hematoxylin and eosin staining) of tumour bearing mice after different treatments: ACEC, albumin/ECNTs, free Ce6, albumin/Ce6 and PBS with or without 630 + 808 nm NIR irradiation (0.15 Wcm^{-2}, 1 min and 1 Wcm^{-2}, 2 min) at 24 h post-treatment. Scale bar: 100 μm. Adapted from [200]. Abbreviations: Ce6, chlorine e6; ECNTs, SWCNT/EB complex; SCC7 cells, murine squamous carcinoma cell line; SWCNT, single-walled carbon nanotube.

Combined PDT/PTT has also been reported with CNH. *In vitro*, concentrations commonly used for this nanomaterial vary from 8 to 26.5 μg mL^{-1} and incubation times are of 24 h. Irradiations are usually performed using lasers with single 650-808 nm wavelengths or dual irradiation where 590 nm irradiation is followed by a treatment at 808 nm. Irradiances vary from 0.5 to 3 Wcm^{-2}, during 1 to 20 minutes. Studies with CNH usually report between 66 and 94.6% cancer cell death after combined therapy. *In vivo*, CNH are often injected intratumorously or intravenously, and concentrations used range between 50.26 and 305 μg mL^{-1}. Irradiations are performed using lasers with a wavelength between 650-808 nm or dual irradiation where 590 nm irradiation is followed by a treatment at 808 nm. Irradiances vary between 0.1 to 1 Wcm^{-2}, during 5 to 20 minutes. A tumour reduction of 90 to 100% is commonly observed, 14 to 21 days after treatment [204-206], with no significant changes observed in the tissues by histology [204, 207]. Gao *et al.* used a SWCNH non-covalently conjugated with ICG (SWCNH-ICG) applied for

combined PDT/PTT in a murine breast cancer cell line. The PDT/PTT properties of ICG were combined with the PTT effect from CNH. Cells were incubated with SWCNH-ICG at a ICG concentration of 4 μg mL^{-1} and irradiated with a laser (808 nm, 0.3 Wcm^{-2}) after 24 h of culture. The treatment resulted in a cancer cell death of 94.6% when synergistic phototherapy was applied, comparing with 36.6% for PDT alone, and 86.5% for PTT. Besides, mice were inoculated with the same cell line. SWCNH-ICG was injected at a concentration of 52 μg mL^{-1} and irradiated twice using the same conditions for 5 minutes. The treatment resulted in over 90% tumour reduction, comparing with the untreated control [208].

In the case of graphene, despite having high NIR absorption, the increased hydrophobicity makes it difficult to apply in phototherapy. Jiang *et al.* produced this CNM by a direct current discharge method and conjugated it with a hydrophobic PS, tetrasulfonic acid tetrasodium salt copper phthalocyanine (TSCuPc), toward combined PTT/PDT as the graphene acts as a PS carrier and PTT agent while TSCuPc acts as a PDT agent. Human cervical cancer cells were incubated with the conjugated graphene at a PS concentration of 15 μg mL^{-1} and irradiated with a laser (650 nm, 3 Wcm^{-2}) for 5 minutes. The treatment resulted in 71% cancer cell death when combined therapy was applied, comparing with 40% for PDT alone [209]. This material has been also studied for combined PDT/PTT and chemotherapy. Su *et al.* conjugated graphene (PTT properties) with BODIPY (PDT properties), methoxy-PEG (biocompatibility) and mitomycin C (chemotherapy). Human cervical cancer cells were incubated with the conjugated CNM at a concentration of 100 μg mL^{-1} and irradiated with a laser (808 nm, 1 Wcm^{-2}, 5 min) followed by another (505 nm, 50 $mWcm^{-2}$, 5 min) after 48 h of culture. The treatment resulted in a 83% cancer cell death when combined therapy was applied, comparing with 25% for chemotherapy alone, 30% for chemotherapy and PDT, and around 70% for chemotherapy and PTT [210].

GO reveals suitable properties to be used as an effective PTT agent, but usually needs further conjugation to improve the production of ROS. However, some studies have suggested that this CNM can act as a PS and produce ROS without loading other molecules, as presented below. *In vitro*, concentrations commonly used for this nanomaterial vary from 3 to 800 μg mL^{-1}, while incubation times range between 4 to 48 h. Irradiations are usually performed using lasers with single 660-808 nm wavelengths or dual irradiations where a 532-808 nm irradiation is followed by a treatment at 808-980 nm, to obtain a synergistic effect. Irradiances vary from 0.05 to 4 Wcm^{-2}, during 3 to 60 minutes. Studies with GO usually report between 41.48 to 97.9% cancer cell death after combined therapy. *In vivo*, GO is often injected intratumorously or intravenously, and concentrations used range between 0.5 and 10 mg kg^{-1}. Irradiations are performed with lasers or LEDs with single 660-808 nm wavelengths or dual irradiations where a 630-650 nm irradiation is followed by a treatment at 808 nm. Irradiances vary between 0.15 to 3 Wcm^{-2}, during 3 to 10 minutes. Tumour reductions of 85 to 100% are observed, 12 to 15 days after treatment [211-213], with low systemic toxicity being usually reported and no significant damage found in histological analysis [212-216]. However, some accumulation has been described in the liver and lung tissues [211]. Hu *et al.* conjugated FA, PEG and fullerenes (C_{60}) onto GO nanosheets for combined PTT (induced by GO) and PDT (induced by fullerenes). Human cervical cancer cells were incubated with the conjugated GO at a concentration of 10 μg mL^{-1} and irradiated with a laser (808 nm, 2 Wcm^{-2}, 3 min) followed by another (532 nm, 0.1 Wcm^{-2}, 5 min) after 24 h of culture. The treatment resulted in 95% cancer cell death when combined therapy was applied, comparing with 65% for PDT alone and 25% for PTT [217]. A study by dos Santos *et al.* associated the increased photothermal activity of GO with the PS MB. A murine breast cancer cell line was incubated with the conjugated GO at a concentration of 12.5 μg mL^{-1} and irradiated with a LED (660 nm, 90.8 J

cm^{-2}, 10 min) followed by a laser (808 nm, 8.3 kJ cm^{-2}, 15 min) after 24 h of culture. The treatment resulted in 95% cancer cell death when combined therapy was applied, comparing with 30% for PTT alone. Besides, mice were inoculated with the same cell line. Conjugated GO was injected at a concentration of 10 mg kg^{-1} and irradiated using the same conditions. The treatment resulted in 100% tumour reduction after 12 days, comparing with untreated control. PTT alone resulted in 70% tumour reduction and PDT in 35% decrease [216]. This result was notable also due to the low concentration of MB used (2.5 µg mL^{-1}), while other studies reported the use of higher concentrations without achieving such efficiencies [218]. Kalluru *et al.* conjugated nanosized GO with PEG and folate to render it effective for simultaneous PDT and PTT. Upon excitation using 980 nm light, ROS production was detected but not using 808 nm. This study is an example where GO is applied as a PS. A melanoma cell line was incubated with the modified GO at a concentration of 75 µg mL^{-1} and irradiated with a laser (980 nm, 320 $mWcm^{-2}$) for 10 minutes after 24 h of culture. The treatment resulted in 85% cancer cell death, attributed by the authors to the combined PDT/PTT effect. PTT alone (808 nm) only resulted in 65% cancer cell death [213].

In the case of rGO, PTT properties have been studied as described in the previous section. However, after conjugation with PS, synergistic therapy has been reported. *In vitro*, concentrations commonly used for this nanomaterial vary from 4.8 to 50 µg mL^{-1}, while incubation times range between 1 and 24 h. Irradiations are usually performed using lasers with single 671-808 nm wavelengths or dual irradiations where a 365-660 nm irradiation is followed by a treatment at 808 nm, to obtain a synergistic effect. Irradiances vary from 0.02 to 1.5 Wcm^{-2}, during 2 to 30 minutes. studies with rGO usually report between 55 and 100% cancer cell death after combined therapy. *In vivo*, rGO is often injected intratumorously or intravenously, and concentrations used range between 0.5 and 1 mg mL^{-1}. Irradiations are performed with lasers or LEDs with single 671 nm wavelength or dual irradiations where a 450 nm irradiation is followed by a treatment at 808 nm. Irradiances vary between 0.02 to 0.5 Wcm^{-2}, during 2 to 20 minutes. Tumour reductions of 100% can be observed, 15 to 18 days after treatment [219, 220]. Wu *et al.* produced copper indium sulphide ($CuInS_2$) and zinc sulfide (ZnS) nanocrystals ($CuInS_2$/ZnS) with PTT and PDT effect and incorporated them into PEGylated rGO nanosheets for achieving increased biocompatibility and enhanced PTT properties. A human esophagus carcinoma cell line was incubated with the conjugated rGO at a concentration of 50 µg mL^{-1} and irradiated with a laser (671 nm) for 20 minutes. The treatment resulted in 100% cancer cell death when $CuInS_2$/ZnS-rGO was used, but rGO and the crystals individually also decreased cancer cell deaths to 95 and 100%, respectively. Besides, mice were inoculated with the same cell line. Conjugated rGO was injected at a concentration of 0.5 mg mL^{-1} and irradiated using the same conditions. The treatment resulted in 100% tumour reduction, comparing with control with only rGO [220].

Combined PDT and PTT requires CNM with combined effect or absorption in relevant wavelengths to be triggered simultaneously or sequentially for PTT and PDT activity. CNM properties can be tuned to meet desired effects by surface modification with polymers, for higher biocompatibility [192, 207], adsorption of PS, when the material lacks PDT characteristics [216, 221] or anticancer drugs, for combined chemo- and phototherapy [193]. The loading of chemotherapeutic drugs in the nanomaterials is advantageous once their release is selective to the tumour tissues, as the cancer cells are more sensitive to the heat created by PTT. Also, drug internalization is higher once the tissues are debilitated due to the ROS generated during PDT. Besides, lower drug concentrations are required, avoiding toxicity and secondary effects, common in chemotherapy. A study loaded fullerenes with DOX at a LC of 48% for achieving enhanced

phototherapeutic effect by combining PDT, PTT and chemotherapy. Also, CNT have been reported to have a LE of PS from 72 to 230% allowing a combined PDT (PS effect) and PTT (CNT effect). GBM have been reported with variable loading conditions, mostly quantifying the loaded PS to obtain the PDT effect and combine it with PTT. GO LC has been found to vary from 15 to 180% and LE from 10 to 85%. For rGO, LC values are quite variable, ranging from 60 to 500%. PS or anticancer drug conjugation has been described above and values are presented in Table 2.3. Generally, enormous discrepancies are found for LC values when GBM are conjugated with drugs, which might be explained by the variable nanoplatelet morphology, size and heterogeneous size distributions among different GBM batches.

As mentioned before, the increased variability of the experimental conditions present in the literature difficult the comparison between different CNM and strategies used. However, two main groups can be observed. On one hand, CNM which can produce ROS when irradiated with UV or visible irradiation but presenting reduced NIR absorbances, such as fullerenes, CD and GQD can be conjugated with PTT agents. This will render such CNM capable of converting NIR into heat, increasing cancer cells permeability, and their susceptibility to ROS, also produced by those CNM. Few studies have been found with this group. Fullerenes have been reported to result in cancer cell deaths of over 95% after low concentrations such as 10 μg mL^{-1} *in vitro*, whereas *in vivo* studies report over 85% tumour reduction, 7 to 29 days after treatment. CD application in PDT/PTT usually resulted in over 79% cancer cell death using concentrations from 200 to 1000 μg mL^{-1} *in vitro,* whereas *in vivo* studies report over 70% tumour reduction, 13 to 22 days after treatment. GQD application usually resulted in over 65% cancer cell death using concentrations from 100 to 500 μg mL^{-1} *in vitro*. Nonetheless, only one *in vivo* study was found with over 55% tumour reduction, 21 days after treatment. On the other hand, CNM with high NIR absorbance, as CNT, CNH and GBM, can produce heat under NIR irradiation. These CNM can load PS due to their large surface area, combining the heat cytotoxicity to cells, with the ROS effect that characterizes this synergistic treatment. Interestingly, a study has reported GO as a ROS producer itself, but further data is required to validate its potential as a single agent for combined phototherapy. CNT application in PTT/PDT usually resulted in over 45% cancer cell death using concentrations from 2.4 to 500 μg mL^{-1}. *In vivo* studies with CNT usually result in over 90% tumour reduction, 9 to 15 days after treatment. PTT/PDT using CNH usually results in over 66% cancer cell death *in vitro*, using concentrations from 8 to 26.5 μg mL^{-1}. CNH application *in vivo* usually resulted in over 90% tumour reduction, 14 to 21 days after treatment. *In vitro* studies for PTT/PDT with GO usually leads to over 41.48% cancer cell death, using concentrations from 3 to 800 μg mL^{-1}, while *in vivo* studies present consistent outcomes with over 85% tumour reduction, 12 to 15 days after treatment. PTT/PDT with rGO usually results in over 55% cancer cell death, with concentrations from 4.8 to 50 μg mL^{-1} being used. Tumour reductions of 100% are usually reported in *in vivo* studies, 15 to 18 days after treatment.

Overall, PDT and PTT combination suggests a complementary action between the two approaches. PTT can improve PDT efficiency once the heat generated after irradiation leads to enhanced cell permeability, ultimately leading to increased PS uptake. This will enhance ROS production, which, in turn, interferes with heat-shock proteins, augmenting cancer cell susceptibility. The described outcomes hold strong potential to overcome cancer cells chemoresistance, given the synergistic interplay between the different actors (nanomaterials, radiation and drugs/PS). Hence, future directions of investigation should include more comprehensive studies on the molecular mechanisms underlying cancer cell death, assuring the

safe application and survival of surrounding healthy tissues, while simultaneously enhancing cancer treatment efficacy.

Table 2.3 - Selected recent studies on carbon nanomaterials for cancer combined phototherapy.

CNM	Particle size	Surface modification	Conjugated drug/PS	Biological studies *in vitro*		Biological studies *in vivo*		Ref.
				Parameters	Cell death	Parameters	Tumour reduction	
Fullerenes	d ≈ 10–16 nm	PEG Folate	Ce6	KB cells [C_{60}] = 10 μg mL^{-1} Incubation: 4 h I: 670 nm, 300 mWcm^{-2}, 10 min	≈ 95%	KB tumour-bearing nude mice [C_{60}] = 10 mg kg^{-1} I: 670 nm, 300 mWcm^{-2}, 10 min t: 7 days	≈ > 85%	[192]
	s ≈ 60 nm	Silica Hyaluronan	DOX LC: 48.5 ± 0.1% ICG	[1]MDA-MB-231 cells and [2]MCF-7 cells [DOX] = 10 μg mL^{-1} Incubation: 12 h I: 800 nm, 1.5 Wcm^{-2}, 3 min	≈ [1]100 and [2]95%	MDA-MB-231 cells injected in athymic female NU/NU nude mice [DOX] = 1.5 mg kg^{-1}, [ICG] = 1.5 mg kg^{-1} I: 800 nm, 0.7 Wcm^{-2}, 3 min t: 29 days	≈ 100%	[193]
CD	d ≈ 2.5–4.3 nm	Copper and Nitrogen (Cu-N) doped	N/A	B16 cells [Cu-N-CD] = 500 μg mL^{-1} Incubation: 24 h I: 808 nm, 1.0 Wcm^{-2}, 10 min	≈ 80%	Female Balb/c nude mice bearing B16 melanoma tumours [Cu-N-CD] = 3.0 mg mL^{-1} I: 808 nm, 1.0 Wcm^{-2}, 10 min t: 14 days	≈ 100%	[194]
	d ≈ 150 nm t ≈ 15 nm	Silica	TiO_2	HepG2 cells [CST NPs] = 1000 μg mL^{-1} Incubation: 10 h I: 650 nm, 10 min	≈ 79.1%	H22 tumour-bearing mice [CST NPs] = 2.0 mg mL^{-1} I: 650 nm, 10 min t: 14 days	≈ > 70%	[195]
	d ≈ 3–9 nm	N/A	N/A	HeLa cells [CD] = 200 μg mL^{-1} I: 800 nm, 0.5 mW, 10 min	≈ 90%	Balb/c nude mice injected with 4T1 cells [CD] = 1 mg mL^{-1} I: 800 nm, 0.5 mW, 10 min t: 22 days	≈ 100%	[196]
	d ≈ 3.7 nm HD ≈ 9.9 nm	N/A	Ce6 LC: 0.56%	[1]HeLa cells, [2]MCF-7 cells and [3]4T1 cells [Ce6-RCD] = 200 μg·mL^{-1} Incubation: 24 h I: 671 nm, 0.50 W·cm^{-2}, 20 min	≈ [1]195, [2]90 and [3]90%	4T1 tumour-bearing Balb/c nude mice [Ce6-RCD] = 1.0 mg·mL^{-1} I: 671 nm, 0.50 W·cm^{-2}, 20 min t: 13 days	≈ > 90%	[197]
GQD	d ≈ 2–8 nm t ≈ 7–10 nm	N/A	N/A	MDA-MB-231 cells [GQD] = 500 μg mL^{-1} Incubation: 12 h I:808 nm, 0.5 Wcm^{-2}, 5 min	≈ 65%	N/A	N/A	[222]
	d ≈ 5 nm	N/A	N/A	MDA-MB-231 cells [cGdots] = 500 μg mL^{-1} I: 670 nm, 0.3 Wcm^{-2}, 30 min	≈ 70%	MDA-MB-231 tumour-bearing mice [cGdots] = 2.5 mg kg^{-1} I: 670 nm, 0.3 Wcm^{-2}, 30 min t: 21 days	≈ > 55%	[198]
	s ≈ 8 ± 3 nm	PEG Aptamer	Porphyrin	[1]A549 cells and [2]MCF-7 cells [GQD-PEG-P] =100 μg mL^{-1} Incubation: 1 h I: 980 nm, 0.72 Wcm^{-2}, 10 min and 635 nm, 0.16 Wcm^{-2}, 10 min	≈ [1]86 and [2]85.9%	N/A	N/A	[223]
CNT	d ≈ 1–3 nm l ≈ 200–700 nm	High density lipoprotein	N/A	NCI-H460 cells I: 808 nm, 800 mW, 10 min	≈ 45%	N/A	N/A	[203]
	N/S	Albumin Evans blue (EB)	Ce6 LE: 72.5%	SCC7 cells [Ce6] = 20 μg mL^{-1}; [ECNTs] = 2.4 μg mL^{-1} Incubation: 24 h I: 630 nm, 0.15 Wcm^{-2}, 1 min and 808 nm, 1 Wcm^{-2}, 2 min	≈ 89.9%	BALB/c nude female mice injected with SCC7 cells [Ce6] = 5 mg kg^{-1}, [CNT] = 0.3 mg kg^{-1} I: 630 nm, 0.15 Wcm^{-2}, 10 min and 808 nm, 1 Wcm^{-2}, 15 min	≈ 100%	[200]

						t: 15 days		
CNT	N/S	Hyaluronic acid nanoparticles (HANPs)	ICG	SCC7 cells [IHANPT] = 500 μg mL^{-1} Incubation: 24 h I: 808 nm, 0.8 Wcm^{-2}, 10 min	≈ 91.4%	Athymic nude mice injected with SCC7 cells [ICG] = 1 mg kg^{-1}, [SWCNT] = 2.72 mg kg^{-1} I: 808 nm, 0.8 Wcm^{-2}, 10 min t: 14 days	≈ 100%	[201]
	d ≈ 0.7−1.3 nm l ≈ 20 nm–several μm	N/A	Ru (II)	HeLa cells [Ru@SWCNT] = 200 μg mL^{-1} Incubation: 12 h I: 808 nm, 0.25 Wcm^{-2}, 5 min	≈ 100%	Nude mice inoculated with HeLa cells [Ru@SWCNT] = 5 mg kg^{-1} I: 808 nm, 0.25 Wcm^{-2}, 5 min t: 15 days	≈ 100%	[202]
	N/S	HAc	HMME LE: ≈ 230%	B16-F10 cells [HMME] = 25 μg mL^{-1} Incubation: 24 h I: 532 nm, 100 $mWcm^{-2}$, 0.5 min and 808 nm, 1.4 $Wcm^{-}2$, 1 min	≈ 85%	C57 mice injected with B16-F10 cells [HMME] = 5 mg kg^{-1}, [HA-CNT] = 2.17 mg kg^{-1} I: 532 nm, 100 $mWcm^{-2}$, 5 min and 808 nm, 1.4 Wcm^{-2}, 1 min t: 9 days	≈ > 90%	[37]
CNH	N/S	N/A	Tetrasulfonic acid tetrasodium salt copper phthalocyanine (TSCuPc)	HeLa cells [TSCuPc] = 15 μg mL^{-1}, [SWNH] = 26.5 μg mL^{-1} Incubation: 24 h I: 650 nm, 3 Wcm^{-2}, 5 min	≈ 82%	N/A	N/A	[224]
	HD ≈ 150 nm d ≈ 100 nm	N/A	Phycocyanin (PC)	^{1}4T1 cells, ^{2}MDA-MB-231 cells [PC] = 40 μg mL^{-1} Incubation: 24 h I: 650 nm, 1.0 Wcm^{-2}, 10 min	≈ ^{1}82 and ^{2}85%	4T1 tumour-bearing mice [PC] = 150 μg mL^{-1}, [SWNH] = 305 μg mL^{-1} I: 650 nm, 1.0 Wcm^{-2}, 5 min t: 14 days	≈ 100%	[204]
	d ≈ 100 nm HD ≈ 85 ± 20 nm	N/A	Hypericin (Hyp)	4T1 cells [Hyp] = 5.2 μg mL^{-1}, [SWNH] = 8.25 μg mL^{-1} Incubation: 24 h I: 590 and 808 nm, 0.5 Wcm^{-2}, 10 min	84.5%	Female mice injected with 4T1 cells [SWNH-Hyp] = 50.26 μg mL^{-1} I: 590 and 808 nm, 0.5 Wcm^{-2}, 5 min t: 14 days	≈ > 90%	[205]
	N/S	BSA	ZnPc	5RP7 cells [ZnPc] = 5 μM, [SWNHox] = 17 μg mL^{-1} Incubation: 24 h I: 670 nm, 160 mW, 20 min	≈ 66%	Nude mice injected with 5RP7 cells [ZnPc] = 50 μM, [SWNHox] = 0.15 mg mL^{-1} I: 670 nm, 15 min t: 21 days	≈ 100%	[206]
	N/S	PEG	Pyro	HeLa cells, LL2 cells, A549 cells and THP-1 cells [CNH-Pyro] = 15 μM Incubation: 24 h I: 660 nm, 100 $mWcm^{-2}$, 20 min	≈ 75%	C57BL/6 mice injected with LL2 cells [CNH-Pyro] = 100 μM I: 660 nm, 0.1 Wcm^{-2}, 20 min t: 14 days	≈ 100%	[207]
	d ≈ 80 nm HD ≈ 70 ± 30 nm	N/A	ICG	4T1 cells [ICG] = 4 μg mL^{-1} Incubation: 24 h I: 808 nm, 0.3 Wcm^{-2}	≈ 94.6%	4T1 tumour-bearing nude mice [SWNH-ICG] = 52 μg mL^{-1} I: 808 nm, 0.3 Wcm^{-2}, 5 min, x2 t: 14 days	≈ > 90%	[208]
Graphene	N/S	N/A	TSCuPc	HeLa cells [TSCuPc] = 15 μg mL^{-1} Incubation: 24 h I: 650 nm, 3 Wcm^{-2}, 5 min	≈ 71%	N/A	N/A	[209]
	d ≈ 282 nm	mPEG	BODIPY Mitomycin C (MMC) LC: 9.9%	HeLa cells [MGBP] = 100 μg mL^{-1} Incubation: 48 h I: 808 nm, 1 Wcm^{-2}, 5 min and 505 nm, 50 $mWcm^{-2}$, 5 min	≈ 83%	N/A	N/A	[210]
GO	s ≈ 40 nm	Ferrocene Acrylic acid	Silicon 2,3-napthalocyanine bis	HeLa cells [$SiNc_4$] = 0.20 μM Incubation: 48 h	≈ 97.9%	N/A	N/A	[225]

		Fluorescein o-methacrylate	(trihexylsilyl oxide) ($SiNc_4$) LE: 8.5%	I: 775 nm, 0.3 Wcm^{-2}, 60 min				
	Th ≈ 0.81 nm t ≈ 3.29 nm	FA PEG	Fullerene (C_{60})	HeLa cells [FA–GO–PEG/C_{60}] = 10 μg mL^{-1} Incubation: 24 h I: 808 nm, 2 Wcm^{-2}, 3 min and 532 nm, 0.1 Wcm^{-2}, 5 min	≈ 95%	N/A	N/A	[217]
	s ≈< 50 nm t ≈ 1 nm	PEG	Ce6 LC: 15%	KB cells [Ce6] = 2.5 μM Incubation: 24 h I: 660 nm, 50 $mWcm^{-2}$, 5 min and 808 nm, 0.3 Wcm^{-2}, 20 min	≈ > 95%	N/A	N/A	[221]
	h ≈ 1.2 nm	PEG Upconversion nanoparticles (UCNP)	ZnPc LE: 11%	HeLa cells [UCNP-NGO/ZnPc] = 80 μg mL^{-1} Incubation: 24 h I: 808 nm, 2 Wcm^{-2}, 10 min and 630 nm, 50 $mWcm^{-2}$, 10 min	≈ 85%	N/A	N/A	[226]
	HD ≈ 441 ± 48.8 nm	HAc	Ce6 R: 21%	A549 cells [Ce6] = 1.8 μM Incubation: 24 h I: 810 nm, 4 Wcm^{-2} and 670 nm, 50 $mWcm^{-2}$	≈ 90%	N/A	N/A	[227]
	t ≈ 30 nm	CuS PEG	ICG LC: 180%	MCF-7 cells [pGO-CuS/ICG] = 50 μg mL^{-1} Incubation: 4 h I: 940 nm, 4.0 Wcm^{-2}, 5 min and 808 nm, 2.0 Wcm^{-2}, 5 min	≈ 90%	N/A	N/A	[228]
	s ≈ 60 ± 15 nm t ≈ 2–3 nm	Gold PEG	ZnPc LC: 1.9×10^6 ZnPc per Au@GON NP	HeLa cells [ZnPc-PEG-Au@GONNPs] = 28×10^{-12} M Incubation: 24 h I: 808 nm, 0.67 Wcm^{-2}, 20 min and 660 nm, 0.2 Wcm^{-2}, 10 min	≈ 93.2%	N/A	N/A	[229]
GO	s ≈ 40.6 ± 2.8 nm	PL-127	Methylene Blue (MB) LC: 22.7 ± 0.6% R: 25%	HeLa cells [nanoGO] = 10 μg mL^{-1}, [MB] = 2 μg mL^{-1} Incubation: 24 h I: 655 nm, 3 min and 808 nm, 3 min	≈ > 70%	Male athymic nude mice implanted with HeLa cells [MB] = 2 mg kg^{-1}, [nanoGO] = 10 mg kg^{-1} I: 650 nm, 150 $mWcm^{-2}$, 10 min and 808 nm, 2 Wcm^{-2}, 3 min t: 15 days	≈ 100%	[211]
	s ≈ 20–40 nm t ≈ 3 nm	PEG PEI	IR-808 LC: 20% R: 10%	A549 cells and LLC cells [IR-808] = 10 μM, [NGO-PEG-BPEI] = 30 μg mL^{-1} Incubation: 24 h I: 808 nm, 2 Wcm^{-2}, 5 min	≈ > 90%	Male C57 BL/6 mice injected with LLC cells Athymic nude mice injected with A549 cells [NGO-808] = 0.5 mg kg^{-1} I: 808 nm, 2 Wcm^{-2}, 5 min t: 15 and 12 days	≈ 100%	[212]
	s ≈ 100 nm	PEG Folate	N/A	B16F0 cells [GO-PEG-folate] = 75 μg mL^{-1} Incubation: 24 h I: 980 nm, 320 $mWcm^{-2}$, 18 min	≈ 85%	C57BL/6 J mice implanted with B16F0 cells [GO-PEG-folate] = 8 mg kg^{-1} I: 980 nm, 250 $mWcm^{-2}$, 10 min t: 14 days	≈ 100%	[213]
	s ≈ 174.8 ± 5.8 nm	Palladium nanoparticles (Pd NP)	N/A	PC3 cells [GO-Pd NPs] = 10 μg mL^{-1} Incubation: 24 h I: 808 nm, 3.0 Wcm^{-2}, 5 min	≈ > 90%	BALB/c nude mice bearing PC3 tumours I: 808 nm, 3.0 Wcm^{-2}, 5 min t: 15 days	≈ 100%	[230]
	d ≈ 100–400 nm	mPEG	C_{60}	HeLa cells [GO] = 40 μg mL^{-1} I: 808 nm, 4 Wcm^{-2}, 7 min	≈ 41.48%	N/A	N/A	[231]
	t ≈ 2.51–4.12 nm	FA	C_{60}	HeLa cells [GO-FA/Py-γ-CD/C_{60}] = 30 μg mL^{-1}	≈ 83.8%	N/A	N/A	[232]

		γ-cyclodextrin (γ-CD)		I: Xe lamp, 2 Wcm^{-2}, 4 min				
GO	d ≈ 20.5 nm t ≈ 1.47 ± 0.82 nm	PEG	Sinoporphyrin sodium (DVDMS) LE: 51%	PC9 cells [GO-PEG] = 3 μg mL^{-1}, [DVDMS] = 6 μg mL^{-1} Incubation: 24 h I: 630 nm, 2 J $well^{-1}$ and 808 nm, 1 Wcm^{-2}, 3 min $well^{-1}$	≈ 90%	Athymic nude mice bearing PC9 tumours [GO-PEG] = 1 mg kg^{-1}, [DVDMS] = 2 mg kg^{-1} I: 630 nm, 50 J and 808 nm, 1.0 Wcm^{-2}, 10 min t: 14 days	≈ 100%	[233]
	s ≈ 400 nm	Gold nanostars (Au NS) PEG	Ce6 LC: 32%	EMT6 cells [GO/AuNS-PEG] = 150 μg mL^{-1} Incubation: 12 h I: 660 nm, 2 Wcm^{-2}, 10 min	≈ 79.3%	EMT6 tumour-bearing mice [GO/AuNS-PEG] = 10 mg kg^{-1} I: 660 nm, 3 Wcm^{-2}, 10 min t: 15 days	≈ 100%	[214]
	s ≈ 100 nm	UCNP PEG	Ce6	HeLa cells and U14 cells [NUC] = 800 μg mL^{-1} I: 808 nm, 10 min	≈ > 85%	U14 tumour-bearing mice I: 808 nm, 10 min t: 14 days	≈ > 85%	[215]
	HD ≈ 112.5 ± 8.45 nm	PL-127	MB R: 71.7%	4T1 cells [NanoGO] = 12.5 μg mL^{-1}, [MB] = 2.5 μg mL^{-1} Incubation: 24 h I: 660 nm, 90.8 J cm^{-2}, 10 min and 808 nm, 8.3 kJ cm^{-2}, 15 min	≈ 95%	Female Balb/c mice implanted with 4T1-Luc cells [NanoGO] = 10 mg kg^{-1}, [MB] = 2.5 mg kg^{-1} I: 660 nm, 90.8 J cm^{-2}, 10 min and 808 nm, 8.3 kJ cm^{-2}, 15 min t: 12 days	≈ 100%	[216]
	HD ≈ 121.8 ± 9.35 nm	PL-127	MB R: 62%	SiHa cells [MB] = 5 μg mL^{-1}, [GO] = 10 μg mL^{-1} Incubation: 24 h I: 660 nm and 808 nm, 0.5 W·cm^{-2}, 10 min	≈ 75%	N/A	N/A	[218]
rGO	s ≈ 200 nm	*Clostridium perfringens* enterotoxin (CPE) Polyethylene glycol spacer (CPC)	Ce6 LC: 20.4 ± 3.4 μg	U87-MG cells [CPC] = 50 μmol L^{-1}, [rGO] = 4.8 μg mL^{-1} Incubation: 1 h I: 660 nm, 20 min and 808 nm, 3 min	92.3%	N/A	N/A	[234]
	s ≈ 100–250 nm	HAc	ZnO	MDA-MB-231 cells [rGO-ZnO-HA] = 50 μg mL^{-1} Incubation: 4 h I: 365 nm, 5 $mWcm^{-2}$, 30 min and 808 nm, 20-400 J cm^{-2}, 30 min	≈ > 70%	N/A	N/A	[235]
	t ≈ 25 nm	PEG	Ru (II) LC: 128% R: 24%	A549 cells [Ru-PEG] = 6.25 μM Incubation: 24 h I: 808 nm, 0.5 Wcm^{-2}, 5 min and 450 nm, 20 $mWcm^{-2}$, 2 min	≈ 91.7%	Female nude mice bearing A549 tumours [rGO] = 1 mg mL^{-1}, [Ru-PEG] = 250 μM I: 808 nm, 0.5 Wcm^{-2}, 5 min and 450 nm, 20 $mWcm^{-2}$, 2 min t: 15 days	≈ 100%	[219]
	l ≈ 250 nm t ≈ 6.38 nm	pDA	Mano zero-valent iron (nZVI)	MCF-7 cells [nZVI/rGO@pDA] = 10 μg mL^{-1} I: 808 nm, 1.5 Wcm^{-2}, 3.5 min	≈ 55%	N/A	N/A	[236]
	s ≈ 100–200 nm	MS pDA HAc	Ce6 LC: 60.5% R: 80%	^{1}HT29 cells and ^{2}HCT-116 cells [Ce6] = 2 × 10^{-6} M I: 808 nm, 1 Wcm^{-2}, 10 min and 660 nm, 0.05 Wcm^{-2}, 5 min	≈ ^{1}90.3 and ^{2}99%	N/A	N/A	[237]
	s ≈ 118.90 ± 62.96 nm	PEG	Copper indium sulphide ($CuInS_2$) Zinc sulfide (ZnS) LC: 500%	Eca-109 cells [$CuInS_2$/ZnS] = 250 μg mL^{-1}, [rGO] = 50 μg mL^{-1} I: 671 nm, 20 min	≈ 100%	Nude mice injected with Eca-109 cells [$CuInS_2$/ZnS] = 2.5 mg mL^{-1}, [rGO] = 0.5 mg mL^{-1} I: 671 nm, 20 min T: 18 days	≈ 100%	[220]

4T1 cells, 4T1 murine breast cancer cell line; 4T1-*luc*-cells, Luciferase expressing breast cancer cell line; 5RP7 cells, Rat fibroblast cell line transformed by the -Ha-ras oncogene; A549 cells, Human lung adenocarcinoma cell line; Au NS, Gold nanostars; B16 cells, murine melanoma cell line; B16F0 cells, B16F0 melanoma cell line; B16-F10 cells, B16-F10 mice melanoma cell line; BODIPY, Boron dipyrromethene; BSA, Bovine serum albumin; C_{60}, Fullerene; CD, Carbon dots; Ce6, Chlorine e6; CNH, Carbon nanohorns; CNM, Carbon nanomaterial; CNT, Carbon nanotubes; CPC, Polyethylene glycol spacer; CPE, *Clostridium perfringens* enterotoxin; $CuInS_2$, Copper indium sulphide; Cu-N, Copper and Nitrogen; CuS, Copper sulfide; d, diameter; DOX, Doxorubicin; DVDMS, Sinoporphyrin sodium; EB, Evans blue; Eca-109 cells, Human esophageal squamous carcinoma cell line; EMT6 cells, murine mammary tumour line; FA, Folic acid; GO, Graphene oxide GQD, Graphene quantum dots; h, height; H22 cells, H22 hepatocellular carcinoma cell line; HAc, Hyaluronic acid; HANPs, Hyaluronic acid nanoparticles; HCT-116 cells, HCT-116 human colon carcinoma cell line; HD, hydrodynamic size; HeLa cells, Human cervical cancer cell line; HepG2 cells, Human hepatocellular carcinoma cell line; HMME, Hematoporphyrin monomethyl ether; HT29 cells, HT29 human colon adenocarcinoma cell line; Hyp, Hypericin; I, Irradiation; ICG, Indocyanine green; KB cells, Human carcinoma KB cell line; l, length; LC, loading capacity; LE, loading efficiency; LL2 cells, Mouse Lewis lung carcinoma cell line; LLC cells, Lewis lung carcinoma cell line; MB, Methylene blue; MCF-7 cells, Human breast cancer cell line; MDA-MB-231 cells, Human breast cancer cell line; MMC, Mitomycin C; mPEG, Methoxy-poly(ethylene glycol); MS, Mesoporous silica; N/A, not applicable; N/S, not studied; NCI-H460 cells, Human lung cancer cell line; PC, Phycocyanin; PC3 cells, Prostate cancer 3 (PC3) cell line; PC9 cells, Prostate cancer 9 (PC9) cell line; Pd NP, Palladium nanoparticles; pDA, Polydopamine; PEG, Poly(ethylene glycol); PEI, Polyethylenimine; PL-127, Pluronic F-127; PS, Photosensitizer; Pyro, Pyropheophorbide *a*; R, release; rGO, Reduced graphene oxide; Ru (II), Ruthenium (II); s, size; SCC7 cells, Murine squamous carcinoma cell line; SiHa cells, Human cervical cancer cell line; $SiNc_4$, Silicon 2,3-napthalocyanine bis (trihexylsilyloxide); t, thickness; T, treatment time; Th, topographic height; THP-1 cells, Human leukemic monocytice cell line; TiO_2, Titanium dioxide; TSCuPc, Tetrasulfonic acid tetrasodium salt copper phthalocyanine; U14 cells, Murine hepatocarcinoma U14 cell line; U87-MG cells, Adherent human glioblastoma (U87-MG) cell line; UCNP, Upconversion nanoparticles; ZnO, Zinc oxide; ZnPc, Zinc phthalocyanine; ZnS, Zinc sulfide; γ-CD, γ-cyclodextrin.

2.4 - Biocompatibility and safety of CNM

When designing phototherapy approaches involving nanomaterials, the biocompatibility and safety of the systems developed have to be taken into account. Each nanoparticle holds a unique structure and characteristics that influence their toxicity, for instance, their size or functionalization. Therefore, the introduction of external molecules or biomaterials into an organism requires a comprehensive characterization of their *in vitro* and *in vivo* effect, both at short and long term [7]. FDA specified that nanomaterials biological effect should be tested in the exact context of its future application [25]. As previously shown, CNM generated great interest in the biomedical field, nonetheless, their biosafety has to be carefully studied to make sure that a particular effective system for PDT/PTT presents no toxicity once introduced in the body [16]. Figure 2.5 summarizes some key parameters that influence CNM toxicity.

The biocompatibility of the nanomaterials is firstly evaluated with *in vitro* studies where CNM should be placed in controlled environments and direct contact with cancer cells, leading to increased cellular uptake and consequently cell death, after irradiation. As previously discussed, in the literature several reports describe this effect *in vitro*. However, some studies have detected cytotoxicity of CNM without irradiation. Fullerenes are usually non-toxic unless photoexcited or used in very high concentrations, which are rarely applied in the case of phototherapy [25]. A relation has been established between their toxicity and their surface chemistry, given that C_{60} has been described as more toxic to human fibroblasts than derivatized fullerenol $C_{60}(OH)_{24}$ [238]. Authors attributed this phenomenon to the elevated amount of hydrophilic groups on the surface that increased biocompatibility. Pristine fullerenes can produce ROS and cause cell death, while the functionalized materials have lower ROS generation capability, therefore, presenting lower toxicity [239]. This study highlighted the importance of surface functionalization, not only to improve water stability, but also biocompatibility. Other reports have shown non-toxic fullerenes against alveolar macrophages [240] or insufficiently toxic to produce an inflammatory reaction [241]. CNT are one of the most controversial CNM, with studies describing cell apoptosis and phagocytic activity inhibition caused by them. Nevertheless, other authors describe the absence of cytotoxicity when using these nanomaterials, especially water-stable modified CNT [242]. Due to the introduction of metallic catalysts during CNT production, even after purification, residues can compose a problem in terms of toxicity. CNH are usually presented as non-toxic in low-uptake conditions, however, increased uptake has been reported as cause for cell death by apoptosis and necrosis [242]. Also, GO effective uptake and degradation by immune cells has

been demonstrated, which prevents infections and other diseases and is very relevant to show their potential biocompatibility [243].

When *in vivo* models are used to study the effect of nanomaterials, multiple parameters are in constant change reducing controllability and increasing biosafety issues. The literature presents several inconsistent results when it comes to CNM *in vivo* challenges. GQD have been reported to have a good biodegradation efficiency [244] and CD to have a good biodistribution in mice and successful excretion through urine [25]. Both GQD and CD usually present no toxicity due to their small size and have been reported to easily be eliminated *in vivo* [104]. CNT in the pristine form have been reported to be usually toxic and to lead to pulmonary inflammation in mice [245, 246]. However, other studies demonstrate that the right surface modification significantly reduces toxicity, avoiding pulmonary complications [247]. Also, CNT have been described as toxic after intravenous injection, being accumulated in the liver and spleen of mice, while functionalized CNT can be gradually excreted through biliary or renal pathways with no toxicity [116, 248]. Regarding *in vivo* biodistribution, the surface modifications used can influence CNT toxicity. A study has demonstrated that a heavily PEGylated CNT resulted in increased tumour uptake but accumulation in mouse skin. However, after optimizing the PEGylation degree, CNT rapidly disappeared from blood circulation into the reticuloendothelial system with a smaller but effective tumour uptake [16]. Besides functionalization, the size has been reported as having a key impact on their toxicological profile. Shorter CNT have been stated to be degraded by macrophages, whereas increased dimensions lead to inflammation and DNA damage [249]. CNT have been also described as potentially carcinogenic in humans. However, this consideration does not apply to every CNT once some functionalized CNT have been reported as non-toxic and biodegradable [243]. Other studies regarding CNT safety include non-interference with neuronal function as the materials supported the attachment and growth of neurons [238]. GO in its pristine form has been reported to cause pulmonary toxicity [250], however, other authors have shown modified GO to have no toxic effects in the same organ [251]. Also, PEGylated GO has been stated to accumulate in the liver and spleen of mice after intravenous administration, while PEGylated nanoGO has been reported as excretable through urinary pathways without consequences for the remaining tissues [252].

Another important parameter to be taken into account regarding *in vivo* studies is the way the nanomaterial is applied. Most successful tumour reduction results are obtained after nanomaterial injection directly into tumours but few studies accomplish them in a systemic way, such as intravenously, an administration route which can be more relevant for clinical applications where the disease site is deeply located [16]. Graphene and its derivatives have reported to be degradable by chemical reactions or natural oxidative enzymes, having GO the highest degradation rate due to the presence of oxygen-containing functional groups. Besides, molecules present in the human plasma, for example, $^{\bullet}OH$ and $^{\bullet}O_2$, have been also proved to degrade this nanomaterial, reinforcing its potential to be eliminated safely from the body [25]. Moreover, GO has been shown to have insignificant effect on the gastrointestinal tract as digested materials were tolerated by Caco-2 cells after 9 days [243]. Unfortunately, animal studies with CNM using orthotopic pathologies models are inexistent. Indeed, all studies up to date have relied on the application of CNM to treat tumour xenografts induced by subcutaneous injection of cancer cell lines. These *in vivo* settings do not consider the native microenvironment of the target tumour tissue, disregarding the complexity of tumour-healthy tissue interactions, particularly in terms of immune cells response, as well as the adequate anatomic condition. Such factors might have an impact on CNM administration route, biodistribution, biodegradation and treatment efficiency.

Finally, there are currently no clinical trials with CNM and multiple challenges that still need to be addressed regarding their biocompatibility and safety. Nevertheless, these nanomaterials are expected to be continuously studied and play significant roles in biomedical applications in the future, namely in cancer and antibacterial phototherapy.

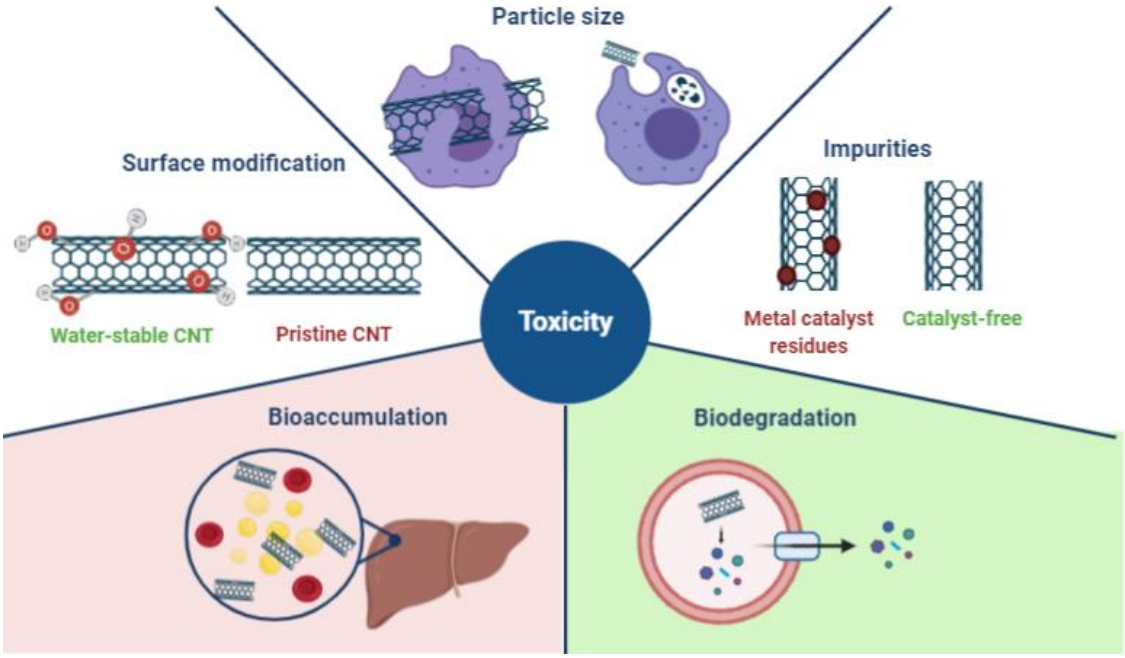

Figure 2.5 – Representation of major factors underlying CNM toxicity. Particle size influences cellular uptake mechanisms, since larger nanomaterials may result in incomplete or mutagenic phagocytosis while smaller ones are successfully phagocyted. Impurities from synthesis processes (*e.g.*, metal impurities) can trigger inflammatory reactions. Surface modifications improve CNM stability and reduce cytotoxicity. Biodegradation must occur to prevent long term blood circulation or even bioaccumulation, thereby minimizing nanomaterial-induced toxicity. Created with Biorender.com. Abbreviations: CNT, carbon nanotubes.

Chapter 3

Materials and Methods

3.1 - GBM production

Two types of graphene-based materials (GBM) were selected for this dissertation work, namely nanographene oxide (GOn) and partially reduced nanographene oxide (p-rGOn). For this purpose, GOn was firstly produced from graphite powder (size ≤ 20 μm, Sigma Aldrich, St. Louis, MO, USA) by oxidation using a modified Hummers method [253]. Briefly, a mixture of 160 mL of sulfuric acid (H_2SO_4, VWR, Darmstadt, Germany) and 40 mL of phosphoric acid (H_3PO_4, Chem-Lab, Zedelgem, Belgium) was added to 4 g of graphite in a Lenz reactor, while stirring, and the dispersion was cooled using a cooling bath (Julabo F12). Then, 24 g of potassium permanganate ($KMnO_4$, JMGS, Odivelas, Portugal) was added gradually and the solution was stirred at 420 rpm. Subsequently, 600 mL of H_2O were slowly added under stirring and temperature was controlled using a cooling bath (< 40 °C). Finally, 26.5 mL of hydrogen peroxide (H_2O_2, VWR, Darmstadt, Germany) was added and the dispersion left to rest overnight, being then decanted to separate the solid phase from the acidic solution, centrifuged at 4000 rpm, and redispersed in distilled water. The process was repeated until the pH in the supernatant was neutral. Then, exfoliation and particle size reduction was done using a home-built circuit with a peristaltic pump (Matson Marlow 323) and an industrial ultrasonic probe (Hielscher) to obtain GOn. Afterwards, GOn was diluted to a concentration of 1 mg mL^{-1}, placed in a Hergeus reactor and photoreduced under magnetic stirring to obtain p-rGOn. The temperature was kept below 40 °C through the use of a cooling bath (Julabo F12). A schematic representation of the production process is presented in Figure 3.1.

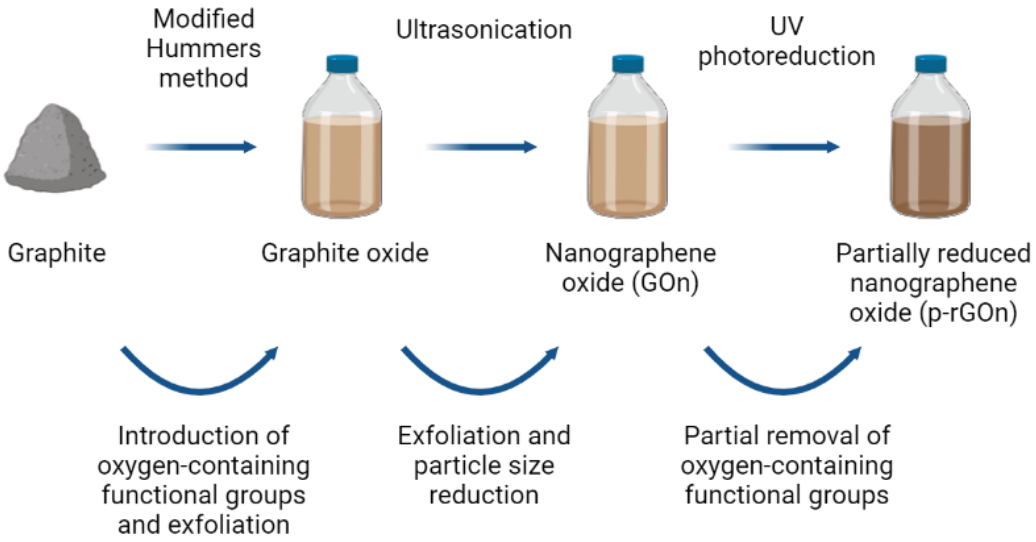

Figure 3.1 – Different used GBM production method steps. Created with Biorender.com.

3.2 - GBM characterization

3.2.1 - Physical characterization

3.2.1.1 - Transmission electron microscopy

Morphology and particle size of GOn and p-rGOn aqueous dispersions were evaluated by transmission electron microscopy (TEM) with a JEOL JEM 1400 TEM (Tokyo, Japan) at a concentration of 40 µg mL^{-1}. Samples were sonicated and 10 µL were deposited on a carbon-coated TEM grid and allowed to sediment for 1 min. After, the material in excess was removed by capillarity with a filter paper. Nanomaterials' lateral dimensions were measured using the ImageJ software.

3.2.1.2 - Particle size measurements by dynamic light scattering

Particle size distributions of GOn and p-rGOn aqueous dispersions were obtained by dynamic light scattering (DLS) using a LS230 particle size analyser (Beckman Coulter, Brea, CA, USA) and a Zetasizer Nano-ZS (Malvern Instruments, Worcestershire, UK), as described below.

3.2.1.2.1 - *LS230 particle size analyser*

GOn and p-rGOn aqueous dispersions were sonicated, diluted to a concentration of 500 µg mL^{-1} and placed in a LS230 Beckerman Coulter. Results were collected using two scans of 60 s, with polarization intensity differential scattering and Fraunhofer's model. This model adopts a spherical structure for every suspended particle so it does not match precise estimations of particle size being a relative evaluation of particle deagglomeration state [254].

3.2.1.2.2 - *Zetasizer*

GOn and p-rGOn aqueous dispersions were sonicated, prepared at a concentration of 25 µg mL and placed in a disposable Zetasizer cuvette (Malvern Instruments, Worcestershire, UK). Measurements were made in triplicate at room temperature and results are reported as mean and standard deviation.

3.2.1.3 - Zeta potential measurements

For zeta potential measurements, GOn and p-rGOn aqueous dispersions were sonicated and prepared at a concentration of 25 µg mL^{-1}. A Zetasizer Nano-ZS (Malvern Instruments, Worcestershire, UK) was used and the aqueous dispersions were placed in a disposable Zetasizer cuvette (Malvern Instruments, Worcestershire, UK). Four measurements were made at room temperature and results are reported as mean and standard deviation.

3.2.2 - Chemical characterization

3.2.2.1 - Fourier transform infrared spectroscopy

Infrared spectra of GOn and p-rGOn dehydrated samples were determined by Fourier transform infrared (FTIR) spectroscopy with a VERTEX 70 FTIR spectrometer (Bruker, Karlsruhe, Germany) in transmittance mode at room temperature. Samples were measured in attenuated total reflection (ATR) mode with a A225/Q PLATINUM ATR Diamond crystal with a single reflection accessory. Spectra were recorded by averaging 64 scans at a resolution of 4 cm^{-1} over the wavenumber range between 4000 and 400 cm^{-1}.

3.2.2.2 - Thermogravimetric analysis

Thermogravimetric analysis (TGA) of GOn and p-rGOn dehydrated samples was performed using a Netzsh STA 449 F3 Jupiter (Selb, Germany). Sample amounts ranged from 6 to 8 mg. The thermograms were recorded between 30 and 1000 °C at a heating rate of 10 °C min^{-1} under nitrogen flow. Results are presented as percentage (%) of weight loss.

3.2.2.3 - Ultraviolet-visible spectroscopy

Absorption spectra of GOn and p-rGOn aqueous dispersions at a concentration of 25 µg mL^{-1} were obtained using a Lambda 35 UV/vis spectrometer (Perkin-Elmer, Waltham, MA, USA). Samples were placed in a 160 µL quartz cuvette (Hellma Analytics, Analytica Munich, Germany) with 10 mm light path length and their spectra were acquired between 200-850 nm. Measurements were made in triplicate at room temperature with baseline correction based on water as a blank control.

3.2.3 - Photothermal properties

For photothermal properties evaluation, 600 µL of GOn and p-rGOn aqueous dispersions at a concentration of 250 µg mL^{-1} were placed in a 48-well plate. Samples were irradiated with a LED-

based source with a peak emission around 810 nm (NIR region) and 150 $mWcm^{-2}$ irradiance. The light-induced temperature change on the samples was recorded for 30 min of irradiation, by placing a type K thermocouple in the centre and half-height in the suspension. Nine replicates were performed per condition and results are presented as mean and standard deviation. Before the irradiation, samples were pre-heated up to 37 °C to replicate the conditions used in the biological assays. Samples were removed from the incubator to perform the irradiation. A control with water only was performed and used to correct temperature decreases caused by equilibrium with room temperature during the assay.

3.3 - Drug loading

5-Fluorouracil (5-FU) was dissolved in MilliQ water, phosphate-buffered saline (PBS) or phosphate buffer at a range of concentrations between 1 and 10 mg mL^{-1}. In the case of water and PBS, the dissolution was accomplished using a Vortex until the drug completely dissolved, which took approximately 10-15 minutes. For phosphate buffer, 5-FU was dissolved by magnetically stirring for 2 h at 25 °C.

To prepare GBM/drug conjugates, GBM aqueous dispersions were firstly prepared at a concentration of 0.25 and 0.5 mg mL^{-1} and mixed with the drug with or without magnetic stirring for 0.5 to 48 h. Controls were prepared without the nanomaterial. Afterwards, samples were centrifuged at 14000 rpm for 30 minutes, supernatants were collected and diluted for analysis. Absorbance of the supernatant was measured using a Lambda 35 UV/vis spectrometer (Perkin-Elmer, Waltham, MA, USA) and quantify of free drug was determined. Samples were placed in a 160 µL quartz cuvette (Hellma Analytics, Analytica Munich, Germany) with 10 mm light path length and their spectra was measured between 200-300 nm. Measurements were made in triplicate at room temperature with baseline correction based on water as a blank control. A calibration curve of 5-FU dissolved in water was made using concentrations between 1 and 15 µg mL^{-1}. Using the equation of this curve, absorbances at 265 nm were converted into concentrations that allowed to determine the quantify of free drug (drug mass in the supernatant). Loading capacity (LC) and loading efficiency (LE) were then calculated as shown in Equation 1.1 and Equation 1.2, respectively.

$$LC = \frac{Initial\ drug\ mass - Drug\ mass\ in\ the\ supernatant}{Initial\ drug\ mass} * 100 \quad (1.1)$$

$$LE = \frac{Initial\ drug\ mass - Drug\ mass\ in\ the\ supernatant}{Initial\ nanoparticles\ mass} * 100 \quad (1.2)$$

3.4 - Hydrogels production

Hydrogels were produced by dispersing Carbopol 974P NF (0.5% w/v) at a final concentration of 5 mg mL^{-1} in water, p-rGOn, 5-FU, or p-rGOn + 5-FU dispersions. The final concentrations of 5-FU were between 0.1-0.25 µg mL^{-1}, and p-rGOn concentration was 100 µg mL^{-1}. The hydrogels were allowed to disperse for approximately 1 h before a 10-minute sonication at 40 °C to assure a complete dispersion and no aggregation. Gelification was achieved through neutralization by dropwise addition of 2% NaOH. Concentrations of 10 mM NaOH were used for Carbopol 974P NF and Carbopol 974P NF/5-FU dispersions, while 12.5 mM NaOH was necessary to achieve the desired viscosity in Carbopol 974P NF/p-rGOn and Carbopol 974P NF/p-rGOn/5-FU dispersions.

3.5 - Hydrogels characterization

3.5.1 - Ultraviolet-visible spectroscopy

Hydrogels containing p-rGOn, 5-FU and Carbopol 974P NF were diluted in distilled water (1:5) to obtain a liquid solution with the desired drug concentration of 0.25 µg mL^{-1}. Samples were analysed in a Lambda 35 UV/vis spectrometer (Perkin-Elmer, Waltham, MA, USA). Samples were placed in a 160 µL quartz cuvette (Hellma Analytics, Analytica Munich, Germany) with 10 mm light path length and their spectra was measured between 200-300 nm. Measurements were made in triplicate at room temperature with baseline correction based on water as a blank control.

3.5.2 - Fourier-transform infrared spectroscopy

Infrared spectra of hydrogels containing p-rGOn, 5-FU and Carbopol 974P NF dehydrated samples were determined by Fourier transform infrared (FTIR) spectroscopy with a VERTEX 70 FTIR spectrometer (Bruker, Karlsruhe, Germany) in transmittance mode at room temperature. Samples were measured in attenuated total reflection (ATR) mode with a A225/Q PLATINUM ATR Diamond crystal with a single reflection accessory. Spectra were recorded by averaging 64 scans at a resolution of 4 cm^{-1} over the wavenumber range between 4000 and 400 cm^{-1}.

3.5.3 - High-performance liquid chromatography

5-FU concentrations in the Carbopol 974P NF hydrogels were assessed by High Performance Liquid Chromatography (HPLC, Merck-Hitachi 7000), by the indirect method. A calibration curve of 5-FU dissolved in water was made using concentrations between 1 and 15 µg mL^{-1}. From the equation of this curve, absorbances were converted into concentrations. The supernatants were collected and tested through Xterra RP188 (5 µm) (Waters Technologies) with a guard column. The mobile phase was composed of acetonitrile and water (5:95, v/v) with a flow rate of 0.7 mL/min and an injection volume of 20 µL. The absorbance wavelength used was 265 nm.

3.6 - *In vitro* biological studies

3.6.1 - Cell culture

Biological studies were performed using A-431 human epidermoid carcinoma cells (ATCC, CRL-1555) and HFF-1 human foreskin fibroblasts (ATCC, SCRC-1041). Cells were cultured in Dulbecco's modified Eagle's medium (DMEM, ATCC) supplemented with 10% (v/v) fetal bovine serum (Alfagene, Carcavelos, Portugal) and 1% (v/v) penicillin/streptomycin (Biowest, Pays De La Loire, France). Cells were maintained in a humidified atmosphere with 5% CO_2 and 95% air at 37 °C. The medium was replaced every 2-3 days and cells were detached upon reaching 80% confluence.

For biological experiments, the effect of 5-FU, GBM alone and GBM/5-FU loaded hydrogels was assessed using both healthy and cancer cells in the presence or absence of NIR irradiation, as described in detail below.

3.6.2 - Cytotoxicity of 5-FU and p-rGOn by resazurin assay

To evaluate the cytotoxic effect of 5-FU or p-rGOn, cells were seeded in 48-well plates at a density of 1×10^4 cells/well for HFF-1 and 4×10^4 cells/well for A-431, incubated at 37 °C and 5% CO_2. Upon sub-confluence (24 h), the culture medium was replaced by either 5-FU or p-rGOn dispersions. In the case of 5-FU, concentrations in a range between 0.1 and 1000 µg mL^{-1} were added using a final volume of 300 µL/well (in complete DMEM). In the case of p-rGOn, the material was added in concentrations ranging from 50 to 500 µg mL^{-1} using a final volume of 600 µL/well (in complete DMEM). Cells were incubated for additional periods of 24, 48, or 72 h. Then, cell viability was quantified using resazurin assay. Briefly, drug or GBM dispersions were removed and cells were incubated in 10% (v/v) resazurin reagent (Sigma-Aldrich, St. Louis, MO, USA) prepared in complete culture medium at 37 °C and 5% CO_2 for 2 h. Fluorescence (λex/em = 530/590 nm) of the supernatant was measured using a microplate reader spectrophotometer (Synergy Mx, Bio-Tek Instruments, Winooski, VT, USA). Negative controls for cell viability decrease were performed by incubating cells with complete DMEM. Data for each sample were normalized to the negative control and results are presented as mean % of control and standard deviation. All assays were performed in triplicate with six replicates for each condition. Additionally, microscopic images of cells were taken using an Olympus inverted optical microscope to evaluate the effect of 5-FU or p-rGOn increasing concentrations on cell morphology over time.

These assays allowed for the selection of suitable concentrations of 5-FU and p-rGOn to be incorporated in the hydrogels in subsequent biological assays in the presence or absence of NIR irradiation.

3.6.3 - Cytocompatibility of p-rGOn/5-FU hydrogels and photothermal irradiation assays

To evaluate the combined effect of p-rGOn/5-FU hydrogels and NIR irradiation, A-431 and HFF-1 cells were seeded as described above and incubated with diluted hydrogels using final concentrations of 100 µg mL^{-1} for p-rGOn and 0.25 µg mL^{-1} for 5-FU. After 2 h of incubation with the hydrogels, cells were irradiated for 10 min using a LED-based source with peak emission around 810 nm (NIR region) and irradiance of 150 $mWcm^{-2}$. After 24, 48 and 72 h post-irradiation, media containing hydrogels were removed, cells were washed with PBS, and analyzed by resazurin assay and live/dead staining.

3.6.3.1 - Resazurin assay

Resazurin assay was performed as described above. For this purpose, negative controls were performed using irradiated cells with complete DMEM. To compare the effects in the presence (LED on) or absence (LED off) of NIR irradiation, results are presented as mean % of control and standard deviation. To compare the effects of NIR irradiation, a negative control in the absence of materials was considered for normalization. All assays were performed in triplicate with six replicates for each condition tested.

3.6.3.2 - Live/dead staining

Live/dead assay using fluorescence labelling was performed to assess cell viability after treatment with irradiated and non-irradiated Carbopol 974P NF/p-rGOn/5-FU. Total cell number was obtained with Hoechst 33342 (Invitrogen) as it permeates cell membranes and stains the nucleus. Live cells were identified using Calcein AM (Invitrogen) that permeates cell membranes and labels both the nucleus and cytoplasm. Dead cells were stained by propidium iodide (PI; BD Biosciences) that only permeates compromised cell membranes and stains the nucleus. Cells were seeded in 48-well plates by a Multidrop™ Combi Reagent Dispenser (Thermo-Scientific). After different treatments, at 24, 48 and 72 h materials were removed, cells were washed with PBS and incubated with a Hoechst 33342 and Calcein AM solution in PBS at 2.5 μg mL^{-1} for 30 min, at 37 °C in the dark. Then, a PI solution at 2 μg mL^{-1} in PBS was added to each well. Samples were visualized by an inverted fluorescence microscope (Carl Zeiss, Axiovert 200M) and three images were acquired per sample using a digital camera (AxioCam MRm5, Zeiss).

3.6.3.3 - Quantitative analysis of cell viability using IN Cell Analyzer

Samples stained in the live/dead assays were analysed using an IN Cell Analyzer 2000 (GE Healthcare), a high content screening imaging system equipped with an automated widefield fluorescence microscope. Images were acquired using a Nikon 10X/0.45 Plan Apo objective, 2×2 binning and 2D acquisition mode. Eight fields were taken for each well and the excitation and emission filters used to detect Hoechst 33342, Calcein AM and PI were DAPI, FITC and Cy3, respectively. Exposure times were 1500 ms for Hoechst 33342, 150 ms for Calcein AM and 250 ms for PI.

3.6.3.4 - Image analysis with IN Cell Investigator Developer Toolbox

Images were analysed with the IN Cell Investigator Developer Toolbox 1.9.2 (GE Healthcare). Nuclei segmentation was performed in the images from the Hoechst 33342 channel (Figure 3.2 (A)). To avoid segmentation errors, post-processing steps were applied: First, the cells' nuclei were segmented using a "Nuclear Segmentation" algorithm (Figure 3.2 (B)). Then, individualized by the use of a "seed" target, this is created by an "erosion" of the initial nuclear mask (Figure 3.2 (C)). The previous "seed" is used to separate neighbouring nuclei touching each other and it is accomplished by the application of a "clump breaking" (Figure 3.2 (D)). Next, a "dilation" of the nuclear mask is performed that expands the nuclear outer boundary, to enlarge this mask for further pixel intensity quantification within the masked area (Figure 3.2 (E)). Finally, to correct for segmentation errors, only nuclei with a Form Factor above 0.6 and an area above 60 μm^2 have been taken into consideration for the quantification. After, the mean pixel intensity for the Calcein AM and PI channels has been determined for each of the segmented nuclei and collected in a spreadsheet. A threshold of mean pixel intensity for Calcein AM and/or PI positive cells has been chosen using the histograms of fluorescence intensity plotted on Spotfire®, a data exploration software.

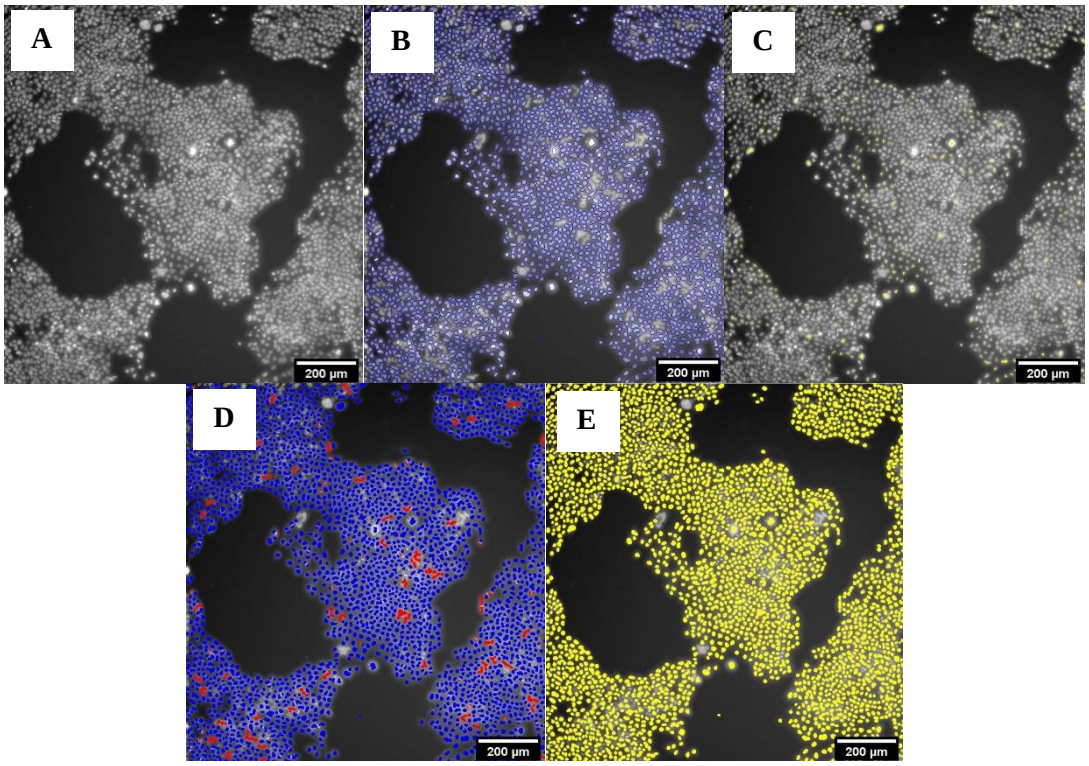

Figure 3.2 – Image analysis protocol used in the IN Cell Investigator Developer Toolbox to assess cell viability. (A) Fluorescence image; (B) "Seed" classification; (C) "Erosion"; (D) "Clump breaking"; (E) "Dilation" and segmentation. Scale bar: 200 µm.

3.6.3.5 - Cell ultrastructure and particle internalization by transmission electron microscopy

To investigate the influence of p-rGOn/5-FU hydrogel on cell morphology and ultrastructure, as well as to assess p-rGOn particle internalization, A-431 and HFF-1 cells were seeded and incubated with p-rGOn/5-FU hydrogel in the presence or absence of NIR irradiation, as described above. Controls without materials or irradiation were made for comparisons. After 72 h, cells were detached, resuspended in complete DMEM and centrifuged to form a pellet. Then, cells were fixed in freshly prepared 2.5% (v/v) glutaraldehyde and 2% (v/v) paraformaldehyde in 0.1 M sodium cacodylate. Afterwards, three washing steps in 0.1 M sodium cacodylate buffer were performed for 5 minutes each time. Post-fixation in 2% osmium tetroxide in 0.1 M sodium cacodylate was done for 2 h at room temperature. Next, samples were prepared in HistoGel™ and washed three times in water for 5 minutes each time. Samples were then incubated with 1% Uranyl acetate in distilled water for 30 minutes at room temperature. Dehydration was accomplished with 10-minute agitation in increasing concentrations of ethanol (50%, 70%, 80%, 6x 100%). Then, samples were included in resin with agitation for 1 h in different proportions of ethanol 100% and EPON resin: 3:1, 1:1, 1:3 and only EPON. Finally, samples were included in resin for 48 h, cut into thin sections and analysed using a JEOL JEM 1400 TEM (Tokyo, Japan).

3.7 - Statistical analysis

Statistical analyses were performed using GraphPad Prism software (version 8.4.2, San Diego, CA, USA). One-way analysis of variance (ANOVA) with Tukey's tests for multiple comparisons were performed for the parametric data and with Dunn's tests for multiple

comparisons for the non-parametric data. Differences between experimental groups were considered significant with a confidence interval of 95%, whenever $p < 0.05$.

Chapter 4

Results

4.1 - GBM characterization

4.1.1 - Physical characterization

Transmission electron microscopy (TEM) allowed the study of GBM nanosheets morphology, as presented in Figure 4.1. The images show well-dispersed sheets with no agglomeration in neither GOn or p-rGOn aqueous dispersions at a concentration of 40 µg mL^{-1}.

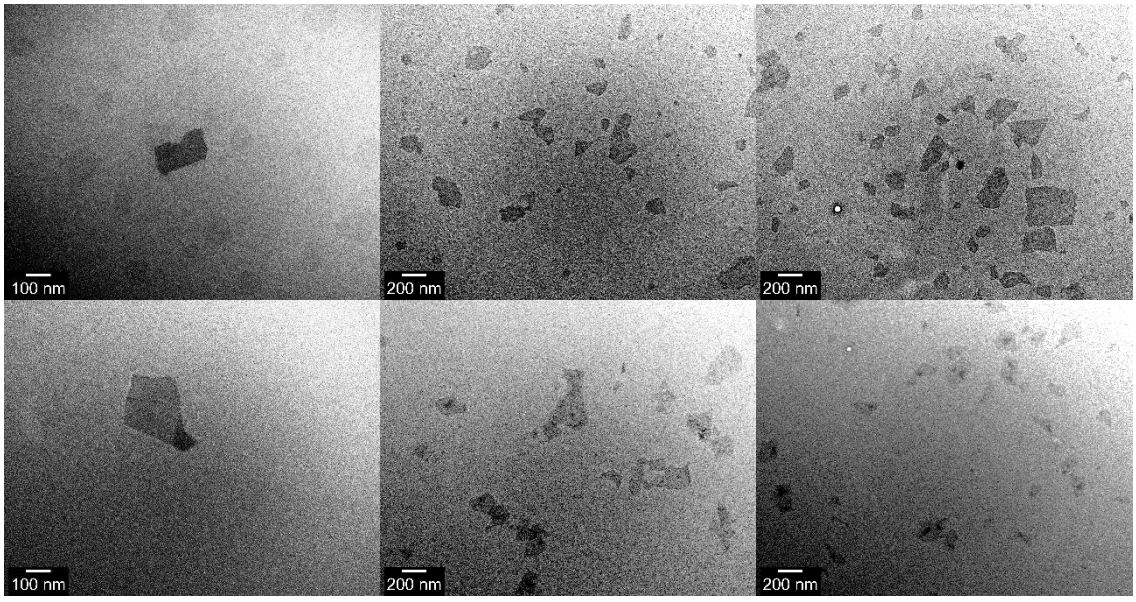

Figure 4.1 – GBM morphology. Representative TEM images of GOn (upper row) and p-rGOn (lower row) aqueous dispersions at a concentration of 40 µg mL^{-1}. Scale bars represent 100 and 200 nm.

Lateral dimensions of GBM were determined by analysing TEM images, as presented in Figure 4.2. Measurements were made of the X and Y axis in each TEM image where the average particle size of GOn revealed to be 114.1 ± 63.3 nm and 99.7 ± 59.7 nm for the X and Y axis, respectively. As for p-rGOn, the average particle size for the X and Y axis were determined to be 181.4 ± 169.6 nm and 156.4 ± 123.8 nm, respectively. Mean values for each GBM resulted in

107.0 ± 62.0 nm for GOn and 168.8 ± 148.7 nm for p-rGOn. Both materials present nanometric sizes, suitable for desired biomedical applications.

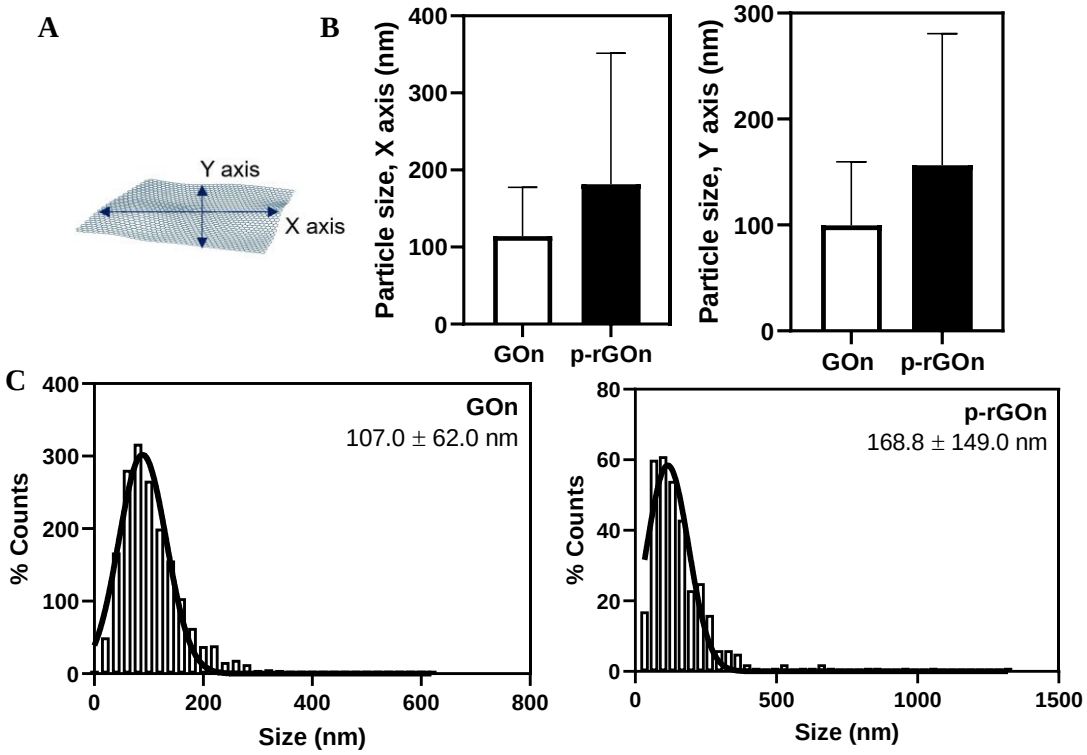

Figure 4.2 – Particle size of GOn and p-rGOn aqueous dispersions, determined by TEM image analysis. (A) Schematic representation of X and Y axis used to measure GBM lateral dimensions; (B) GOn and p-rGOn particle sizes determined using the X (left) or Y (right) axis; (C) GOn (left) and p-rGOn (right) particle size distributions based on X and Y axis determinations and mean and standard deviation.

Particle size distribution was also evaluated by dynamic light scattering (DLS) using Coulter and Zetasizer equipment (Figure A1 and Table 4.1).

Table 4.1 – Particle size and polydispersity index of GOn and p-rGOn aqueous dispersions at a concentration of 25 μg mL^{-1}, determined by DLS with a Zetasizer equipment (n = 5).

GBM	Size (nm)	Polydispersity index (PDI)
GOn	284.2 ± 38.4	0.490 ± 0.06
p-rGOn	218.5 ± 25.7	0.431 ± 0.06

As Zetasizer applies the DLS principle, higher size values were expected than the ones obtained with TEM image analysis, because this technique assumes a spherical model for every particle while GBM are 2D-sheets. GOn and p-rGOn presented a particle size of 284.2 ± 38.4 nm and 218.5 ± 25.7 nm, respectively. The numerical value of the polydispersity index (PDI) ranges from 0.0 (for a perfectly uniform sample with respect to the particle size) to 1.0 (for a highly polydisperse sample with multiple particle size populations) [255]. Furthermore, a PDI between 0.2 and 0.5 indicates a wide particle size distribution [256], as it is the case of the produced GBM. GOn had a PDI of 0.490 ± 0.06, while the value for p-rGOn was of 0.431 ± 0.06.

GOn and p-rGOn surface charges were also determined by Zetasizer analysis and are presented in Figure 4.3. Obtained values were of - 44 and -38 mV for GOn and p-rGOn, respectively, below - 30 mV for both materials, which indicates high water stability [255]. This

characteristic was additionally confirmed by direct observation of the water dispersions. Four months after production, GBM maintained their stability without material precipitation, as observed in Figure 4.4.

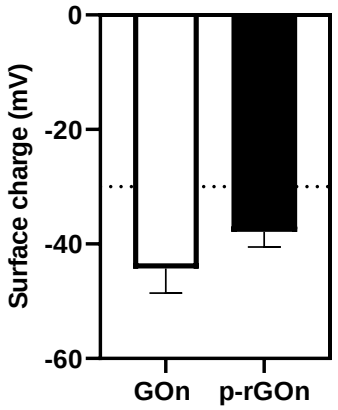

Figure 4.3 – Surface charge of GOn and p-rGOn aqueous dispersions at a concentration of 25 µg mL^{-1}, determined by Zetasizer equipment (n = 5). The dashed line indicates the good water stability limit set at - 30 mV.

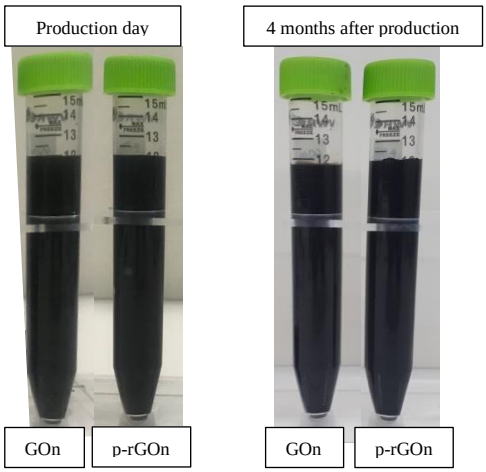

Figure 4.4 – GBM aqueous dispersions for stability evaluation. From left to right: GOn and p-rGOn dispersions immediately after production day at a concentration of 8.9 mg mL^{-1} and 0.8 mg mL^{-1}, respectively (Production day); GOn and p-rGOn dispersions 4 months after production.

4.1.2 - Chemical characterization

Fourier-transform infrared spectroscopy (FTIR) spectra were obtained to study the presence of GOn oxygen functionalities along with its partial reduction into p-rGOn (Figure 4.5). GOn spectra showed a broad band with a wavenumber range between 3000 cm^{-1} and 3600 cm^{-1} that corresponds to O-H stretching vibrations. These values are normally attributed to adsorbed water molecules, hydroxyl and carboxyl groups. C=O stretching vibrations are present around 1731 cm^{-1}, representing the carbonyl and carboxyl molecules. The stretching of cyclic alkene (C=C) is also present at approximately 1621 cm^{-1} due to the unoxidized graphite. The presence of ethers is demonstrated by absorption bands at around 1166 cm^{-1} and 1041 cm^{-1} corresponding to C-O stretching vibrations and through epoxides with C-O bending vibrations around 875 cm^{-1} [35, 257]. p-rGOn spectra present a reduction of the intensity of the oxygen-containing groups compared with GOn, confirming that the reduction procedure was successful. FTIR spectra show a significant decrease at around 3400 cm^{-1}, indicating that a large amount of O-H groups was

removed during the reduction. However, the presence of some oxygen-containing groups is confirmed by the C=O stretching at around 1729 cm^{-1} or C-O bending at 1041 cm^{-1}.

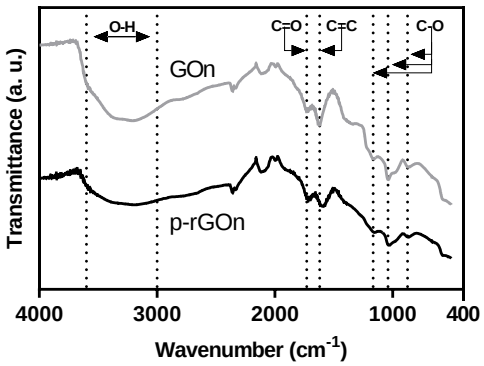

Figure 4.5 – FTIR spectra of GOn and p-rGOn. The lines indicate the contribution of different surface functionalities.

Thermogravimetric analysis (TGA) allowed the study of the thermal stability of the produced GBM. Thermograms (Figure 4.6) reveal three main weight loss steps during the heating above 100 °C. Below that temperature, there is a weight loss of approximately 10%, attributed to water evaporation. The first weight loss step was observed between 100 °C and 225 °C. GOn and p-rGOn presented weight losses of approximately 24.9 and 25%, respectively, which corresponds to the loss of reactive oxygen-containing functional groups such as carboxyl and epoxy. The second weight-loss step occurred between 225 and 600 °C with a weight loss of 21.3% for GOn and 15.8% for p-rGOn, corresponding to the partial combustion of the carbon skeleton and other stable oxygen-containing functional groups, for example, carbonyls and hydroxyls. The smaller weight loss in p-rGOn suggests the presence of a smaller amount of stable oxygen-containing groups, which also confirms a successful reduction. The third and last weight loss step happened between 600 and 1000 °C where GOn showed a weight loss of 31.9% and p-rGOn 11.6%. This step corresponds to the continuous combustion of the carbon skeleton. Oxygenated groups are thermolabile so the decreased amount of these functional groups in p-rGOn allows superior thermal stability when compared with GOn that possesses increased oxygen-functional groups.

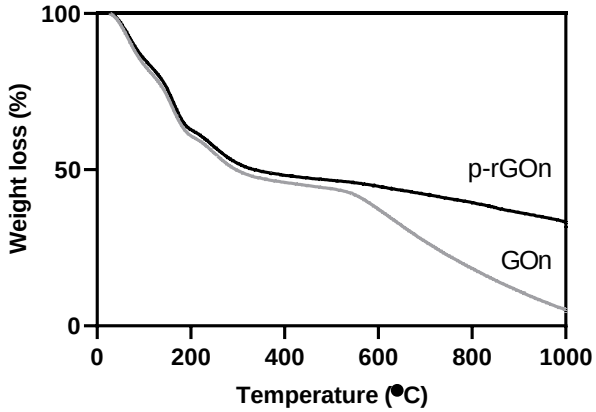

Figure 4.6 – Thermogravimetric analysis of GOn and p-rGOn, under a nitrogen atmosphere.

The optical properties of both nanomaterials were studied by UV-Vis spectroscopy (Figure 4.7). For GOn, the absorption spectrum reveals a maximum absorbance peak around 230 nm

which results from the π-π* electronic transitions in sp^2 clusters and a shoulder peak around 300 nm typical from the n-π* transitions of free electron pairs in the oxygen atoms present in the double bonds between carbon and oxygen. For the p-rGOn, the spectrum shows a 4.4-fold increment in NIR absorbance (810 nm) compared with GOn. Also, the shoulder peak is not present due to the reduction having removed oxygen-containing functional groups.

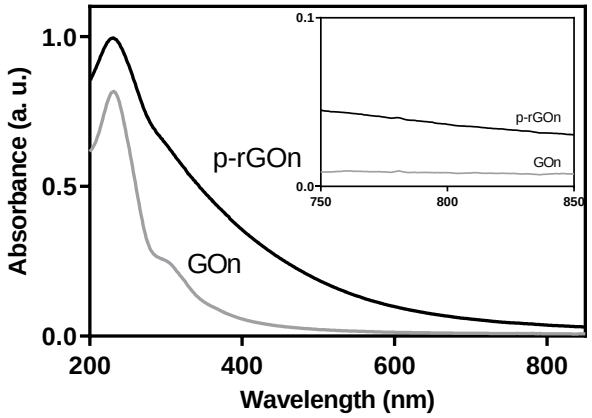

Figure 4.7 – UV-Vis absorption curves of GOn and p-rGOn. The inset shows a zoom-in view of the curves in the NIR range (750-850 nm).

4.1.3 – Photothermal properties

To evaluate the capacity of the nanomaterials to convert NIR light into heat, aqueous dispersions of GOn and p-rGOn with a concentration of 250 μg mL^{-1} and an initial temperature of 37 °C were irradiated with a custom-build LED NIR device (810 nm, 150 $mWcm^{-2}$) and temperature measured at different time points. Figure 4.8 shows that after 30 minutes of NIR irradiation, GOn presented a temperature of approximately 38 °C while p-rGOn showed temperature increased to 52 °C. The reduction process restored the aromatic structure of p-rGOn that showed enhanced NIR absorbance and consequent heat production after NIR irradiation. Hyperthermia (43 - 50 °C) has been described to lead to enhanced cancer cell membrane permeability that increases anticancer drug uptake. Hence, the produced material is innovative due to its water stability, NIR absorbance and conversion to high temperatures, demonstrating its potential for the desired phototherapeutic application and being selected for further biological studies.

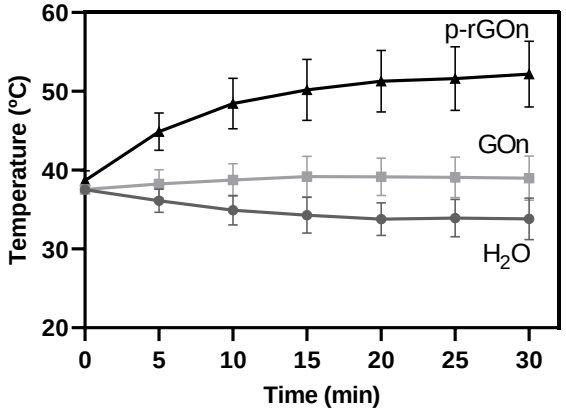

Figure 4.8 – Photothermal heating curves of water, and GOn and p-rGOn aqueous dispersions at a concentration of 250 µg mL^{-1} in water.

4.2 - Drug loading

Drug loading capacity (LC) and loading efficiency (LE) were quantified at different GBM (0.25 and 0.5 mg mL^{-1}) and 5-FU (1-10 mg mL^{-1}) concentrations by measuring the drug optical absorption at 265 nm in aqueous solutions. Initially, the LC seemed to be concentration-dependent, as observed in Figure 4.9 (A). A 5-FU concentration of 5 µg mL^{-1} resulted in a LC of 1.2 mg 5-FU/mg GOn when using GOn concentrations of 0.25 and 0.5 µg mL^{-1}. For a higher drug concentration of 10 mg mL^{-1}, superior LC values of 2.7 mg 5-FU/mg GOn were obtained, for 0.25 µg mL^{-1} of GOn, while a slightly lower LC of 1.0 mg 5-FU/mg GOn was observed with 0.5 mg mL^{-1} GOn. Similarly, this assay was performed with p-rGOn and 10 mg mL^{-1} of 5-FU. Higher LC values were obtained with 0.25 mg mL^{-1} of p-rGOn (3 mg 5-FU/mg p-rGOn), compared with when a concentration of 0.5 mg mL^{-1} (1.4 mg 5-FU/mg p-rGOn) was used. (Figure 4.9 (B)). However, these results were not reproducible as sometimes LC and LE turned out positive and other times negative or even both (Figure 4.9 (C, D)). After testing multiple conditions such as dissolving both GBM and 5-FU in different mediums (water, PBS, phosphate buffer), trying different centrifugation velocities (13400, 14000 rpm), dissolving the dispersions for multiple time points (0, 0.5, 1, 24 and 48 h) this approach was abandoned due to lack of time to optimize it in the duration of the thesis work, and a strategy with more probability of leading to desired results followed, combining both GBM and 5-FU by dispersing them (without previous surface adsorption) in hydrogels suitable for target applications.

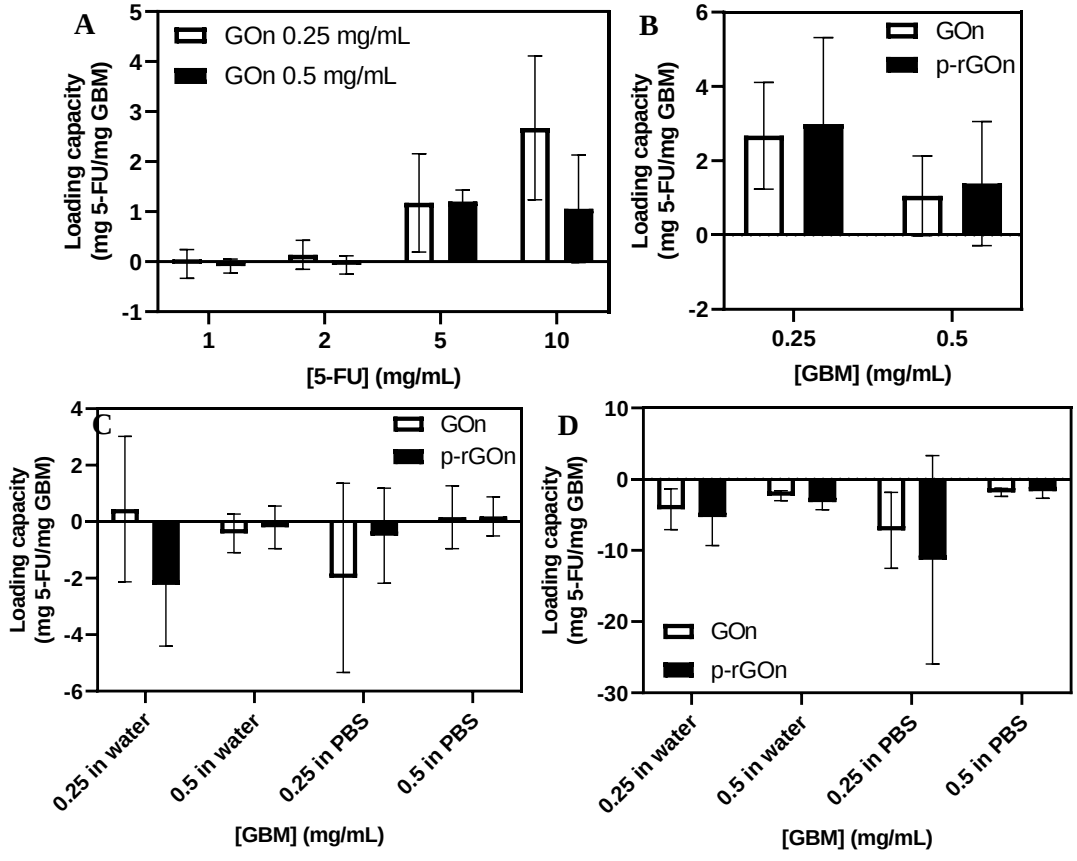

Figure 4.9 – GBM loading capacity of 5-FU after different concentrations.

4.3 - Hydrogels characterization

Carbopol 974P NF hydrogels were prepared containing p-rGOn and 5-FU. Controls with only Carbopol 974P NF, Carbopol 974P NF/5-FU and Carbopol 974P NF/p-rGOn were also produced to assess their effect in biological studies. The Carbopol 974P NF and Carbopol 974P NF/5-FU hydrogels were transparent while the Carbopol 974P NF/p-rGOn and the Carbopol 974P NF/p-rGOn/5-FU presented a dark brown colour due to p-rGOn presence (Figure 4.10).

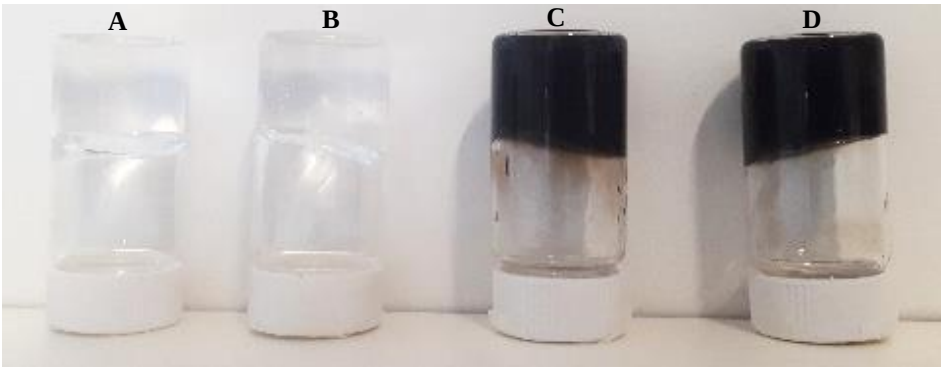

Figure 4.10 – Images of prepared hydrogels in glass vials upside down. (A) Carbopol 974P NF hydrogel (0.5% w/v); (B) Carbopol 974P NF/5-FU hydrogel (1.5 µg mL^{-1}); (C) Carbopol 974P NF/p-rGOn (600 µg mL^{-1}); (D) Carbopol 974P NF/p-rGOn/5-FU (600 µg mL^{-1} of p-rGOn and 1.5 µg mL^{-1} of 5-FU).

To assess the phototherapeutic properties of the produced hydrogels, NIR irradiation assays were performed as previously described. After 30 minutes, the Carbopol 974P NF/p-rGOn/5-FU hydrogel reached 45.9 ± 1.9 °C, within the values required for achieving a mild hyperthermia effect of interest for cancer treatment (Figure 4.11).

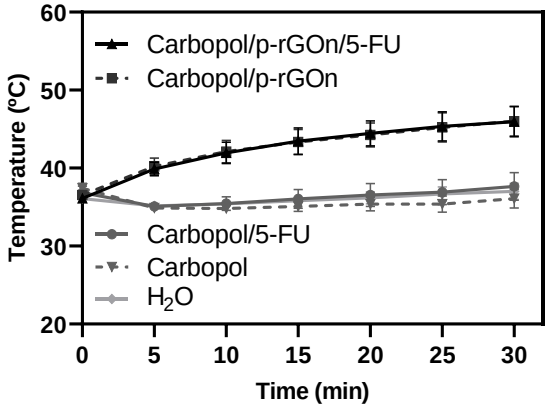

Figure 4.11 – Photothermal heating curves of water, and Carbopol 974P NF hydrogel, Carbopol 974P NF/5-FU, Carbopol 974P NF/p-rGOn, Carbopol 974P NF/p-rGOn/5-FU aqueous dispersions at a concentration of 100 µg mL^{-1} of p-rGOn and 0.25 µg mL^{-1} of 5-FU.

The produced hydrogels were characterized by UV/vis spectroscopy, spectra of 5-FU and p-rGOn only were also obtained. The p-rGOn concentration included in the hydrogels (100 µg mL^{-1}) resulted in absorbance values over 1, which is the equipment's detection limit (Figure 4.12 (A)). Characterization of GBM is usually performed in the order of 25 µg mL^{-1} to obtain absorbances below 1 (results presented in Section 4.1.2). Therefore, for this assay, the concentration of p-rGOn was decreased by dilution with water to 10 µg mL^{-1}, consequently diminishing the 5-FU

concentration to 0.025 µg ml^{-1} in the hydrogel with both components. The control made with 5-FU (only) at a concentration of 0.25 µg mL^{-1}, revealed a typical spectrum with the characteristic peak around 265 nm [258], however, the spectra presented low definition, due to the very small amount of drug present (Figure 4.12 (B)). Carbopol 974P NF presents optical absorption in the UV region around 200 nm [259]. When p-rGOn was present in the hydrogels, absorbance at 230 nm increased by 6.13-fold, which was expected because this region corresponds to GBM maximum absorbance peak. Unfortunately, UV-visible spectroscopy was not sensitive enough to detect the 5-FU after incorporation in the hydrogels, because the concentration present was very low and the drug, Carbopol 974P NF and p-rGOn present optical absorption in similar regions (Figure 4.12 (C)).

FTIR was also used to characterize the hydrogels after dehydration. Carbopol 974P NF spectra presented peaks correspondent to hydroxyl stretching vibrations and intramolecular hydrogen bonding between 2970 cm^{-1} and 2910 cm^{-1}. A carbonyl stretching peak is observed at 1700 cm^{-1}, while between 1450 cm^{-1} and 1400 cm^{-1} C-O stretching and O-H deformation peaks are observed [260]. Nevertheless, the Carbopol 974P NF spectrum seemed to overlap p-rGOn and 5-FU peaks, as all spectra revealed to have no identifiable differences. This might be explained due to the low concentrations of GBM and drug present in the hydrogel (Figure 4.12 (D)).

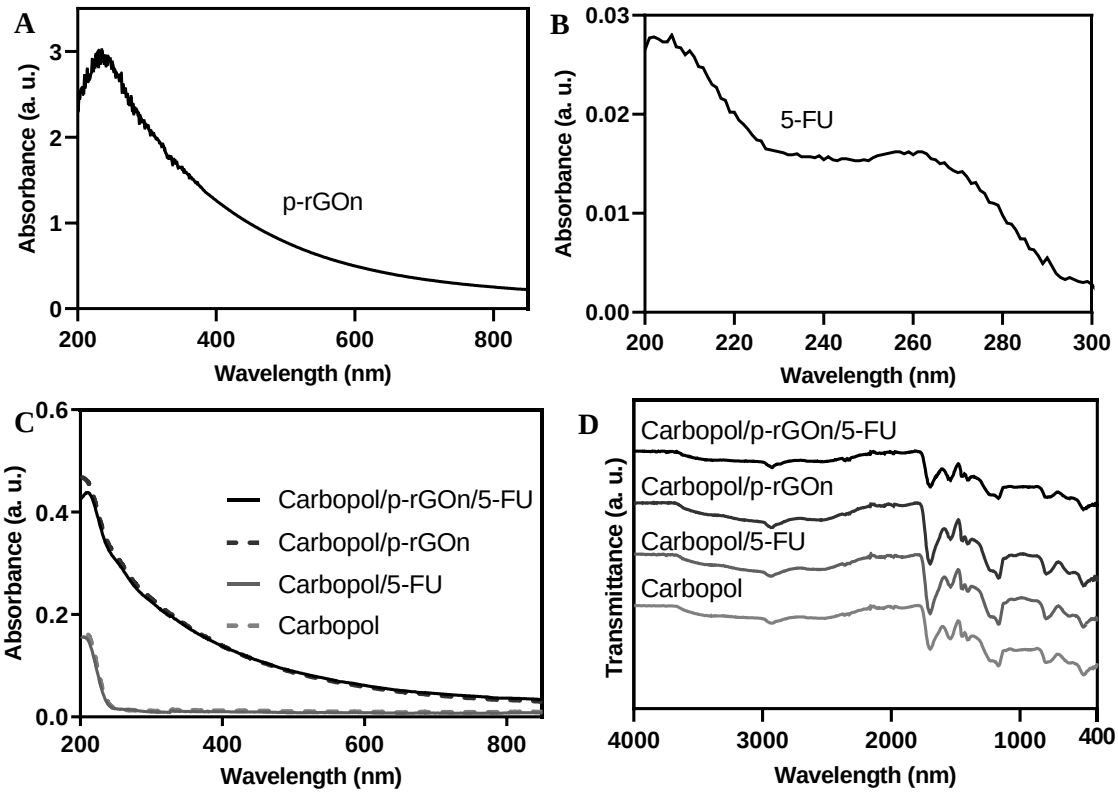

Figure 4.12 – Hydrogel characterization (Carbopol 974P NF, Carbopol 974P NF/5-FU, Carbopol 974P NF/p-rGOn, Carbopol 974P NF/p-rGOn/5-FU). (A) UV-Vis absorption curve of p-rGOn at a concentration of 100 µg mL^{-1}; (B) UV-Vis absorption curve of 5-FU at a concentration of 0.25 µg mL^{-1} (C) UV-Vis absorption curves of the hydrogels at a p-rGOn concentration of 10 µg mL^{-1} and a 5-FU concentration of 0.025 µg mL^{-1}. (D) FTIR spectra of the hydrogels.

Since due to the low amount of 5-FU present in the hydrogels, it has not been possible to confirm its presence by UV-vis or FTIR, HPLC was used for the purpose. Despite a low concentration of 0.25 µg mL^{-1} being used, the equipment was able to quantify it. A retention time of approximately 5.5 minutes was obtained for 5-FU, similar to other reports [261]. When the

drug was present, a clear and sharp peak was observed at this retention time, as it is the case of the 5-FU solution, Carbopol 974P NF/5-FU dispersion and Carbopol 974P NF/p-rGOn/5-FU dispersion (Figure 4.13). Other peaks with other retention times represent other compounds present in the hydrogels. Through a 5-FU calibration curve, the areas were converted to concentrations. The obtained values of 0.20 µg mL^{-1} for Carbopol 974P NF/5-FU and 0.22 µg mL^{-1} for Carbopol 974P NF/p-rGOn/5-FU were similar to the desired value of 0.25 µg mL^{-1} (Table 4.2), being the errors associated with sample preparation measurements under 20%.

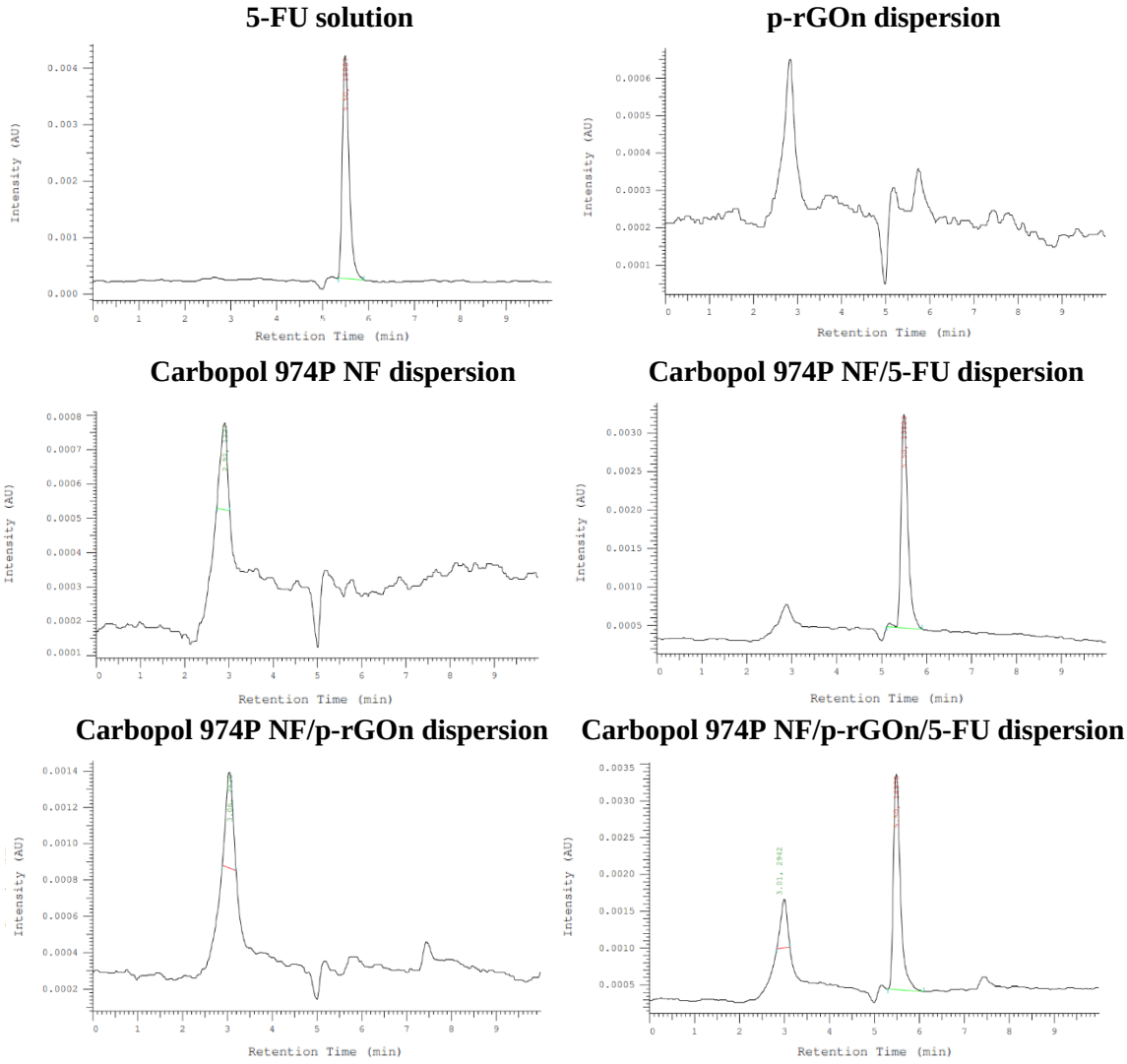

Figure 4.13 – HPLC chromatogram obtained from the produced hydrogels in acetonitrile and water (5:95, v/v).

Table 4.2 – Peak areas for tested conditions and concentrations.

Sample	Area	Concentration (µg mL^{-1})
p-rGOn solution	0	0
Carbopol 974P NF solution	0	0
Carbopol 974P NF/5-FU solution	13817	0.20
Carbopol 974P NF/p-rGOn solution	0	0
Carbopol 974P NF/p-rGOn/5-FU solution	14973	0.22

4.4 - *In vitro* studies

4.4.1 - 5-FU cytotoxicity

The cytotoxic effect of 5-FU on human skin cells has been evaluated firstly with the goal to identify the concentrations that would allow achieving cancer cell death without damaging healthy tissues. HFF-1 and A-431 cells were used as *in vitro* models of human normal skin and human skin carcinoma, respectively. Cells were incubated with increasing concentrations (0.1-1000 μg mL^{-1}) of the anticancer drug for 24, 48 and 72 h. These time points were chosen once it has been observed in the literature that the best outcomes with this anticancer drug occur after 48 h, as some time is needed for interference with cell replication to be observed [262, 263]. At each time point, cell viability was assessed through the resazurin assay (Figure 4.14). Controls were made without the addition of 5-FU. When incubated with human skin fibroblasts (HFF-1), 5-FU was not considered toxic after 24 and 48 h for all concentrations tested. After 72 h, despite cell viability decreases with concentrations higher than 0.1 μg mL^{-1}, 5-FU is considered non-toxic in concentrations up to 1 μg mL^{-1}, as cell viability values were higher than 70%, which is considered the toxicity limit (ISO 10993-5:2009(E)). At higher concentrations, a tendency for cell viability decreasing as concentration increases was noticed at 72 h. In contrast, for A-431 cancer cells, after 24 h a cell viability of only 60% is observed, for a concentration of 500 μg mL^{-1}. At 48 h only 0.5 μg mL^{-1} are already enough to decrease cell viability to 58%, and after 72 h, even 0.1 μg mL^{-1} already led to a cell viability value of 55%, while for example a concentration of 100 μg mL^{-1} reduced cell viability by 84%. These results can be explained by the mechanism of action of 5-FU that interferes with DNA replication. The accelerated cell division characteristic of cancer cells translates into a faster cytotoxic effect being caused by 5-FU. In opposition, the slow growth of the fibroblasts delays the harmful effect. These results support the efficiency of this anticancer drug for desired purposes, once combined PTT-chemotherapy has the goal to cause selective cancer cell death, without harming normal skin cells. After this assay, a concentration range from 0.1 to 1 μg mL^{-1} was selected as safe for the skin fibroblasts and toxic for the skin cancer cells.

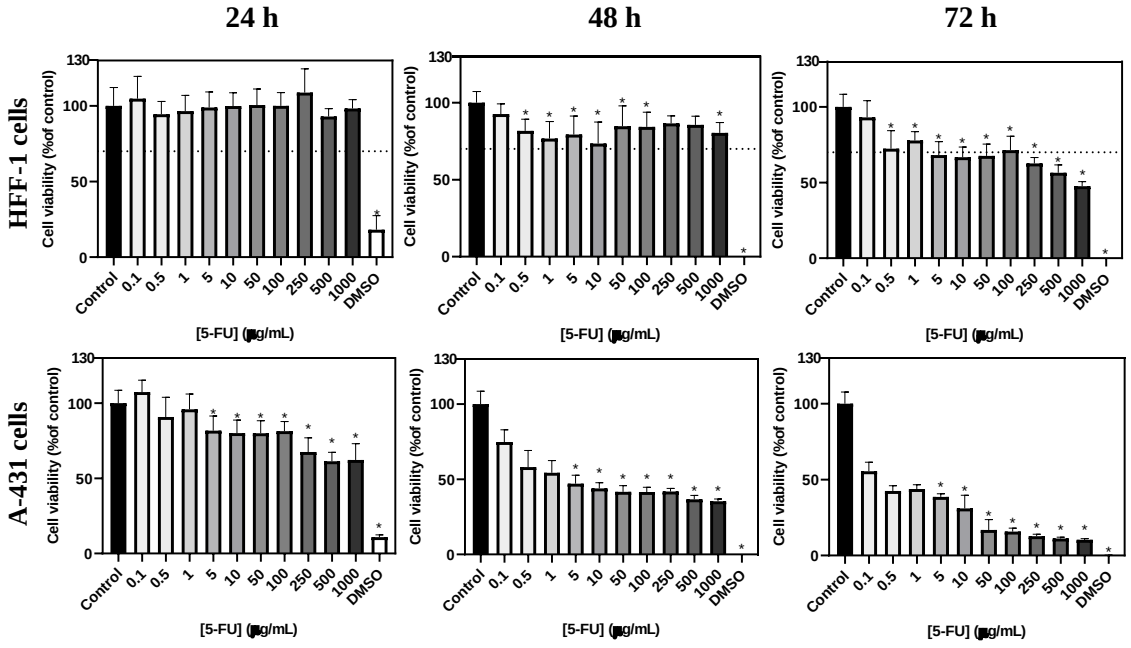

Figure 4.14 – Cellular viability for HFF-1 cells (upper row) and A-431 cells (lower row) incubated with 5-FU and determined using the resazurin assay after 24, 48 and 72 h. Results are normalized to values obtained for the control

incubated in complete DMEM without 5-FU. Results are presented as average and standard deviation (n = 6). Statistically significant differences against the control with complete DMEM are shown as * $p < 0.05$. Dashed line marks the toxicity limit (ISO 10993-5:2009(E)).

The HFF-1 cell line consists of spindle-like fibroblasts, being the typical elongated cell shape, identified and presented in Figure 4.15. After being exposed to 1 mg mL^{-1} of 5-FU, a decrease in the number of cells could be observed. The A-431 cell line has an epithelial morphology with a tendency to grow in clusters as can be observed in Figure 4.16. After being incubated with 1 mg mL^{-1} of 5-FU, a change in the morphology is also noticeable with cells losing the characteristic shape and clustering, becoming spherical and individualized.

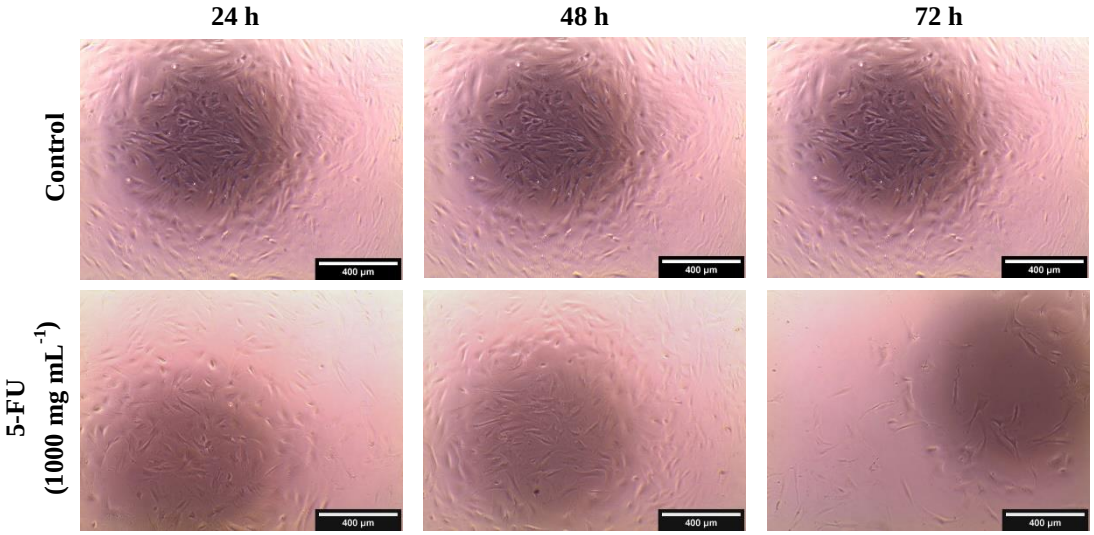

Figure 4.15 – Microscopy images of human foreskin fibroblasts (HFF-1) incubated with 5-FU for 24, 48 and 72 h at the highest concentration studied (1000 µg mL^{-1}). Controls correspond to cells incubated in complete DMEM without the addition of the anticancer drug. Scale bar represents 400 µm.

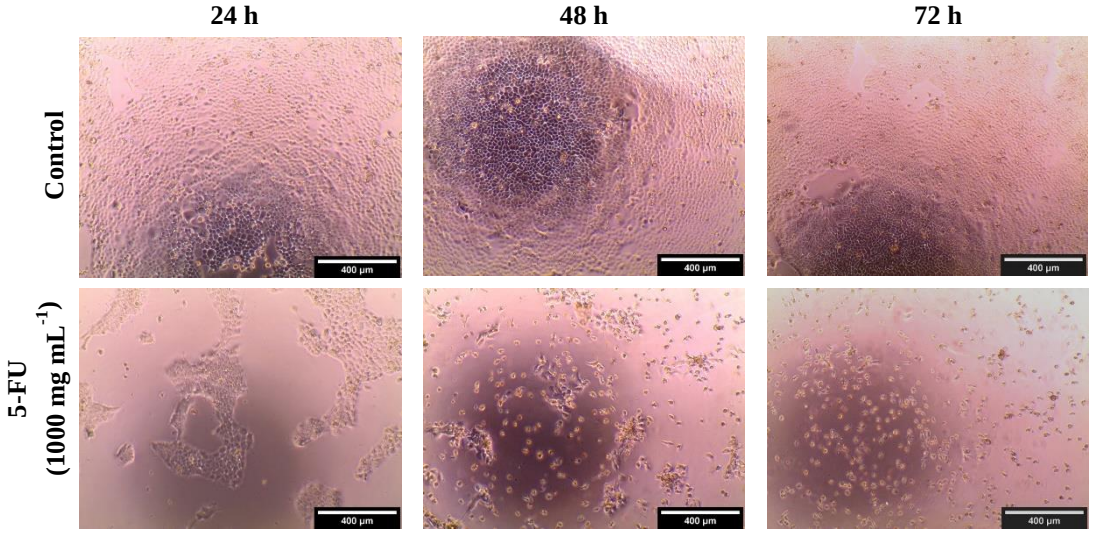

Figure 4.16 – Microscopy images of human epidermoid carcinoma cells (A-431) incubated with 5-FU for 24, 48 and 72 h at the highest concentration studied (1000 µg mL^{-1}). Controls correspond to cells incubated in complete DMEM without the addition of the anticancer drug. Scale bar represents 400 µm.

4.4.2 - p-rGOn cytotoxicity

HFF-1 cells were incubated with increasing p-rGOn concentrations (50-250 µg mL^{-1}) for 24, 48 and 72 h. At each time point, cell viability was assessed through the resazurin assay (Figure A2). Controls were made with cell culture media without the addition of p-rGOn. The results were not reliable as many values have surpassed 150% of cell viability, while in the microscopic images, cells did not appear to be that confluent (Figure A3). In some assays, GBM influence the resazurin assay, by a mechanism that we were not able to identify or control. To surpass this problem, live/dead assays were performed as described below. Nevertheless, the obtained results showed a tendency for cytotoxicity, only after 72 h, at a concentration of 250 µg mL^{-1}.

Live/dead staining of HFF-1 cells was performed using Calcein, as live cells metabolize it and are stained in green, and propidium iodide to see the dead or dying cells, stained in red, as the compromised membranes allow its penetration resulting in nuclear staining. Images were taken after 24 and 48 h (Figure A4) and 72 h (Figure 4.17) of incubation with p-rGOn in concentrations between 50 and 250 µg mL^{-1}. The concentrations of 50 and 100 µg mL^{-1} resulted in low cell death values of 11 and 13%, respectively. However, at the highest concentrations of 175 and 250 µg mL^{-1} only the Calcein staining worked, while dead cell's nucleus were not marked by PI. Graphene seems to interfere with the fluorescence, forming a layer above cells. Analysing the results obtained here and in the resazurin assay, a concentration of 100 µg mL^{-1} was selected for further assays, in order to minimize any toxicity eventually caused by p-rGOn, that might not have been identified due to the reported limitation of the characterization methods available.

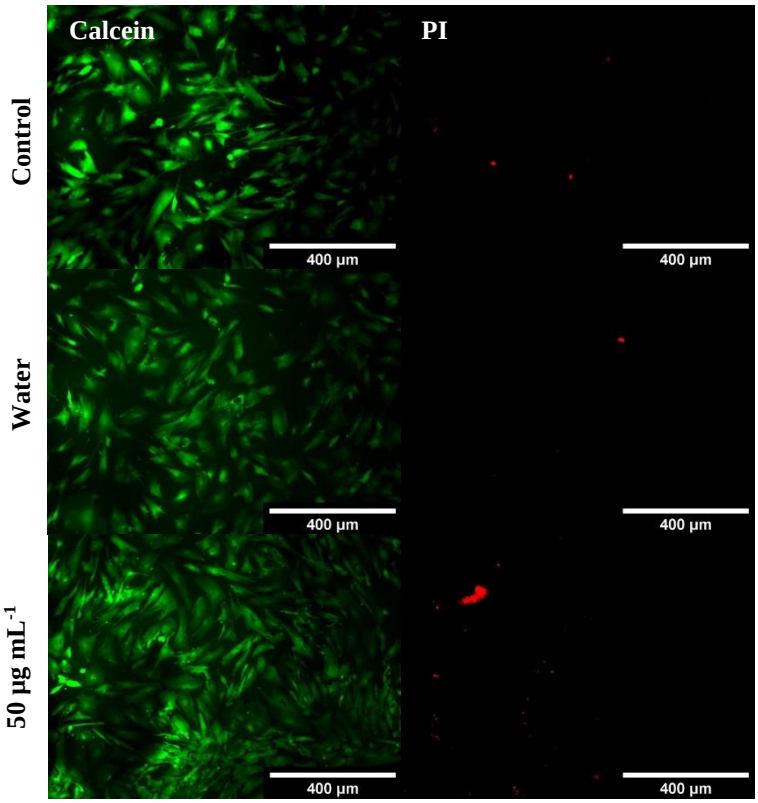

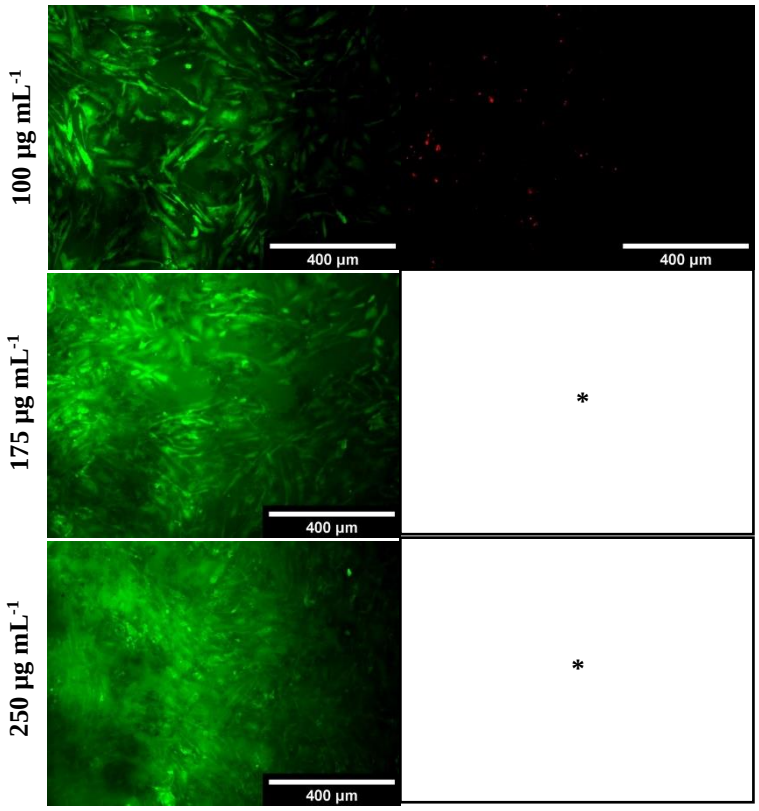

Figure 4.17 – Live/dead staining of HFF-1 cells incubated with increasing p-rGOn concentrations (50-250 µg mL^{-1}) for 72 h. Controls correspond to cells incubated in complete DMEM without the addition of the GBM. Live cells metabolize Calcein (green) and dead cells were stained with PI (red). Scale bar represents 400 µm. * Not possible to obtain an image due to interference with the signal.

4.4.3 - 5-FU hydrogels cytotoxicity

As mentioned before, 5-FU concentrations in the range between 0.1 and 1 µg mL^{-1} were found to be non-toxic for HFF-1 cells (Section 4.4.1.1). However, it was important to assure that the drug remains biocompatible and effective after incorporated in the Carbopol 974P NF hydrogel. Therefore, hydrogels containing 0.1, 0.5 and 1 µg mL^{-1} 5-FU, were incubated with HFF-1 cells. Even though very high cell viability values were obtained, the concentration of 1 µg mL^{-1} appeared to be toxic after 48 h, as cell viability values were below the 70% toxicity limit, according to ISO 10993-5:2009(E) (Figure A5). Therefore, a maximum concentration of 0.5 µg mL^{-1} was tested against the cancer cells to guarantee treatment efficiency, with minimal damage to normal cells.

A-431 carcinoma cells were exposed to 0.1, 0.25 and 0.5 µg mL^{-1} 5-FU and incubated for 24, 48, and 72 h. After 24 h, cell viability was unaffected for all concentrations tested (Figure 4.18). However, after 48 h a cell death of 31% was observed for the 0.5 µg mL^{-1} concentration. Finally, after 72 h of incubation, a cell death of 45% was observed for a concentration of 0.5 µg mL^{-1}, while a concentration of 0.25 µg mL^{-1} resulted in approximately 30% cell death. Also, a decrease in the number of cancer cells is observed (Figure 4.19) after incubation with 0.5 µg mL^{-1} of 5-FU, namely after 48 and 72 h, comparing with the control where cells were exposed to cell culture medium only. Considering above-mentioned results, a concentration of 0.25 µg mL^{-1} has been selected for further assays.

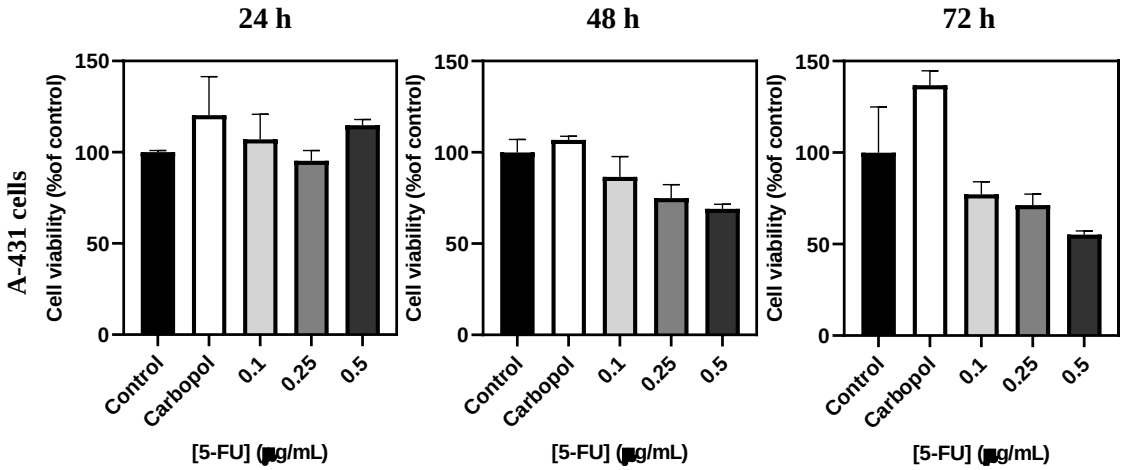

Figure 4.18 – Cellular viability for A-431 cells incubated with 5-FU hydrogels determined using the resazurin assay after 24, 48, and 72 h. Results are normalized concerning values of the control incubated in complete DMEM without 5-FU hydrogel. Results are presented as average and standard deviation (n = 3).

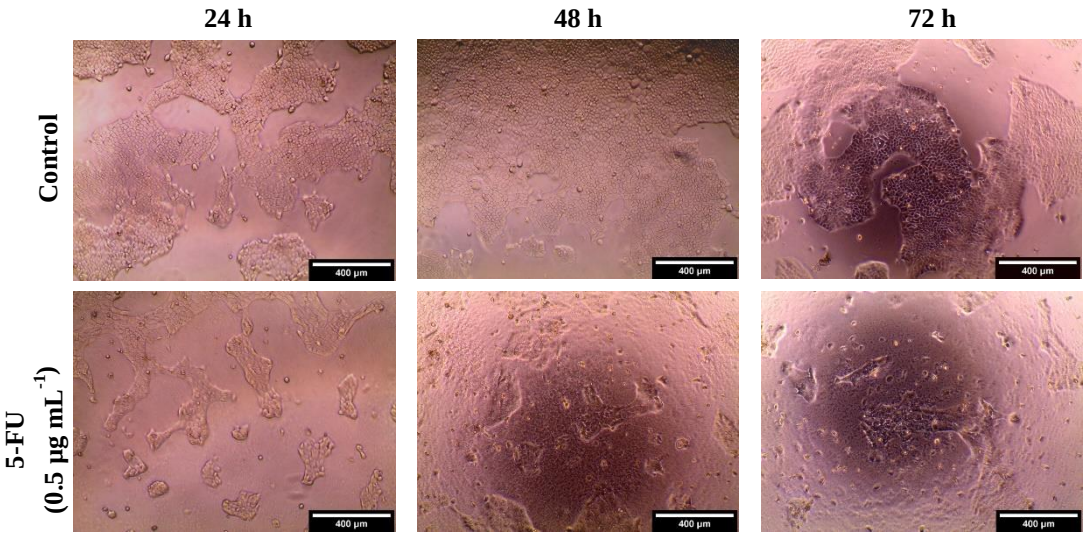

Figure 4.19 – Microscopy images of human epidermoid carcinoma cells (A-431) incubated with 5-FU hydrogels for 24, 48 and 72 h at the highest concentration studied. Controls correspond to cells incubated in complete DMEM without the addition of the hydrogel. Scale bar represents 400 µm.

4.4.4 - p-rGOn hydrogels cytotoxicity with irradiation

To evaluate the ideal irradiation time for obtaining a phototherapeutic effect A-431 cells were incubated with Carbopol 974P NF/p-rGOn hydrogels at a concentration of 100 µg mL^{-1} and irradiated with NIR for 5, 10 and 15 minutes. An irradiation time of 10 minutes resulted in a 15% cancer cell death, while 15-minute irradiation originated a 53% cell death after 72 h at the same p-rGOn concentration (Figure 4.20). The PTT effect of the irradiated Carbopol 974P NF/p-rGOn is reflected in the decreased number of cells identified after 24, 48 and 72 h (Figure 4.21).

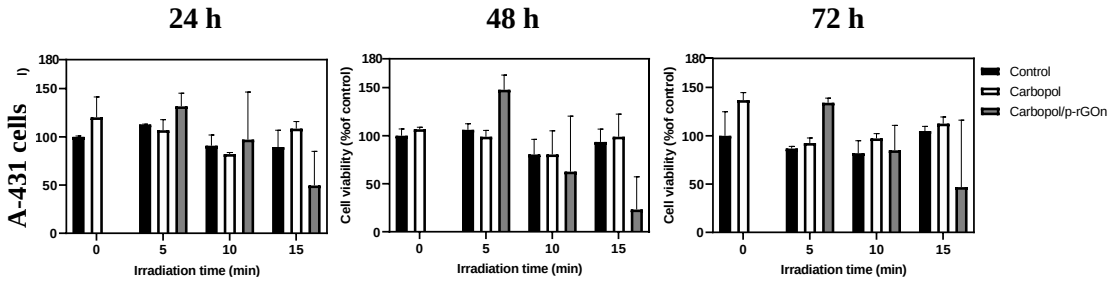

Figure 4.20 – Cellular viability for A-431 cells incubated with irradiated p-rGOn hydrogels at a concentration of 100 µg mL^{-1} determined using the resazurin assay after 24, 48 and 72 h. Results are normalized concerning values of the control incubated in complete DMEM without p-rGOn hydrogel. Results are presented as average and standard deviation (n = 3).

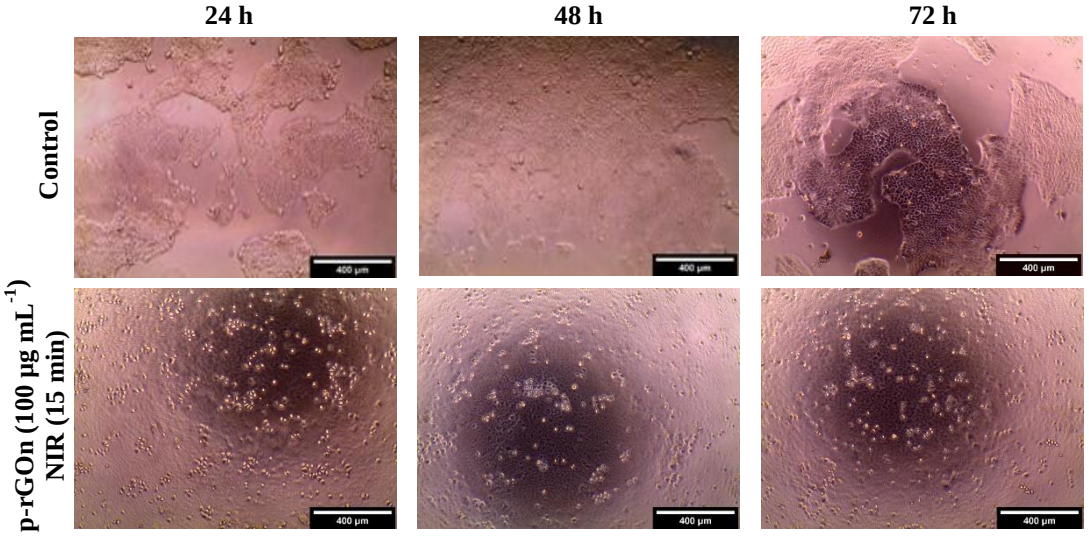

Figure 4.21 – Microscopy images of human epidermoid carcinoma cells (A-431) incubated with p-rGOn hydrogels at 100 µg mL^{-1} for 24, 48 and 72 h with 15 min irradiation. Controls correspond to cells incubated in complete DMEM without the addition of the hydrogel. Scale bar represents 400 µm.

4.4.5 - p-rGOn/5-FU hydrogels cytotoxicity with and without irradiation

The cytotoxicity of the Carbopol 974P NF/p-rGOn/5-FU hydrogels was assessed in HFF-1 and A-431 cells at the previously selected conditions of 100 µg mL^{-1} of p-rGOn, 0.25 µg mL^{-1} of 5-FU, and a 10-minute NIR irradiation. The results were inconclusive as high cell viability values were obtained (≈ 200%), while cells were not confluent when observed under the microscope. The resazurin assay was not further used as it is unclear the influence that GBM are having on the method, that might lead to non-valid results in several assays (Figure A7, A8 and A9). Nevertheless, the results presented a tendency for A-431 cell death without lowering HFF-1 cell viability.

Live/dead assays were performed using HFF-1 and A-431 cells, to evaluate the cytotoxicity profiles of the produced hydrogels with and without 10 and 30-minute NIR irradiation.

Cells were incubated with p-rGOn/5-FU hydrogels (100 µg mL^{-1} p-rGOn, 0.25 µg mL^{-1} 5-FU), in the presence or absence of NIR irradiation (810 nm, 150 mWcm^{-2}, 10 min). Controls were made with DMEM, Carbopol 974P NF, Carbopol 974P NF/p-rGOn and Carbopol 974P NF/5-FU to assess the effect of each component. The results are presented as cell number and cell percentage. The values for live and dead cells are calculated by the Developer toolbox, as described before (Section 3.6.3.3.2), Hoechst 33342 stained nuclei allow determining the total

number of cells present, while Calcein stained cells are counted as live, and dead ones are stained by PI. As both cell lines are adherent, the cells that died from the treatment detach, and, after replacing the medium to apply the staining, these cells are removed from the well without being counted. Therefore, the cells considered by the software are the live and dying ones. This explains the high cell viability values present in the cell percentage results presented next. The cell number results allow a more correct analysis as it considers the cells removed during the staining, which were dead.

Regarding the cancer cells, after each timepoint, a decrease in the number of cells in the tested therapeutic conditions is observed when compared with the control (Figure A11, A12, 4.22, 4.23 and 4.24). After 24 h, the effect of the treatment was noticeable with a statistically significant ($p \leq 0.05$) lower number of cells in the non-irradiated Carbopol 974P NF/p-rGOn/5-FU condition (≈ 36% reduction), comparing with the control with cell culture medium only (Figure 4.22). However, the correspondent live/dead percentage showed that ≈ 99% of the cells were alive meaning that there was a reduction in the number of cells but the ones that remained in the well were alive. The NIR effect was only significant ($p \leq 0.05$) for Carbopol 974P NF/p-rGOn, which induced a 31% decrease in the number of cells without irradiation, while when irradiated a decrease of 65% in the cell number has been observed. After 48 h, a similar cell number reduction occurred in the irradiated Carbopol 974P NF/p-rGOn/5-FU (≈ 63%), without statistically significant differences being found comparing with the non-irradiated condition. Carbopol 974P NF/5-FU led to a statistically significant ($p \leq 0.05$) cell number decrease of 60% without irradiation, compared with the control, confirming that the anticancer drug increases its effect over time. The irradiated condition presented a lower number of cells (≈ 69%), however, not significantly different from the non-irradiated one, which could arise from a higher drug internalization, potentiated by an eventual cell membrane permeability increase after irradiation and local temperature increase. In opposite, irradiated Carbopol 974P NF/p-rGOn induced a lower cell number decrease (≈ 41%) at 48 h, when compared with the value obtained at 24 h, which might indicate that the treatment was not powerful enough to completely stop cell proliferation.

After 72 h, a statistically different ($p \leq 0.05$) number of cells has been identified between the non-irradiated Carbopol 974P NF/p-rGOn (≈ 46% reduction), Carbopol 974P NF/5-FU (≈ 80% reduction) and Carbopol 974P NF/p-rGOn/5-FU (≈ 77% reduction), while no significant differences were found when NIR irradiation is applied to those conditions. Also, the irradiated controls (cells in culture medium only, and Carbopol 974P NF only), haven´t shown any changes after the treatment. These results point out that the irradiation time might have been too low, as the photothermal effect is only identified in one case (Carbopol 974P NF/p-rGOn, 24 h). As expected, the anticancer drug increased its effect compared with the previous time points, being the treatment that results in higher cell death after 72 h. The chemo-phototherapeutic synergistic effect is also not observed, as the irradiated Carbopol 974P NF/5-FU results in a higher decrease in the number of cells (≈ 82%) than the irradiated Carbopol 974P NF/p-rGOn/5-FU (≈ 78% reduction). To address this problem, a higher irradiation time was tested and results presented next. Figure A10 and Figure 4.23 provide representative images from stained nuclei, to allow observation of the total number of cells present in each condition and Figure A11 and Figure 4.24 present Calcein and PI stained representative images.

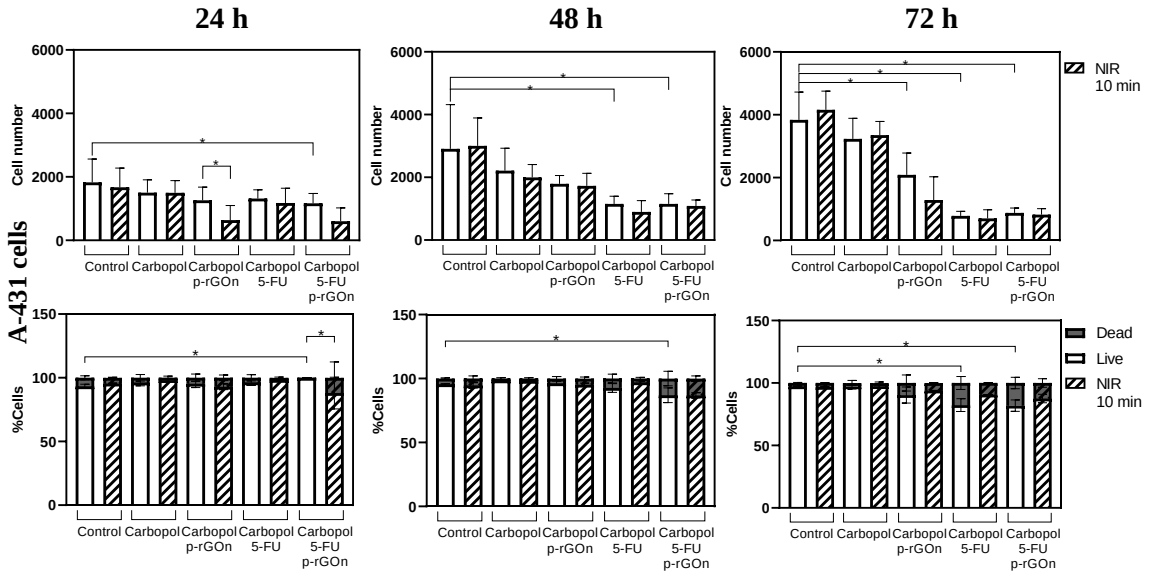

Figure 4.22 – Live/Dead assay. Carbopol 974P NF hydrogels (100 μg mL^{-1} of p-rGOn and 0.25 μg mL^{-1} of 5-FU) effect on A-431 cells, with and without a 10-minute NIR irradiation, after 24, 48 and 72 h, in cell number per 0.0225 cm^2 (upper row) and percentage of live/dead cells (lower row). Statistically significant differences are presented as * ($p < 0.05$) ($n = 3$).

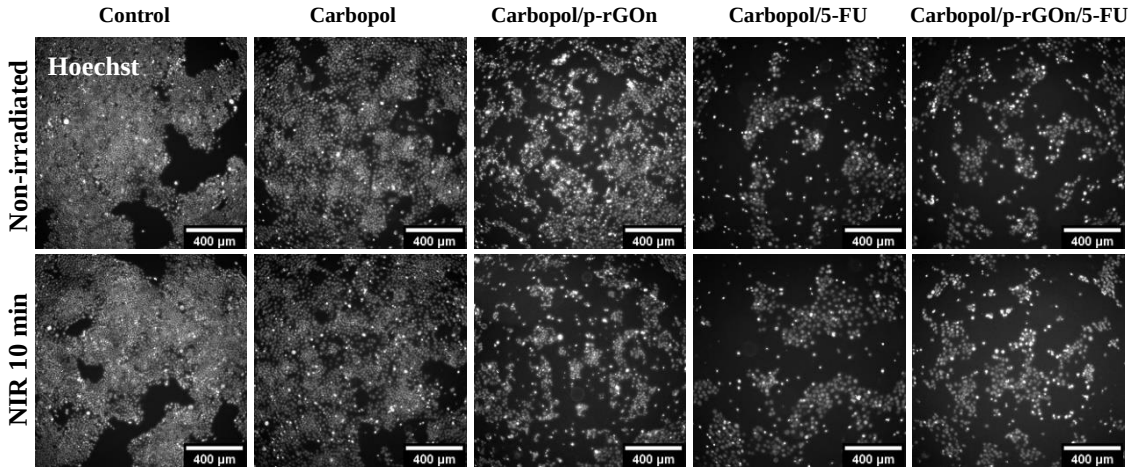

Figure 4.23 – Hoechst 33342 fluorescence representative images of A-431 nuclei incubated with selected hydrogels (100 μg mL^{-1} of p-rGOn and 0.25 μg mL^{-1} of 5-FU) with and without a 10-minute NIR irradiation, after 72 h. Scale bar represents 400 μm.

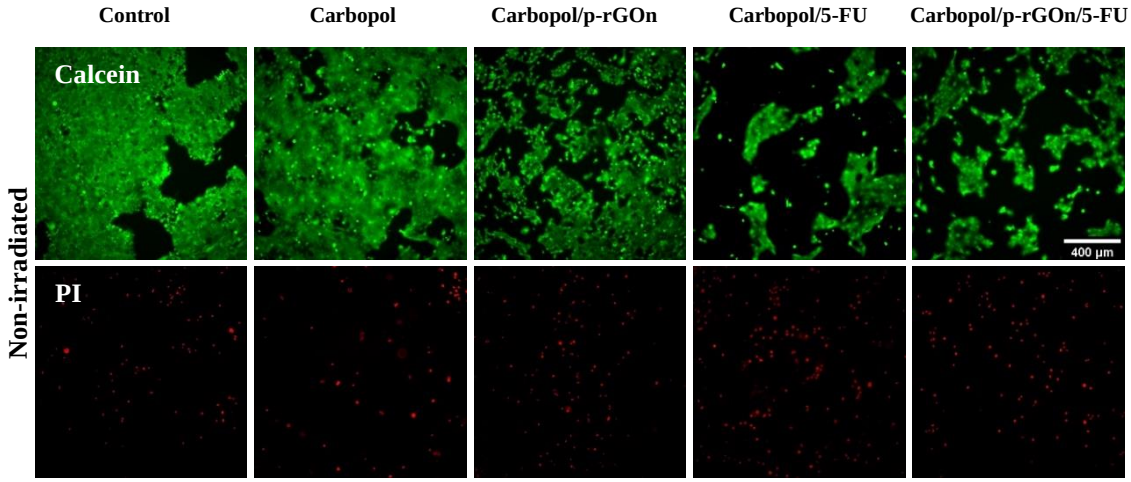

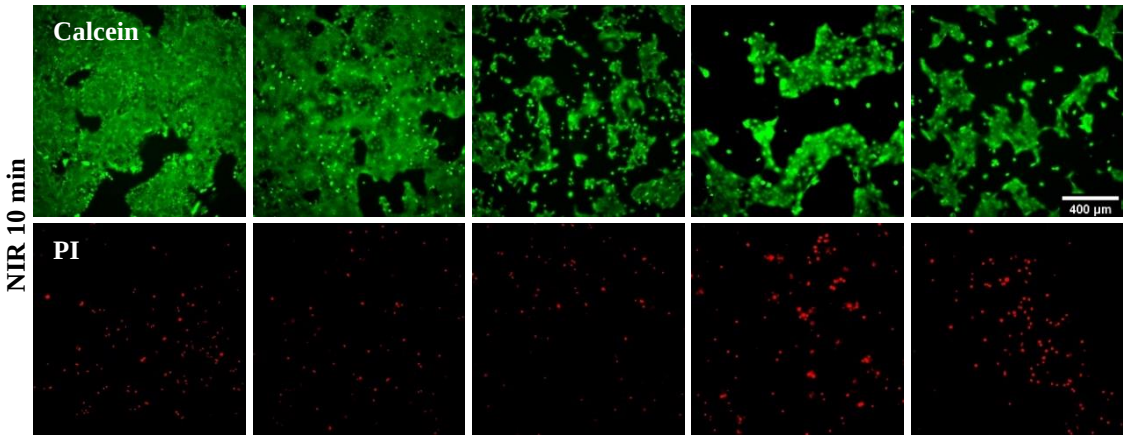

Figure 4.24 – Live/Dead assay. Representative images of A-431 cells incubated with selected hydrogels (100 µg mL^{-1} of p-rGOn and 0.25 µg mL^{-1} of 5-FU) with and without a 10-minute NIR irradiation, after 72 h. Live cells are stained with Calcein and dead cells with PI. Scale bar represents 400 µm.

For human skin fibroblasts (HFF-1), after each timepoint, the number of cells in the wells where the treatment applied, remained relatively close to the controls with cell culture medium only, and above the 70% toxicity limit (ISO 10993-5:2009(E)), which indicates that the treatment can be considered generally non-toxic when using the Carbopol 974P NF loaded with p-rGOn (100 µg mL^{-1}), 5-FU (0.25 µg mL^{-1}) or both, until a maximum irradiation time of 10 min (Figure A12, A13, 4.25, 4.26 and 4.27). Exceptionally, an unsuitable Hoechst 33342 staining at the non-irradiated Carbopol 974P NF/p-rGOn after 24 h (Figure 4.26), led to incorrect image segmentation. Nevertheless, the Calcein and PI stained cells were manually counted and the non-toxicity of the condition was confirmed (≈ 113% cell viability). This problem had occurred before due to graphene and it will be further discussed. Also, due to an experimental error, the non-irradiated Carbopol 974P NF/p-rGOn/5-FU condition were not obtained at 24 h, and there was no time to repeat the assays before the completion of the thesis. After 48 h, statistically significant differences ($p \leq 0.05$) were identified for both the non-irradiated (≈ 122% cell viability) and irradiated Carbopol 974P NF/p-rGOn (≈ 73% cell viability). After 72 h, similar cell number decreases can be observed in Figure 4.25, all above the toxicity limit. HFF-1 exposed to non-irradiated Carbopol 974P NF/p-rGOn presented cell viabilities of around ≈ 87%, while irradiated ones had values of 80%. A cell viability of ≈ 85% was obtained when using non-irradiated Carbopol 974P NF/5-FU, which decreased to 71% when irradiated. Cell viabilities of ≈ 91 and 78% were obtained for the non-irradiated and irradiated Carbopol 974P NF/p-rGOn/5-FU, respectively. Figure A12 and Figure 4.26 provide representative images from stained nuclei, to allow observation of the total number of cells present in each condition and Figure A13 and Figure 4.27 present Calcein and PI stained representative images.

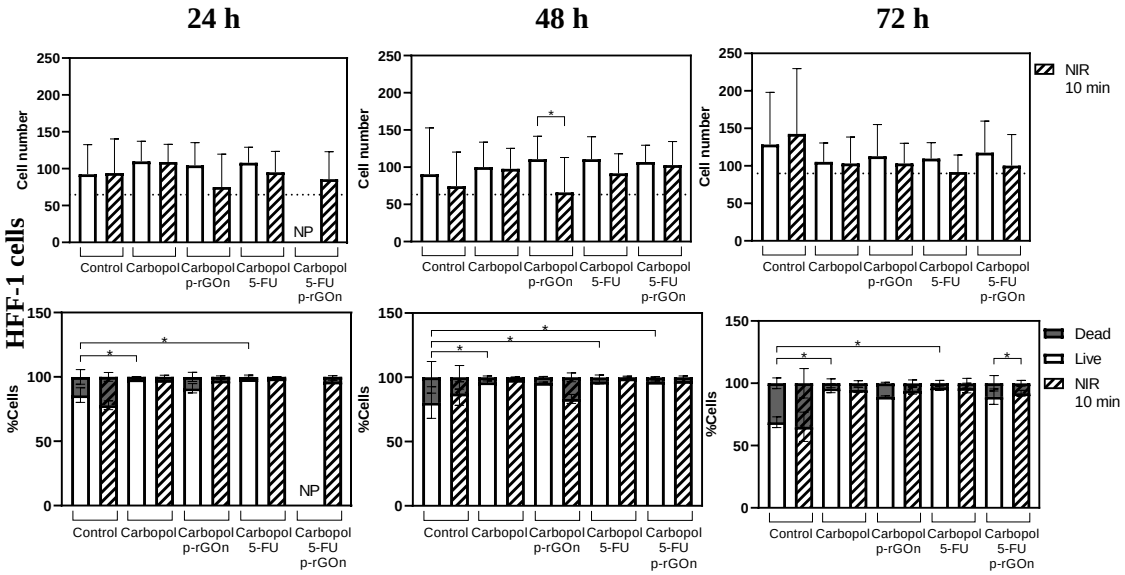

Figure 4.25 – Live/Dead assay. Carbopol 974P NF hydrogels (100 µg mL^{-1} of p-rGOn and 0.25 µg mL^{-1} of 5-FU) effect on HFF-1 cells, with and without a 10-minute NIR irradiation, after 24, 48 and 72 h, in cell number per 0.0225 cm^2 (upper row) and percentage of live/dead cells (lower row). Dashed line marks the toxicity limit (ISO 10993-5:2009(E)) Statistically significant differences are present as * (p < 0.05) (n = 3). NP - Not performed due to an experimental error.

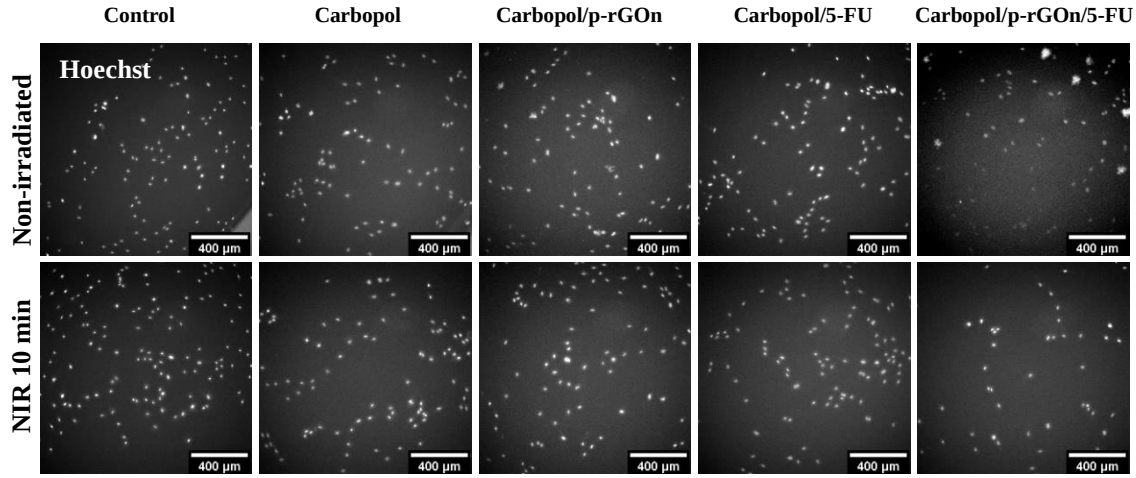

Figure 4.26 – Hoechst 33342 fluorescence representative images of HFF-1 nuclei incubated with selected hydrogels (100 µg mL^{-1} of p-rGOn and 0.25 µg mL^{-1} of 5-FU) with and without a 10-minute NIR irradiation, after 72 h. Scale bar represents 400 µm.

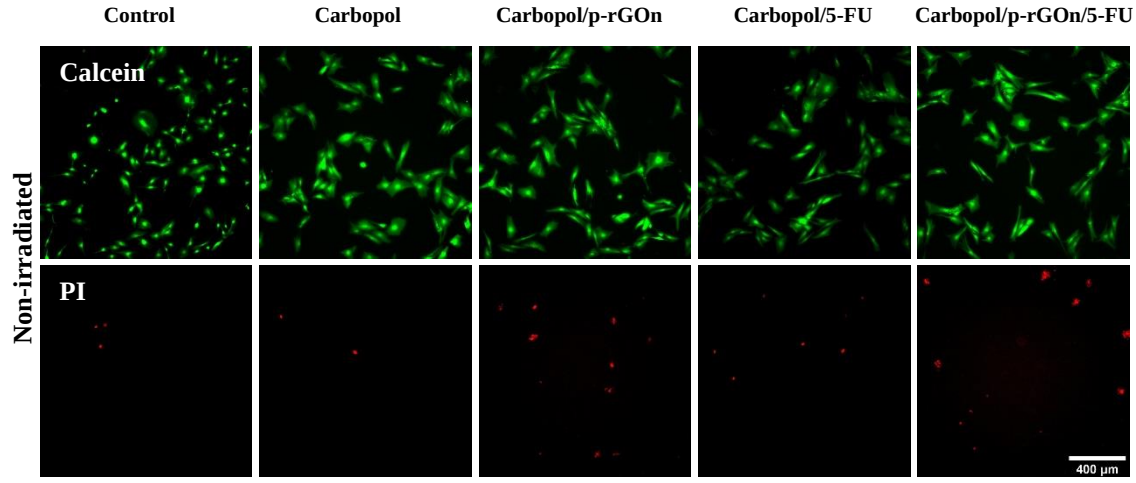

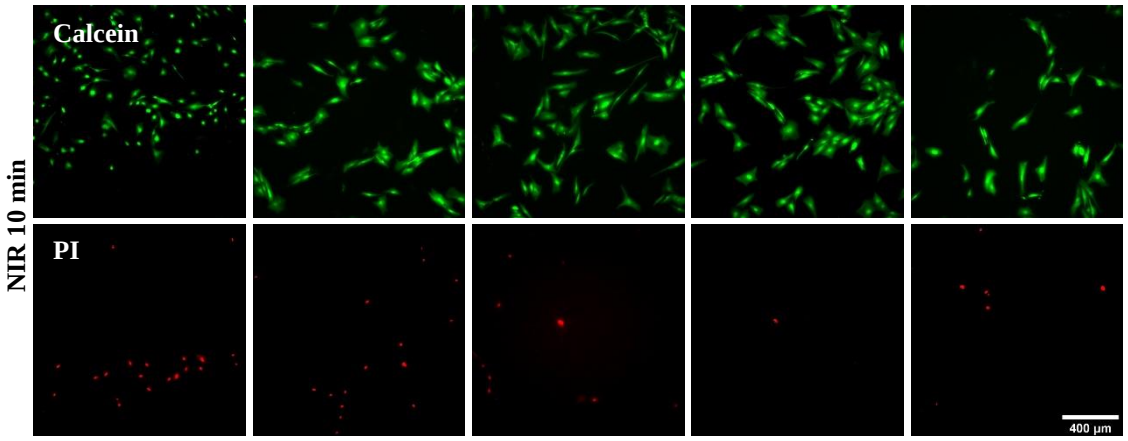

Figure 4.27 – Live/Dead assay. Representative images of HFF-1 cells incubated with selected hydrogels (100 µg mL^{-1} of p-rGOn and 0.25 µg mL^{-1} of 5-FU) with and without a 10-minute NIR irradiation, after 72 h. Live cells are stained with Calcein and dead cells with PI. Scale bar represents 400 µm.

Since an irradiation of 10 minutes was not enough to achieve an ideal PTT effect, NIR irradiation time has been increased to 30 min, seeking attaining higher cancer death values. As previously observed, the number of cells in the other tested conditions was decreased when compared with the control with cell culture medium only (Figure A14, A15, 4.28, 4.29 and 4.30). After 24 h, significant differences ($p \leq 0.05$) were obtained between the non-irradiated and the irradiated Carbopol 974P NF/p-rGOn. However, a decrease of ≈ 22% in the cell number was obtained in the irradiated Carbopol 974P NF/p-rGOn/5-FU, smaller than the one with the irradiated Carbopol 974P NF/p-rGOn (≈ 53%). Therefore a synergistic effect between 5-FU and p-rGOn under irradiation could not be observed. Furthermore, statistically significant difference between non-irradiated and irradiated Carbopol 974P NF/p-rGOn/5-FU have not been observed.

At 48 h, statistically significant differences ($p \leq 0.05$) were found when NIR irradiation was applied or not to both Carbopol 974P NF/p-rGOn and Carbopol 974P NF/5-FU/p-rGOn. Carbopol 974P NF/p-rGOn + NIR irradiation induced a 74% A-431 cell number reduction, presenting 21% less cells than when non-irradiated. While Carbopol 974P NF/5-FU/p-rGOn + NIR irradiation induced a 45% A-431 cell number reduction, presenting 34% less cells than when non-irradiated. After 72 h, the irradiated Carbopol 974P NF/p-rGOn led to a 86% A-431 cell number reduction, presenting 24% less cells than the non-irradiated condition, being the difference statistically significant ($p \leq 0.05$). Carbopol 974P NF/p-rGOn/5-FU with NIR irradiation originated a 90% cell number reduction, presenting 36% less cells than the non-irradiated ($p \leq 0.05$). Also, from the cells that remained in the wells, 80% were dead, highlighting the treatment efficiency, as the few cells that did not detached from the wells already are dead or dying. Statistically significant differences ($p \leq 0.05$) between the non-irradiated and irradiated p-rGOn hydrogels were identified, highlighting the PTT effect. Furthermore, the non-irradiated Carbopol 974P NF/5-FU and Carbopol 974P NF/p-rGOn/5-FU demonstrated cell number reductions of ≈ 80 and 72%, respectively. Images of the cells' nuclei after being exposed to the different treatments are presented in Figure A14 and 4.29 and live/dead cells in Figure A15 and 4.30. The low drug concentration of 0.25 µg mL^{-1} applied was powerful enough to cause extensive eradication (80% reduction without irradiation and 84% with irradiation) of A-431 cells, however, a statistically significant synergistic effect when combined with p-rGOn + NIR irradiation has not been identified.

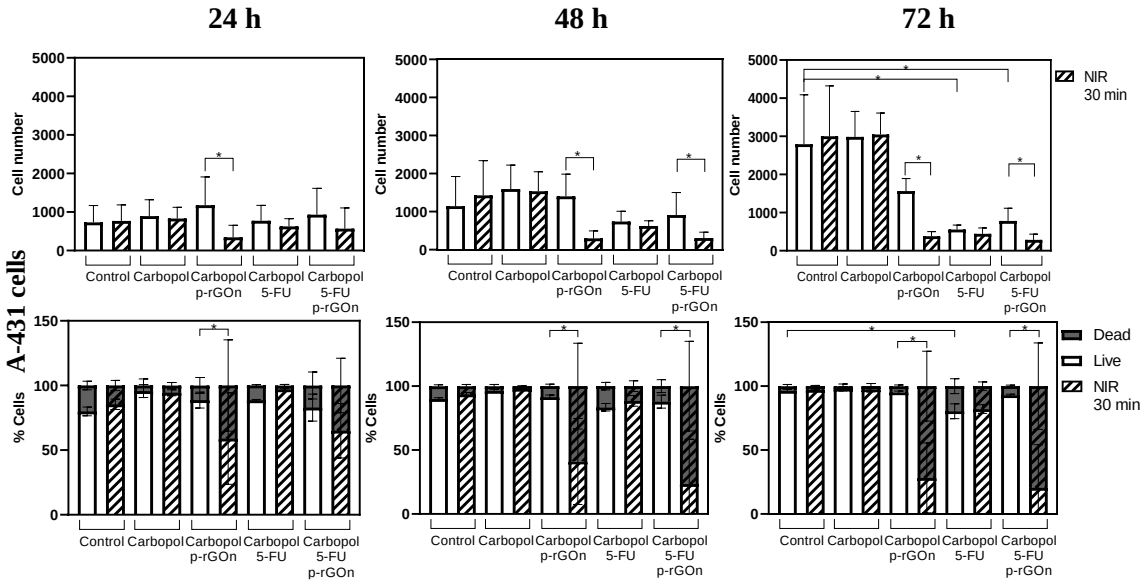

Figure 4.28 – Live/Dead assay. Carbopol 974P NF hydrogels (100 μg mL^{-1} of p-rGOn and 0.25 μg mL^{-1} of 5-FU) effect on A-431 cells, with and without a 30-minute NIR irradiation, after 24, 48 and 72 h, in cells number per 0.0225 cm^2 (upper row) and percentage of live/dead cells (lower row). Statistically significant differences are present as * ($p < 0.05$) ($n = 3$).

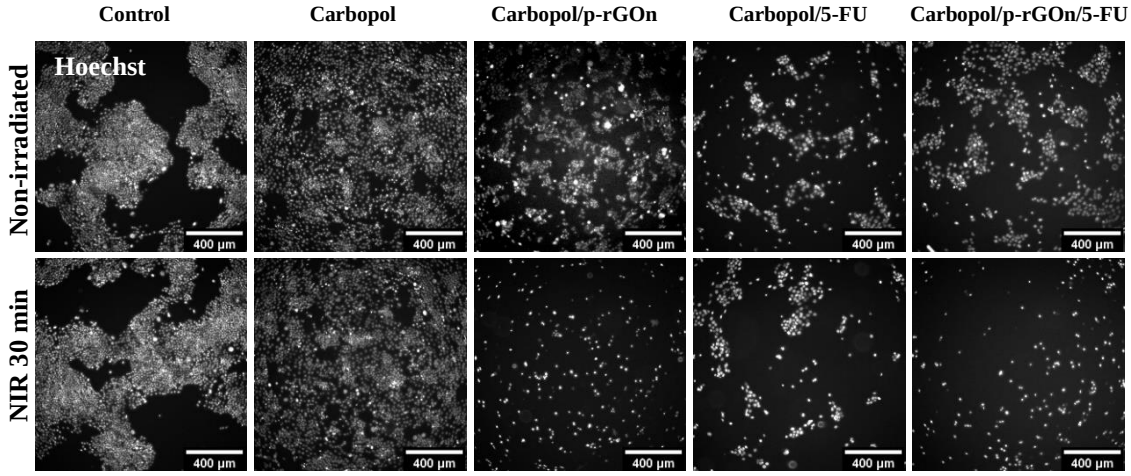

Figure 4.29 – Hoechst 33342 fluorescence representative images of A-431 nuclei incubated with selected hydrogels (100 μg mL^{-1} of p-rGOn and 0.25 μg mL^{-1} of 5-FU) with and without a 30-minute NIR irradiation, after 72 h. Scale bar represents 400 μm.

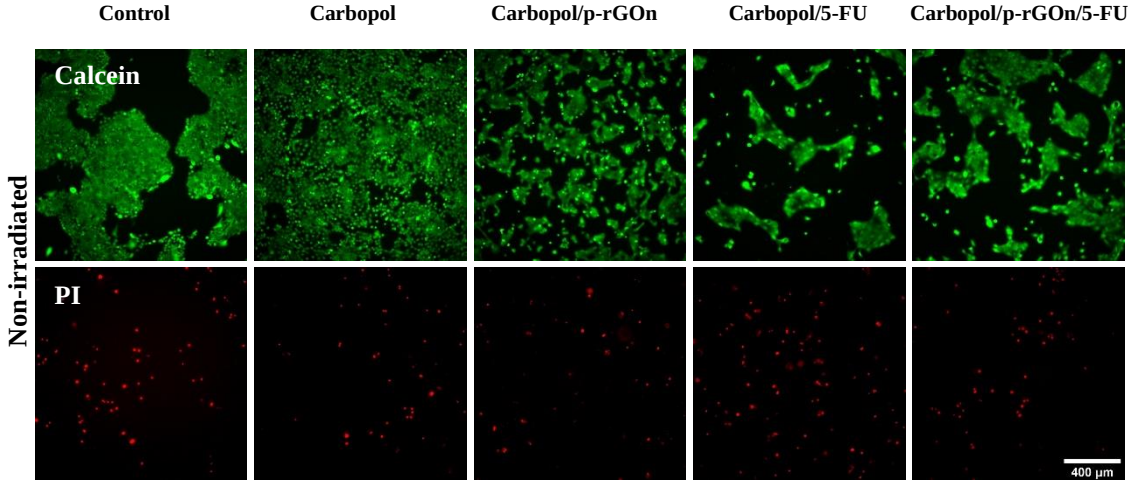

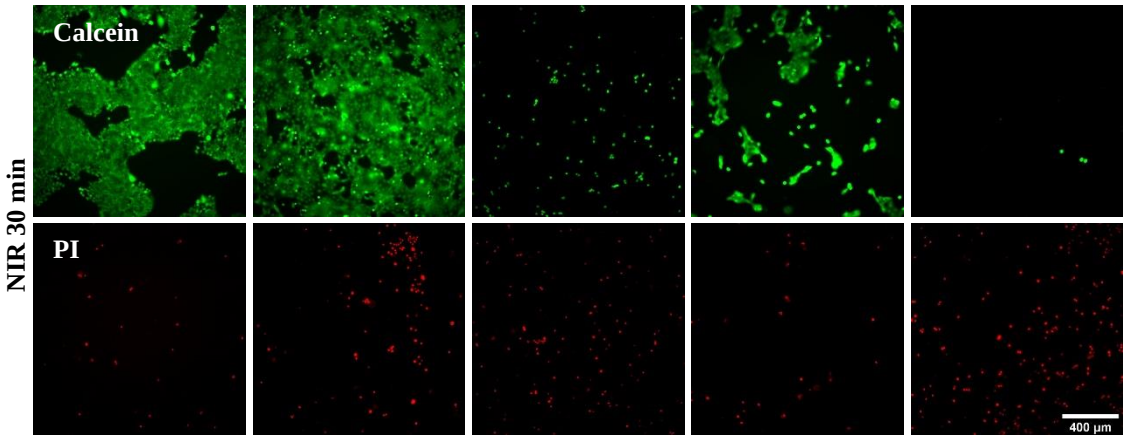

Figure 4.30 – Live/Dead assay. Representative images of HFF-1 cells incubated with selected hydrogels (100 µg mL^{-1} of p-rGOn and 0.25 µg mL^{-1} of 5-FU) with and without a 10-minute NIR irradiation, after 72 h. Live cells are stained with Calcein and dead cells with PI. Scale bar represents 400 µm.

Increasing the irradiation time led to almost complete A-431 cancer cells eradication, however human skin fibroblasts (HFF-1) were also killed in the process. After 24 and 48 h, statistically significant differences ($p \leq 0.05$) were obtained between HFF-1 exposed to non-irradiated and irradiated Carbopol 974P NF/p-rGOn and Carbopol 974P NF/p-rGOn/5-FU. After 24 h, cell number decreases of ≈ 73 and 79% were obtained for irradiated Carbopol 974P NF/p-rGOn and Carbopol 974P NF/p-rGOn/5-FU, respectively. At 48 h, for the same conditions in the same order, cell number reductions were of ≈ 72 and 85%. Also, the irradiated Carbopol 974P NF/5-FU had a cell number reduction of 45%, which might indicate cell membrane permeability increase after irradiation, which facilitates drug internalization. After 72 h, a cell number reduction of 80% was observed, indicating that the irradiation has been performed for too long and that selective effect was not achieved (Figure 4.31). Representative images of the cells' nuclei after being exposed to the different treatments are presented in Figure A 16 and 4.32 and live/dead cells in Figure A17 and 4.33.

Therefore, this cancer phototherapy treatment could only be used with careful placement of the formulations at the tumour site and with radiation focused on it, to minimize damages in healthy cells. Future work will focus on optimizing the irradiation doses needed to achieve a selective treatment, and achieve synergy between p-rGOn and 5-FU effects if possible. Different drugs will also be screened for joint action with PTT, and surface functionalization strategies will be explored.

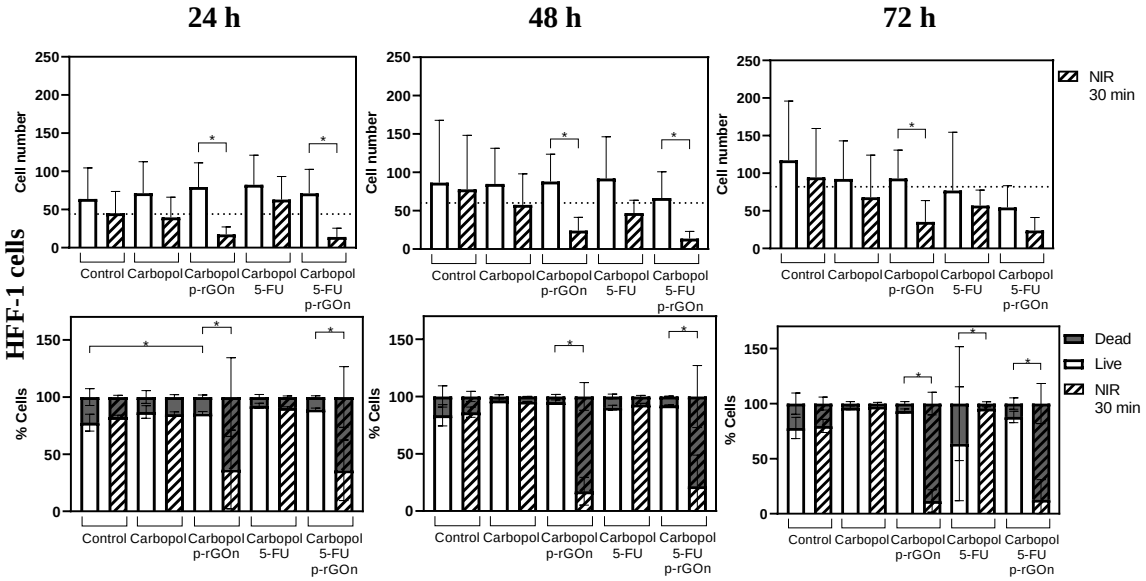

Figure 4.31 – Live/Dead assay. Carbopol 974P NF hydrogels (100 µg mL^{-1} of p-rGOn and 0.25 µg mL^{-1} of 5-FU) effect on HFF-1 cells, with and without a 30-minute NIR irradiation, after 24, 48 and 72 h, in cells number per 0.0225 cm^2 (upper row) and percentage of live/dead cells (lower row). Dashed line marks the toxicity limit (ISO 10993-5:2009(E)) Statistically significant differences are present as * ($p < 0.05$) ($n = 3$).

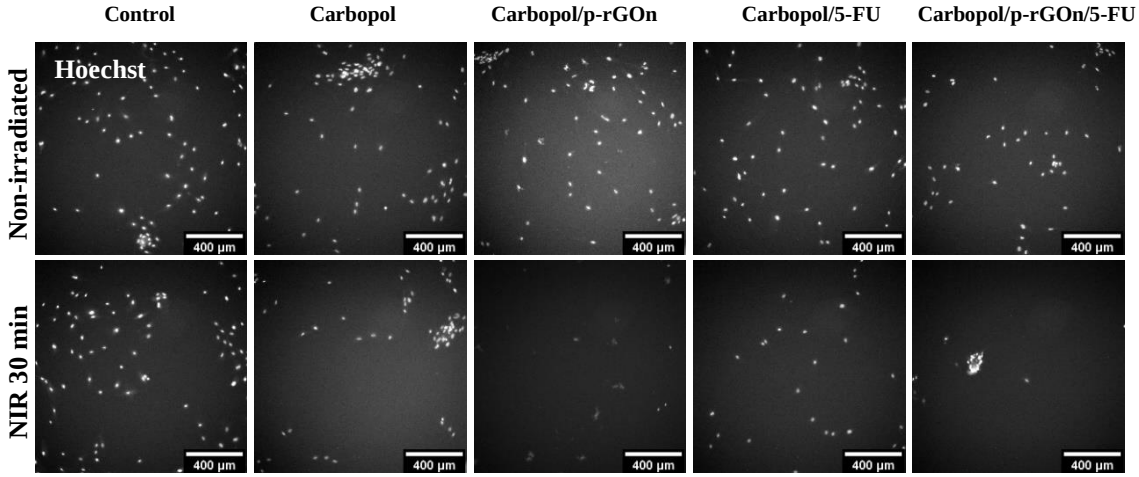

Figure 4.32 – Hoechst 33342 fluorescence representative images of HFF-1 nuclei incubated with selected hydrogels (100 µg mL^{-1} of p-rGOn and 0.25 µg mL^{-1} of 5-FU) with and without a 30-minute NIR irradiation, after 72 h. Scale bar represents 400 µm.

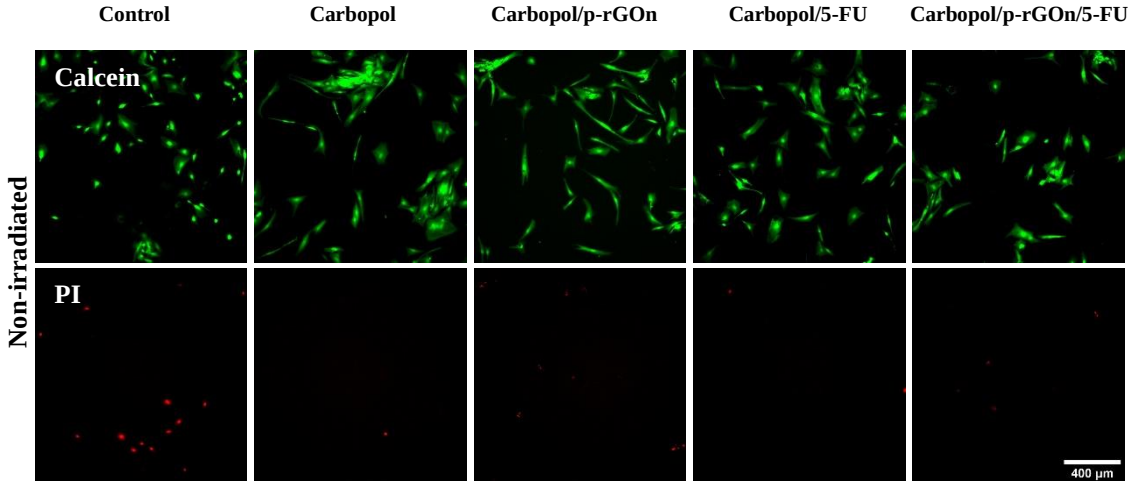

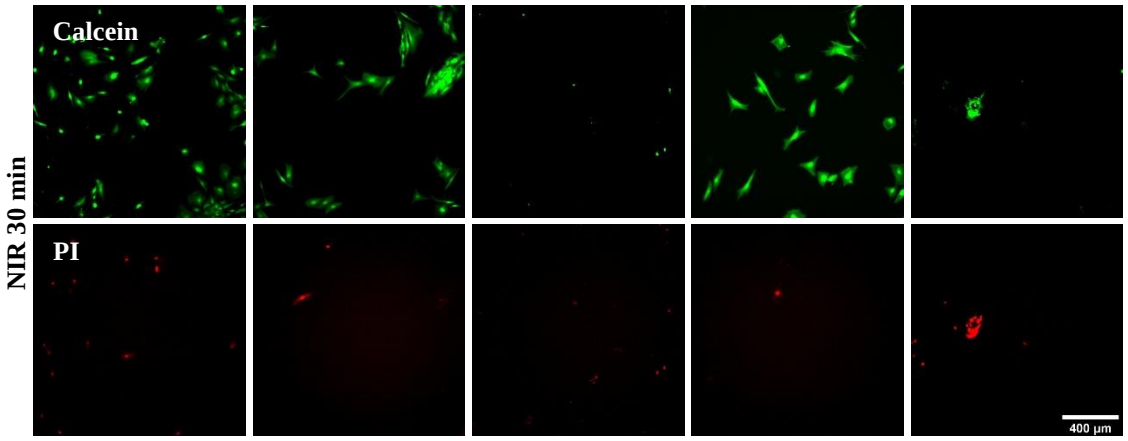

Figure 4.33 – Live/Dead assay. Representative images of HFF-1 cells incubated with selected hydrogels (100 µg mL^{-1} of p-rGOn and 0.25 µg mL^{-1} of 5-FU) with and without a 10-minute NIR irradiation, after 72 h. Live cells are stained with Calcein and dead cells with PI. Scale bar represents 400 µm.

4.4.6 - Cell ultrastructure and particle internalization

Cell ultrastructure and particle internalization were assessed by TEM. A-431 and HFF-1 cells were incubated with cell culture medium, non-irradiated and irradiated hydrogels (100 µg mL^{-1} of p-rGOn and 0.25 µg mL^{-1} of 5-FU) for 72 h. TEM images indicate the presence of particles (highlighted in white circles) in the conditions with the hydrogels but to obtain a confirmation other analysis would be required. Nevertheless, similar laminated-like structures have been identified in the literature as GBM [264].

For A-431 cells, the particles were not observed in non-irradiated conditions. In the 10-minute irradiated conditions, few materials were found in the cytoplasm with no organelle or membrane damage being observed. However, an increased amount of lipid droplets was noticed after incubation with the hydrogels. HFF-1 cells presented some organelle disruption after incubation with the hydrogels, while some particles were present in the cytoplasm and inside vesicles. Due to an experimental error, the controls of HFF-1 were not obtained and the images presented below are from previous works in the team. Furthermore, ribosomal accumulation was observed after incubation with the hydrogels, which might indicate a metabolism activation. Further studies are necessary to understand the obtained results (Figure 4.34).

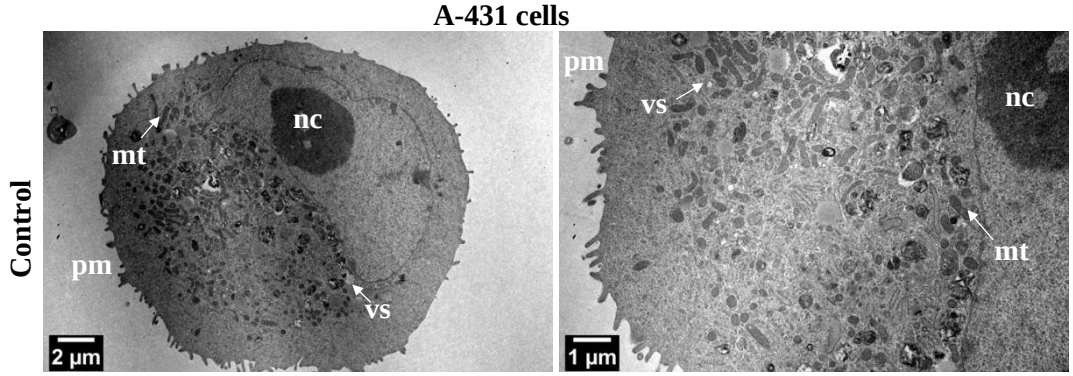

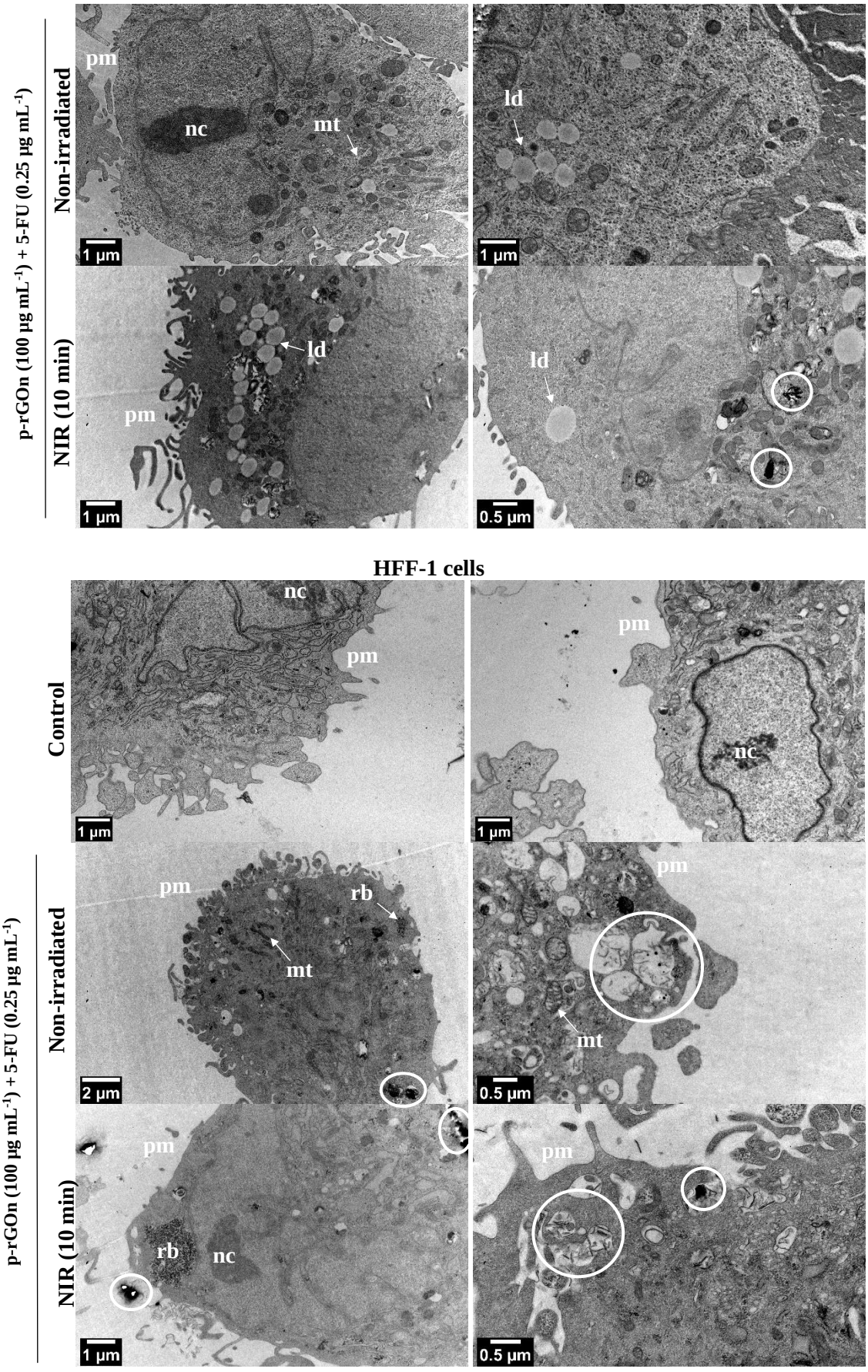

Figure 4.34 – Representative TEM images of A-431 and HFF-1 cells incubated with cell culture medium, non-irradiated and irradiated hydrogels (100 µg mL^{-1} of p-rGOn and 0.25 µg mL^{-1} of 5-FU) after 72 h. ld, lipid droplets; nc, nucleus; pm, plasma membrane; rb, ribosome; vs, vesicle; white circles indicate possible hydrogel presence.

Chapter 5

Discussion

The main goal of this dissertation was to develop graphene-based materials (GBM) and anticancer drug-containing hydrogels for combined chemotherapy and photothermal therapy of skin cancer, namely basal cell carcinoma. To achieve this purpose, objectives were set: production of GBM, namely nanographene oxide (GOn) and partially reduced nanographene oxide (p-rGOn); characterization of GBM; production and characterization of GBM/anticancer drug-containing Carbopol 974P NF hydrogels; evaluation of hydrogels biocompatibility and phototherapeutic effect under near-infrared radiation (NIR).

The most common way to obtain graphene oxide (GO) from graphite for biomedical applications is the modified Hummers method [253], that is solidly implemented in our laboratory and has been therefore used for this study [35]. Furthermore, to achieve high water stability, biocompatibility and skin penetration sizes below 200 nm are preferable, a recirculation system has been implemented to break down GO particles under high-power ultrasonication [265]. This method allows to obtain nanographene oxide (GOn) with sizes as low as 100 nm. Also, to achieve high NIR radiation absorption and temperatures of interest for phototherapy (> 45 °C), GOn has been subjected to UV photoreduction, with the goal to obtain a water-stable partially reduced nanographene oxide (p-rGOn).

Upon both GBM production, physicochemical characterization has been performed to evaluate their morphology, size, water and thermal stability, oxygen functionalities, NIR absorption and heat production. Transmission electron microscopy (TEM) revealed that most sheets were individualized with no extensive agglomeration being found, with particle size for both materials being below 200 nm, which was the target taking into consideration the desired applications. Usually, the removal of oxygen-containing functional groups leads to the formation of unstable aqueous dispersions, limiting their potential for biomedical applications. The oxygen-containing functional groups are responsible for the high water stability of GO, and their removal during reduction translates into lower water stability. Hence the partial reduction achieved in this work allowed the production of a GBM with fewer oxygen-containing functional groups, useful to increase NIR absorption properties while maintaining its water stability, necessary for biological applications. The produced p-rGOn presented good water stability, being water stable for 4 months and revealing a zeta potential value below -30 mV. Dispersions with zeta potential values higher than 30 or lower than -30 are considered to have high stability [255].

The presence (GOn) and partial removal (p-rGOn) of oxygen-containing functional groups were confirmed by Fourier transform infrared spectroscopy (FTIR). GOn spectra revealed a band between 3000 and 3600 cm^{-1}, reported to correspond to O-H stretching vibrations. This same band presented decreased intensity in the p-rGOn spectra, confirming the removal of some oxygen-containing functional groups. However, the presence of absorption bands in 1731, 1166, 1041 and 875 cm^{-1}, indicate the incomplete reduction as it corresponds to the presence of C=O and C-O bonds [35].

GBM thermal stability was tested by thermogravimetric analysis (TGA) where both materials revealed three main weight loss steps above 100 °C. Values below this limit have been attributed to water evaporation as reported in the literature [257, 266, 267]. The first step between 100-225 °C corresponds to the loss of reactive oxygen-containing groups such as carboxyl and epoxy [35, 257]. Both GBM presented an approximate weight loss of 25% which was expected once the p-rGOn is only partially reduced and still presents some oxygen-containing functional groups. The second loss (225-600 °C) is attributed to the partial combustion of the carbon skeleton and stable oxygen-containing functional groups like carbonyl and hydroxyl [35, 268]. In this step, GOn presented a higher weight loss (21.3%) than p-rGOn (15.8%), due to the presence of a higher amount of oxygen-containing functional groups. The partial removal of the thermolabile oxygen-containing functional groups resulted in p-rGOn increased thermal stability [267]. The third and final step (600-1000 °C) can be assigned to the complete combustion of the carbon skeleton. Values of 31.9% and 11.6% were obtained for GOn and p-rGOn, respectively. The increased total weight loss of 95.5% from GOn compared to the 68.9% from p-rGOn supports the partial reduction that allowed superior thermal stability.

Optical properties evaluation revealed that p-rGOn NIR absorption in the region of interest for phototherapy (750-850 nm) increased 4.4-fold, compared with GOn, once UV-reduction restored the aromatic structure partially [159]. Furthermore, a higher light to heat conversion ability was observed for p-rGOn after a 30-minute NIR irradiation (810 nm, 150 $mWcm^{-2}$), when compared with GOn. Phototherapeutic temperatures of 52 °C were obtained for p-rGOn, compared to the lower value (38 °C) achieved by GOn. While in the literature, most studies use high irradiance NIR lasers (< 3 Wcm^{-2}), which increase GBM temperatures above 50 °C, causing necrosis of the irradiated tissues unselectively [36, 166]. Herein the irradiation system we have developed is based on LEDs with lower irradiance (150 $mWcm^{-2}$) but still reaching temperatures within the mild PTT range (43-50 °C) sufficient to increase membrane permeation, facilitating GBM and anticancer drug internalization, to maximize treatment efficiency and selectivity. Due to p-rGOn presenting superior photothermal performance, it was selected for further assays.

5-FU is an anticancer drug commonly used for skin cancer treatment, however, high recurrence rates in the case of non-melanoma skin cancer can be observed, and high 5-FU doses can lead to toxicity [269]. One of the goals of this work was to combine the chemotherapeutic properties of this drug with phototherapy using p-rGOn, reducing 5-FU required doses, targeting a synergistic effect that would result in more effective and selective treatment, reducing associated toxicity and side effects. Guimarães *et al.* reported 50% A-431 cancer cell death and 40% 3T3-L1 fibroblasts cell death, after 72 h incubation with 12.5 µg mL^{-1} of 5-FU [270]. In the thesis work, higher A-431 cell death of 70% was obtained with a drug concentration of 10 µg mL^{-1}, and a lower human skin fibroblasts (HFF-1) cell death of ≈ 35% was obtained, using the same 5-FU concentration. The cytotoxic effect of this anticancer drug was assessed in HFF-1 and A-431 cells after 24, 48 and 72 h as it was observed in the literature that higher efficiency is obtained after 48 h [258, 259]. The drug was considered non-toxic for human skin fibroblasts in every concentration

tested (0.1-1000 μg mL^{-1}) after 24 and 48 h. Considering the toxicity limit (ISO 10993-5:2009(E)) a tendency for toxicity was observed after 5 μg mL^{-1} when cell viabilities below 70% were obtained after 72 h. In contrast, a low concentration of 0.1 μg mL^{-1} is enough to decreased skin cancer cells viability to 55%, after 72 h. These results might be explained by 5-FU's influence on DNA replication. After this assay, a concentration range from 0.1 to 1 μg mL^{-1} was selected as safe for the fibroblasts and toxic for the cancer cells.

The cytotoxic effect of p-rGOn was studied using HFF-1 cells incubated with increasing concentrations from 50 to 250 μg mL^{-1} and evaluated with the resazurin assay. High cell viability values were obtained (>≈ 150%) while a low confluence was observed in the wells of the cell culture plates by microscopy. Jiao *et al.* have reported graphene's influence with the reagents used in MTT or CCK-8 assays due to factors such as adsorption, optical properties or electron transfer. Furthermore, these authors have brought attention to the fact that this same influence can be present in other *in vitro* assays, as is the case of the resazurin assay or Hoechst staining [271]. Other reports of this influence have been made [272]. Nevertheless, a tendency for toxicity only after 250 μg mL^{-1} was identified in the present work based on the data obtained. Due to the difficulties in using the resazurin assay, the Live/Dead assay was adopted as a more reliable method, since it involves direct observation of the cells. p-rGOn concentrations of 50 and 100 μg mL^{-1} led to low HFF-1 cell death. GBM's influence was identified at the concentrations of 175 and 250 μg mL^{-1}, as cells labelled with Calcein were less visible and propidium iodide (PI) staining did not work. Nevertheless, a concentration of 100 μg mL^{-1} was chosen for further assays based on the resazurin and live/dead results. Liao *et al.* described no toxicity in human skin fibroblasts (BJ) when exposed to rGO concentrations up to 200 μg mL^{-1}, after 24 h of incubation [272].

5-FU potential for selective anticancer therapy after incorporation in Carbopol 974P NF hydrogels was assessed using HFF-1 and A-431 cell lines. The previously selected range between 0.1 and 1 μg mL^{-1} was used, with a tendency for toxicity in the HFF-1 cell line being observed above 1 μg mL^{-1}, which led us to set the maximum concentration to be used in the formulations in 0.5 μg mL^{-1}. Against A-431 cancer cells, a concentration of 0.25 μg mL^{-1} was enough to cause approximately 30% cell death, being that value selected for further assays with the hydrogels. No similar studies have been found in the literature with Carbopol 974P NF/5-FU hydrogels.

p-rGOn photothermal effect after incorporated in the Carbopol 974P NF hydrogels was also tested at the selected concentration of 100 μg mL^{-1}, using an A-431 cell line. After incubation with Carbopol 974P NF/p-rGOn, an irradiation time of 10 minutes was tested with a LED-based system (810 nm, 150 $mWcm^{-2}$), leading to approximately 15% cancer cell death. The previously mentioned conditions were selected for further assays, combining both p-rGOn and 5-FU, to assure biocompatibility and hoping for a synergistic effect.

HFF-1 and A-431 cells were exposed to Carbopol 974P NF/p-rGOn/5-FU hydrogels (p-rGOn 100 μg, mL^{-1}, 5-FU 0.25 μg mL^{-1}) with or without a 10-minute NIR irradiation. Despite p-rGOn slightly influencing the resazurin assay, as high cell viability values were obtained (>≈ 150%) a tendency for biocompatibility in the normal cell line and phototherapeutic effect in the cancer cell line was observed (≈ 55% cell death). To confirm these results, the Live/Dead assay was performed in the same conditions. This approach has been used before by Rehman *et al.* to assess rGO hydrogels toxicity in endothelial, keratinocyte and fibroblast cells [273]. In the thesis work, results are presented as total cell number per condition and live/dead cell percentages, as most of the dead cells detached during the staining procedure, therefore not being counted as dead in the results of live/death percentage. For that reason, both results of total cell number per condition

and live/death cell percentages need to be evaluated together to withdraw conclusions on the biocompatibility and effectiveness of the treatments.

After a 10-minute NIR irradiation, the number of A-431 cells decreased in the tested therapeutic conditions after each evaluated time point (24, 48 and 72 h) indicating that the treatment is either killing them or inhibiting their growth. After 72 h, the irradiated Carbopol 974P NF/p-rGOn/5-FU had a cell number reduction of about 78%, compared with the control. Nevertheless, the irradiated Carbopol 974P NF/p-rGOn only presented a 66% cell number reduction, indicating that the PTT effect from p-rGOn is not the main effect when both PTT and chemotherapy are combined. This was further confirmed after the irradiated Carbopol 974P NF/5-FU presenting a superior cell number reduction of 82%. Therefore, a synergistic effect was not observed. In order to increase the PTT effect, a longer irradiation time of 30 min was tested, using the same irradiance of 150 $mWcm^{-2}$. Such an increase led to a 86% A-431 cell number reduction for irradiated Carbopol 974P NF/p-rGOn. Irradiated Carbopol 974P NF/5-FU caused a cell number reduction of 84%. Finally, irradiated Carbopol 974P NF/p-rGOn/5-FU led to a 90% cell number reduction. Furthermore, the assays with HFF-1 cells demonstrated that 30 minutes was a too high irradiation time to assure normal skin cells viability, as the irradiated Carbopol 974P NF/p-rGOn/5-FU led to a 80% cell number reduction, after 72 h. Hence the presented approach could only be employed with a selective application of the hydrogels at the tumour site and directed irradiation to prevent side effects in the healthy surrounding tissues. No study was found in the literature using Carbopol 974P NF/rGO/5-FU hydrogels for combined PTT and chemotherapy but some similar strategies have been explored. Zhou *et al.* applied a doxorubicin-loaded SWNT hydrogel for gastric cancer chemo-PTT. The hydrogel presented no toxicity against a BGC-823 gastric cancer cell line, but induced cell death after being irradiated with a NIR laser (976 nm, 200 $mWcm^{-2}$) for 3 minutes (≈ 30%) [274]. Zhu *et al.* prepared a functionalized GO hydrogel loaded with the anticancer drug docetaxel for combined chemotherapy with PTT. The hydrogel resulted in an inhibition rate of over 80% of breast cancer cells (MCF-7) [275]. Yang *et al.* studied 5-FU/rGO/*Brassica chinensis* extract hydrogels for combined chemotherapy, PTT and PDT. After 5 minutes of NIR laser irradiation (808 nm, 1 Wcm^{-2}), the hydrogel originated approximately 60% cell death of a cervical cancer cell line (HeLa) with low toxicity (80% cell viability) to a normal cell line (Chinese hamster ovary cells) [276]. Chang *et al.* combined spinach extract, rGO, gold nanocages and 5-FU in a hybrid hydrogel for multimodal cancer therapy. After a 10-minute NIR laser irradiation (660 nm, 200 $mWcm^{-2}$) and a 48 h incubation with the hydrogels, HeLa cell viability decreased to 1.2% while CHO cell viability remained above 50% [23].

Despite several studies have explored GBM different technical and biomedical applications, not much effort has been done in understanding their biological interaction or toxicity. Some proposed mechanisms include cell membrane damage, mitochondrial activity loss, oxidative stress and DNA damage, ultimately resulting in cell death through apoptosis and/or necrosis [264]. In this work, after 72 h incubation with the selected hydrogels, A-431 cells demonstrated a higher lipid production, while HFF-1 cells showed a ribosome accumulation, which was not present in the controls. However, no studies were found with the same outcomes. Liao *et al.* reported GBM as disruptors of the plasma membrane of erythrocytes [272]. In opposite, Chang *et al.* did not observe significant side adverse from GBM on the plasma membrane integrity of human lung cell line A459 [277].

Finally, there is still much to explore using the Carbopol 974P NF/p-rGOn/5-FU hydrogels. The present work demonstrates their potential for PTT but a selective treatment and a synergetic

effect with chemotherapy is not yet observable. Future work perspectives are presented in the conclusions.

Chapter 5

Conclusions

The present dissertation focuses on the development of Carbopol 974P NF/p-rGOn/5-FU hydrogels for combined photothermal therapy and chemotherapy of skin cancer. Currently, available therapies effectiveness and safety are not ideal, therefore new strategies are required to offer more selective and effective treatments to patients, such as phototherapy.

The state-of-the-art review shows that CNM have great potential to be used in cancer phototherapy. PDT, PTT, and combined PDT/PTT studies have revealed two major CNM groups. The first comprises fullerenes, CD and GQD, with excellent PS activity through ROS generation but poor NIR absorption if unmodified. These materials have been increasingly explored to bypass the need for using photoactive agents. A second group includes CNT, CNH and GBM, which exhibit poor PDT performance if unmodified, but hold strong potential for PTT through their intrinsic NIR absorption capability and consequent local heat generation for cancer thermal ablation. These CNM are often combined with PS agents in PDT therapies. In the case of PTT, GBM have been the most extensively studied CNM in the literature. In the future, these materials are expected to play significant roles in cancer phototherapy due to efficient outcomes already presented in the literature. However, there are still some biocompatibility and safety challenges to be addressed. Among the discussed nanomaterials, GBM have been selected due to their unique characteristics such as large surface area and increased NIR absorption that makes them ideal platforms for photothermal therapy. Overall, the variable experimental settings (CNM and drug/photosensitizer (PS) concentration, incubation times and irradiation times) and, most often, the poor methodological description found in the literature hinder the reproducibility of the studies and make comparisons quite difficult. The state-of-the-art review performed sets a call for attention toward future studies to include careful and detailed experimental reports, enabling a better understanding of the role of CNM and their potential translation to clinics.

GOn was produced using the modified Hummers method (MHM), followed by recirculation through a custom-built high-power ultrasonication probe, while p-rGOn was partially photo-reduced by UV irradiation. Physical characterization by TEM and Zetasizer revealed that graphene sheets with nanometric sizes were achieved, ideal for biomedical applications. Particle size measured by TEM image analysis was 107.0 ± 62.0 and 168.8 ± 149.0 nm for GOn and p-rGOn, respectively. Both materials presented very good water stability for at least 4 months, having zeta potential values below -30 mV. Typical oxygen-containing functional groups were

identified in GO and the intensity of their bands decreased after UV reduction. Similarly, TGA revealed weight losses of 95.5% in GOn correspondent to oxygen-functionalities, which were lower in p-rGOn (68.9%), further confirming that an effective partial reduction took place. UV-Vis spectroscopy demonstrated that p-rGOn presented a 4.4 fold NIR (810 nm) absorption increase, compared with GOn. NIR irradiation assays (810 nm, 150 $mWcm^{-2}$, 30 min) revealed that p-rGOn presented a higher light to heat conversion, within temperatures of interest for phototherapy (> 50 °C), while GOn only achieved a maximum temperature of ≈ 38 °C when irradiated. After identification of p-rGOn increased photoproperties, and previous confirmation of its water stability, this material was selected for further assays envisioning the desired phototherapeutic application. The achievement of a material with such properties constitutes a complete novelty. The new GBM, p-rGOn, was further studied envisioning incorporation in a Carbopol 974P NF hydrogel together with 5-FU, to assess a potential combined PTT and chemotherapeutic effect.

Regarding the biological assays, first, 5-FU was incubated with human skin fibroblasts (HFF-1) to select a safe range that could be used in pharmaceutical formulations. Concentrations between 0.1 and 1 μg mL^{-1} were considered non-toxic after an exposure time of 72 h (> 70% cell viability, ISO 10993-5:2009(E)). Similarly, 5-FU concentrations that could induce cancer cell death were studied. It has been observed that a concentration of 0.1 μg mL^{-1} was enough to lead to 45% A-431 cancer cells death, after 72 h of incubation.

The biocompatibility of p-rGOn was also evaluated envisioning assuring treatment selectivity. Concentrations below 100 μg mL^{-1} were considered non-toxic to HFF-1 cells after 72 h of incubation. 5-FU was then incorporated in a Carbopol 974P NF hydrogel and incubated with the same cells in the same concentration range, to assess its efficacy when included in the hydrogel. The maximum non-toxic concentration was identified to be 0.5 μg mL^{-1}. Regarding anti-cancer efficacy, a concentration of 0.25 μg mL^{-1} was found to be sufficient to kill 30% of A-431 cells after 72 h.

After ideal p-rGOn (100 μg mL^{-1}) and 5-FU (0.25 μg mL^{-1}) concentrations for incorporation in the Carbopol 974P NF being selected, both HFF-1 and A-431 cells were exposed to NIR irradiation (810 nm, 150 $mWcm^{-2}$, 10 min) in presence of Carbopol 974P NF/p-rGOn/5-FU hydrogels. It has been observed that after 72 h, A-431 cell number reductions of about 78% were achieved. However, without irradiation, similar values were obtained. Moreover, no synergistic effect was observed between 5-FU and p-rGOn. However, all conditions tested were non-toxic for HFF-1 cells.

Hence, a higher irradiation time of 30 minutes was tested, which resulted in almost complete eradication of the cancer cells (90%) after incubation for 72 h with Carbopol 974P NF/p-rGOn/5-FU. However, the increased exposure to irradiation also caused a reduction of 80% on HFF-1 cell number. Therefore, this cancer phototherapy treatment could only be used with careful placement of the formulations at the tumour site and with NIR irradiation focused on it, to avoid damages in healthy cells.

Future work will focus on optimizing the irradiation doses needed to achieve a selective treatment, and achieve synergy between p-rGOn and 5-FU effects if possible. Different drugs will also be screened for joint action with PTT, and surface functionalization strategies will be explored. Nevertheless, this dissertation breaks ground for the development of GBM/anticancer drugs-based selective phototherapy of cancer.

Appendix A

Supplementary material for Chapter 4

In this Appendix, a supplementary figure with GBM particle size distribution (Figure A1) is presented. Regarding biological studies, inconclusive p-rGOn cytotoxicity assays with HFF-1 are presented in Figure A2, as well as the respective microscopy images in Figure A3. 5-FU hydrogels cytotoxicity assays results, after incubation with HFF-1 cells are shown in Figure A4. p-rGOn/5-FU hydrogels effect, with and without 10-minute irradiation are presented in Figure A5. Figure A6 and A7 present the respective microscopy images. Results from the live/dead assay with HFF-1 incubated with p-rGOn, at 24 and 48 h are presented in Figure A8. Figure A9 to Figure A1 present fluorescence images of the live/dead assay, where cells were incubated with p-rGOn/5-FU hydrogels, with or without a 10 or 30-minute irradiation, at 24 and 48 h.

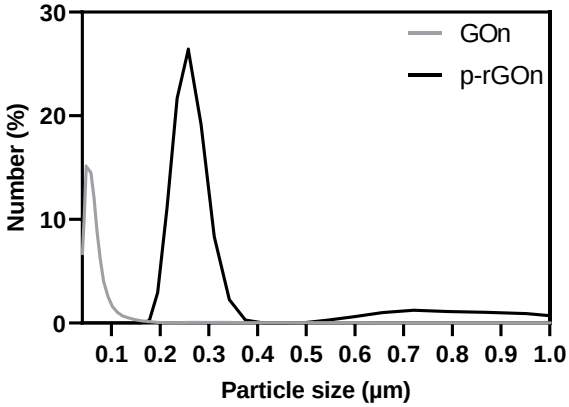

Figure A1 – Particle size distribution of GOn and p-rGOn aqueous dispersions at a concentration of 500 µg mL^{-1} in number (%), determined by DLS with Coulter equipment.

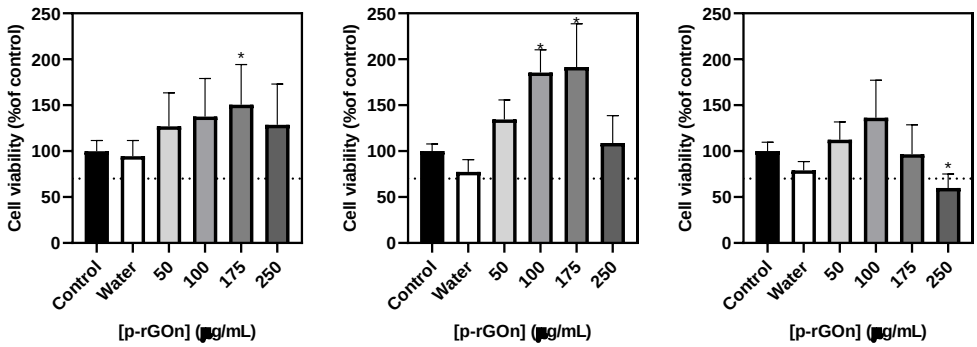

Figure A2 – p-rGOn cytotoxicity in HFF-1 cells after 24, 48 and 72 h (n = 17). Dashed line marks the toxicity limit (ISO 10993-5:2009(E)). Statistically significant differences are present as * ($p < 0.05$).

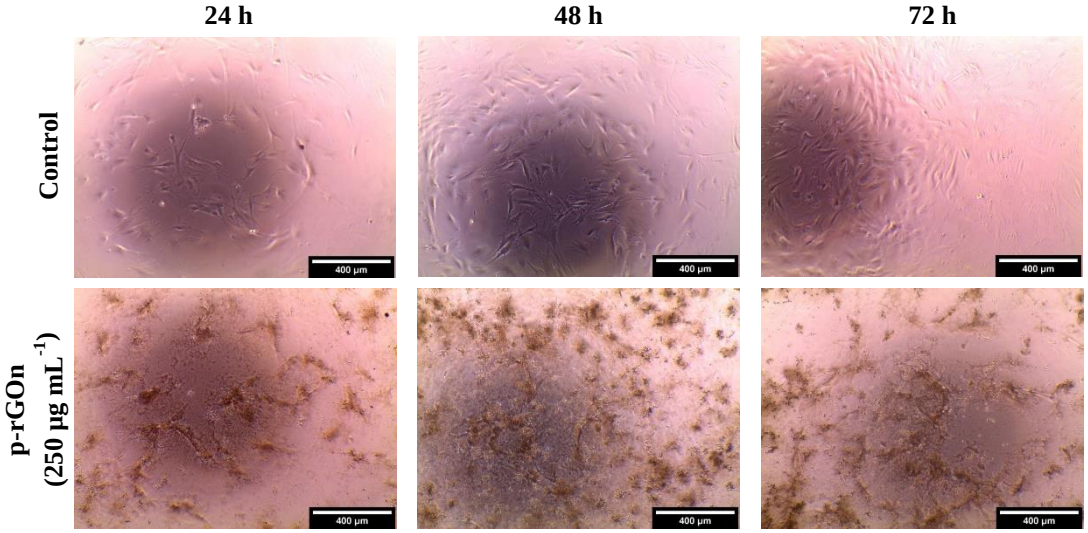

Figure A3 – Microscopy images of human foreskin fibroblasts (HFF-1) incubated with p-rGOn for 24, 48 and 72 h at the highest concentration studied. Controls correspond to cells incubated in complete DMEM without the addition of the GBM. Scale bar represents 400 µm.

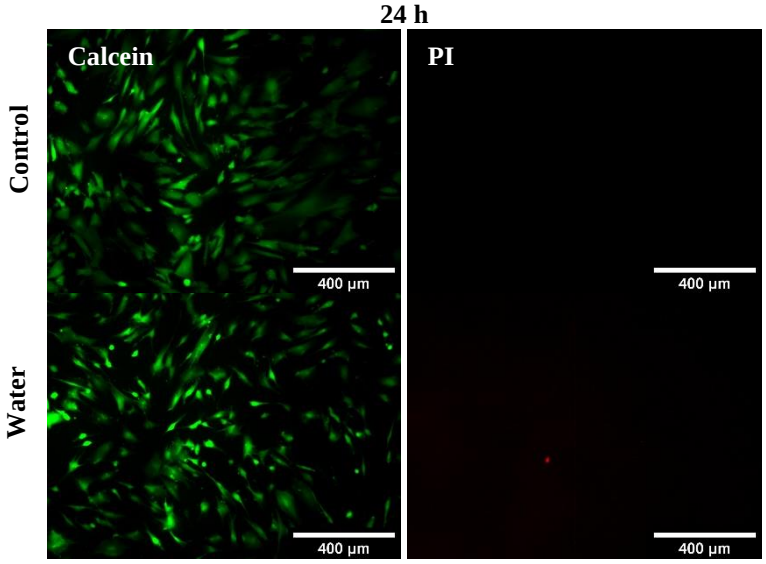

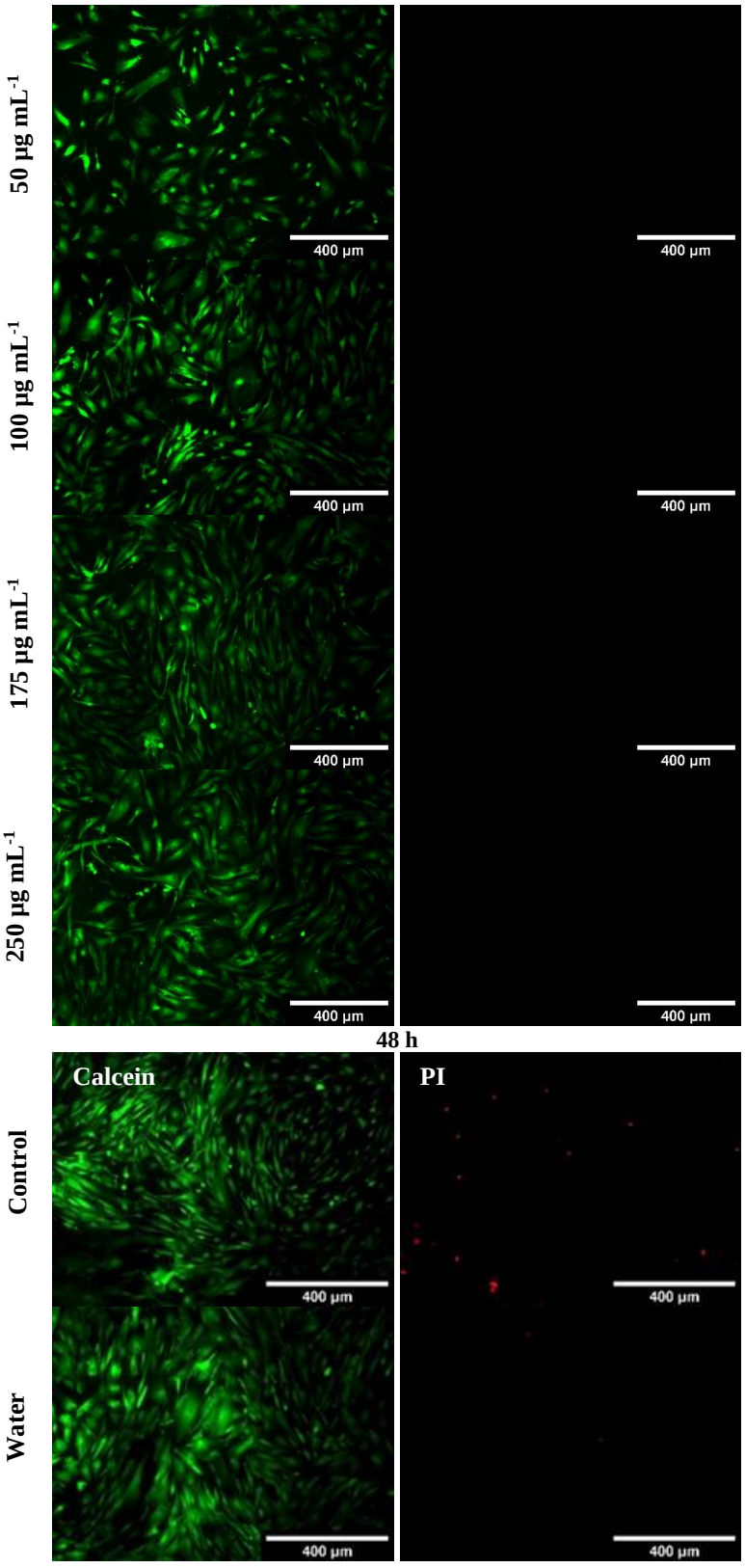
50 µg mL-1
100 µg mL-1
175 µg mL-1
250 µg mL-1
400 µm
48 h
Calcein
PI
Control
Water

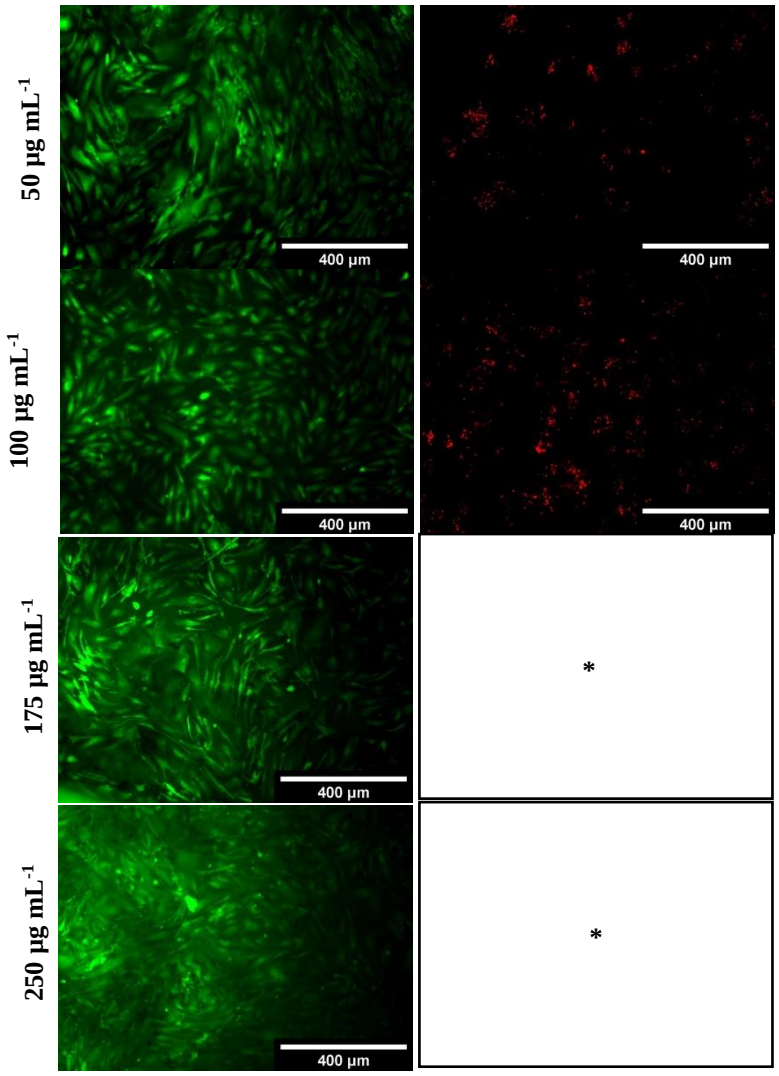

Figure A4 – Live/dead staining of HFF-1 cells incubated with increasing p-rGOn concentrations (50-250 µg mL^{-1}) for 48 h. Controls correspond to cells incubated in complete DMEM without the addition of the GBM. Live cells metabolize Calcein (green) and dead cells were stained with PI (red). Scale bar represents 400 µm. * Not possible to obtain an image due to interference with the signal.

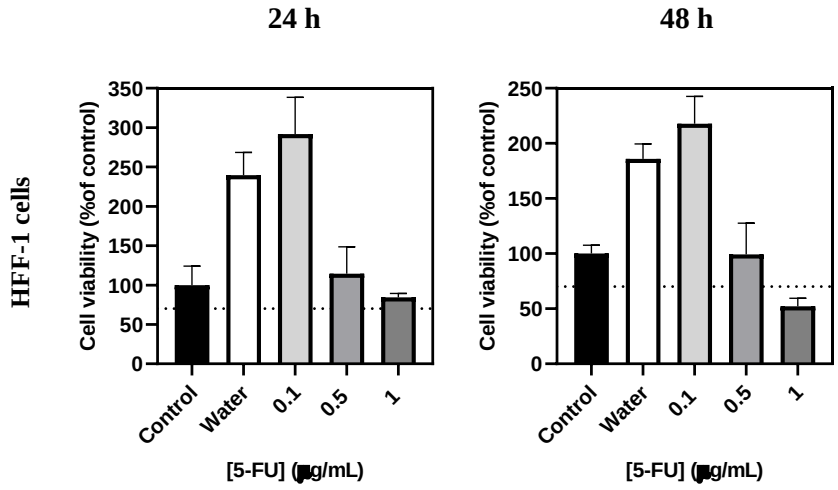

Figure A5 – 5-FU hydrogels cytotoxicity in HFF-1 cells after 24 and 48 h (*n* = 3). Dashed line marks the toxicity limit (ISO 10993-5:2009(E)).

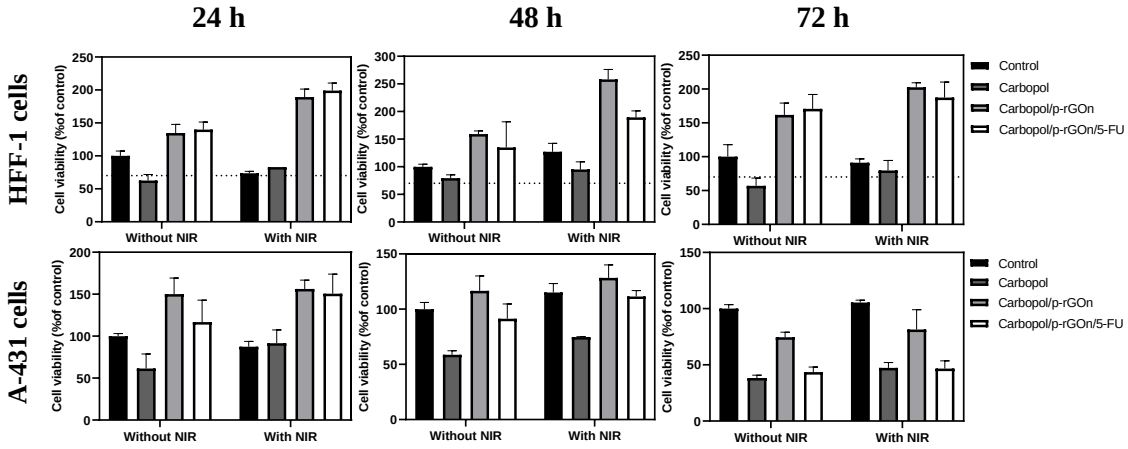

Figure A6 – p-rGOn/5-FU hydrogels cytotoxicity after 10 minutes of NIR irradiation in HFF-1 (upper row) and A-431 (lower row) cells after 24, 48 and 72 h (n = 3). Dashed line marks the toxicity limit (ISO 10993-5:2009(E)).

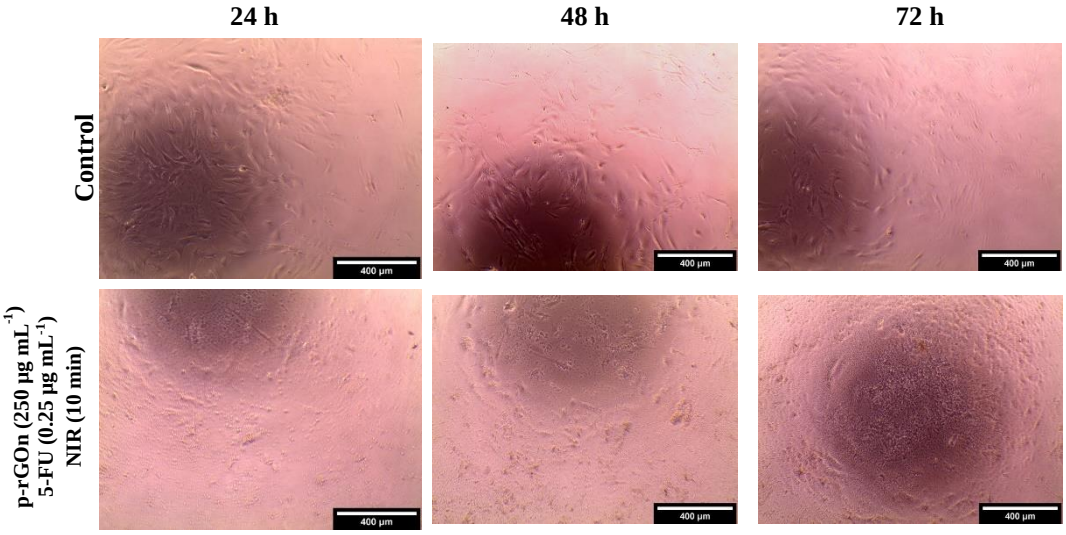

Figure A7 – Microscopy images of human foreskin fibroblasts (HFF-1) incubated with selected hydrogels for 24, 48 and 72 h with 10 minutes of NIR irradiation. Controls correspond to cells incubated in complete DMEM without the addition of the hydrogels. Scale bar represents 400 µm.

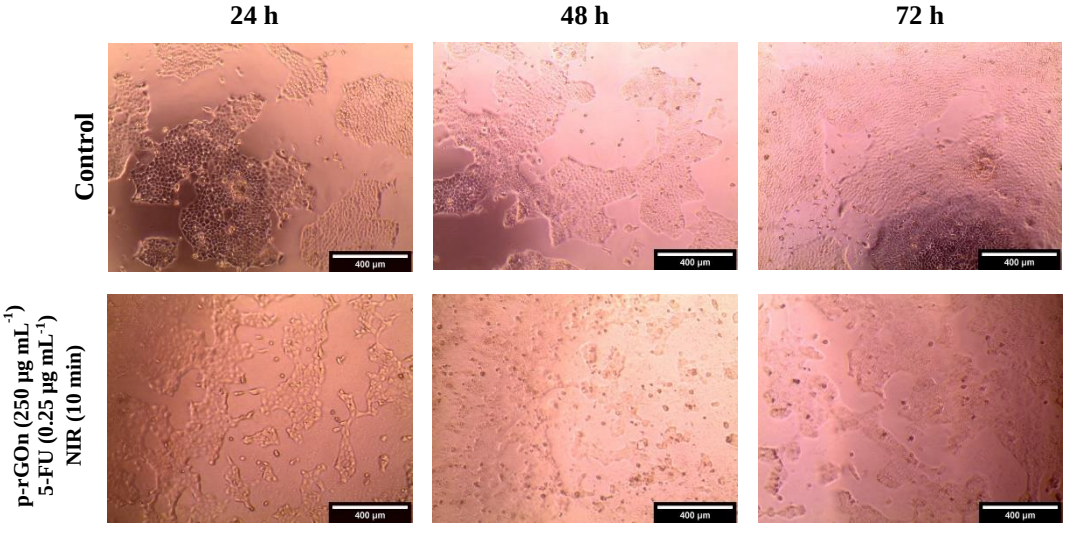

Figure A8 – Microscopy images of human foreskin fibroblasts (HFF-1) incubated with the selected hydrogels for 24, 48 and 72 h with 10 minutes of NIR irradiation. Controls correspond to cells incubated in complete DMEM without the addition of the hydrogels. Scale bar represents 400 µm.

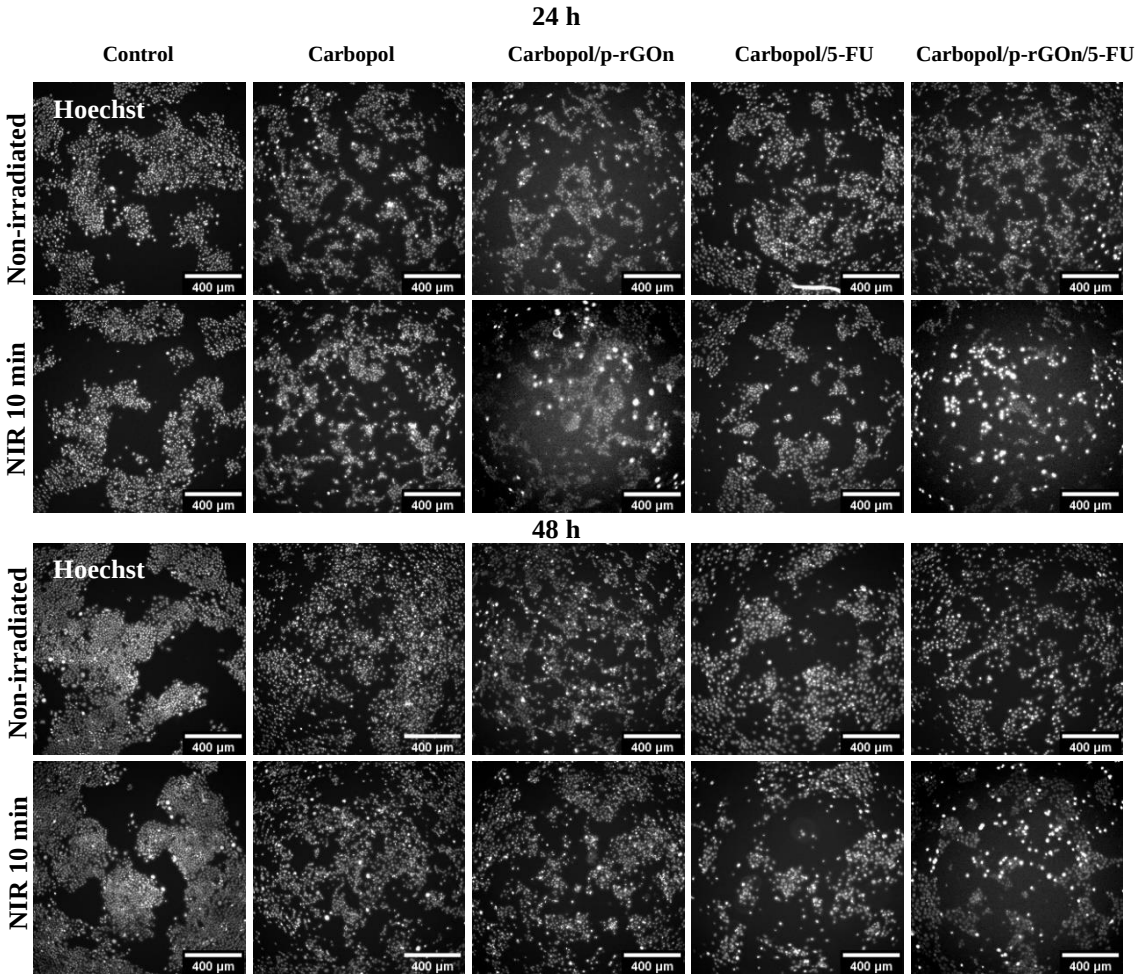

Figure A9 – Hoechst 33342 fluorescence representative images of A-431 nuclei incubated with produced hydrogels (100 µg mL^{-1} of p-rGOn and 0.25 µg mL^{-1} of 5-FU) with and without a 10-minute NIR irradiation, after 24 and 48 h.

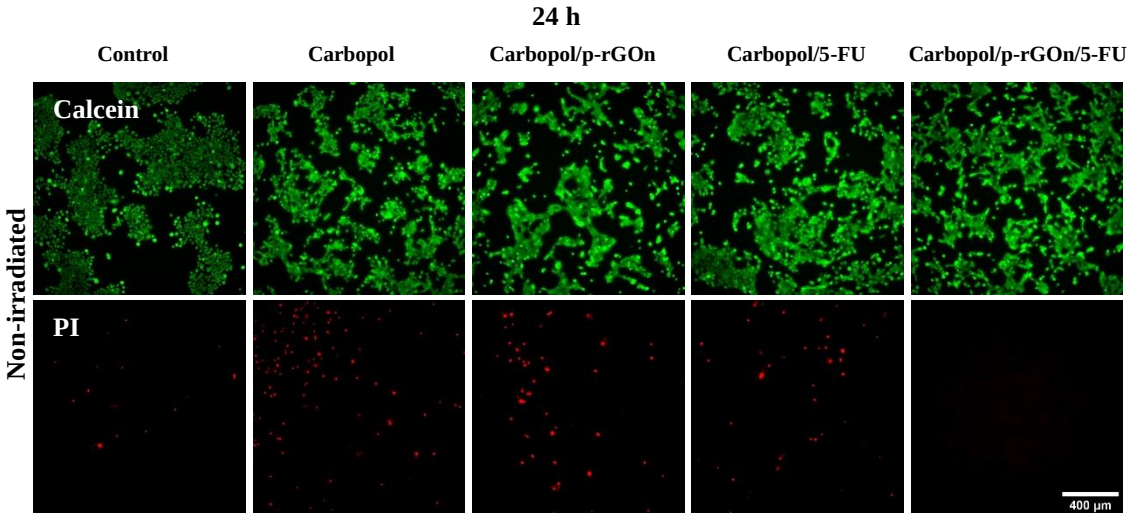

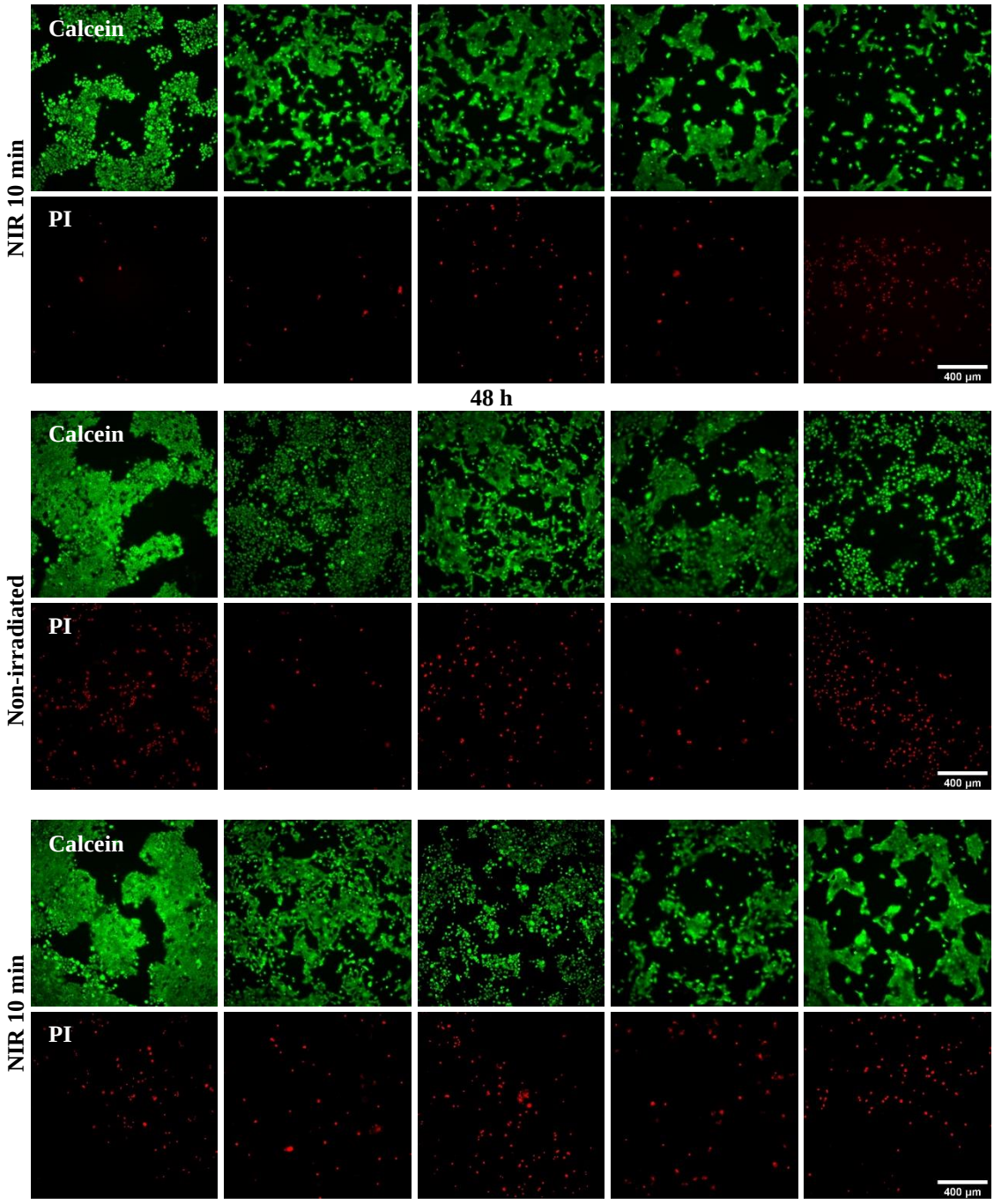

Figure A10 – Live/Dead assay. Representative images of HFF-1 cells incubated with produced hydrogels (100 µg mL^{-1} of p-rGOn and 0.25 µg mL^{-1} of 5-FU) with and without a 10-minute NIR irradiation, after 24 and 48 h. Live cells are stained with Calcein and dead cells with PI. Scale bar represents 400 µm.

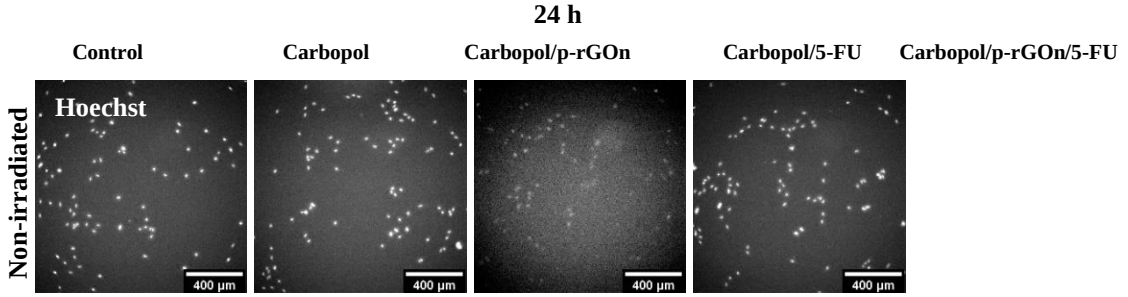

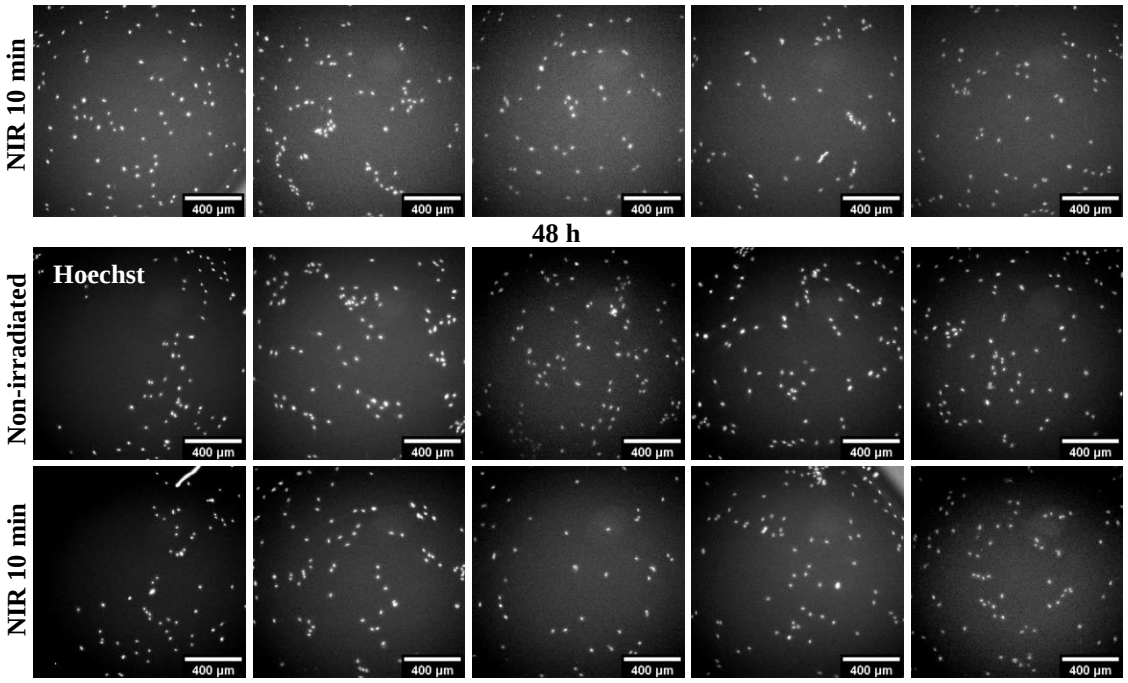

Figure A11 – Hoechst 33342 fluorescence representative images of HFF-1 nuclei incubated with produced hydrogels (100 µg mL^{-1} of p-rGOn and 0.25 µg mL^{-1} of 5-FU) with and without a 10-minute NIR irradiation, after 24 and 48 h.

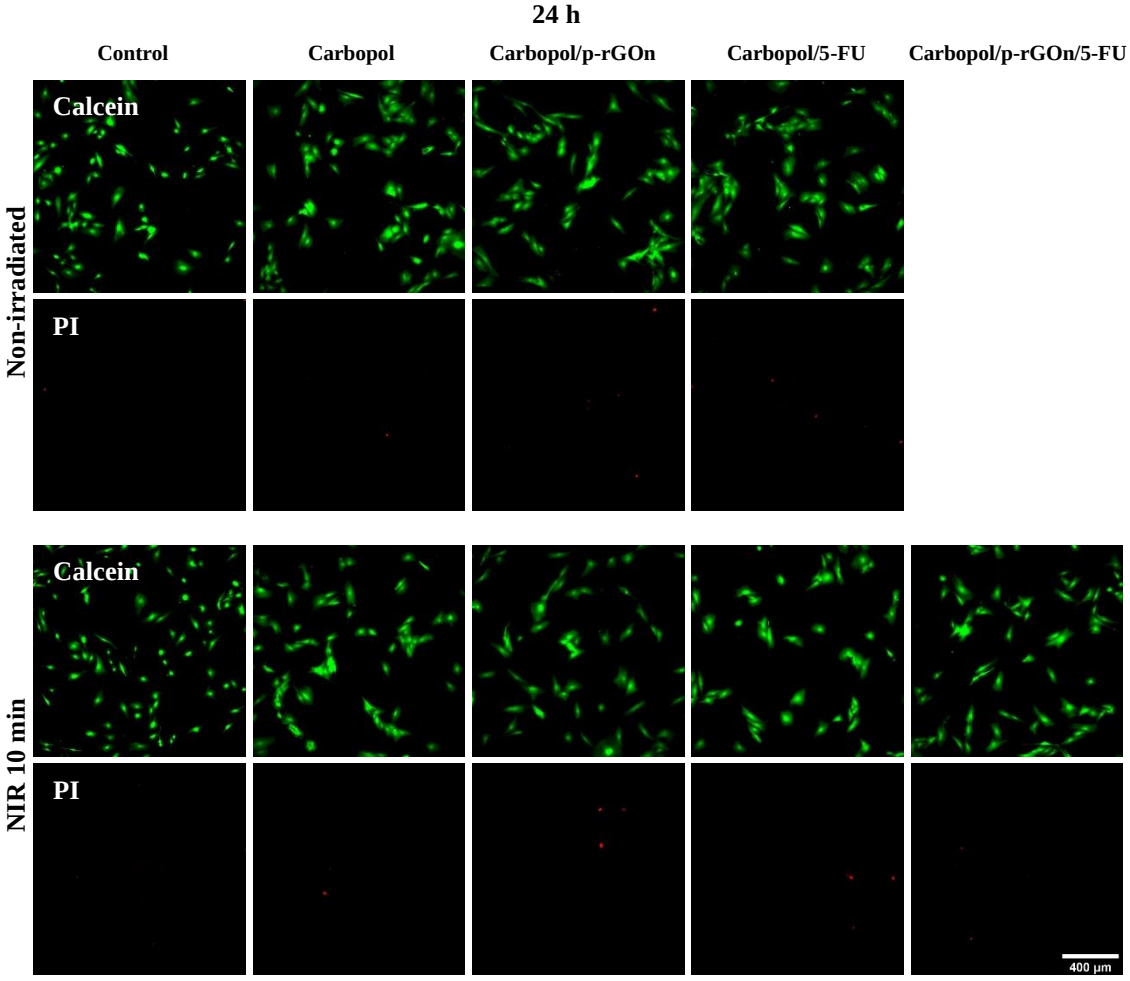

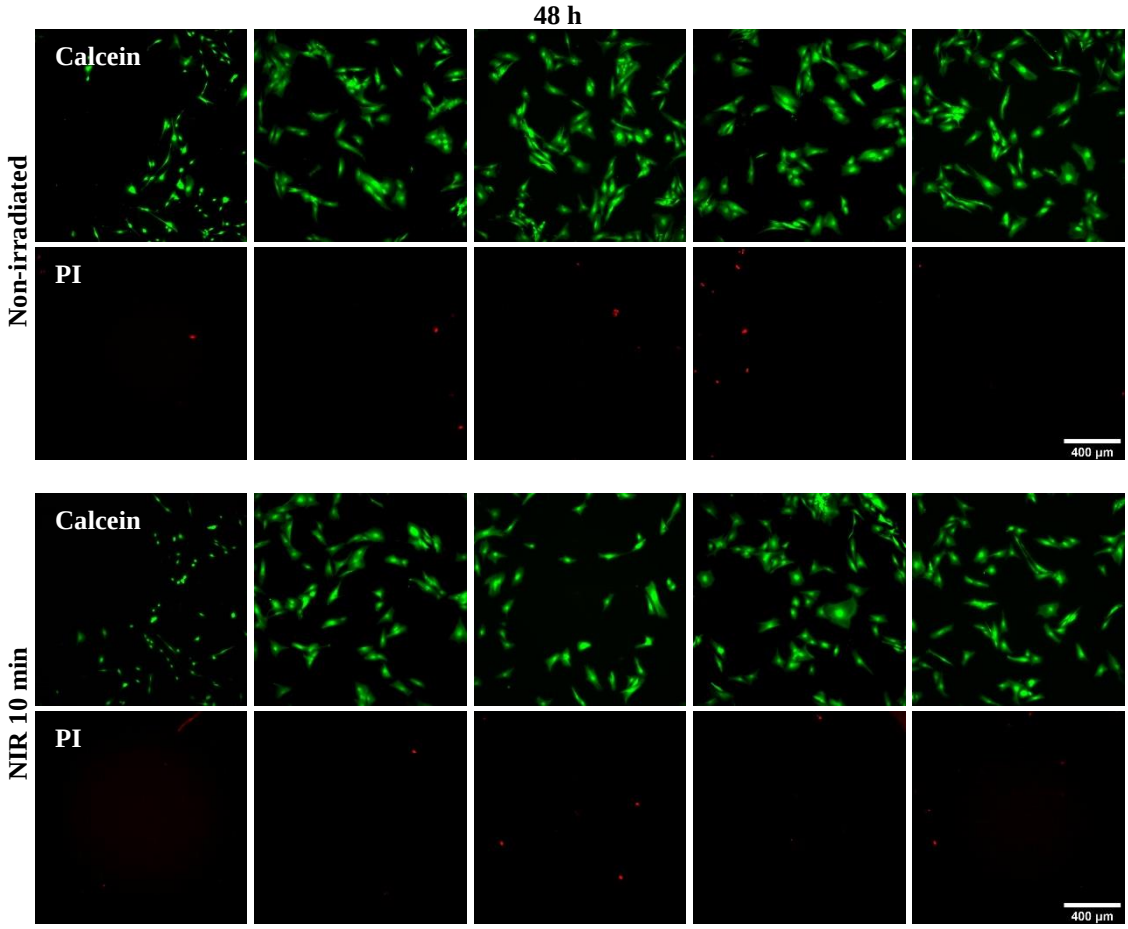

Figure A12 – Live/Dead assay. Representative images of HFF-1 cells incubated with produced hydrogels (100 µg mL^{-1} of p-rGOn and 0.25 µg mL^{-1} of 5-FU) with and without a 10-minute NIR irradiation, after 72 h. Live cells are stained with Calcein and dead cells with PI. Scale bar represents 400 µm.

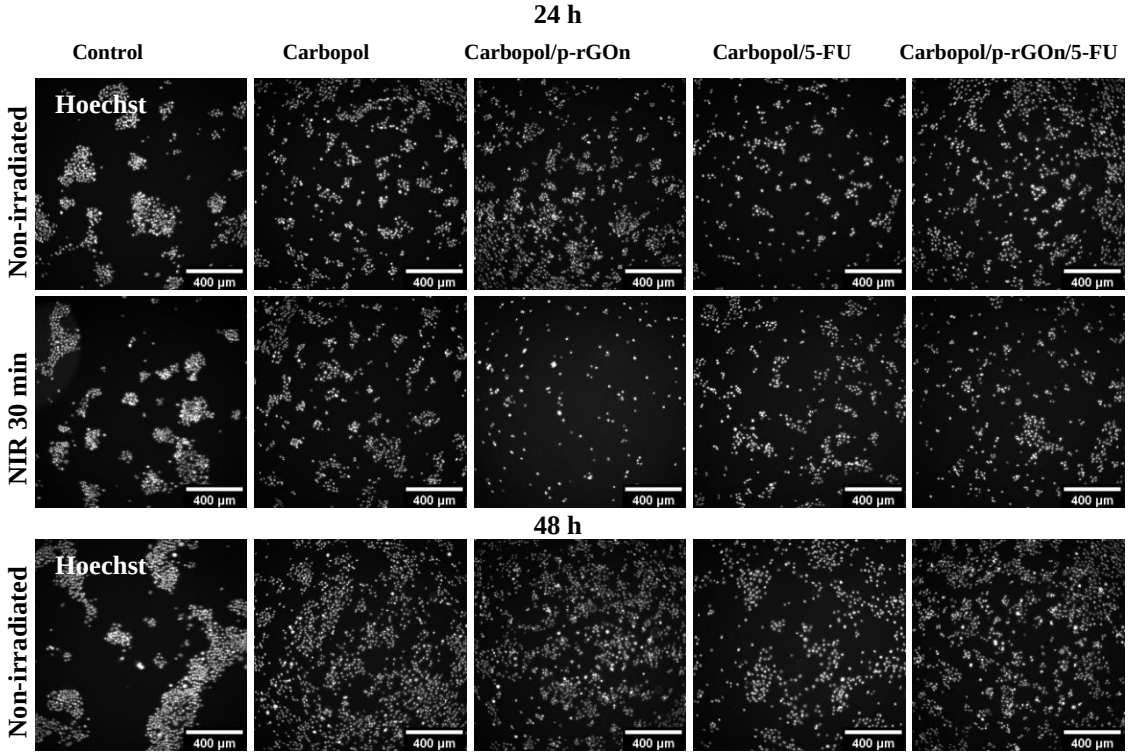

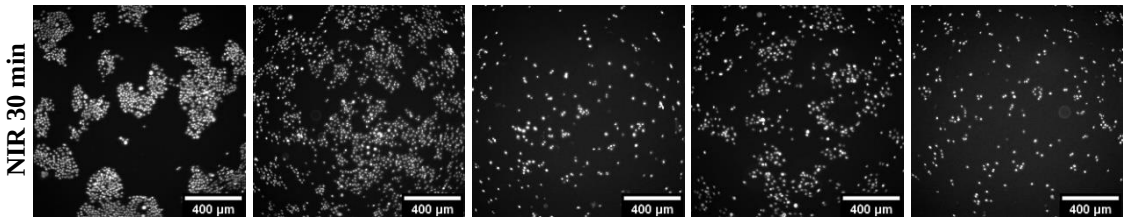

Figure A13 – Hoechst 33342 fluorescence representative images of A-431 nuclei incubated with produced hydrogels (100 µg mL^{-1} of p-rGOn and 0.25 µg mL^{-1} of 5-FU) with and without a 30-minute NIR irradiation, after 48 h.

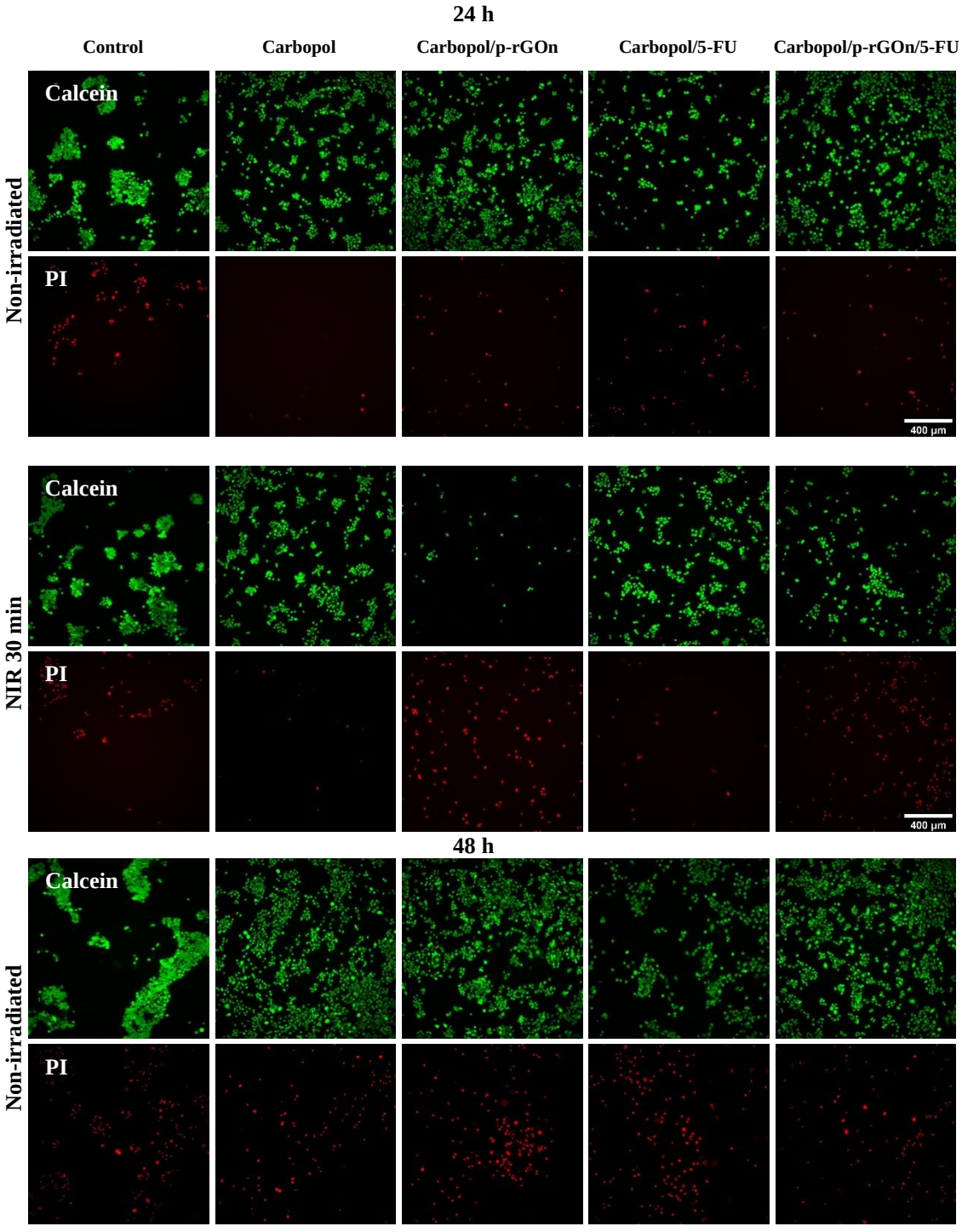

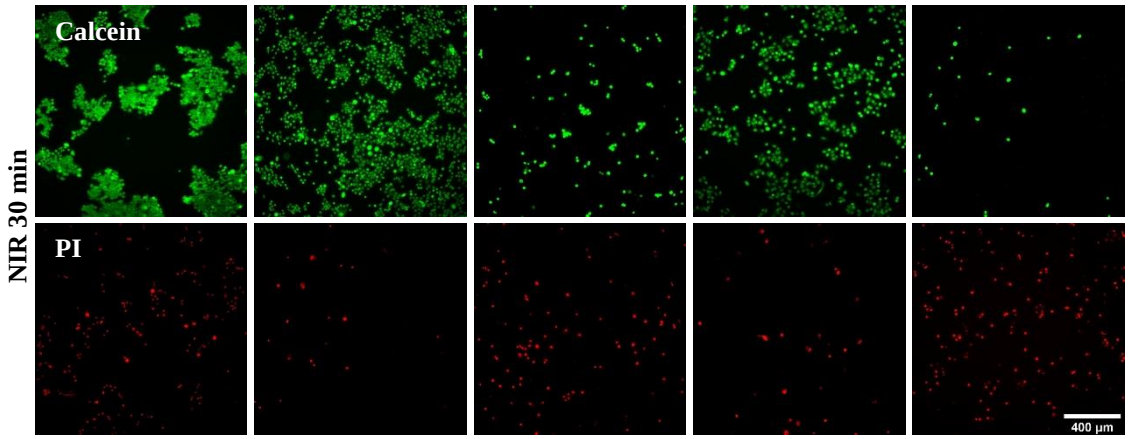

Figure A14 – Live/Dead assay. Representative images of A-431 cells incubated with produced hydrogels (100 µg mL^{-1} of p-rGOn and 0.25 µg mL^{-1} of 5-FU) with and without a 30-minute NIR irradiation, after 24 and 48 h. Live cells are stained with Calcein and dead cells with PI. Scale bar represents 400 µm.

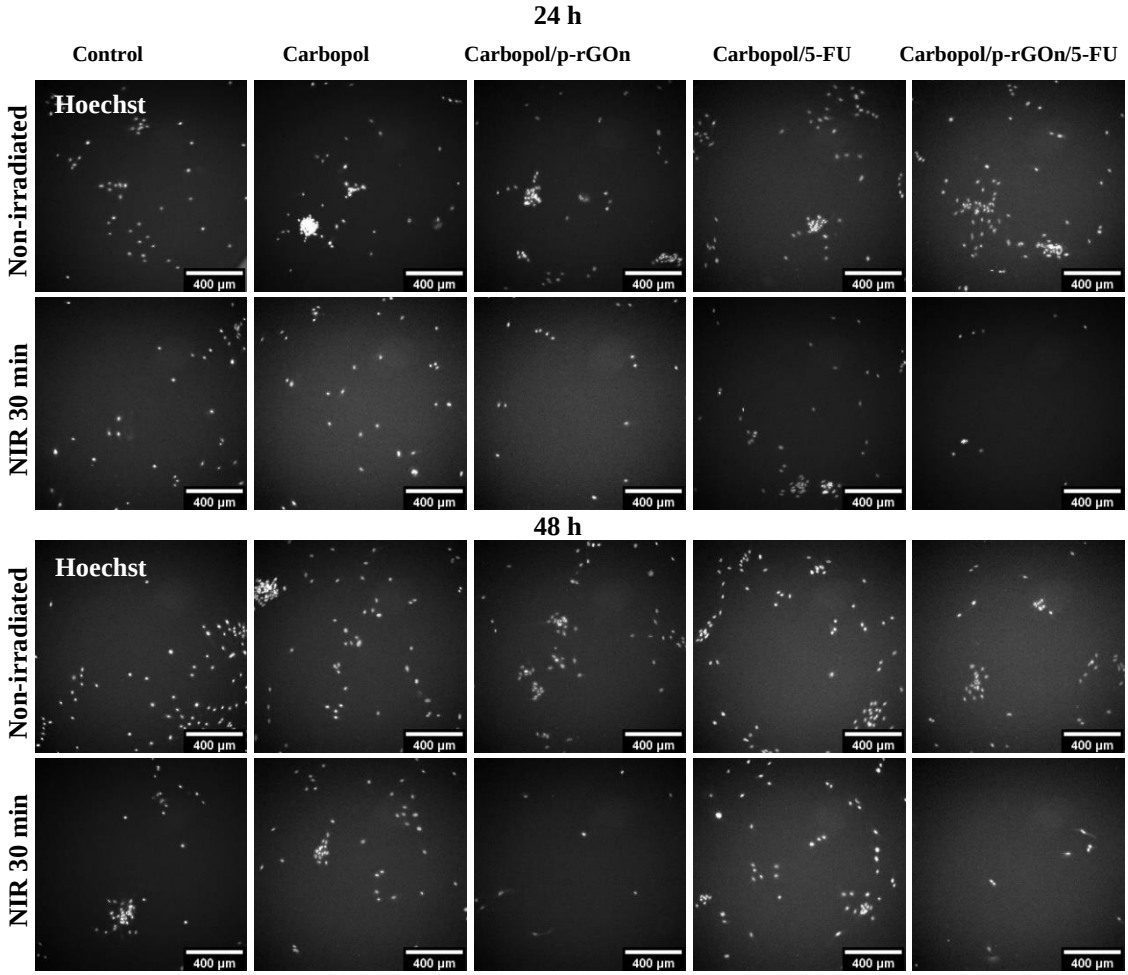

Figure A15 – Hoechst 33342 fluorescence representative images of HFF-1 nuclei incubated with produced hydrogels (100 µg mL^{-1} of p-rGOn and 0.25 µg mL^{-1} of 5-FU) with and without a 30-minute NIR irradiation, after 48 h.

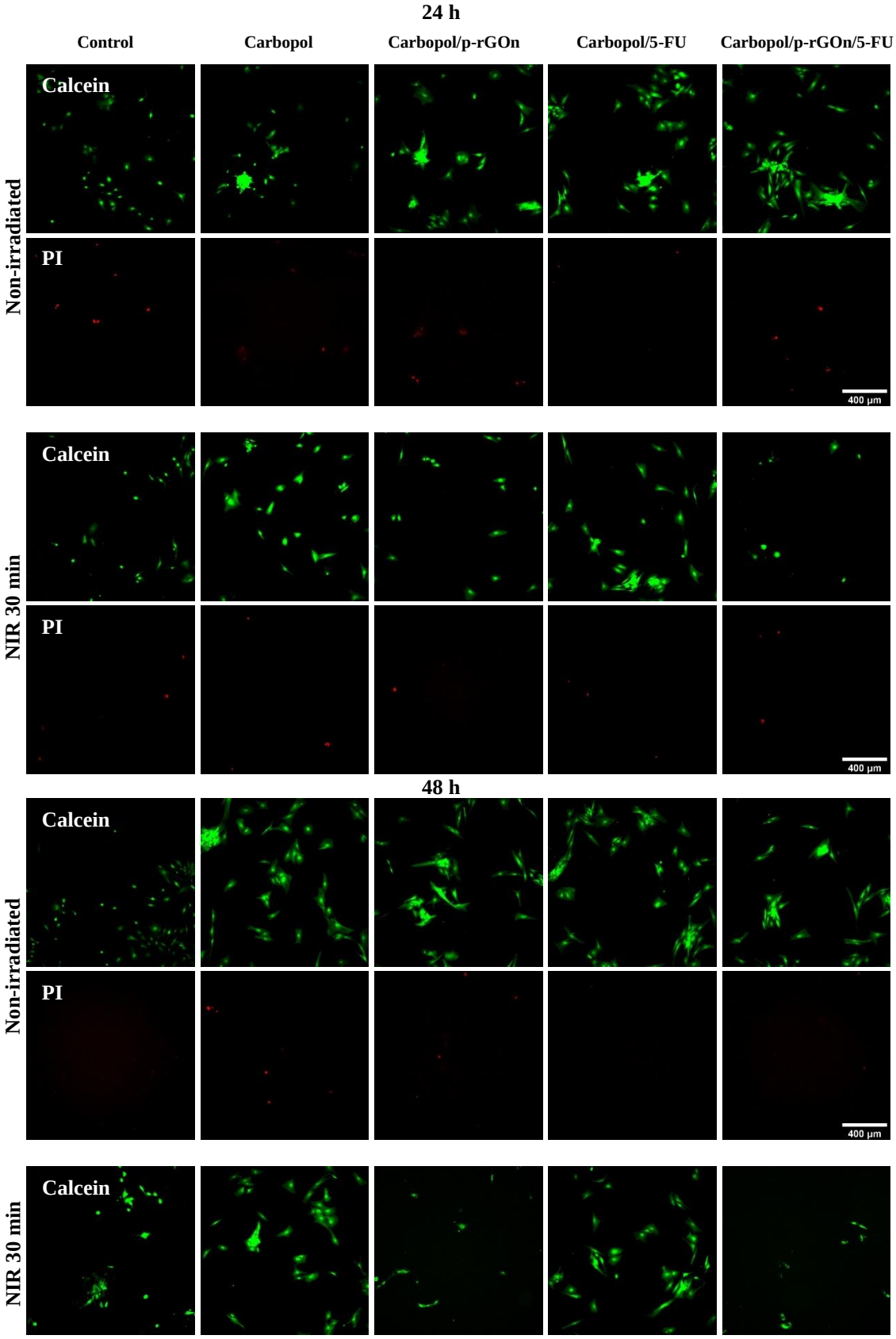
24 h
Control
Carbopol
Carbopol/p-rGOn
Carbopol/5-FU
Carbopol/p-rGOn/5-FU
Non-irradiated
Calcein
PI
NIR 30 min
Calcein
PI
48 h
Non-irradiated
Calcein
PI
NIR 30 min
Calcein
400 µm

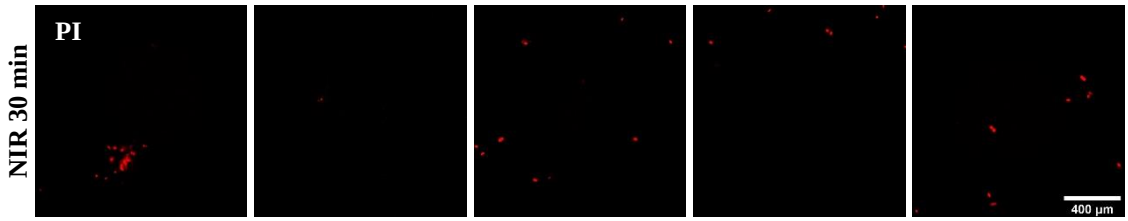

Figure A16 – Live/Dead assay. Representative images of HFF-1 cells incubated with produced hydrogels (100 µg mL^{-1} of p-rGOn and 0.25 µg mL^{-1} of 5-FU) with and without a 30-minute NIR irradiation, after 24 and 48 h. Live cells are stained with Calcein and dead cells with PI. Scale bar represents 400 µm.

Appendix B

List of publications

1. F. A. L. S. Silva, R. Costa-Almeida, L. Timochenco, S. I. Amaral, S. Pinto, I. C. Gonçalves, J. R. Fernandes, F. D. Magalhães, B. Sarmento, A. M. Pinto, "Graphene Oxide Topical Administration: Skin Permeability Studies", *Materials,* vol. 14, no. 11, p. 2810, 2021.

Appendix C

List of presentations

1. S. I. Amaral, F. Silva, L. Timochenco, S. Azevedo, J. R. Fernandes, B. Sarmento, F. D. Magalhães, I. C. Gonçalves, R. Costa-Almeida, A. M. Pinto, “Reduced nanographene oxide hydrogels for combined chemotherapy and photothermal therapy of skin cancer”, IJUP, 2021.

2. S. Azevedo, L. Timochenco, F. Silva, S. I. Amaral, M. Bessa-Gonçalves, K. Chattahy, J. R. Fernandes, F. D. Magalhães, R. Costa-Almeida, S. G. Santos, A. M. Pinto, “Immunomodulatory effects of nanographene oxide and reduced nanographene oxide in combination with phototherapy”, IJUP 2021.

Appendix D

Funding and institutional acknowledgements

This work was financed by FEDER funds through the COMPETE 2020 - Operacional Programme for Competitiveness and Internationalisation (POCI), Portugal 2020, and by national funds (PIDDAC) through FCT/MCTES in the framework of the project POCI-01-0145-FEDER-031143, and Base Funding - UIDB/00511/2020 of the Laboratory for Process Engineering, Environment, Biotechnology and Energy – LEPABE. Project 2SMART - engineered Smart materials for Smart citizens, with reference NORTE-01-0145-FEDER-000054, supported by Norte Portugal Regional Operational Programme (NORTE 2020), under the PORTUGAL 2020 Partnership Agreement, through the European Regional Development Fund (ERDF). Artur Pinto thanks the Portuguese Foundation for Science and Technology (FCT) for the financial support of his work contract through the Scientific Employment Stimulus - Individual Call – [CEECIND/03908/2017].

Additionally, the authors would like to thank: Rui Fernandes and Ana Rita Malheiro from the Histology and Electron Microscopy Service (HEMS) of i3S, Porto, for the assistance with TEM studies; André Maia from the BioSciences Screening of i3S, Porto, for the assistance with LIVE/DEAD studies; Biointerfaces and Nanotechnology (BN) Laboratory for the assistance with laboratory issues.

Bibliography

[1] A. Rembielak and T. Ajithkumar, "Non-Melanoma Skin Cancer–An Underestimated Global Health Threat?," *Clinical Oncology*, vol. 31, no. 11, pp. 735-737, 2019.

[2] A. I. Rubin, E. H. Chen, and D. Ratner, "Basal-cell carcinoma," *New England Journal of Medicine*, vol. 353, no. 21, pp. 2262-2269, 2005.

[3] A. G. Marzuka and S. E. Book, "Basal cell carcinoma: pathogenesis, epidemiology, clinical features, diagnosis, histopathology, and management," *The Yale journal of biology and medicine*, vol. 88, no. 2, pp. 167-179, 2015.

[4] S. F. Taveira and R. V. Lopez, "Topical administration of anticancer drugs for skin cancer treatment," *Topical Administration of anticancer drugs for skin cancer treatment*, pp. 247-272, 2011.

[5] X. Li, J. F. Lovell, J. Yoon, and X. Chen, "Clinical development and potential of photothermal and photodynamic therapies for cancer," *Nature Reviews Clinical Oncology*, vol. 17, no. 11, pp. 657-674, 2020.

[6] B. P. Jiang, B. Zhou, Z. Lin, H. Liang, and X. C. Shen, "Recent advances in carbon nanomaterials for cancer phototherapy," *Chemistry–A European Journal*, vol. 25, no. 16, pp. 3993-4004, 2019.

[7] G. Hong, S. Diao, A. L. Antaris, and H. Dai, "Carbon nanomaterials for biological imaging and nanomedicinal therapy " *Chemical reviews*, vol. 115, no. 19, pp. 10816-10906, 2015.

[8] X. Dai, T. Du, and K. Han, "Engineering Nanoparticles for Optimized Photodynamic Therapy," *ACS Biomaterials Science & Engineering*, vol. 5, no. 12, pp. 6342-6354, 2019.

[9] C. A. Robertson, D. H. Evans, and H. Abrahamse, "Photodynamic therapy (PDT): a short review on cellular mechanisms and cancer research applications for PDT," *Journal of Photochemistry and Photobiology B: Biology*, vol. 96, no. 1, pp. 1-8, 2009.

[10] B. Zhang, Y. Wang, J. Liu, and G. Zhai, "Recent Developments of Phototherapy Based on Graphene Family Nanomaterials," *Curr Med Chem*, vol. 24, no. 3, pp. 268-291, 2017.

[11] L. Zou, H. Wang, B. He, L. Zeng, T. Tan, H. Cao, X. He, Z. Zhang, S. Guo, and Y. Li, "Current approaches of photothermal therapy in treating cancer metastasis with nanotherapeutics," *Theranostics*, vol. 6, no. 6, p. 762, 2016.

[12] D. Kalyane, N. Raval, R. Maheshwari, V. Tambe, K. Kalia, and R. K. Tekade, "Employment of enhanced permeability and retention effect (EPR): Nanoparticle-based precision tools for targeting of therapeutic and diagnostic agent in cancer," *Materials Science and Engineering: C*, vol. 98, pp. 1252-1276, 2019.

[13] D. Van Straten, V. Mashayekhi, H. S. De Bruijn, S. Oliveira, and D. J. Robinson, "Oncologic photodynamic therapy: basic principles, current clinical status and future directions," *Cancers*, vol. 9, no. 2, p. 19, 2017.

[14] L. Cheng, X. Wang, F. Gong, T. Liu, and Z. Liu, "2D nanomaterials for cancer theranostic applications," *Advanced Materials*, p. 1902333, 2019.

[15] Y. Ma, J. Huang, S. Song, H. Chen, and Z. Zhang, "Cancer-targeted nanotheranostics: recent advances and perspectives," *Small*, vol. 12, no. 36, pp. 4936-4954, 2016.

[16] L. Cheng, C. Wang, L. Feng, K. Yang, and Z. Liu, "Functional nanomaterials for phototherapies of cancer," *Chemical reviews*, vol. 114, no. 21, pp. 10869-10939, 2014.

[17] J. Li and D. J. Mooney, "Designing hydrogels for controlled drug delivery," *Nature Reviews Materials*, vol. 1, no. 12, pp. 1-17, 2016.

[18] M. Patel, B. Patel, R. Patel, J. Patel, P. Bharadia, and M. Patel, "Carbopol: A versatile polymer," *Drug Delivery Technology*, pp. 36-41, 2006.

[19] D. Gadhave, N. Rasal, R. Sonawane, M. Sekar, and C. Kokare, "Nose-to-brain delivery of teriflunomide-loaded lipid-based carbopol-gellan gum nanogel for glioma: Pharmacological and

in vitro cytotoxicity studies," *International Journal of Biological Macromolecules,* vol. 167, pp. 906-920, 2021.

[20] F. Hayati, S. M. Ghamsari, M. M. Dehghan, and A. Oryan, "Effects of carbomer 940 hydrogel on burn wounds: an in vitro and in vivo study," *Journal of Dermatological Treatment,* vol. 29, no. 6, pp. 593-599, 2018.

[21] J. Wang, Y. Yuan, C. Liu, D. Zhu, X. Shen, and B. Yang, "Preparation and pharmaceutical/pharmacodynamic evaluation of topical brucine-loaded liposomal hydrogel," *Journal of Materials Science: Materials in Medicine,* vol. 20, no. 10, pp. 2075-2084, 2009.

[22] K. Yang, S. Zhang, G. Zhang, X. Sun, S. T. Lee, and Z. Liu, "Graphene in mice: ultrahigh in vivo tumor uptake and efficient photothermal therapy," *Nano letters,* vol. 10, no. 9, pp. 3318-3323, 2010.

[23] G. Chang, S. Li, F. Huang, X. Zhang, Y. Shen, and A. Xie, "Multifunctional reduced graphene oxide hydrogel as drug carrier for localized and synergic photothermal/photodynamics/chemo therapy," *Journal of Materials Science & Technology,* vol. 32, no. 8, pp. 753-762, 2016.

[24] Q. Zhang, Z. Wu, N. Li, Y. Pu, B. Wang, T. Zhang, and J. Tao, "Advanced review of graphene-based nanomaterials in drug delivery systems: Synthesis, modification, toxicity and application," *Materials Science and Engineering: C,* vol. 77, pp. 1363-1375, 2017.

[25] W. R. Wagner, S. E. Sakiyama-Elbert, G. Zhang, and M. J. Yaszemski, *Biomaterials Science: An Introduction to Materials in Medicine*. Elsevier Science, 2020.

[26] C. J. Serpell, K. Kostarelos, and B. G. Davis, "Can carbon nanotubes deliver on their promise in biology? Harnessing unique properties for unparalleled applications," *ACS central science,* vol. 2, no. 4, pp. 190-200, 2016.

[27] N. Karousis, I. Suarez-Martinez, C. P. Ewels, and N. Tagmatarchis, "Structure, properties, functionalization, and applications of carbon nanohorns," *Chemical reviews,* vol. 116, no. 8, pp. 4850-4883, 2016.

[28] A. M. Pinto, I. C. Gonçalves, and F. D. Magalhães, "Graphene-based materials biocompatibility: a review," *Colloids Surf B Biointerfaces,* vol. 111, pp. 188-202, 2013.

[29] Q. Liu, L. Xu, X. Zhang, N. Li, J. Zheng, M. Guan, X. Fang, C. Wang, and C. Shu, "Enhanced Photodynamic Efficiency of an Aptamer-Guided Fullerene Photosensitizer toward Tumor Cells," *Chemistry–An Asian Journal,* vol. 8, no. 10, pp. 2370-2376, 2013.

[30] W. Zhang, Z. Guo, D. Huang, Z. Liu, X. Guo, and H. Zhong, "Synergistic effect of chemo-photothermal therapy using PEGylated graphene oxide," *Biomaterials,* vol. 32, no. 33, pp. 8555-8561, 2011.

[31] D. Chen, C. A. Dougherty, K. Zhu, and H. Hong, "Theranostic applications of carbon nanomaterials in cancer: Focus on imaging and cargo delivery," *Journal of Controlled Release,* vol. 210, pp. 230-245, 2015.

[32] Q. Jia, J. Ge, W. Liu, X. Zheng, S. Chen, Y. Wen, H. Zhang, and P. Wang, "A Magnetofluorescent Carbon Dot Assembly as an Acidic H2O2-Driven Oxygenerator to Regulate Tumor Hypoxia for Simultaneous Bimodal Imaging and Enhanced Photodynamic Therapy " *Advanced Materials* vol. 30, no. 13, p. 1706090, 2018.

[33] P. Sundaram and H. Abrahamse, "Effective photodynamic therapy for colon cancer cells using chlorin e6 coated hyaluronic acid-based carbon nanotubes," *International journal of molecular sciences,* vol. 21, no. 13, p. 4745, 2020.

[34] R. Lima-Sousa, D. de Melo-Diogo, C. G. Alves, E. C. Costa, P. Ferreira, R. O. Louro, and I. J. Correia, "Hyaluronic acid functionalized green reduced graphene oxide for targeted cancer photothermal therapy " *Carbohydrate polymers,* vol. 200, pp. 93-99, 2018.

[35] R. Costa-Almeida, D. Bogas, J. R. Fernandes, L. Timochenco, F. A. Silva, J. Meneses, I. C. Gonçalves, F. D. Magalhães, and A. M. Pinto, "Near-Infrared Radiation-Based Mild Photohyperthermia Therapy of Non-Melanoma Skin Cancer with PEGylated Reduced Nanographene Oxide," *Polymers,* vol. 12, no. 8, p. 1840, 2020.

[36] J. Chen, H. Liu, C. Zhao, G. Qin, G. Xi, T. Li, X. Wang, and T. Chen, "One-step reduction and PEGylation of graphene oxide for photothermally controlled drug delivery," *Biomaterials,* vol. 35, no. 18, pp. 4986-95, 2014.

[37] J. Shi, R. Ma, L. Wang, J. Zhang, R. Liu, L. Li, Y. Liu, L. Hou, X. Yu, and J. Gao, "The application of hyaluronic acid-derivatized carbon nanotubes in hematoporphyrin monomethyl ether-based photodynamic therapy for in vivo and in vitro cancer treatment," *International Journal of Nanomedicine,* vol. 8, p. 2361, 2013.

[38] L. Zhou, S. Wei, X. Ge, J. Zhou, H. Jiang, F. Li, and J. Shen, "Combination of chemotherapy and photodynamic therapy using graphene oxide as drug delivery system," *Journal of Photochemistry and Photobiology B: Biology,* vol. 135, pp. 7-16, 2014.

[39] J. Xu, F. Zeng, H. Wu, C. Yu, and S. Wu, "Dual-targeting nanosystem for enhancing photodynamic therapy efficiency," *ACS Applied Materials & Interfaces,* vol. 7, no. 17, pp. 9287-9296, 2015.

[40] P. Huang, C. Xu, J. Lin, C. Wang, X. Wang, C. Zhang, X. Zhou, S. Guo, and D. Cui, "Folic acid-conjugated graphene oxide loaded with photosensitizers for targeting photodynamic therapy," *Theranostics,* vol. 1, p. 240, 2011.

[41] Q. Li, R. Zhou, Y. Xie, Y. Li, Y. Chen, and X. Cai, "Sulphur-doped carbon dots as a highly efficient nano-photodynamic agent against oral squamous cell carcinoma," *Cell Proliferation,* vol. 53, no. 4, p. e12786, 2020.

[42] P. Liu, X. Xie, M. Liu, S. Hu, J. Ding, and W. Zhou, "A smart MnO2-doped graphene oxide nanosheet for enhanced chemo-photodynamic combinatorial therapy via simultaneous oxygenation and glutathione depletion," *Acta Pharmaceutica Sinica B,* vol. 11, no. 3, 2021.

[43] K. Yang, L. Feng, X. Shi, and Z. Liu, "Nano-graphene in biomedicine: theranostic applications," *Chemical Society Reviews,* vol. 42, no. 2, pp. 530-547, 2013.

[44] X. Yang, C. Fan, and H. Zhu, "Photo-induced cytotoxicity of malonic acid [C60] fullerene derivatives and its mechanism," *Toxicology in vitro,* vol. 16, no. 1, pp. 41-46, 2002.

[45] M. Guan, J. Ge, J. Wu, G. Zhang, D. Chen, W. Zhang, Y. Zhang, T. Zou, M. Zhen, C. Wang, T. Chu, X. Hao, and C. Shu, "Fullerene/photosensitizer nanovesicles as highly efficient and clearable phototheranostics with enhanced tumor accumulation for cancer therapy " *Biomaterials* vol. 103 pp. 75-85, 2016.

[46] M. Akiyama, A. Ikeda, T. Shintani, Y. Doi, J.-i. Kikuchi, T. Ogawa, K. Yogo, T. Takeya, and N. Yamamoto, "Solubilisation of [60] fullerenes using block copolymers and evaluation of their photodynamic activities," *Organic & Biomolecular Chemistry,* vol. 6, no. 6, pp. 1015-1019, 2008.

[47] Y. Doi, A. Ikeda, M. Akiyama, M. Nagano, T. Shigematsu, T. Ogawa, T. Takeya, and T. Nagasaki, "Intracellular uptake and photodynamic activity of water-soluble [60]-and [70] fullerenes incorporated in liposomes," *Chemistry–A European Journal,* vol. 14, no. 29, pp. 8892-8897, 2008.

[48] A. Ikeda, M. Nagano, M. Akiyama, M. Matsumoto, S. Ito, M. Mukai, M. Hashizume, J. i. Kikuchi, K. Katagiri, and T. Ogawa, "Photodynamic Activity of C70 Caged within Surface-Cross-Linked Liposomes," *Chemistry–An Asian Journal,* vol. 4, no. 1, pp. 199-205, 2009.

[49] A. Ikeda, Y. Doi, K. Nishiguchi, K. Kitamura, M. Hashizume, J.-i. Kikuchi, K. Yogo, T. Ogawa, and T. Takeya, "Induction of cell death by photodynamic therapy with water-soluble lipid-membrane-incorporated [60] fullerene," *Organic & biomolecular chemistry,* vol. 5, no. 8, pp. 1158-1160, 2007.

[50] J. Liu, S.-i. Ohta, A. Sonoda, M. Yamada, M. Yamamoto, N. Nitta, K. Murata, and Y. Tabata, "Preparation of PEG-conjugated fullerene containing Gd3+ ions for photodynamic therapy," *Journal of Controlled Release,* vol. 117, no. 1, pp. 104-110, 2007.

[51] J. Liu and Y. Tabata, "Photodynamic antitumor activity of fullerene modified with poly (ethylene glycol) with different molecular weights and terminal structures," *Journal of Biomaterials Science, Polymer Edition,* vol. 22, no. 1-3, pp. 297-312, 2011.

[52] Y. Tabata, Y. Murakami, and Y. Ikada, "Photodynamic effect of polyethylene glycol–modified fullerene on tumor," *Japanese Journal of Cancer Research,* vol. 88, no. 11, pp. 1108-1116, 1997.

[53] J. Shi, Z. Wang, L. Wang, H. Wang, L. Li, X. Yu, J. Zhang, R. Ma, and Z. Zhang, "Photodynamic therapy of a 2-methoxyestradiol tumor-targeting drug delivery system mediated by Asn-Gly-Arg in breast cancer," *International Journal of Nanomedicine,* vol. 8, p. 1551, 2013.

[54] J. Shi, X. Yu, L. Wang, Y. Liu, J. Gao, J. Zhang, R. Ma, R. Liu, and Z. Zhang, "PEGylated fullerene/iron oxide nanocomposites for photodynamic therapy, targeted drug delivery and MR imaging," *Biomaterials,* vol. 34, no. 37, pp. 9666-9677, 2013.

[55] J. Liu and Y. Tabata, "Photodynamic therapy of fullerene modified with pullulan on hepatoma cells," *Journal of drug targeting,* vol. 18, no. 8, pp. 602-610, 2010.

[56] A. Grebinyk, S. Prylutska, O. Chepurna, S. Grebinyk, Y. Prylutskyy, U. Ritter, T. Y. Ohulchanskyy, O. Matyshevska, T. Dandekar, and M. Frohme, "Synergy of chemo-and photodynamic therapies with C60 fullerene-doxorubicin nanocomplex," *Nanomaterials,* vol. 9, no. 11, p. 1540, 2019.

[57] X. Liu, M. Zheng, X. Kong, Y. Zhang, Q. Zeng, Z. Sun, W. J. Buma, and H. Zhang, "Separately doped upconversion-C 60 nanoplatform for NIR imaging-guided photodynamic therapy of cancer cells," *Chemical Communications,* vol. 49, no. 31, pp. 3224-3226, 2013.

[58] H. Chen, Y. Qiu, D. Ding, H. Lin, W. Sun, G. D. Wang, W. Huang, W. Zhang, D. Lee, and G. Liu, "Gadolinium-encapsulated graphene carbon nanotheranostics for imaging-guided photodynamic therapy," *Advanced Materials,* vol. 30, no. 36, p. 1802748, 2018.

[59] Y. Choi, S. Kim, M. H. Choi, S. R. Ryoo, J. Park, D. H. Min, and B. S. Kim, "Highly biocompatible carbon nanodots for simultaneous bioimaging and targeted photodynamic therapy in vitro and in vivo," *Advanced Functional Materials,* vol. 24, no. 37, pp. 5781-5789, 2014.

[60] S. Chen, T. Sun, M. Zheng, and Z. Xie, "Carbon dots based nanoscale covalent organic frameworks for photodynamic therapy," *Advanced Functional Materials,* vol. 30, no. 43, p. 2004680, 2020.

[61] H. He, X. Zheng, S. Liu, M. Zheng, Z. Xie, Y. Wang, M. Yu, and X. Shuai, "Diketopyrrolopyrrole-based carbon dots for photodynamic therapy," *Nanoscale,* vol. 10, no. 23, pp. 10991-10998, 2018.

[62] N. Xu, J. Du, Q. Yao, H. Ge, H. Li, F. Xu, F. Gao, L. Xian, J. Fan, and X. Peng, "Precise photodynamic therapy: Penetrating the nuclear envelope with photosensitive carbon dots," *Carbon,* vol. 159, pp. 74-82, 2020.

[63] D.-W. Zheng, B. Li, C.-X. Li, J.-X. Fan, Q. Lei, C. Li, Z. Xu, and X.-Z. Zhang, "Carbon-dot-decorated carbon nitride nanoparticles for enhanced photodynamic therapy against hypoxic tumor via water splitting," *ACS nano,* vol. 10, no. 9, pp. 8715-8722, 2016.

[64] D. Du, K. Wang, Y. Wen, Y. Li, and Y. Y. Li, "Photodynamic graphene quantum dot: reduction condition regulated photoactivity and size dependent efficacy," *ACS Applied Materials & Interfaces,* vol. 8, no. 5, pp. 3287-3294, 2016.

[65] D. Zhang, L. Wen, R. Huang, H. Wang, X. Hu, and D. Xing, "Mitochondrial specific photodynamic therapy by rare-earth nanoparticles mediated near-infrared graphene quantum dots," *Biomaterials,* vol. 153, pp. 14-26, 2018.

[66] J. Ge, M. Lan, B. Zhou, W. Liu, L. Guo, H. Wang, Q. Jia, G. Niu, X. Huang, and H. Zhou, "A graphene quantum dot photodynamic therapy agent with high singlet oxygen generation," *Nature communications,* vol. 5, no. 1, pp. 1-8, 2014.

[67] Y. Liu, Y. Xu, X. Geng, Y. Huo, D. Chen, K. Sun, G. Zhou, B. Chen, and K. Tao, "Synergistic Targeting and Efficient Photodynamic Therapy Based on Graphene Oxide Quantum Dot-Upconversion Nanocrystal Hybrid Nanoparticles," *Small,* vol. 14, no. 19, p. 1800293, 2018.

[68] J. Ju, S. Regmi, A. Fu, S. Lim, and Q. Liu, "Graphene quantum dot based charge-reversal nanomaterial for nucleus-targeted drug delivery and efficiency controllable photodynamic therapy," *Journal of biophotonics,* vol. 12, no. 6, p. e201800367, 2019.

[69] S. Y. Choi, S. H. Baek, S.-J. Chang, Y. Song, R. Rafique, K. T. Lee, and T. J. Park, "Synthesis of upconversion nanoparticles conjugated with graphene oxide quantum dots and their use against cancer cell imaging and photodynamic therapy," *Biosensors and Bioelectronics,* vol. 93, pp. 267-273, 2017.

[70] P. Huang, J. Lin, D. Yang, C. Zhang, Z. Li, and D. Cui, "Photosensitizer-loaded dendrimer-modified multi-walled carbon nanotubes for photodynamic therapy," *Journal of Controlled Release,* vol. 152, 2011.

[71] H. Xiao, B. Zhu, D. Wang, Y. Pang, L. He, X. Ma, R. Wang, C. Jin, Y. Chen, and X. Zhu, "Photodynamic effects of chlorin e6 attached to single wall carbon nanotubes through noncovalent interactions," *Carbon,* vol. 50, no. 4, pp. 1681-1689, 2012.

[72] R. O. Ogbodu, I. Ndhundhuma, A. Karsten, and T. Nyokong, "Photodynamic therapy effect of zinc monoamino phthalocyanine–folic acid conjugate adsorbed on single walled carbon nanotubes on melanoma cells," *Spectrochimica Acta Part A: Molecular and Biomolecular Spectroscopy,* vol. 137, pp. 1120-1125, 2015.

[73] L. Wang, J. Shi, R. Liu, Y. Liu, J. Zhang, X. Yu, J. Gao, C. Zhang, and Z. Zhang, "Photodynamic effect of functionalized single-walled carbon nanotubes: a potential sensitizer for photodynamic therapy," *Nanoscale,* vol. 6, no. 9, pp. 4642-4651, 2014.

[74] Z. Hu, J. Li, C. Li, S. Zhao, N. Li, Y. Wang, F. Wei, L. Chen, and Y. Huang, "Folic acid-conjugated graphene–ZnO nanohybrid for targeting photodynamic therapy under visible light irradiation," *Journal of Materials Chemistry B,* vol. 1, no. 38, pp. 5003-5013, 2013.

[75] L. Zhou, W. Wang, J. Tang, J. H. Zhou, H. J. Jiang, and J. Shen, "Graphene oxide noncovalent photosensitizer and its anticancer activity in vitro," *Chemistry–A European Journal,* vol. 17, no. 43, pp. 12084-12091, 2011.

[76] F. Li, S.-J. Park, D. Ling, W. Park, J. Y. Han, K. Na, and K. Char, "Hyaluronic acid-conjugated graphene oxide/photosensitizer nanohybrids for cancer targeted photodynamic therapy," *Journal of Materials Chemistry B,* vol. 1, no. 12, pp. 1678-1686, 2013.

[77] Y. Cho and Y. Choi, "Graphene oxide-photosensitizer conjugate as a redox-responsive theranostic agent," *Chem Commun (Camb),* vol. 48, no. 79, pp. 9912-4, 2012.

[78] L. Zhou, H. Jiang, S. Wei, X. Ge, J. Zhou, and J. Shen, "High-efficiency loading of hypocrellin B on graphene oxide for photodynamic therapy," *Carbon,* vol. 50, no. 15, pp. 5594-5604, 2012.

[79] H. Dong, Z. Zhao, H. Wen, F. Guo, A. Shen, F. Pilger, C. Lin, and D. Shi, "Poly (ethylene glycol) conjugated nano-graphene oxide for photodynamic therapy," *Science China Chemistry*, vol. 53, no. 11, pp. 2265-2271, 2010.

[80] P. Rong, K. Yang, A. Srivastan, D. O. Kiesewetter, X. Yue, F. Wang, L. Nie, A. Bhirde, Z. Wang, and Z. Liu, "Photosensitizer loaded nano-graphene for multimodality imaging guided tumor photodynamic therapy," *Theranostics*, vol. 4, no. 3, p. 229, 2014.

[81] W. Miao, G. Shim, S. Lee, S. Lee, Y. S. Choe, and Y.-K. Oh, "Safety and tumor tissue accumulation of pegylated graphene oxide nanosheets for co-delivery of anticancer drug and photosensitizer," *Biomaterials*, vol. 34, no. 13, pp. 3402-3410, 2013.

[82] P. Huang, S. Wang, X. Wang, G. Shen, J. Lin, Z. Wang, S. Guo, D. Cui, M. Yang, and X. Chen, "Surface functionalization of chemically reduced graphene oxide for targeted photodynamic therapy," *Journal of biomedical nanotechnology*, vol. 11, no. 1, pp. 117-125, 2015.

[83] S. Shuvra Smita, A. Das, and A. Barui, "Surface Functionalization of Green-synthesized Reduced Graphene Oxide with PPIX Enhances Photosensitization of Cancer Cells," *Photochemistry and Photobiology*, vol. 96, no. 6, pp. 1283-1293, 2020.

[84] K. Vinothini, N. K. Rajendran, M. Rajan, A. Ramu, N. Marraiki, and A. M. Elgorban, "A magnetic nanoparticle functionalized reduced graphene oxide-based drug carrier system for a chemo-photodynamic cancer therapy," *New Journal of Chemistry*, vol. 44, no. 14, pp. 5265-5277, 2020.

[85] M. G. Alvarez, C. Prucca, M. E. Milanesio, E. N. Durantini, and V. Rivarola, "Photodynamic activity of a new sensitizer derived from porphyrin-C60 dyad and its biological consequences in a human carcinoma cell line," *The international journal of biochemistry & cell biology*, vol. 38, no. 12, pp. 2092-2101, 2006.

[86] P. Mroz, A. Pawlak, M. Satti, H. Lee, T. Wharton, H. Gali, T. Sarna, and M. R. Hamblin, "Functionalized fullerenes mediate photodynamic killing of cancer cells: Type I versus Type II photochemical mechanism," *Free Radical Biology and Medicine*, vol. 43, no. 5, pp. 711-719, 2007.

[87] L. Y. Chiang, P. A. Padmawar, J. E. Rogers-Haley, G. So, T. Canteenwala, S. Thota, L.-S. Tan, K. Pritzker, Y.-Y. Huang, and S. K. Sharma, "Synthesis and characterization of highly photoresponsive fullerenyl dyads with a close chromophore antenna–C 60 contact and effective photodynamic potential," *Journal of materials chemistry*, vol. 20, no. 25, pp. 5280-5293, 2010.

[88] F. Rancan, M. Helmreich, A. Mölich, N. Jux, A. Hirsch, B. Röder, C. Witt, and F. Böhm, "Fullerene-pyropheophorbide a complexes as sensitizer for photodynamic therapy: uptake and photo-induced cytotoxicity on Jurkat cells," *Journal of Photochemistry and Photobiology B: Biology*, vol. 80, no. 1, pp. 1-7, 2005.

[89] A. Ikeda, M. Matsumoto, M. Akiyama, J.-i. Kikuchi, T. Ogawa, and T. Takeya, "Direct and short-time uptake of [70] fullerene into the cell membrane using an exchange reaction from a [70] fullerene–γ-cyclodextrin complex and the resulting photodynamic activity," *Chemical Communications*, no. 12, pp. 1547-1549, 2009.

[90] P. Mroz, Y. Xia, D. Asanuma, A. Konopko, T. Zhiyentayev, Y. Y. Huang, S. K. Sharma, T. Dai, U. J. Khan, T. Wharton, and M. R. Hamblin, "Intraperitoneal photodynamic therapy mediated by a fullerene in a mouse model of abdominal dissemination of colon adenocarcinoma " *Nanomedicine: Nanotechnology, Biology and Medicine* vol. 7, no. 6, pp. 965-974, 2011.

[91] J. Wang, M. Xu, D. Wang, Z. Li, F. L. Primo, A. C. Tedesco, and H. Bi, "Copper-Doped Carbon Dots for Optical Bioimaging and Photodynamic Therapy," *Inorganic chemistry*, vol. 58, no. 19, pp. 13394-13402, 2019.

[92] L. Yue, H. Li, Q. Sun, J. Zhang, X. Luo, F. Wu, and X. Zhu, "Red-Emissive Ruthenium-Containing Carbon Dots for Bioimaging and Photodynamic Cancer Therapy," *ACS Applied Nano Materials*, vol. 3, no. 1, pp. 869-876, 2020.

[93] Z. M. Markovic, B. Z. Ristic, K. M. Arsikin, D. G. Klisic, L. M. Harhaji-Trajkovic, B. M. Todorovic-Markovic, D. P. Kepic, T. K. Kravic-Stevovic, S. P. Jovanovic, M. M. Milenkovic, D. D. Milivojevic, V. Z. Bumbasirevic, M. D. Dramicanin, and V. S. Trajkovic, "Graphene quantum dots as autophagy-inducing photodynamic agents " *Biomaterials* vol. 33, no. 29, pp. 7084-7092, 2012.

[94] S. Ahirwar, S. Mallick, and D. Bahadur, "Photodynamic therapy using graphene quantum dot derivatives," *Journal of Solid State Chemistry*, vol. 282, p. 121107, 2020.

[95] Y. Zhang, C. Yang, D. Yang, Z. Shao, Y. Hu, J. Chen, L. Yuwen, L. Weng, Z. Luo, and L. Wang, "Reduction of graphene oxide quantum dots to enhance the yield of reactive oxygen species for photodynamic therapy," *Physical Chemistry Chemical Physics*, vol. 20, no. 25, pp. 17262-17267, 2018.

[96] Z. Hu, Y. Huang, S. Sun, W. Guan, Y. Yao, P. Tang, and C. Li, "Visible light driven photodynamic anticancer activity of graphene oxide/TiO2 hybrid," *Carbon,* vol. 50, no. 3, pp. 994-1004, 2012.

[97] R. Xing, T. Jiao, Y. Liu, K. Ma, Q. Zou, G. Ma, and X. Yan, "Co-assembly of graphene oxide and albumin/photosensitizer nanohybrids towards enhanced photodynamic therapy," *Polymers,* vol. 8, no. 5, p. 181, 2016.

[98] K. Bartoň Tománková, A. Opletalová, K. Poláková, S. Kalytchuk, J. Jiravová, J. Malohlava, L. Malina, and H. Kolářová, "Size-Selected Graphene Oxide Loaded with Photosensitizer (TMPyP) for Targeting Photodynamic Therapy In Vitro," *Processes,* vol. 8, no. 2, p. 251, 2020.

[99] Y. Wei, F. Zhou, D. Zhang, Q. Chen, and D. Xing, "A graphene oxide based smart drug delivery system for tumor mitochondria-targeting photodynamic therapy," *Nanoscale,* vol. 8, no. 6, pp. 3530-3538, 2016.

[100] H. Shang, D. Han, M. Ma, S. Li, W. Xue, and A. Zhang, "Enhancement of the photokilling effect of TiO2 in photodynamic therapy by conjugating with reduced graphene oxide and its mechanism exploration," *Journal of Photochemistry and Photobiology B: Biology,* vol. 177, pp. 112-123, 2017.

[101] V. Krishna, A. Singh, P. Sharma, N. Iwakuma, Q. Wang, Q. Zhang, J. Knapik, H. Jiang, S. R. Grobmyer, and B. Koopman, "Polyhydroxy fullerenes for non-invasive cancer imaging and therapy," *Small,* vol. 6, no. 20, pp. 2236-2241, 2010.

[102] V. Krishna, N. Stevens, B. Koopman, and B. Moudgil, "Optical heating and rapid transformation of functionalized fullerenes," *Nature Nanotechnology,* vol. 5, no. 5, pp. 330-334, 2010.

[103] B. Geng, D. Yang, D. Pan, L. Wang, F. Zheng, W. Shen, C. Zhang, and X. Li, "NIR-responsive carbon dots for efficient photothermal cancer therapy at low power densities," *Carbon,* vol. 134, pp. 153-162, 2018.

[104] X. Bao, Y. Yuan, J. Chen, B. Zhang, D. Li, D. Zhou, P. Jing, G. Xu, Y. Wang, and K. Holá, "In vivo theranostics with near-infrared-emitting carbon dots—highly efficient photothermal therapy based on passive targeting after intravenous administration," *Light: Science & Applications,* vol. 7, no. 1, pp. 1-11, 2018.

[105] Y. Shen, X. Zhang, L. Liang, J. Yue, D. Huang, W. Xu, W. Shi, C. Liang, and S. Xu, "Mitochondria-targeting supra-carbon dots: Enhanced photothermal therapy selective to cancer cells and their hyperthermia molecular actions," *Carbon,* vol. 156, pp. 558-567, 2020.

[106] S. Sun, L. Zhang, K. Jiang, A. Wu, and H. Lin, "Toward high-efficient red emissive carbon dots: facile preparation, unique properties, and applications as multifunctional theranostic agents," *Chemistry of Materials,* vol. 28, no. 23, pp. 8659-8668, 2016.

[107] Y. Li, G. Bai, S. Zeng, and J. Hao, "Theranostic carbon dots with innovative NIR-II emission for in vivo renal-excreted optical imaging and photothermal therapy," *ACS Applied Materials & Interfaces,* vol. 11, no. 5, pp. 4737-4744, 2019.

[108] A. R. Gul, T. N. Le, M. W. Kim, S. K. Kailasa, K. T. Oh, and T. J. Park, "One-pot synthesis of carbon dots with intrinsic folic acid for synergistic imaging-guided photothermal therapy of prostate cancer cells," *Biomaterials science,* vol. 7, no. 12, pp. 5187-5196, 2019.

[109] S. Pandey, M. Thakur, A. Mewada, D. Anjarlekar, N. Mishra, and M. Sharon, "Carbon dots functionalized gold nanorod mediated delivery of doxorubicin: tri-functional nano-worms for drug delivery, photothermal therapy and bioimaging," *Journal of Materials Chemistry B,* vol. 1, no. 38, pp. 4972-4982, 2013.

[110] R. Justin, K. Tao, S. Román, D. Chen, Y. Xu, X. Geng, I. M. Ross, R. T. Grant, A. Pearson, and G. Zhou, "Photoluminescent and superparamagnetic reduced graphene oxide–iron oxide quantum dots for dual-modality imaging, drug delivery and photothermal therapy," *Carbon,* vol. 97, pp. 54-70, 2016.

[111] X. Wang, X. Sun, H. He, H. Yang, J. Lao, Y. Song, Y. Xia, H. Xu, X. Zhang, and F. Huang, "A two-component active targeting theranostic agent based on graphene quantum dots," *Journal of Materials Chemistry B,* vol. 3, no. 17, pp. 3583-3590, 2015.

[112] S. H. Hu, Y. W. Chen, W. T. Hung, I. W. Chen, and S. Y. Chen, "Quantum-dot-tagged reduced graphene oxide nanocomposites for bright fluorescence bioimaging and photothermal therapy monitored in situ," *Advanced Materials,* vol. 24, no. 13, pp. 1748-1754, 2012.

[113] S. Li, S. Zhou, Y. Li, X. Li, J. Zhu, L. Fan, and S. Yang, "Exceptionally high payload of the IR780 iodide on folic acid-functionalized graphene quantum dots for targeted photothermal therapy," *ACS Applied Materials & Interfaces,* vol. 9, no. 27, pp. 22332-22341, 2017.

[114] H. Wang, Q. Mu, K. Wang, R. A. Revia, C. Yen, X. Gu, B. Tian, J. Liu, and M. Zhang, "Nitrogen and boron dual-doped graphene quantum dots for near-infrared second window imaging and photothermal therapy," *Applied materials today,* vol. 14, pp. 108-117, 2019.

[115] M. Guo, H.-J. Xiang, Y. Wang, Q.-L. Zhang, L. An, S.-P. Yang, Y. Ma, Y. Wang, and J.-G. Liu, "Ruthenium nitrosyl functionalized graphene quantum dots as an efficient nanoplatform for NIR-light-controlled and mitochondria-targeted delivery of nitric oxide combined with photothermal therapy," *Chemical Communications*, vol. 53, no. 22, pp. 3253-3256, 2017.

[116] N. W. S. Kam, M. O'Connell, J. A. Wisdom, and H. Dai, "Carbon nanotubes as multifunctional biological transporters and near-infrared agents for selective cancer cell destruction," *Proceedings of the National Academy of Sciences*, vol. 102, no. 33, pp. 11600-11605, 2005.

[117] X. Wang, C. Wang, L. Cheng, S.-T. Lee, and Z. Liu, "Noble metal coated single-walled carbon nanotubes for applications in surface enhanced Raman scattering imaging and photothermal therapy," *Journal of the American Chemical Society*, vol. 134, no. 17, pp. 7414-7422, 2012.

[118] H. K. Moon, S. H. Lee, and H. C. Choi, "In vivo near-infrared mediated tumor destruction by photothermal effect of carbon nanotubes," *ACS nano*, vol. 3, no. 11, pp. 3707-3713, 2009.

[119] B. Zhang, H. Wang, S. Shen, X. She, W. Shi, J. Chen, Q. Zhang, Y. Hu, Z. Pang, and X. Jiang, "Fibrin-targeting peptide CREKA-conjugated multi-walled carbon nanotubes for self-amplified photothermal therapy of tumor," *Biomaterials*, vol. 79, pp. 46-55, 2016.

[120] N. Huang, H. Wang, J. Zhao, H. Lui, M. Korbelik, and H. Zeng, "Single-wall carbon nanotubes assisted photothermal cancer therapy: Animal study with a murine model of squamous cell carcinoma," *Lasers in surgery and medicine*, vol. 42, no. 9, pp. 798-808, 2010.

[121] Z. Lin, Y. Liu, X. Ma, S. Hu, J. Zhang, Q. Wu, W. Ye, S. Zhu, D. Yang, and D. Qu, "Photothermal ablation of bone metastasis of breast cancer using PEGylated multi-walled carbon nanotubes," *Scientific reports*, vol. 5, p. 11709, 2015.

[122] S. Wang, Q. Zhang, P. Yang, X. Yu, L.-Y. Huang, S. Shen, and S. Cai, "Manganese oxide-coated carbon nanotubes as dual-modality lymph mapping agents for photothermal therapy of tumor metastasis," *ACS Applied Materials & Interfaces*, vol. 8, no. 6, pp. 3736-3743, 2016.

[123] J. Liu, C. Wang, X. Wang, X. Wang, L. Cheng, Y. Li, and Z. Liu, "Mesoporous silica coated single-walled carbon nanotubes as a multifunctional light-responsive platform for cancer combination therapy," *Advanced Functional Materials*, vol. 25, no. 3, pp. 384-392, 2015.

[124] Z. Sobhani, M. A. Behnam, F. Emami, A. Dehghanian, and I. Jamhiri, "Photothermal therapy of melanoma tumor using multiwalled carbon nanotubes," *International Journal of Nanomedicine*, vol. 12, p. 4509, 2017.

[125] J. W. Fisher, S. Sarkar, C. F. Buchanan, C. S. Szot, J. Whitney, H. C. Hatcher, S. V. Torti, C. G. Rylander, and M. N. Rylander, "Photothermal response of human and murine cancer cells to multiwalled carbon nanotubes after laser irradiation," *Cancer research*, vol. 70, no. 23, pp. 9855-9864, 2010.

[126] A. Burke, X. Ding, R. Singh, R. A. Kraft, N. Levi-Polyachenko, M. N. Rylander, C. Szot, C. Buchanan, J. Whitney, and J. Fisher, "Long-term survival following a single treatment of kidney tumors with multiwalled carbon nanotubes and near-infrared radiation," *Proceedings of the National Academy of Sciences*, vol. 106, no. 31, pp. 12897-12902, 2009.

[127] F. Zhou, X. Da, Z. Ou, B. Wu, D. E. Resasco, and W. R. Chen, "Cancer photothermal therapy in the near-infrared region by using single-walled carbon nanotubes," *Journal of biomedical optics*, vol. 14, no. 2, p. 021009, 2009.

[128] L. Wang, M. Zhang, N. Zhang, J. Shi, H. Zhang, M. Li, C. Lu, and Z. Zhang, "Synergistic enhancement of cancer therapy using a combination of docetaxel and photothermal ablation induced by single-walled carbon nanotubes," *International Journal of Nanomedicine*, vol. 6, p. 2641, 2011.

[129] J. T. Robinson, K. Welsher, S. M. Tabakman, S. P. Sherlock, H. Wang, R. Luong, and H. Dai, "High performance in vivo near-IR (> 1 μm) imaging and photothermal cancer therapy with carbon nanotubes," *Nano research*, vol. 3, no. 11, pp. 779-793, 2010.

[130] X. Liu, H. Tao, K. Yang, S. Zhang, S.-T. Lee, and Z. Liu, "Optimization of surface chemistry on single-walled carbon nanotubes for in vivo photothermal ablation of tumors," *Biomaterials*, vol. 32, no. 1, pp. 144-151, 2011.

[131] A. L. Antaris, J. T. Robinson, O. K. Yaghi, G. Hong, S. Diao, R. Luong, and H. Dai, "Ultra-low doses of chirality sorted (6, 5) carbon nanotubes for simultaneous tumor imaging and photothermal therapy," *ACS nano*, vol. 7, no. 4, pp. 3644-3652, 2013.

[132] X. Dong, Z. Sun, X. Wang, and X. Leng, "An innovative MWCNTs/DOX/TC nanosystem for chemo-photothermal combination therapy of cancer," *Nanomedicine: Nanotechnology, Biology and Medicine*, vol. 13, no. 7, pp. 2271-2280, 2017.

[133] J. Yang, H. Su, W. Sun, J. Cai, S. Liu, Y. Chai, and C. Zhang, "Dual chemodrug-loaded single-walled carbon nanohorns for multimodal imaging-guided chemo-photothermal therapy of tumors and lung metastases," *Theranostics*, vol. 8, no. 7, p. 1966, 2018.

[134] J. Wang, R. Wang, F. Zhang, Y. Yin, L. Mei, F. Song, M. Tao, W. Yue, and W. Zhong, "Overcoming multidrug resistance by a combination of chemotherapy and photothermal therapy mediated by carbon nanohorns," *Journal of Materials Chemistry B*, vol. 4, no. 36, pp. 6043-6051, 2016.

[135] J. R. Whitney, S. Sarkar, J. Zhang, T. Do, T. Young, M. K. Manson, T. A. Campbell, A. A. Puretzky, C. M. Rouleau, K. L. More, D. B. Geohegan, C. G. Rylander, H. C. Dorn, and M. N. Rylander, "Single walled carbon nanohorns as photothermal cancer agents," *Lasers in surgery and medicine*, vol. 43, no. 1, 2011.

[136] Z. M. Markovic, L. M. Harhaji-Trajkovic, B. M. Todorovic-Markovic, D. P. Kepić, K. M. Arsikin, S. P. Jovanović, A. C. Pantovic, M. D. Dramićanin, and V. S. Trajkovic, "In vitro comparison of the photothermal anticancer activity of graphene nanoparticles and carbon nanotubes. ," *Biomaterials*, vol. 32, no. 4, pp. 1121-1129, 2011.

[137] X. Qin, Z. Guo, Z. Liu, W. Zhang, M. Wan, and B. Yang, "Folic acid-conjugated graphene oxide for cancer targeted chemo-photothermal therapy," *Journal of Photochemistry and Photobiology B: Biology*, vol. 120, pp. 156-162, 2013.

[138] P. Gong, F. Wang, F. Guo, J. Liu, B. Wang, X. Ge, S. Li, J. You, and Z. Liu, "Fluorescence turn-off Ag/fluorinated graphene composites with high NIR absorption for effective killing of cancer cells and bacteria," *Journal of Materials Chemistry B*, vol. 6, no. 47, pp. 7926-7935, 2018.

[139] J. H. Lim, E.-J. Kim, C. D. Ahrberg, and B. G. Chung, "Functional graphene oxide-based nanosheets for photothermal therapy," *Macromolecular Research*, vol. 26, no. 6, pp. 557-565, 2018.

[140] Y.-W. Wang, Y.-Y. Fu, Q. Peng, S.-S. Guo, G. Liu, J. Li, H.-H. Yang, and G.-N. Chen, "Dye-enhanced graphene oxide for photothermal therapy and photoacoustic imaging," *Journal of Materials Chemistry B*, vol. 1, no. 42, pp. 5762-5767, 2013.

[141] Y. Liu, J. Bai, X. Jia, X. Jiang, and Z. Guo, "Fabrication of multifunctional SiO2@ GN-serum composites for chemo-photothermal synergistic therapy," *ACS Applied Materials & Interfaces*, vol. 7, no. 1, pp. 112-121, 2015.

[142] S. Su, J. Wang, E. Vargas, J. Wei, R. Martínez-Zaguilán, S. R. Sennoune, M. L. Pantoya, S. Wang, J. Chaudhuri, and J. Qiu, "Porphyrin immobilized nanographene oxide for enhanced and targeted photothermal therapy of brain cancer," *ACS Biomaterials Science & Engineering*, vol. 2, no. 8, pp. 1357-1366, 2016.

[143] X. Wang, Q. Han, N. Yu, J. Li, L. Yang, R. Yang, and C. Wang, "Aptamer–conjugated graphene oxide–gold nanocomposites for targeted chemo-photothermal therapy of cancer cells," *Journal of Materials Chemistry B*, vol. 3, no. 19, pp. 4036-4042, 2015.

[144] L. Yang, Y.-T. Tseng, G. Suo, L. Chen, J. Yu, W.-J. Chiu, C.-C. Huang, and C.-H. Lin, "Photothermal therapeutic response of cancer cells to aptamer–gold nanoparticle-hybridized graphene oxide under NIR illumination," *ACS Applied Materials & Interfaces*, vol. 7, no. 9, pp. 5097-5106, 2015.

[145] M. Guo, J. Huang, Y. Deng, H. Shen, Y. Ma, M. Zhang, A. Zhu, Y. Li, H. Hui, and Y. Wang, "pH-responsive cyanine-grafted graphene oxide for fluorescence resonance energy transfer-enhanced photothermal therapy," *Advanced Functional Materials*, vol. 25, no. 1, pp. 59-67, 2015.

[146] X. Shi, Gong, H., Li, Y., Wang, C., Cheng, L., & Liu, Z. , "Graphene-based magnetic plasmonic nanocomposite for dual bioimaging and photothermal therapy," *Biomaterials* vol. 34, no. 20, pp. 4786-4793, 2013.

[147] S. Wang, Q. Zhang, X. F. Luo, J. Li, H. He, F. Yang, Y. Di, C. Jin, X. G. Jiang, and S. Shen, "Magnetic graphene-based nanotheranostic agent for dual-modality mapping guided photothermal therapy in regional lymph nodal metastasis of pancreatic cancer," *Biomaterials*, vol. 35, no. 35, pp. 9473-9483, 2014.

[148] H. Xiong, Z. Guo, W. Zhang, H. Zhong, S. Liu, and Y. Ji, "Redox-responsive biodegradable PEGylated nanographene oxide for efficiently chemo-photothermal therapy: A comparative study with non-biodegradable PEGylated nanographene oxide," *Journal of Photochemistry and Photobiology B: Biology*, vol. 138, pp. 191-201, 2014.

[149] J. Bai, Y. Liu, and X. Jiang, "Multifunctional PEG-GO/CuS nanocomposites for near-infrared chemo-photothermal therapy," *Biomaterials*, vol. 35, no. 22, pp. 5805-5813, 2014.

[150] J. Li, Z. Lyv, Y. Li, H. Liu, J. Wang, W. Zhan, H. Chen, H. Chen, and X. Li, "A theranostic prodrug delivery system based on Pt (IV) conjugated nano-graphene oxide with synergistic effect to enhance the therapeutic efficacy of Pt drug," *Biomaterials*, vol. 51, pp. 12-21, 2015.

[151] H.-W. Yang, Y.-J. Lu, K.-J. Lin, S.-C. Hsu, C.-Y. Huang, S.-H. She, H.-L. Liu, C.-W. Lin, M.-C. Xiao, and S.-P. Wey, "EGRF conjugated PEGylated nanographene oxide for targeted chemotherapy and photothermal therapy," *Biomaterials*, vol. 34, no. 29, pp. 7204-7214, 2013.

[152] Y. Pang, Z. Mai, B. Wang, L. Wang, L. Wu, X. Wang, and T. Chen, "Artesunate-modified nano-graphene oxide for chemo-photothermal cancer therapy," *Oncotarget,* vol. 8, no. 55, p. 93800, 2017.

[153] Y. Wang, K. Wang, J. Zhao, X. Liu, J. Bu, X. Yan, and R. Huang, "Multifunctional mesoporous silica-coated graphene nanosheet used for chemo-photothermal synergistic targeted therapy of glioma," *Journal of the American Chemical Society,* vol. 135, no. 12, pp. 4799-4804, 2013.

[154] T. H. Tran, H. T. Nguyen, T. T. Pham, J. Y. Choi, H.-G. Choi, C. S. Yong, and J. O. Kim, "Development of a graphene oxide nanocarrier for dual-drug chemo-phototherapy to overcome drug resistance in cancer," *ACS Applied Materials & Interfaces,* vol. 7, no. 51, pp. 28647-28655, 2015.

[155] H. S. Jung, W. H. Kong, D. K. Sung, M.-Y. Lee, S. E. Beack, D. H. Keum, K. S. Kim, S. H. Yun, and S. K. Hahn, "Nanographene oxide–hyaluronic acid conjugate for photothermal ablation therapy of skin cancer," *ACS nano,* vol. 8, no. 1, pp. 260-268, 2014.

[156] L. Hou, Q. Feng, Y. Wang, H. Zhang, G. Jiang, X. Yang, J. Ren, X. Zhu, Y. Shi, and Z. Zhang, "Multifunctional nanosheets based on hyaluronic acid modified graphene oxide for tumor-targeting chemo-photothermal therapy," *Journal of Nanoparticle Research,* vol. 17, no. 3, p. 162, 2015.

[157] C. Xu, D. Yang, L. Mei, Q. Li, H. Zhu, and T. Wang, "Targeting chemophotothermal therapy of hepatoma by gold nanorods/graphene oxide core/shell nanocomposites," *ACS Applied Materials & Interfaces,* vol. 5, no. 24, pp. 12911-12920, 2013.

[158] Y. Jin, J. Wang, H. Ke, S. Wang, and Z. Dai, "Graphene oxide modified PLA microcapsules containing gold nanoparticles for ultrasonic/CT bimodal imaging guided photothermal tumor therapy," *Biomaterials,* vol. 34, no. 20, pp. 4794-4802, 2013.

[159] J. T. Robinson, S. M. Tabakman, Y. Liang, H. Wang, H. S. Casalongue, D. Vinh, and H. Dai, "Ultrasmall reduced graphene oxide with high near-infrared absorbance for photothermal therapy " *Journal of the American Chemical Society,* vol. 133, no. 17, pp. 6825-6831, 2011.

[160] L. Wang, M. Wang, B. Zhou, F. Zhou, C. Murray, R. A. Towner, N. Smith, D. Saunders, G. Xie, and W. R. Chen, "PEGylated reduced-graphene oxide hybridized with Fe3O4 nanoparticles for cancer photothermal-immunotherapy," *Journal of Materials Chemistry B,* vol. 7, no. 46, pp. 7406-7414, 2019.

[161] K. Turcheniuk, C.-H. Hage, L. Heliot, S. Railian, V. Zaitsev, J. Spadavecchia, R. Boukherroub, and S. Szunerits, "Infrared photothermal therapy with water soluble reduced graphene oxide: shape, size and reduction degree effects," *Nano Life,* vol. 5, no. 1, p. 1540002, 2015.

[162] H. Kim, D. Lee, J. Kim, T.-i. Kim, and W. J. Kim, "Photothermally triggered cytosolic drug delivery via endosome disruption using a functionalized reduced graphene oxide," *ACS nano,* vol. 7, no. 8, pp. 6735-6746, 2013.

[163] L. Shao, R. Zhang, J. Lu, C. Zhao, X. Deng, and Y. Wu, "Mesoporous silica coated polydopamine functionalized reduced graphene oxide for synergistic targeted chemo-photothermal therapy," *ACS Applied Materials & Interfaces,* vol. 9, no. 2, pp. 1226-1236, 2017.

[164] J. Yu, Y. H. Lin, L. Yang, C. C. Huang, L. Chen, W. C. Wang, G. W. Chen, J. Yan, S. Sawettanun, and C. H. Lin, "Improved anticancer photothermal therapy using the bystander effect enhanced by antiarrhythmic peptide conjugated dopamine-modified reduced graphene oxide nanocomposite," *Advanced healthcare materials,* vol. 6, no. 2, p. 1600804, 2017.

[165] Z. Sheng, L. Song, J. Zheng, D. Hu, M. He, M. Zheng, G. Gao, P. Gong, P. Zhang, and Y. Ma, "Protein-assisted fabrication of nano-reduced graphene oxide for combined in vivo photoacoustic imaging and photothermal therapy," *Biomaterials,* vol. 34, no. 21, pp. 5236-5243, 2013.

[166] Y. A. Cheon, J. H. Bae, and B. G. Chung, "Reduced graphene oxide nanosheet for chemo-photothermal therapy," *Langmuir,* vol. 32, no. 11, pp. 2731-2736, 2016.

[167] W. Miao, G. Shim, G. Kim, S. Lee, H.-J. Lee, Y. B. Kim, Y. Byun, and Y.-K. Oh, "Image-guided synergistic photothermal therapy using photoresponsive imaging agent-loaded graphene-based nanosheets," *Journal of Controlled Release,* vol. 211, pp. 28-36, 2015.

[168] M. Abdolahad, M. Janmaleki, S. Mohajerzadeh, O. Akhavan, and S. Abbasi, "Polyphenols attached graphene nanosheets for high efficiency NIR mediated photodestruction of cancer cells," *Materials Science and Engineering: C,* vol. 33, no. 3, pp. 1498-1505, 2013.

[169] C. Wang, X. Wang, Y. Chen, and Z. Fang, "In-vitro photothermal therapy using plant extract polyphenols functionalized graphene sheets for treatment of lung cancer," *Journal of Photochemistry and Photobiology B: Biology,* vol. 204, p. 111587, 2020.

[170] C. C. Barrera, H. Groot, W. L. Vargas, and D. M. Narváez, "Efficacy and Molecular Effects of a Reduced Graphene Oxide/Fe3O4 Nanocomposite in Photothermal Therapy Against Cancer," *International Journal of Nanomedicine,* vol. 15, p. 6421, 2020.

[171] K. Yang, J. Wan, S. Zhang, B. Tian, Y. Zhang, and Z. Liu, "The influence of surface chemistry and size of nanoscale graphene oxide on photothermal therapy of cancer using ultra-low laser power," *Biomaterials,* vol. 33, no. 7, pp. 2206-2214, 2012.

[172] K. Yang, L. Hu, X. Ma, S. Ye, L. Cheng, X. Shi, C. Li, Y. Li, and Z. Liu, "Multimodal imaging guided photothermal therapy using functionalized graphene nanosheets anchored with magnetic nanoparticles," *Advanced Materials,* vol. 24, no. 14, pp. 1868-1872, 2012.

[173] J. Wu, Z. Li, Y. Li, A. Pettitt, and F. Zhou, "Photothermal effects of reduced graphene oxide on pancreatic cancer," *Technology in cancer research & treatment,* vol. 17, p. 1533034618768637, 2018.

[174] L. Feng, K. Li, X. Shi, M. Gao, J. Liu, and Z. Liu, "Smart pH-responsive nanocarriers based on nano-graphene oxide for combined chemo-and photothermal therapy overcoming drug resistance," *Advanced healthcare materials,* vol. 3, no. 8, pp. 1261-1271, 2014.

[175] C. Hou, M. Wang, L. Guo, Q. Jia, and J. Ge, "Carbon Dot Assemblies for Enhanced Cellular Uptake and Photothermal Therapy In Vitro," *ChemistrySelect,* vol. 2, no. 33, pp. 10860-10864, 2017.

[176] Y. Bai, B. Zhang, L. Chen, Z. Lin, X. Zhang, D. Ge, W. Shi, and Y. Sun, "Facile one-pot synthesis of polydopamine carbon dots for photothermal therapy," *Nanoscale Research Letters,* vol. 13, no. 1, pp. 1-9, 2018.

[177] Z. Tian, X. Yao, K. Ma, X. Niu, J. Grothe, Q. Xu, L. Liu, S. Kaskel, and Y. Zhu, "Metal–organic framework/graphene quantum dot nanoparticles used for synergistic chemo-and photothermal therapy," *ACS omega,* vol. 2, no. 3, pp. 1249-1258, 2017.

[178] A. Burlaka, S. Lukin, S. Prylutska, O. Remeniak, Y. Prylutskyy, M. Shuba, S. Maksimenko, U. Ritter, and P. Scharff, "Hyperthermic effect of multi-walled carbon nanotubes stimulated with near infrared irradiation for anticancer therapy: in vitro studies," *Experimental Oncology,* vol. 32, no. 1, pp. 48-50, 2010.

[179] S. V. Torti, F. Byrne, O. Whelan, N. Levi, B. Ucer, M. Schmid, F. M. Torti, S. Akman, J. Liu, and P. M. Ajayan, "Thermal ablation therapeutics based on CNx multi-walled nanotubes," *International Journal of Nanomedicine,* vol. 2, no. 4, p. 707, 2007.

[180] C. Liang, S. Diao, C. Wang, H. Gong, T. Liu, G. Hong, X. Shi, H. Dai, and Z. Liu, "Tumor metastasis inhibition by imaging-guided photothermal therapy with single-walled carbon nanotubes," *Advanced Materials,* vol. 26, no. 32, pp. 5646-5652, 2014.

[181] Y. Zhu, Q. Sun, Y. Liu, T. Ma, L. Su, S. Liu, X. Shi, D. Han, and F. Liang, "Decorating gold nanostars with multiwalled carbon nanotubes for photothermal therapy," *Royal Society Open Science,* vol. 5, no. 8, p. 180159, 2018.

[182] L. F. Neves, J. J. Krais, B. D. Van Rite, R. Ramesh, D. E. Resasco, and R. G. Harrison, "Targeting single-walled carbon nanotubes for the treatment of breast cancer using photothermal therapy," *Nanotechnology,* vol. 24, no. 37, p. 375104, 2013.

[183] L. Meng, W. Xia, L. Liu, L. Niu, and Q. Lu, "Golden single-walled carbon nanotubes prepared using double layer polysaccharides bridge for photothermal therapy," *ACS Applied Materials & Interfaces,* vol. 6, no. 7, pp. 4989-4996, 2014.

[184] D. Chen, C. Wang, F. Jiang, Z. Liu, C. Shu, and L.-J. Wan, "In vitro and in vivo photothermally enhanced chemotherapy by single-walled carbon nanohorns as a drug delivery system," *Journal of Materials Chemistry B,* vol. 2, no. 29, pp. 4726-4732, 2014.

[185] O. Akhavan, E. Ghaderi, S. Aghayee, Y. Fereydooni, and A. Talebi, "The use of a glucose-reduced graphene oxide suspension for photothermal cancer therapy," *Journal of Materials Chemistry,* vol. 22, no. 27, pp. 13773-13781, 2012.

[186] L.-X. Gai, W.-Q. Wang, X. Wu, X.-J. Su, and F.-C. Yang, "NIR absorbing reduced graphene oxide for photothermal radiotherapy for treatment of esophageal cancer," *Journal of Photochemistry and Photobiology B: Biology,* vol. 194, pp. 188-193, 2019.

[187] X. Chen, C. Li, X. Wang, and X. Zhao, "Infrared heating of reduced graphene oxide nanosheets as photothermal radiation therapeutic agents for tumor regressions," *Materials Research Express,* vol. 6, no. 8, p. 085080, 2019.

[188] H. Wan, Y. Zhang, Z. Liu, G. Xu, G. Huang, Y. Ji, Z. Xiong, Q. Zhang, J. Dong, and W. Zhang, "Facile fabrication of a near-infrared responsive nanocarrier for spatiotemporally controlled chemo-photothermal synergistic cancer therapy," *Nanoscale,* vol. 6, no. 15, pp. 8743-8753, 2014.

[189] H. Liu, T. Li, Y. Liu, G. Qin, X. Wang, and T. Chen, "Glucose-reduced graphene oxide with excellent biocompatibility and photothermal efficiency as well as drug loading," *Nanoscale research letters,* vol. 11, no. 1, pp. 1-10, 2016.

[190] J. Chen, H. Liu, C. Zhao, G. Qin, G. Xi, T. Li, X. Wang, and T. Chen, "One-step reduction and PEGylation of graphene oxide for photothermally controlled drug delivery," *Biomaterials,* vol. 35, no. 18, pp. 4986-4995, 2014.

[191] S. C. Patel, S. Lee, G. Lalwani, C. Suhrland, S. M. Chowdhury, and B. Sitharaman, "Graphene-based platforms for cancer therapeutics," *Therapeutic delivery,* vol. 7, no. 2, pp. 101-116, 2016.

[192] D. J. Lee, Y. S. Ahn, Y. S. Youn, and E. S. Lee, "Poly (ethylene glycol)-crosslinked fullerenes for high efficient phototherapy," *Polymers for advanced technologies,* vol. 24, no. 2, pp. 220-227, 2013.

[193] H. Wang, P. Agarwal, S. Zhao, J. Yu, X. Lu, and X. He, "Combined cancer therapy with hyaluronan-decorated fullerene-silica multifunctional nanoparticles to target cancer stem-like cells," *Biomaterials,* vol. 97, pp. 62-73, 2016.

[194] X.-L. Guo, Z.-Y. Ding, S.-M. Deng, C.-C. Wen, X.-C. Shen, B.-P. Jiang, and H. Liang, "A novel strategy of transition-metal doping to engineer absorption of carbon dots for near-infrared photothermal/photodynamic therapies," *Carbon,* vol. 134, pp. 519-530, 2018.

[195] B. Wei, F. Dong, W. Yang, C. Luo, Q. Dong, Z. Zhou, Z. Yang, and L. Sheng, "Synthesis of carbon-dots@ SiO2@ TiO2 nanoplatform for photothermal imaging induced multimodal synergistic antitumor," *Journal of Advanced Research,* vol. 23, pp. 13-23, 2020.

[196] M. Lan, L. Guo, S. Zhao, Z. Zhang, Q. Jia, L. Yan, J. Xia, H. Zhang, P. Wang, and W. Zhang, "Carbon dots as multifunctional phototheranostic agents for photoacoustic/fluorescence imaging and photothermal/photodynamic synergistic cancer therapy," *Advanced Therapeutics,* vol. 1, no. 6, p. 1800077, 2018.

[197] S. Sun, J. Chen, K. Jiang, Z. Tang, Y. Wang, Z. Li, C. Liu, A. Wu, and H. Lin, "Ce6-modified carbon dots for multimodal-imaging-guided and single-NIR-laser-triggered photothermal/photodynamic synergistic cancer therapy by reduced irradiation power," *ACS Applied Materials & Interfaces,* vol. 11, no. 6, pp. 5791-5803, 2019.

[198] M. Nurunnabi, Z. Khatun, G. R. Reeck, D. Y. Lee, and Y.-k. Lee, "Photoluminescent graphene nanoparticles for cancer phototherapy and imaging," *ACS Applied Materials & Interfaces,* vol. 6, no. 15, pp. 12413-12421, 2014.

[199] F. Wo, R. Xu, Y. Shao, Z. Zhang, M. Chu, D. Shi, and S. Liu, "A multimodal system with synergistic effects of magneto-mechanical, photothermal, photodynamic and chemo therapies of cancer in graphene-quantum dot-coated hollow magnetic nanospheres," *Theranostics,* vol. 6, no. 4, p. 485, 2016.

[200] L. Xie, G. Wang, H. Zhou, F. Zhang, Z. Guo, C. Liu, X. Zhang, and L. Zhu, "Functional long circulating single walled carbon nanotubes for fluorescent/photoacoustic imaging-guided enhanced phototherapy," *Biomaterials,* vol. 103, pp. 219-228, 2016.

[201] G. Wang, F. Zhang, R. Tian, L. Zhang, G. Fu, L. Yang, and L. Zhu, "Nanotubes-embedded indocyanine green–hyaluronic acid nanoparticles for photoacoustic-imaging-guided phototherapy," *ACS Applied Materials & Interfaces,* vol. 8, no. 8, pp. 5608-5617, 2016.

[202] P. Zhang, H. Huang, J. Huang, H. Chen, J. Wang, K. Qiu, D. Zhao, L. Ji, and H. Chao, "Noncovalent ruthenium (II) complexes–single-walled carbon nanotube composites for bimodal photothermal and photodynamic therapy with near-infrared irradiation," *ACS Applied Materials & Interfaces,* vol. 7, no. 41, pp. 23278-23290, 2015.

[203] T. Murakami, H. Nakatsuji, M. Inada, Y. Matoba, T. Umeyama, M. Tsujimoto, S. Isoda, M. Hashida, and H. Imahori, "Photodynamic and photothermal effects of semiconducting and metallic-enriched single-walled carbon nanotubes," *Journal of the American Chemical Society,* vol. 134, no. 43, pp. 17862-17865, 2012.

[204] Z. Lin, B.-P. Jiang, J. Liang, C. Wen, and X.-C. Shen, "Phycocyanin functionalized single-walled carbon nanohorns hybrid for near-infrared light-mediated cancer phototheranostics," *Carbon,* vol. 143, pp. 814-827, 2019.

[205] C. Gao, J. Jian, Z. Lin, Y.-X. Yu, B.-P. Jiang, H. Chen, and X.-C. Shen, "Hypericin-Loaded Carbon Nanohorn Hybrid for Combined Photodynamic and Photothermal Therapy in Vivo," *Langmuir,* vol. 35, no. 25, pp. 8228-8237, 2019.

[206] M. Zhang, T. Murakami, K. Ajima, K. Tsuchida, A. S. Sandanayaka, O. Ito, S. Iijima, and M. Yudasaka, "Fabrication of ZnPc/protein nanohorns for double photodynamic and hyperthermic cancer phototherapy," *Proceedings of the National Academy of Sciences,* vol. 105, no. 39, pp. 14773-14778, 2008.

[207] Z. Zhou, Y. Zheng, C. C. Zhang, J. Gao, Y. Tang, and Q. Wang, "In vitro and in vivo studies of a chlorin-based carbon nanocarrier with photodynamic therapy features," *Photochemical & Photobiological Sciences,* vol. 17, no. 10, pp. 1329-1336, 2018.

[208] C. Gao, P. Dong, Z. Lin, X. Guo, B. P. Jiang, S. Ji, H. Liang, and X. C. Shen, "Near-infrared light responsive imaging-guided photothermal and photodynamic synergistic therapy nanoplatform based on carbon Nanohorns for efficient cancer treatment," *Chemistry–A European Journal*, vol. 24, no. 49, pp. 12827-12837, 2018.

[209] B. P. Jiang, L. F. Hu, D. J. Wang, S. C. Ji, X. C. Shen, and H. Liang, "Graphene loading water-soluble phthalocyanine for dual-modality photothermal/photodynamic therapy via a one-step method," *Journal of Materials Chemistry B*, vol. 2, no. 41, pp. 7141-7148, 2014.

[210] Y. Su, N. Wang, B. Liu, Y. Du, R. Li, Y. Meng, Y. Feng, Z. Shan, and S. Meng, "A phototheranostic nanoparticle for cancer therapy fabricated by BODIPY and graphene to realize photo-chemo synergistic therapy and fluorescence/photothermal imaging," *Dyes and Pigments*, vol. 177, p. 108262, 2020.

[211] A. Sahu, W. I. Choi, J. H. Lee, and G. Tae, "Graphene oxide mediated delivery of methylene blue for combined photodynamic and photothermal therapy," *Biomaterials*, vol. 34, no. 26, pp. 6239-6248, 2013.

[212] S. Luo, Z. Yang, X. Tan, Y. Wang, Y. Zeng, Y. Wang, C. Li, R. Li, and C. Shi, "Multifunctional photosensitizer grafted on polyethylene glycol and polyethylenimine dual-functionalized nanographene oxide for cancer-targeted near-infrared imaging and synergistic phototherapy," *ACS Applied Materials & Interfaces*, vol. 8, no. 27, pp. 17176-17186, 2016.

[213] P. Kalluru, R. Vankayala, C. S. Chiang, and K. C. Hwang, "Nano-graphene oxide-mediated In vivo fluorescence imaging and bimodal photodynamic and photothermal destruction of tumors," *Biomaterials*, vol. 95, pp. 1-10, 2016.

[214] C. Wu, D. Li, L. Wang, X. Guan, Y. Tian, H. Yang, S. Li, and Y. Liu, "Single wavelength light-mediated, synergistic bimodal cancer photoablation and amplified photothermal performance by graphene/gold nanostar/photosensitizer theranostics," *Acta biomaterialia*, vol. 53, pp. 631-642, 2017.

[215] A. Gulzar, J. Xu, D. Yang, L. Xu, F. He, S. Gai, and P. Yang, "Nano-graphene oxide-UCNP-Ce6 covalently constructed nanocomposites for NIR-mediated bioimaging and PTT/PDT combinatorial therapy," *Dalton Transactions*, vol. 47, no. 11, pp. 3931-3939, 2018.

[216] M. S. C. dos Santos, A. L. Gouvêa, L. D. de Moura, L. G. Paterno, P. E. N. de Souza, A. P. Bastos, E. A. M. Damasceno, F. H. Veiga-Souza, R. B. de Azevedo, and S. N. Báo, "Nanographene oxide-methylene blue as phototherapies platform for breast tumor ablation and metastasis prevention in a syngeneic orthotopic murine model," *Journal of nanobiotechnology*, vol. 16, no. 1, pp. 1-17, 2018.

[217] Z. Hu, J. Li, Y. Huang, L. Chen, and Z. Li, "Functionalized graphene/C 60 nanohybrid for targeting photothermally enhanced photodynamic therapy," *RSC advances*, vol. 5, no. 1, pp. 654-664, 2015.

[218] M. Ma, L. Cheng, A. Zhao, H. Zhang, and A. Zhang, "Pluronic-based graphene oxide-methylene blue nanocomposite for photodynamic/photothermal combined therapy of cancer cells," *Photodiagnosis and Photodynamic Therapy*, vol. 29, p. 101640, 2020.

[219] D.-Y. Zhang, Y. Zheng, C.-P. Tan, J.-H. Sun, W. Zhang, L.-N. Ji, and Z.-W. Mao, "Graphene oxide decorated with Ru (II)–polyethylene glycol complex for lysosome-targeted imaging and photodynamic/photothermal therapy," *ACS Applied Materials & Interfaces*, vol. 9, no. 8, pp. 6761-6771, 2017.

[220] Q. Wu, M. Chu, Y. Shao, F. Wo, and D. Shi, "Reduced graphene oxide conjugated with CuInS2/ZnS nanocrystals with low toxicity for enhanced photothermal and photodynamic cancer therapies," *Carbon*, vol. 108, pp. 21-37, 2016.

[221] B. Tian, C. Wang, S. Zhang, L. Feng, and Z. Liu, "Photothermally enhanced photodynamic therapy delivered by nano-graphene oxide," *ACS nano*, vol. 5, no. 9, pp. 7000-7009, 2011.

[222] M. Thakur, M. K. Kumawat, and R. Srivastava, "Multifunctional graphene quantum dots for combined photothermal and photodynamic therapy coupled with cancer cell tracking applications," *RSC advances*, vol. 7, no. 9, pp. 5251-5261, 2017.

[223] Y. Cao, H. Dong, Z. Yang, X. Zhong, Y. Chen, W. Dai, and X. Zhang, "Aptamer-conjugated graphene quantum dots/porphyrin derivative theranostic agent for intracellular cancer-related microRNA detection and fluorescence-guided photothermal/photodynamic synergetic therapy," *ACS Applied Materials & Interfaces*, vol. 9, no. 1, pp. 159-166, 2017.

[224] B.-P. Jiang, L.-F. Hu, X.-C. Shen, S.-C. Ji, Z. Shi, C.-J. Liu, L. Zhang, and H. Liang, "One-step preparation of a water-soluble carbon nanohorn/phthalocyanine hybrid for dual-modality photothermal and photodynamic therapy," *ACS Applied Materials & Interfaces*, vol. 6, no. 20, pp. 18008-18017, 2014.

[225] G. Gollavelli and Y.-C. Ling, "Magnetic and fluorescent graphene for dual modal imaging and single light induced photothermal and photodynamic therapy of cancer cells," *Biomaterials*, vol. 35, no. 15, pp. 4499-4507, 2014.

[226] Y. Wang, H. Wang, D. Liu, S. Song, X. Wang, and H. Zhang, "Graphene oxide covalently grafted upconversion nanoparticles for combined NIR mediated imaging and photothermal/photodynamic cancer therapy," *Biomaterials*, vol. 34, no. 31, pp. 7715-7724, 2013.

[227] Y. Cho, H. Kim, and Y. Choi, "A graphene oxide–photosensitizer complex as an enzyme-activatable theranostic agent," *Chemical Communications*, vol. 49, no. 12, pp. 1202-1204, 2013.

[228] C. Wu, A. Zhu, D. Li, L. Wang, H. Yang, H. Zeng, and Y. Liu, "Photosensitizer-assembled PEGylated graphene-copper sulfide nanohybrids as a synergistic near-infrared phototherapeutic agent," *Expert opinion on drug delivery*, vol. 13, no. 1, pp. 155-165, 2016.

[229] Y. K. Kim, H. K. Na, S. Kim, H. Jang, S. J. Chang, and D. H. Min, "One-Pot Synthesis of Multifunctional Au@ Graphene Oxide Nanocolloid Core@ Shell Nanoparticles for Raman Bioimaging, Photothermal, and Photodynamic Therapy," *Small*, vol. 11, no. 21, pp. 2527-2535, 2015.

[230] R. K. Thapa, Z. C. Soe, W. Ou, K. Poudel, J. H. Jeong, S. G. Jin, S. K. Ku, H. G. Choi, Y. M. Lee, C. S. Yong, and J. O. Kim, "Palladium nanoparticle-decorated 2-D graphene oxide for effective photodynamic and photothermal therapy of prostate solid tumors," *Colloids and Surfaces B: Biointerfaces*, vol. 169, pp. 429-437, 2018.

[231] Q. Li, L. Hong, H. Li, and C. Liu, "Graphene oxide-fullerene C60 (GO-C60) hybrid for photodynamic and photothermal therapy triggered by near-infrared light," *Biosensors and Bioelectronics*, vol. 89, pp. 477-482, 2017.

[232] Z. Hu, C. Wang, F. Zhao, X. Xu, S. Wang, L. Yu, D. Zhang, and Y. Huang, "Fabrication of a graphene/C 60 nanohybrid via γ-cyclodextrin host–guest chemistry for photodynamic and photothermal therapy," *Nanoscale*, vol. 9, no. 25, pp. 8825-8833, 2017.

[233] X. Yan, H. Hu, J. Lin, A. J. Jin, G. Niu, S. Zhang, P. Huang, B. Shen, and X. Chen, "Optical and photoacoustic dual-modality imaging guided synergistic photodynamic/photothermal therapies," *Nanoscale*, vol. 7, no. 6, pp. 2520-2526, 2015.

[234] G. Shim, M. G. Kim, H. Jin, J. Kim, and Y. K. Oh, "Claudin 4-targeted nanographene phototherapy using a Clostridium perfringens enterotoxin peptide-photosensitizer conjugate," *Acta Pharmacologica Sinica*, vol. 38, no. 6, pp. 954-962, 2017.

[235] Z. Chen, Z. Li, J. Wang, E. Ju, L. Zhou, J. Ren, and X. Qu, "A multi-synergistic platform for sequential irradiation-activated high-performance apoptotic cancer therapy," *Advanced Functional Materials*, vol. 24, no. 4, pp. 522-529, 2014.

[236] C.-H. Lin, Y.-C. Chen, and P.-I. Huang, "Preparation of Multifunctional Dopamine-Coated Zerovalent Iron/Reduced Graphene Oxide for Targeted Phototheragnosis in Breast Cancer," *Nanomaterials*, vol. 10, no. 10, p. 1957, 2020.

[237] W. Jiang, F. Mo, X. Jin, L. Chen, L. J. Xu, L. Guo, and F. Fu, "Tumor-Targeting Photothermal Heating-Responsive Nanoplatform Based on Reduced Graphene Oxide/Mesoporous Silica/Hyaluronic Acid Nanocomposite for Enhanced Photodynamic Therapy," *Advanced Materials Interfaces*, vol. 4, no. 20, p. 1700425, 2017.

[238] S. Singh and H. S. Nalwa, "Nanotechnology and health safety–toxicity and risk assessments of nanostructured materials on human health," *Journal of nanoscience and nanotechnology*, vol. 7, no. 9, pp. 3048-3070, 2007.

[239] C. M. Sayes, J. D. Fortner, W. Guo, D. Lyon, A. M. Boyd, K. D. Ausman, Y. J. Tao, B. Sitharaman, L. J. Wilson, and J. B. Hughes, "The differential cytotoxicity of water-soluble fullerenes," *Nano letters*, vol. 4, no. 10, pp. 1881-1887, 2004.

[240] G. Jia, H. Wang, L. Yan, X. Wang, R. Pei, T. Yan, Y. Zhao, and X. Guo, "Cytotoxicity of carbon nanomaterials: single-wall nanotube, multi-wall nanotube, and fullerene," *Environmental science & technology*, vol. 39, no. 5, pp. 1378-1383, 2005.

[241] S. Fiorito, A. Serafino, F. Andreola, and P. Bernier, "Effects of fullerenes and single-wall carbon nanotubes on murine and human macrophages," *Carbon*, vol. 44, no. 6, pp. 1100-1105, 2006.

[242] X. Yuan, X. Zhang, L. Sun, Y. Wei, and X. Wei, "Cellular toxicity and immunological effects of carbon-based nanomaterials," *Particle and fibre toxicology*, vol. 16, no. 1, p. 18, 2019.

[243] B. Fadeel, C. Bussy, S. Merino, E. Vázquez, E. Flahaut, F. Mouchet, L. Evariste, L. Gauthier, A. J. Koivisto, and U. Vogel, "Safety assessment of graphene-based materials: focus on human health and the environment," *ACS nano*, vol. 12, no. 11, pp. 10582-10620, 2018.

[244] B. Ma, C. Martín, R. Kurapati, and A. Bianco, "Degradation-by-design: how chemical functionalization enhances the biodegradability and safety of 2D materials," *Chemical Society Reviews*, vol. 49, no. 17, pp. 6224-6247, 2020.

[245] C.-W. Lam, J. T. James, R. McCluskey, and R. L. Hunter, "Pulmonary toxicity of single-wall carbon nanotubes in mice 7 and 90 days after intratracheal instillation," *Toxicological sciences*, vol. 77, no. 1, pp. 126-134, 2004.

[246] D. B. Warheit, B. R. Laurence, K. L. Reed, D. H. Roach, G. A. Reynolds, and T. R. Webb, "Comparative pulmonary toxicity assessment of single-wall carbon nanotubes in rats," *Toxicological sciences*, vol. 77, no. 1, pp. 117-125, 2004.

[247] G. k. M. Mutlu, G. S. Budinger, A. A. Green, D. Urich, S. Soberanes, S. E. Chiarella, G. F. Alheid, D. R. McCrimmon, I. Szleifer, and M. C. Hersam, "Biocompatible nanoscale dispersion of single-walled carbon nanotubes minimizes in vivo pulmonary toxicity," *Nano letters*, vol. 10, no. 5, pp. 1664-1670, 2010.

[248] Z. Liu, W. Cai, L. He, N. Nakayama, K. Chen, X. Sun, X. Chen, and H. Dai, "In vivo biodistribution and highly efficient tumour targeting of carbon nanotubes in mice," *Nature nanotechnology*, vol. 2, no. 1, pp. 47-52, 2007.

[249] C. A. Poland, R. Duffin, I. Kinloch, A. Maynard, W. A. Wallace, A. Seaton, V. Stone, S. Brown, W. MacNee, and K. Donaldson, "Carbon nanotubes introduced into the abdominal cavity of mice show asbestos-like pathogenicity in a pilot study," *Nature nanotechnology*, vol. 3, no. 7, p. 423, 2008.

[250] X. Zhang, J. Yin, C. Peng, W. Hu, Z. Zhu, W. Li, C. Fan, and Q. Huang, "Distribution and biocompatibility studies of graphene oxide in mice after intravenous administration," *Carbon*, vol. 49, no. 3, pp. 986-995, 2011.

[251] M. C. Duch, G. S. Budinger, Y. T. Liang, S. Soberanes, D. Urich, S. E. Chiarella, L. A. Campochiaro, A. Gonzalez, N. S. Chandel, and M. C. Hersam, "Minimizing oxidation and stable nanoscale dispersion improves the biocompatibility of graphene in the lung," *Nano letters*, vol. 11, no. 12, pp. 5201-5207, 2011.

[252] K. Yang, J. Wan, S. Zhang, Y. Zhang, S.-T. Lee, and Z. Liu, "In vivo pharmacokinetics, long-term biodistribution, and toxicology of PEGylated graphene in mice," *ACS nano*, vol. 5, no. 1, pp. 516-522, 2011.

[253] D. C. Marcano, D. V. Kosynkin, J. M. Berlin, A. Sinitskii, Z. Sun, A. Slesarev, L. B. Alemany, W. Lu, and J. M. Tour, "Improved synthesis of graphene oxide," *ACS nano*, vol. 4, no. 8, pp. 4806-4814, 2010.

[254] A. M. Pinto, F. D. Magalhães, and I. C. Gonçalves, "Polymer surface adsorption as a strategy to improve the biocompatibility of graphene nanoplatelets," *Colloids and Surfaces B: Biointerfaces*, vol. 146, pp. 818-824, 2016.

[255] A. Kumar and C. K. Dixit, "Methods for characterization of nanoparticles," in *Advances in nanomedicine for the delivery of therapeutic nucleic acids*: Elsevier, 2017, pp. 43-58.

[256] J. Amaro-Gahete, A. Benítez, R. Otero, D. Esquivel, C. Jiménez-Sanchidrián, J. Morales, Á. Caballero, and F. J. Romero-Salguero, "A comparative study of particle size distribution of graphene nanosheets synthesized by an ultrasound-assisted method," *Nanomaterials*, vol. 9, no. 2, p. 152, 2019.

[257] A. F. Rodrigues, L. Newman, N. Lozano, S. P. Mukherjee, B. Fadeel, C. Bussy, and K. Kostarelos, "A blueprint for the synthesis and characterisation of thin graphene oxide with controlled lateral dimensions for biomedicine," *2D Materials*, vol. 5, no. 3, p. 035020, 2018.

[258] R. Ibrahim, F. S. A. Suhail, and H. K. Al-Hakeim, "Stability of anticancer drug 5-fluorouracil in aqueous solution: an assessment of kinetic behavior," *Nano Biomed. Eng*, vol. 10, no. 3, pp. 224-234, 2018.

[259] M. J. Al-Awady, A. Fauchet, G. M. Greenway, and V. N. Paunov, "Enhanced antimicrobial effect of berberine in nanogel carriers with cationic surface functionality," *Journal of Materials Chemistry B*, vol. 5, no. 38, pp. 7885-7897, 2017.

[260] S. Sahoo, C. Chakraborti, S. Naik, S. Mishra, and U. Nanda, "Structural analysis of ciprofloxacin-carbopol polymeric composites by X-Ray diffraction and Fourier transform infra-red spectroscopy," *Tropical Journal of Pharmaceutical Research*, vol. 10, no. 3, 2011.

[261] Y. Gu, R. Lu, D. Si, and C. Liu, "Determination of 5-fluorouracil in human plasma by high-performance liquid chromatography (HPLC)," *Transactions of Tianjin University*, vol. 16, no. 3, pp. 167-173, 2010.

[262] J. Dun, X. Chen, H. Gao, Y. Zhang, H. Zhang, and Y. Zhang, "Resveratrol synergistically augments anti-tumor effect of 5-FU in vitro and in vivo by increasing S-phase arrest and tumor apoptosis," *Experimental Biology and Medicine*, vol. 240, no. 12, pp. 1672-1681, 2015.

[263] R. Petrilli, J. O Eloy, R. FV Lopez, and R. J Lee, "Cetuximab immunoliposomes enhance delivery of 5-FU to skin squamous carcinoma cells," *Anti-Cancer Agents in Medicinal Chemistry (Formerly Current Medicinal Chemistry-Anti-Cancer Agents)*, vol. 17, no. 2, pp. 301-308, 2017.

[264] T. Lammel, P. Boisseaux, M.-L. Fernández-Cruz, and J. M. Navas, "Internalization and cytotoxicity of graphene oxide and carboxyl graphene nanoplatelets in the human hepatocellular carcinoma cell line Hep G2," (in eng), *Particle and fibre toxicology,* vol. 10, pp. 27-27, 2013.

[265] L. Timochenco, R. Costa-Almeida, D. Bogas, F. A. Silva, J. Silva, A. Pereira, F. D. Magalhães, and A. M. Pinto, "High-yield production of nano-lateral size graphene oxide by high-power ultrasonication," *Materials,* vol. 14, no. 8, p. 1916, 2021.

[266] J. Shen, Y. Hu, M. Shi, X. Lu, C. Qin, C. Li, and M. Ye, "Fast and facile preparation of graphene oxide and reduced graphene oxide nanoplatelets," *Chemistry of materials,* vol. 21, no. 15, pp. 3514-3520, 2009.

[267] S. Stankovich, D. A. Dikin, R. D. Piner, K. A. Kohlhaas, A. Kleinhammes, Y. Jia, Y. Wu, S. T. Nguyen, and R. S. Ruoff, "Synthesis of graphene-based nanosheets via chemical reduction of exfoliated graphite oxide," *Carbon,* vol. 45, no. 7, pp. 1558-1565, 2007.

[268] M. Wojtoniszak, X. Chen, R. J. Kalenczuk, A. Wajda, J. Łapczuk, M. Kurzewski, M. Drozdzik, P. K. Chu, and E. Borowiak-Palen, "Synthesis, dispersion, and cytocompatibility of graphene oxide and reduced graphene oxide," *Colloids and Surfaces B: Biointerfaces,* vol. 89, pp. 79-85, 2012.

[269] I. A. Alvi, J. Madan, D. Kaushik, S. Sardana, R. S. Pandey, and A. Ali, "Comparative study of transfersomes, liposomes, and niosomes for topical delivery of 5-fluorouracil to skin cancer cells: preparation, characterization, in-vitro release, and cytotoxicity analysis," *Anti-cancer drugs,* vol. 22, no. 8, pp. 774-782, 2011.

[270] P. P. G. Guimarães, S. R. Oliveira, G. de Castro Rodrigues, S. M. L. Gontijo, I. S. Lula, M. E. Cortés, Â. M. L. Denadai, and R. D. Sinisterra, "Development of sulfadiazine-decorated PLGA nanoparticles loaded with 5-fluorouracil and cell viability," *Molecules,* vol. 20, no. 1, pp. 879-899, 2015.

[271] G. Jiao, X. He, X. Li, J. Qiu, H. Xu, N. Zhang, and S. Liu, "Limitations of MTT and CCK-8 assay for evaluation of graphene cytotoxicity," *Rsc Advances,* vol. 5, no. 66, pp. 53240-53244, 2015.

[272] K.-H. Liao, Y.-S. Lin, C. W. Macosko, and C. L. Haynes, "Cytotoxicity of graphene oxide and graphene in human erythrocytes and skin fibroblasts," *ACS applied materials & interfaces,* vol. 3, no. 7, pp. 2607-2615, 2011.

[273] S. R. ur Rehman, R. Augustine, A. A. Zahid, R. Ahmed, M. Tariq, and A. Hasan, "Reduced graphene oxide incorporated GelMA hydrogel promotes angiogenesis for wound healing applications," *International Journal of Nanomedicine,* vol. 14, p. 9603, 2019.

[274] M. Zhou, S. Liu, Y. Jiang, H. Ma, M. Shi, Q. Wang, W. Zhong, W. Liao, and M. M. Xing, "Doxorubicin-loaded single wall nanotube thermo-sensitive hydrogel for gastric cancer chemo-photothermal therapy," *Advanced Functional Materials,* vol. 25, no. 29, pp. 4730-4739, 2015.

[275] X. Zhu, Y. Zhang, H. Huang, H. Zhang, L. Hou, and Z. Zhang, "Functionalized graphene oxide-based thermosensitive hydrogel for near-infrared chemo-photothermal therapy on tumor," *Journal of biomaterials applications,* vol. 30, no. 8, pp. 1230-1241, 2016.

[276] Y. Yang, L. Zhu, F. Xia, B. Gong, A. Xie, S. Li, F. Huang, S. Wang, Y. Shen, and D. T. Weaver, "A novel 5-FU/rGO/Bce hybrid hydrogel shell on a tumor cell: one-step synthesis and synergistic chemo/photo-thermal/photodynamic effect," *RSC advances,* vol. 7, no. 5, pp. 2415-2425, 2017.

[277] Y. Chang, S. T. Yang, J. H. Liu, E. Dong, Y. Wang, A. Cao, Y. Liu, and H. Wang, "In vitro toxicity evaluation of graphene oxide on A549 cells," (in eng), *Toxicol Lett,* vol. 200, no. 3, pp. 201-10, Feb 5 2011.